

## ABSTRACT

Title of Dissertation:           **PREDICTION OF PERMANENT  
DEFORMATION IN ASPHALT CONCRETE**

Regis Luis Egual de Carvalho, Doctor of  
Philosophy, 2012

Directed By:                   Professor Charles W. Schwartz  
Department of Civil and Environmental Engineering

Permanent deformation is a major distress in flexible pavements that leads to the development of rutting along the wheel path of heavily trafficked roads. Early detection of rutting is very important for preventive maintenance programs and design of rehabilitation strategies. Rutting by definition is the accumulated permanent deformation that remains after removal of the load. Rigorous modeling of permanent deformations using nonlinear finite element analysis based on the correct physical mechanism of residual deformations after removal of the load provides important insights into the rutting problem. This dissertation documents the study of permanent deformation in asphalt concrete in pavement structures using a fully mechanistic model based on Schapery's viscoelasticity and Perzyna's viscoplasticity theories. The model is calibrated and implemented in a 3D finite element commercial software package. Two calibration procedures are performed and discussed. Two immediate

practical applications are shown and a simulation of full scale accelerated pavement test is performed.

This research demonstrates that the Perzyna-HiSS viscoplastic model can be successfully calibrated using either research-grade creep and recovery tests or the more simple and production-oriented Flow Number test. The importance of induced shear stress reversals under a moving wheel load is documented. The 3D finite element simulation is then used to identify the fundamental differences on how rutting develops in different pavement structures in terms of the differences in the transverse profile and distribution of rutting within the layer. The analysis results are used to develop new pavement-specific depth functions for potential future incorporation into the AASHTO Mechanistic-Empirical Pavement Design Guide (MEPDG). Lastly, the 3D finite element model is used to predict rutting at one lane of the FHWA's full-scale Accelerated Load Facility experiment. After correction for some anomalies during the early loading cycles in the experiment, the predicted and measured rutting at the center of the wheel path were in good agreement.

**PREDICTION OF PERMANENT DEFORMATION IN ASPHALT  
CONCRETE**

By

Regis Luis Igual de Carvalho

Dissertation submitted to the Faculty of the Graduate School of the  
University of Maryland, College Park, in partial fulfillment  
of the requirements for the degree of  
Doctor of Philosophy  
2012

Advisory Committee:  
Professor Charles W. Schwartz, Chair  
Professor. Ahmet H. Aydilek  
Professor. Dimitrios G. Goulias  
Professor M. Sherif Aggour  
Dr. Nelson H. Gibson  
Professor Sung Lee

© Copyright by

Regis Luis Carvalho

2012

## **DEDICATION**

To my wife Ana for her patience, unconditional love and support during this long journey. Her strength and dedication to our family proved to be the foundation necessary to conclude this research. Thank you, Tita. To my daughter Aila, who was born during this research, for bringing me joy, happiness and much needed inspiration. Thank you, my Beluginha.

I love you both very much.

## ACKNOWLEDGEMENTS

As I reach the final frontier of my academic training in what I hope will be a continuation of an interesting and rewarding career in pavement engineering, I would like to acknowledge the support of many without whom this work would not have been possible.

First and foremost, I wish to thank my advisor, Professor Charles W. Schwartz for his guidance, encouragement, support and patience. His dedication and sincere interest in science and engineering inspired me to always try my best. I am grateful for having him as a mentor. I will take his valuable advice with me for the challenges ahead.

I would like to thank my committee members, Professor Sherif Aggour, Dr. Dimitrios Goulias, Dr. Ahmet Aydilek, Professor Sung Lee and Dr. Nelson H. Gibson for their very helpful insights, comments, suggestions and valuable advice.

This research was partially supported by the National Cooperative Highway Research Program (NCHRP) of the Transportation Research Board, division of the National Research Council. I would like to express my gratitude to Mr. Harold Von Quintus, Principal Investigator, and Ed Harrigan, NCHRP program manager for the NCHRP Project 9-30A.

I would like to also acknowledge the support of Federal Highway Administration, and specially Dr. Nelson H. Gibson, for providing all laboratory specimens used in this research, for sharing laboratory test results and participating in important discussions that led to the results of this research.

I must express my gratitude to the many friends I made during my academic years at the University of Maryland for their support and valuable discussions, in special, Dr. Nelson Gibson, Dr. Mehmet Melih Demirkan, Dr. Emin Kutay, Dr. Haejin Kim, and Dr. Bora Cetin. Additionally, I would like to acknowledge all the staff of the Department of Civil and Environmental Engineering for providing technical support and assistance throughout these years.

My gratitude to many colleagues I made during my professional career at Dynatest Engenharia, Applied Research Associates and Dynatest Consulting, in special, Dr. Ernesto Preussler, Mr. Rui Margarido, Dr. André Vale, Dr. Douglas Negrão, Mr. Josiley Prado, Dr. Manuel Ayres Jr., Dr. Samuel Hautequest Cardoso, Dr. Edith Arámbula, Mr. Richard Stubstad, Mr. Robert Briggs, Mr. Salil Gokhale and Dr. Kurt Keifer.

Finally, I would like to express my endless gratitude to my family, my brother Arthur, my sisters Nathalia and Lele, my mother Vitória Regia, Edu and Flavia Vila, Candy and Heloisa Vila for their love and support, and specially to my father eng. Luiz Antônio Carvalho, who always believed in me and encouraged me to pursue my dreams.

## TABLE OF CONTENTS

<b>Chapter 1 Introduction.....</b>	<b>1</b>
1.1. Problem Statement.....	3
1.2. Objective.....	5
1.3. Document Layout .....	6
<b>Chapter 2 Modeling Permanent Deformation of Asphalt Concrete.....</b>	<b>8</b>
2.1. Introduction.....	8
2.2. Mechanistic-Empirical Modeling .....	12
2.2.1. Mechanistic-Empirical Modeling Limitations .....	19
2.3. Asphalt Concrete Mechanistic Modeling .....	26
2.3.1. Linear Viscoelastic Behavior .....	28
2.3.2. Viscoelastic Continuum Damage Behavior .....	36
2.3.3. Viscoplastic Behavior .....	41
2.4. Summary .....	48
<b>Chapter 3 Materials and Test Equipment .....</b>	<b>51</b>
3.1. Mixture Characteristics.....	52
3.2. Specimen Preparation .....	53
3.3. Testing Equipment.....	57
3.4. Summary .....	59
<b>Chapter 4 Model Calibration .....</b>	<b>60</b>
4.1. Linear Viscoelastic Component.....	60
4.1.1. Complex Modulus Testing.....	61

4.1.2. Dynamic Modulus Master Curve.....	64
4.1.3. Relaxation Modulus and Creep Compliance .....	69
4.2. Continuum Damage Model.....	73
4.2.1. Constant Strain Rate Tests to Failure.....	75
4.2.2. Calibration of Damage Function $C_{11}$ .....	77
4.2.3. Calibration of Damage Function $C_{12}$ .....	79
4.2.4. Calibration of Damage Function $C_{22}$ .....	81
4.3. Viscoplastic Model .....	82
4.3.1. Multi-Stress/Load Duration Tests.....	84
4.3.2. Viscoplastic Model Calibration .....	87
4.3.3. Validation with the Flow Number Test .....	89
4.4. Calibration of the Viscoplastic Model Using the Flow Number Test .	91
4.4.1. Validation with the Multi-Stress/Load Duration Test.....	93
4.5. Summary .....	94
<b>Chapter 5 Finite Element Modeling .....</b>	<b>96</b>
5.1. Introduction.....	96
5.2. Finite Element Method .....	97
5.2.1. Geometric Model and Boundary Conditions .....	98
5.2.2. Meshing and Element Definition .....	99
5.2.3. Material Property Specification .....	102
5.2.4. Loading Conditions.....	103
5.2.5. Simulation .....	104
5.3. Viscoelastic-Viscoplastic Model Implementation .....	105

5.3.1. Numerical Difficulties and Simplifications .....	109
5.4. Model Verification.....	112
5.5. Summary .....	115
<b>Chapter 6 Numerical Applications .....</b>	<b>116</b>
6.1. Introduction.....	116
6.2. Simplified Finite Element Modeling Approach.....	117
6.3. Influence of Shear Stress Reversals.....	120
6.4. Practical Applications of Finite Element Simulations.....	129
6.4.1. Predicted Rutting Comparison between Different Pavement Structures .....	130
6.4.2. Analysis of the MEPDG Depth Factor for Rutting Predictions..	135
6.4.3. Conclusions.....	141
6.5. Field rutting predictions.....	142
6.5.1. Description of FHWA ALF .....	142
6.5.2. Numerical Simulation .....	146
6.5.3. Conclusions.....	154
<b>Chapter 7 Conclusions and Recommendations .....</b>	<b>156</b>
7.1. Model Calibration.....	158
7.2. Moving Wheel Analyses.....	160
7.3. Effect of Different Pavement Structures.....	160
7.4. MEPDG Depth Factor for Rutting Predictions.....	162
7.5. Field Rutting Predictions .....	162
7.6. Recommendations.....	163

<b>Appendix A. Viscoelastic-Viscoplastic UMAT .....</b>	<b>166</b>
<b>Appendix B. Elasto-Viscoplastic UMAT .....</b>	<b>205</b>
<b>References.....</b>	<b>237</b>

## LIST OF TABLES

Table 1. Laboratory mixture design.....	53
Table 2. Stresses applied in the dynamic modulus test.....	63
Table 3. Summary of dynamic modulus testing. ....	63
Table 4. Dynamic master curve and temperature shift factors. ....	69
Table 5. Prony series constants for relaxation modulus and creep compliance.....	72
Table 6. Damage function $C_{12}$ calibration coefficients.....	80
Table 7. Deviatoric stress and frequency used on multi-stress/load duration test. ....	85
Table 8. Viscoplastic model calibration coefficients.....	87
Table 9. Comparison between the two viscoplastic model calibrations. ....	92
Table 10. Material properties used for studying the effects of the bouncing versus the moving wheel.....	126
Table 11. Structure-based depth function coefficients . ....	141

## LIST OF FIGURES

Figure 1. Components of measured surface rutting.....	8
Figure 2. Effects of rutting concentration in different layers on permanent deformation surface profile of flexible pavements: (a) asphalt concrete, (b) granular base, and (c) subbase/subgrade (White et al., 2002) .....	9
Figure 3. Rutting development versus load applications.....	11
Figure 4. Influence of depth function $\beta_{\sigma_3}$ on calculated permanent vertical strains from the MEPDG model (150 mm HMA layer over crushed stone base, first load cycle).....	22
Figure 5. Computed total strains beneath tire center at peak load: (a) vertical; (b) horizontal (Schwartz and Carvalho, 2008). .....	23
Figure 6. Residual total strains from the EPFE analysis after removal of load. ....	24
Figure 7. Residual total vertical strains beneath the tire center from EPFE analyses for different number of cycles. ....	25
Figure 8. Generalized Maxwell model.....	32
Figure 9. Complex modulus response.....	33
Figure 10. Example of master curve. ....	35
Figure 11. Example of temperature shift function. ....	35
Figure 12. One-dimensional elasto-viscoplastic rheological model. ....	42
Figure 13. Three-dimensional representation of HiSS surface in principal stress space (Gibson, 2006). ....	47
Figure 14. Schematic of flow rule and surface hardening (Gibson, 2006). ....	48

Figure 15. Asphalt concrete mixture aggregate gradation.....	52
Figure 16. Axial LVDT instrumentation.....	55
Figure 17. Radial LVDT setup.....	56
Figure 18. Dynamic modulus master curve.....	66
Figure 19. Temperature shift function.....	67
Figure 20. Comparison between MEPDG and Hirsch master curves.....	69
Figure 21. Storage modulus master curve.....	71
Figure 22. Relaxation modulus and creep compliance.....	72
Figure 23. Unconfined strain rate tests at 10°C: stress <i>versus</i> strain curves for strain rates of 0.0001 and 0.0008 $\epsilon$ /second.....	76
Figure 24. Confined strain rate tests at 10°C: stress <i>versus</i> strain curves for strain rates of 0.0001 and 0.0008 $\epsilon$ /second.....	77
Figure 25. Damage function $C_{11}$ versus $S$ for all replicates at 10°C.....	78
Figure 26. Poisson's ratio variation during the strain rate tests.....	80
Figure 27. Damage function $C_{12}$ versus $S$ for all replicates at 10°C.....	81
Figure 28. Damage function $C_{22}$ versus $S$ for all replicates at 10°C.....	82
Figure 29. Example of multi-stress/load duration creep and recovery test.....	86
Figure 30. Creep and recovery viscoplastic strains versus load cycles.....	86
Figure 31. Viscoplastic model calibration using cyclic creep and recovery tests: (a) unconfined and (b) confined.....	88
Figure 32. Predicted versus measured strains in the Flow Number validation test....	90
Figure 33. Viscoplastic model calibration using the Flow Number test.....	92

Figure 34. Predicted versus measured viscoplastic strains from multi-stress/load duration creep and recovery tests: (a) unconfined and (b) confined. Predicted strains computed using the FN-calibrated model.....	93
Figure 35. 3D solid model. ....	99
Figure 36. Plan (surface) view of geometric model.....	101
Figure 37. Surface layer mesh in plan view.....	101
Figure 38. 3D finite element mesh.....	102
Figure 39. Schematic of moving load. ....	104
Figure 40. Example of HiSS surface and the limit where normal vectors to the surface can be calculated. ....	111
Figure 41. Schematics of creep and recovery test at fixed stress level and varying loading time. ....	113
Figure 42. Fixed stress test with 1,500 kPa deviator stress, unconfined, tested at 35°C. ....	114
Figure 43. Fixed stress test with 1,500 kPa deviator stress and 250 kPa confining stress, tested at 35°C. ....	114
Figure 44. Influence of temperature on viscoplastic behavior of asphalt concrete in a simulated creep and recovery test. ....	118
Figure 45. Comparison between viscoelastic-viscoplastic and elasto-viscoplastic simulation of creep and recovery at two different temperatures.....	119
Figure 46. Permanent deformation comparison between a moving wheel load and repeated vertical load (Brown et al., 1996).....	122

Figure 47. Stress distributions over time at the location of maximum shear for one moving wheel pass.....	123
Figure 48. Stress distributions over time at the location of maximum shear for one bouncing wheel load. ....	123
Figure 49. Comparison between permanent vertical strains induced by loading histories with and without principal stress rotations.....	125
Figure 50. Comparison between stress state paths induced by moving and bouncing wheel at the location of highest shear stress. ....	125
Figure 51. Comparison between moving and bouncing wheel finite element simulations.....	127
Figure 52. Comparison between strain distributions within the asphalt concrete surface layer when moving and bouncing wheel are considered. MnRoad rutting distribution from trench studies is shown in the inset.....	128
Figure 53. Pavement structures: (a) conventional flexible, (b) full depth asphalt concrete, and (c) composite. ....	132
Figure 54. Asphalt rutting for different pavement structures. ....	132
Figure 55. Comparison of rutting transverse profiles for different pavement structures. ....	134
Figure 56. Comparison of permanent strain distributions with depth for different pavement structures. ....	135
Figure 57. MEPDG depth function analysis for the conventional flexible pavement. ....	138

Figure 58. Calibrated depth function results for the full depth asphalt concrete pavement.....	139
Figure 59. Calibrated depth function results for the composite pavement .....	140
Figure 60. Layout of the 12 as-built pavement lanes (Qi et al., 2004). .....	143
Figure 61. Layer deformation measurement assembly used to measure rut depth (Gibson, 2011) .....	145
Figure 62. Rutting measurements at Lane 11 of the ALF.....	145
Figure 63. Load equivalency – equivalent accumulated load cycles <i>versus</i> tire pass. ....	148
Figure 64. Computed permanent deformation for 100-cycle sequential and 500-cycle load equivalent. ....	149
Figure 65. EVP finite element predicted rutting for the first 100 cycles.....	150
Figure 66. Ratio $a_N/a_{100}$ as function of number of cycles. ....	151
Figure 67. Predicted and measured rutting for the ALF lane 11. ....	153
Figure 68. Comparison between predictions using moving and bouncing wheel for the ALF lane 11. ....	154

## **Chapter 1 Introduction**

Permanent deformation occurs in most of the pavement layers and causes the development of ruts along the wheel path at the surface. Early detection of rutting is very important for preventive maintenance programs and design of rehabilitation strategies.

Rutting is defined as a longitudinal surface depression occurring in the wheel paths of roadways (FHWA, 2003). It is often followed in later stages by an upheaval along the sides of the rut. It can lead to structural failure and potential danger from hydroplaning. Rutting accumulates incrementally with small permanent deformations from each load application over the pavement's service life. Rutting is by definition a load-related pavement distress.

The total rutting is the combination of accumulated permanent deformation in all layers in the pavement structure. Some research suggests that the shape of the surface profile can indicate which layer is responsible for the failure of the pavement structure due to rutting. In well-designed flexible pavements, trench studies show that nearly all of the total rutting occurred within the top 150 mm of surface asphalt concrete layer.

Two mechanisms are the main causes of rutting development. Compaction is the primary mechanism at initial stages of loading, in which the material volume decreases underneath the wheel path with no significant upheaval along the sides of the wheel path. After this initial stage is complete, distortion without volume alteration occurs and the material beneath the wheel path migrates to the edge forming the upheaval along the. This deformation mode is essentially caused by shear. Excessive accumulation of shear deformation leads to structural failure.

Three types of models are used to compute permanent deformations: empirical, mechanistic-empirical and fully mechanistic. Examples of empirical models are regression equations fitted to observed field data. They are often the simplest mathematical form and include no material related properties or site parameters and are commonly used in specific applications such as performance predictions in pavement management systems. The intention in these cases is to estimate future performance based solely on the recorded distress history as a mere extrapolation.

Mechanistic-empirical models (M-E) are based on a combination of simple mechanistic response predictions coupled with empirical distress models, also called transfer functions, for predicting field performance (e.g., rutting, cracking). During application, the mechanistic portion of the model is obtained through a structural analysis of the pavement subjected to traffic loading and environmental inputs. Linear elasticity is often used for its relatively simple formulation and fast computer calculations.

Fully mechanistic models rely on complex constitutive models to directly predict permanent deformations, cracking and other distresses. With the vast capabilities of the mechanistic approach, the influence of different loading (e.g., duration, magnitude) and environmental (e.g., temperature) conditions can be evaluated and incorporated directly into the constitutive model. Since mechanistic models are capable of directly predicting pavement distresses, there is no need for empirical transfer functions. However, mechanistic models are complex, expensive to calibrate, and computationally expensive to execute. Applications of advanced constitutive models to analyze the behavior of asphalt concrete in pavement structures have been limited. Applied mechanistic modeling is at the leading edge of pavement research.

## 1.1. Problem Statement

There are significant limitations to the use of mechanistic-empirical models to predict permanent deformation in flexible pavements. The most fundamental limitation relies on the simple definition of an empirical relationship—i.e., the use of observed data instead of theory to model a phenomenon. The practical implication is that purely empirical models are generally not applicable to conditions that are significantly different from those used for the model calibration.

The incorporation of mechanistic responses reduces the limitations by making the model dependent on pavement stress and/or strain response that can be calculated for each desired condition. Unfortunately, this improvement has its own limitations and shortfalls. The most basic limitation involves the choice of stress conditions for calibrating the material response and how these compare to actual stress states in the field. An example of this is the development of rutting prediction models based on unconfined repeated load testing performed in the laboratory. In the field the material is constantly subjected to varying confining stresses that drastically change its resistance to permanent deformations.

There are several issues not yet fully resolved for predicting rutting in the asphalt concrete layers in flexible and composite pavement systems. There is still no clear consensus whether rutting is due primarily to axial permanent strains beneath the tire centerline or to shear permanent strains beneath the tire edge. Current M-E rutting models relate permanent strains (axial or shear) to resilient strains computed using multilayer elastic theory. However, in the absence of correction factors, rutting predicted from these resilient strains is in sharp disagreement with field observations. Thickness or depth

correction factors are required to bring predictions in line with observations, which significantly weaken the mechanistic linkage between computed strains and predicted rutting. Current M-E models often assume that the mechanisms and distributions of permanent strains are similar for asphalt concrete layers in any pavement type (e.g., flexible pavements versus overlays on rigid pavements), which is generally not true. And finally, current M-E models are not capable of predicting the entire rutting profile, which includes the settlement at the center of the wheel path and side heaves at the edge of the wheel paths.

Moreover, multidimensional confinement and plastic flow interactions, which intuitively should strongly influence the permanent deformation response, are treated only in a very approximate way via the empirical thickness/depth corrections in M-E models. There are simpler alternatives based on nonlinear constitutive models, such as elasto-plasticity, that are capable of qualitatively correcting these discrepancies, but are not capable of fully addressing the behavior of asphalt concrete mixtures.

Advanced mechanistic modeling employs theories of mechanics that are more suitable for describing the real material behavior. A major shortcoming is the complexity of these theories, and in particular the constitutive models. The constitutive model is the mathematical formulation representing the relationship between stresses, strains, and temperatures (and perhaps other state variables) that governs the material deformation under induced load and environmental conditions.

Asphalt concrete is a complex material in which recoverable and irrecoverable strains are dependent on temperature, stress and strain rates. Therefore, viscoelasticity and viscoplasticity theories are most appropriate to model the recoverable and

irrecoverable behavior respectively. The use of advanced mechanistic modeling implemented in a more rigorously nonlinear finite element model can help address some of the issues mentioned and reduce the gap between rutting predictions and field measured performance.

## **1.2. Objective**

The objective of this research is to implement an advanced constitutive model in a finite element analysis framework to predict permanent deformation in asphalt concrete pavements. The model, developed in previous research, is based on Schapery's viscoelasticity and Perzyna's viscoplasticity theories.

To achieve this objective, the model formulation is reviewed. Laboratory testing of a modified asphalt concrete mixture used in the Federal Highway Administration's full-scale Accelerated Loading Facility (ALF) is used to calibrate and validate the model. A particular focus of the calibration is the viscoplastic model component, which is the most relevant for the rutting problem. Two calibration procedures are tried, one using a research-grade creep and recovery test designed specifically for this research, and one using the Flow Number test intended for routine mix design evaluation. The calibrated model is implemented as a user defined material constitutive model in the commercial finite element package ABAQUS™.

The finite element model is used to simulate a moving wheel and to analyze the permanent deformation behavior in the asphalt concrete layer in three dimensional pavement structures. The results are compared with the widely used bouncing wheel loading, which is the most typical simplification of traffic loading in pavement analyzes.

In addition, different pavement structures are evaluated. The results are used to evaluate the depth correction functions used in the AASHTO's Mechanistic-Empirical Pavement Design Guide (MEPDG). Finally, the model is used to predict rutting in one of the FHWA's ALF tests. This predicted rutting is compared against field measurements.

### **1.3. Document Layout**

The dissertation is organized as follows. Asphalt concrete permanent deformation modeling techniques are described in Chapter 2, including a brief overview of past empirical models and description of more recent mechanistic-empirical models. Advantages and pitfalls observed in current models are discussed in greater detail and advanced modeling is introduced as an alternative to overcome some of these pitfalls. Chapter 2 concludes with a theoretical description of the viscoelastic-viscoplastic (VEVP) model used in this research. Chapter 3 describes the material and the laboratory equipment used to calibrate the VEVP model. The calibration process is provided in Chapter 4, in which laboratory tests, calibration techniques and results are discussed. Chapter 5 presents the implementation of the VEVP constitutive model as a user defined material model in ABAQUS™ finite element software. Numerical applications of the finite element model are provided in Chapter 6. A simplified finite element model is introduced. The importance of considering traffic loading as a moving wheel instead of bouncing wheel – typically used to represent traffic loading – is discussed. Two practical applications of the finite element model are also presented. Chapter 6 concludes with the description and simulation of an accelerated field pavement testing using the finite

element model. The overall summary, conclusions and recommendations from this research are presented in Chapter 7.

## Chapter 2 Modeling Permanent Deformation of Asphalt Concrete

### 2.1. Introduction

Rutting is a major distress in flexible pavements. Changes in traffic conditions, mainly in tire and axle configurations, contributed significantly to make rutting a predominant mode of failure of flexible pavements in the 1980s and 90s. Rutting is defined as a longitudinal surface depression occurring in the wheel paths of roadways (FHWA, 2003). It is often followed in later stages by an upheaval along the sides of the rut. It can lead to structural failure and potential danger from hydroplaning. Rutting accumulates continuously and incrementally with small permanent deformations from each load application. Rutting is by definition a load-related pavement distress.

There are many techniques for measuring permanent deformations at the surface of the pavement layer. One of the simplest approaches is to use a straightedge, as shown in Figure 1. The total measured rutting is a combination of the settlement in the center and the heave at the edges of the wheel path. Although traffic wander tends to reduce the heave at the edges of the wheel path, it can be a prominent feature in heavily rutted pavements, especially in combination with channelized traffic.

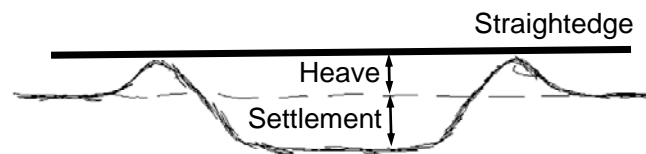


Figure 1. Components of measured surface rutting.

The total rutting is the combination of accumulated permanent deformation in all layers in the pavement structure. Some research suggests that the shape of the surface profile can indicate which layer is responsible for the failure of the pavement structure due to rutting (Simpson et al., 1995; White et al., 2002). Figure 2 shows three transverse profiles typical of three different scenarios in which majority of rutting comes from (a) asphalt concrete surface layer, (b) granular base and (c) subbase/subgrade. If the majority of rutting originates in the underlying unbound base and subbase layers, little or no heave is observed. When the asphalt concrete layer is responsible for total rutting, heave is observed. In extreme situations of very stiff underlying layers – e.g., composite pavement with a Portland cement (PCC) slab acting as a base layer – the heave may dominate the settlement portion. The majority of the failures from rutting are due to excessive deformation in the asphalt concrete layer (White et al., 2002).

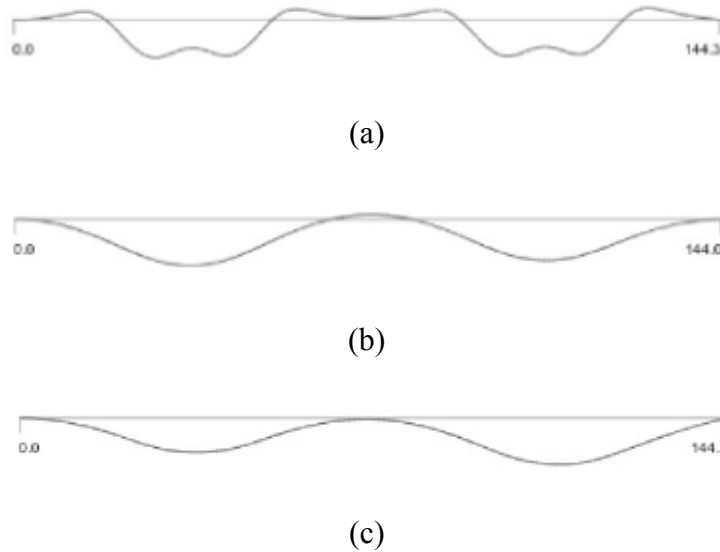


Figure 2. Effects of rutting concentration in different layers on permanent deformation surface profile of flexible pavements: (a) asphalt concrete, (b) granular base, and (c) subbase/subgrade (White et al., 2002)

Forensic trenches are the preferred approach for determining the permanent deformation in each layer. However, very few field pavement test sites have been trenched. Test tracks such as Westrack and MnRoad are the best sources for trench data. Researchers found that nearly all of the total rutting occurred within the top 150 mm of HMA at Westrack (Epps *et al.* 2002). Additional detailed data from the MnRoad test sections, where permanent deformations were measured for every 40 to 50 mm of the asphalt layer, further suggests that most of the rutting occurs within the top 100 to 150 mm of the surface layer (Mulvaney and Worel, 2002).

Two mechanisms are the main causes of rutting development. Compaction is the primary mechanism at initial stages of loading. Compaction (i.e., densification) occurs as the material volume decreases underneath the wheel path with no significant upheaval along the sides of the wheel path. After this initial stage is complete, further volume decrease of material beneath the wheel path at each load application approximately equals the volume increase in the upheaval along the sides. This deformation mode is essentially caused by shear (i.e., distortion without volume alteration). When enough distortion has occurred, the asphalt concrete undergoes shear flow and deformations increase rapidly at an increasing rate termed tertiary flow. Figure 3 depicts rutting development versus load application in which region 1 is mainly caused by material densification, region 2 is predominately shear deformations, and region 3 is tertiary flow to shear failure.

The primary stage, represented by region 1 in Figure 3, happens early on in the pavement's service life, usually within the first year. The pavement will probably be rehabilitated prior to reaching the tertiary stage (region 3) due to rutting already reaching

the agency's threshold or another distress triggering the need for maintenance. Therefore, rutting modeling is usually restricted to the secondary stage (region 2).

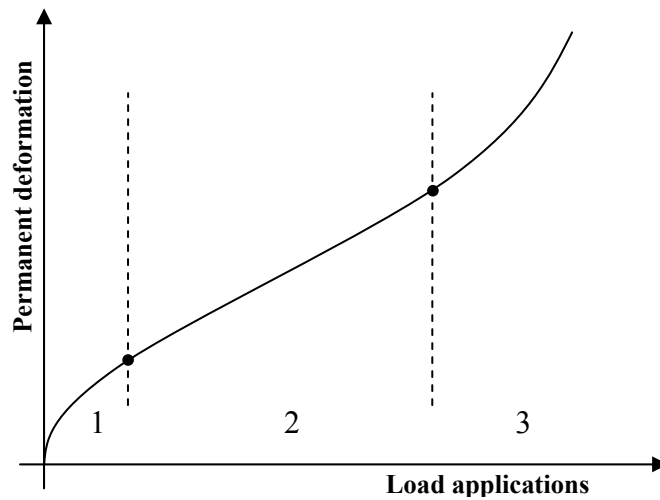


Figure 3. Rutting development versus load applications.

Three types of model are used to compute permanent deformations: empirical, mechanistic-empirical and fully mechanistic. Examples of empirical models are regression equations fitted to observed field data. They are often the simplest mathematical form for representing relationships in the data. They often include no material related properties or site parameters and are commonly used in specific applications such as performance predictions in pavement management systems. The intention in these cases is to estimate future performance based solely on the recorded distress history as a mere extrapolation.

Mechanistic-empirical models (ME) are developed based on a combination of simple mechanistic response predictions (i.e., often using elasticity theory) with empirical equations calibrated using laboratory testing in which stress conditions representing field conditions are replicated. The calculated mechanistic response is used as input in the

empirical model, also called transfer function, to predict field performance (e.g., rutting, cracking). The influence of temperature and loading conditions (e.g., frequency) can be incorporated. During application, the mechanistic portion of the model is obtained through a structural analysis of the pavement subjected to traffic loading and environmental inputs. Linear elasticity is often used for its relatively simple formulation and fast computer calculations.

Fully mechanistic models also use a structural analysis program to evaluate the stresses and strains in the pavement structure due to traffic loading and environmental conditions. Complex constitutive models are used to represent the different aspects of material behavior and to directly predict permanent deformations, cracking and other distresses. With the vast capabilities of the mechanistic approach, the influence of different load conditions (e.g., duration, magnitude and temperature) can be easily evaluated and incorporated directly into the constitutive model. Since mechanistic models are capable of directly predicting pavement distresses, there is no need for empirical transfer functions. However, mechanistic models are complex, expensive to calibrate, and computationally expensive to execute. Few researches have been done to implement mechanistic models to predict asphalt concrete behavior. Applied mechanistic modeling is still ahead of the frontline of research.

## **2.2. Mechanistic-Empirical Modeling**

Early attempts to model rutting date to the 1950's, when Kerkhoven and Dormon (1953) first suggested the use of vertical compressive strain on the top of the subgrade as a failure criterion to minimize permanent deformation. Dormon and Metcalf (1965)

incorporated strain-based criteria in a mechanistic-empirical procedure using 1940's Burmister multi-layer linear elastic solutions. Later, this criterion was used as part of the Asphalt Institute design method (Shook et al., 1982). The classic pavement design approach considered Kerkhoven and Dormon's failure criterion for rutting and a similar one for fatigue cracking (i.e., the tensile strain at the bottom of the surface asphalt concrete layer). The rutting shear resistance of the asphalt concrete was considered only in the mix design, through the Marshal method.

Following test track experiments from the 1950's and 1960's, including the AASHO Road Test, researchers developed rutting models based on regression analysis of observed field data. Finn et al. (1977) developed a rutting regression model relating surface deflection to the vertical compressive stress in the asphalt concrete layer. Claussen et al. (1977) developed an empirical rutting model based on subgrade vertical strain, which was incorporated into the Shell pavement design procedure.

At this same time there were initial efforts to develop models based on laboratory tests that could provide a better representation of the loading condition in the field. One of the first models developed incorporated results from unconfined repeated load permanent deformation (RLPD) tests and was implemented in the VESYS program (Kenis et al., 1977). This followed work done previously with granular base materials and soils done by Barksdale (1972) and Monismith (1975). Moreover, this model formulation was the first to describe asphalt concrete rutting as power law:

$$\Delta\varepsilon_p(N) = \varepsilon\mu N^{-\alpha} \quad (1)$$

in which  $\Delta\varepsilon_p(N)$  is the incremental permanent vertical strain caused by the  $N^{th}$  load cycle,  $\varepsilon$  is the mechanistically-computed peak total vertical strain (usually taken as the resilient

strain,  $\varepsilon_e$ ), and  $\mu$  and  $\alpha$  are material parameters determined from laboratory RLPD tests. The VESYS model is considered the predecessor of the current power law models. This type of model is particularly useful because it fits quite well the secondary stage of rutting behavior (i.e. linear in log-log space).

Repeated load permanent deformation testing became a typical laboratory procedure for characterizing rutting behavior of asphalt mixtures. Allen and Deen (1980) developed a regression model based on unconfined RLPD with different deviator stresses and temperatures. The third order polynomial model resulting from the regression analysis had the following general form:

$$\log(\varepsilon_p) = C_0 + C_1(\log N) - C_2(\log N)^2 + C_3(\log N)^3 \quad (2)$$

Rauhut (1980) presented some quantitative influence of mixture type and deviator stress on  $\mu$  and  $\alpha$  in Eq. (1) based on limited unconfined RLPD data analysis. Leahy (1989) increased the number of experiments and enhanced these correlations including temperature and some material characteristics (i.e., effective binder content, air voids and binder viscosity). Over 250 asphalt concrete specimens encompassing two aggregate types, two binder types, three binder contents, three stress levels, and three temperatures were tested. The model formulation is as follows:

$$\log\left(\frac{\varepsilon_p}{\varepsilon_r}\right) = -6.631 + 0.435\log N + 2.767\log T + 0.110\log \sigma_d + 0.118\log \eta + 0.930\log V_{beff} + 0.501\log V_a \quad (3)$$

in which  $\varepsilon_p$  is the permanent strain,  $\varepsilon_r$  is the resilient strain,  $N$  is number of load cycles,  $T$  is temperature ( $^{\circ}$  F),  $\sigma_d$  is deviatoric stress (psi),  $\eta$  is binder viscosity at 70 $^{\circ}$ F ( $\times 10^6$  poise),

$V_{beff}$  is effective binder volume and  $V_a$  is air voids. The R-squared value for Eq. (3) was 0.76.

Ayres (1997) re-analyzed Leahy's original data plus additional laboratory test data and recommended a model of the form:

$$\log\left(\frac{\varepsilon_p}{\varepsilon_r}\right) = -4.8066 + 0.4296 \log N + 2.5816 \log T \quad (4)$$

in which the parameters are as defined previously for Eq. (3). The slightly lower  $R^2$  of 0.72 for this model is the consequence of removing four mix-related parameters from the Leahy model, Eq. (3). This small drop confirmed the relatively small importance of these parameters as compared to temperature and number of load repetitions.

Kaloush (2001) further improved the rutting model in Eq. (4) by combining Leahy's original data with the very large number of repeated load permanent deformation test results from NCHRP Project 9-19, yielding a revised model of the form:

$$\log\left(\frac{\varepsilon_p}{\varepsilon_r}\right) = -3.1555 + 0.3994 \log N + 1.7340 \log T \quad (5)$$

in which the parameters are as defined previously. The lower  $R^2$  value of 0.64 compared to Ayres' was attributed to the much broader and more diverse data set analyzed by Kaloush (El-Basyouny, 2004). Kaloush's regression model was the starting point for the rutting model implemented in the newly developed Mechanistic –Empirical Pavement Design Guide (MEPDG) (NCHRP, 2004).

Field calibration of Eq. (5) was performed as part of the MEPDG development in NCHRP Project 1-37A. The Long Term Pavement Performance (LTPP) database was the main source of data for the calibration (El-Basyouny, 2004). Recent work done under NCHRP Project 1-40D (NCHRP 1-40D, 2006) revised the field calibration, producing

the rutting model implemented in the most recent version of the MEPDG software (version 1.1):

$$\frac{\varepsilon_p}{\varepsilon_r} = \left[ 10^{-3.3542} T^{1.5606} N^{0.4792} \right] \quad (6)$$

in which all variables are defined as previously.

The database underlying Eq. (3) through Eq. (5) is based only on unconfined conditions. In reality, substantial horizontal stresses develop in an asphalt layer during wheel loading/unloading, ranging from compression at the top to tension at the bottom (assuming a linear elastic asphalt concrete response) and varying through the HMA thickness. A depth correction factor was developed in the MEPDG to adjust the computed plastic strain due to confining pressure at different depths:

$$\beta_{\sigma_3} = (C_1 + C_2 \cdot depth) \cdot 0.328196^{depth}$$

$$C_1 = -0.1039 \cdot h_{AC}^2 + 2.4868 \cdot h_{AC} - 17.342 \quad (7)$$

$$C_2 = 0.0172 \cdot h_{AC}^2 - 1.7331 \cdot h_{AC} + 27.428$$

in which *depth* is depth to the computational point of strain calculation, and  $h_{AC}$  is the thickness of the asphalt layer. The final rutting model, including the depth factor is:

$$\frac{\varepsilon_p}{\varepsilon_r} = \beta_{\sigma_3} \left[ 10^{-3.3542} T^{1.5606} N^{0.4792} \right] \quad (8)$$

Another variation of the elastic vertical strain power law model was proposed by Verstraeten (1977, 1982). In this model, the vertical elastic strain is replaced by the ratio between deviatoric stress and the dynamic modulus of the mixture:

$$\varepsilon_p = A \frac{\sigma_1 - \sigma_3}{|E^*|} \left( \frac{N}{1000f} \right)^{b_{AC}} \quad (9)$$

in which,  $\epsilon_p$  is the permanent shear strain,  $\sigma_l$  and  $\sigma_r$  are respectively vertical and radial stresses,  $|E^*|$  is the dynamic modulus of HMA mixture,  $N$  is the number of load cycles,  $f$  is the frequency of loads,  $A$  and  $b_{AC}$  are material parameters. Temperature is also implicitly included in Eq. (9) through its influence on dynamic modulus. For conventional mixtures, the recommended values for the regression coefficients are  $A=57.5$  and  $b_{AC}=0.25$  (D'Apuzzo et al., 2004). It is unclear from the references how  $A$  and  $b_{AC}$  are determined. However it seems plausible to assume that RLPD tests would suffice in determine these calibration coefficients. The inclusion of load frequency as a normalizing factor for the number of load application makes this model different from the VESYS power law model.

An alternative type of empirical model relates permanent deformation to maximum shear strains observed in the asphalt concrete surface layer. Researchers at the Westrack developed this type of model, which excludes densification and assumes shear deformations as the solely rutting mechanism (Monismith et al., 2006). Shear plastic strains are computed using a power law model, which considers the number of load applications and the elastic shear strains as follows:

$$\gamma_p = ae^{b\tau} \gamma_e N^c \quad (10)$$

in which  $\gamma_p$  is the permanent shear strain,  $\tau$  is mechanistically-determined elastic shear stress,  $\gamma_e$  is the mechanistically-determined elastic shear strain, and  $a$ ,  $b$ , and  $c$  are material parameters. The maximum elastic shear stress and strain are expected to be located at the edge of the tire at a depth of 2 inches below the surface. This location was defined based on elastic analysis of two-layer structures with different load conditions and asphalt concrete stiffness (Sousa et al., 1994).

The mechanistically computed elastic shear strain,  $\gamma_{e,t}$ , varies over time in response to traffic variations and influence of temperature on the asphalt concrete stiffness. A time-hardening principle similar to that implemented in the MEPDG is used to estimate the accumulation of permanent strains in the asphalt concrete under varying traffic loading conditions:

$$\begin{aligned}\gamma_{p,1} &= a_1 [\Delta N_1]^c \\ \gamma_{p,t} &= a_t \left[ \left( \frac{\gamma_{p,t-1}}{a_t} \right)^{\frac{1}{c}} + \Delta N_t \right]^c \\ a_t &= a e^{b\tau} \gamma_{e,t}\end{aligned}\tag{11}$$

in which  $\gamma_{e,t}$  is the elastic shear strain for the  $t^{\text{th}}$  period of loading,  $\gamma_{p,t}$  is the corresponding permanent shear strain, and  $\Delta N_t$  is the number of load applications during the  $t^{\text{th}}$  period.

The total rut depth in the asphalt concrete layer is estimated from the permanent shear strain using the following semi-empirical relation:

$$RD_{HMA} = K_r \gamma_{p,t}\tag{12}$$

in which  $K_r$  is a coefficient relating rut depth to permanent strain.  $K_r$  is a function of the asphalt layer thickness; values for  $K_r$  are determined from finite element analyses of representative pavement structures range from about 5.5 for a 6 inch layer to 10 for a 12 inch layer (Deacon et al., 2002).

The regression coefficients  $a$ ,  $b$ , and  $c$  in Eq. (10) and Eq. (11) are determined from repeated load simple shear tests conducted at constant height (RSST-CH). Monismith et al. (2006) describe the calibration process in greater detail. The model scheme was developed, calibrated, and validated for the Westrack sections. Mixtures

commonly used by Caltrans have also been calibrated using RSST-CH test data and validated using Heavy Vehicle Simulation (HVS) full scale accelerated pavement testing system.

### *2.2.1. Mechanistic-Empirical Modeling Limitations*

There are significant limitations to the use of mechanistic-empirical models to predict permanent deformation in flexible pavements. The most fundamental limitation relies on the simple definition of an empirical relationship—i.e., the use of observed experimentation instead of theory to model a phenomenon. The practical implication is that purely empirical models are generally not applicable to conditions that are significantly different from used for the model calibration.

The incorporation of mechanistic responses reduces the limitations by making the model dependent on pavement stress and or strain response that can be calculated for each desired condition. Unfortunately, this improvement also has limitations and shortfalls. The most basic limitation involves the choice of stress conditions from which the model has been calibrated and how they compare to actual stress states in the field, which brings back the problem of conditions during calibration *versus* design/service. An example of this is the development of rutting prediction models based on unconfined repeated load testing performed in the laboratory. In the field the material is constantly subjected to varying confining stresses that drastically change the resistance to permanent deformations.

The methods for determining the required mechanistic responses are another important source of limitation in mechanistic-empirical models. Linear elastic multilayer

theory is most often used to compute the mechanistic responses because it is easy to implement in computer algorithms and comparatively fast to execute. However, this simplification brings many shortfalls.

The mechanistic strains vary with depth and horizontal location within the HMA layers. The specific variation will be a function of the pavement structure, material properties, load configuration, and other factors. M-E rutting models must rationally account for these strain variations within the HMA and other pavement layers when accumulating the predicted permanent deformation at the surface. Empirical calibration factors attempt to bring the predicted surface deformations into better agreement with measured field performance over a wide range of pavement conditions.

There are several issues not yet fully resolved in this framework for predicting rutting in the asphalt concrete layers in flexible and composite pavement systems. First, there is still no clear consensus whether rutting is due primarily to axial permanent strains beneath the tire centerline (e.g., NCHRP, 2004; D'Apuzzo et al., 2004) or to shear permanent strains beneath the tire edge (e.g., Deacon *et al.*, 2002; Monismith et al., 2006). Second, current M-E rutting models relate permanent strains (axial or shear) to resilient strains computed using multilayer elastic theory. However, in the absence of correction factors, the influence of layer thickness on the rutting predicted from these resilient strains is in sharp disagreement with field observations. Thickness or depth correction factors are required to bring predictions in line with observations. These correction factors further weaken the mechanistic linkage between predicted rutting and computed strains in the M-E approach. Third, current M-E models often assume that the mechanisms and distributions of permanent strains are similar for HMA layers in flexible

pavements vs. HMA overlays on rigid pavements, which is generally not true. And fourth, current M-E models do not explicitly consider the contribution of heaving at the edge of the wheel paths (see Figure 1), although this may be implicitly included in the field calibration corrections, given how rutting measurements are taken in the field.

Both the MEPDG depth function  $\beta_{\sigma_3}$  in Eq. (6) and the Westrack  $K_r$  factor in Eq. (12) can be viewed as attempts to compensate for deficiencies in using linearly elastic stress and strain distributions to estimate permanent deformations. Figure 4 compares the variations of the uncorrected versus corrected permanent strains from the MEPDG model. (Note: The standard mechanics sign convention of positive tension applies to this figure.) As dictated by Eq. (6), the uncorrected computed permanent strains are proportional to the mechanistically determined vertical resilient strains, which are largest at the bottom of the HMA layer due to the combination of the direct vertical compression and the compressive Poisson strains induced by the horizontal tensions. As a consequence, the permanent deformations are concentrated in the lower depths of the HMA layer contrary to field experience. The empirical depth correction function distorts both the magnitude and shape of the permanent strain distribution as it attempts to force the majority of the permanent deformations into the upper portions of the HMA layer. The depth correction function dominates the permanent strain values used to compute the total rutting for the layer and, in the process, seriously undermines the “mechanistic” portion of the modeling.

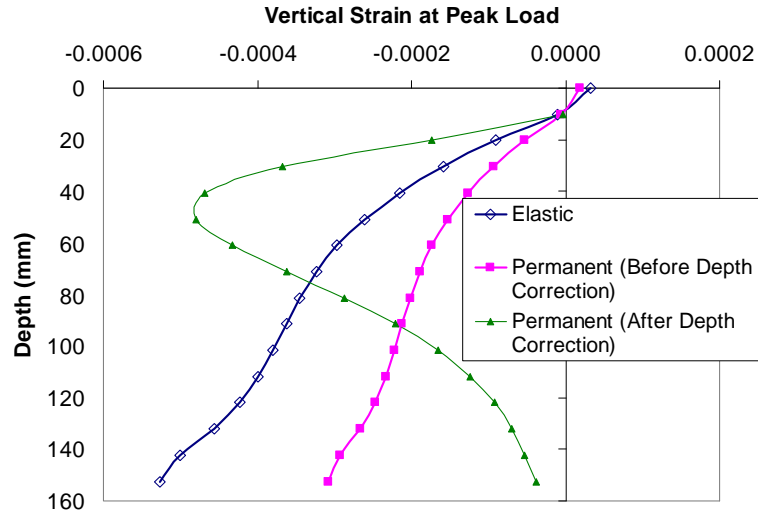


Figure 4. Influence of depth function  $\beta_{\sigma_3}$  on calculated permanent vertical strains from the MEPDG model (150 mm HMA layer over crushed stone base, first load cycle).

The lack on of influence of pavement structure on predictions of mechanistic-empirical models can be demonstrated by using a simple finite element exercise (Schwartz and Carvalho, 2007 and 2008). One typical flexible pavement was modeled using an elasto-plastic finite element model (EPFE). The HMA layer was modeled as an elasto-plastic material using the Drucker-Prager frictional plasticity model with a linear yield surface and an isotropic piecewise linear hardening law. The other materials were modeled as linear elastic. A fully elastic finite element analysis was also performed for comparison.

The impact of plastic yielding on the vertical and horizontal total strains in the HMA layer is shown in Figure 5 for the conventional flexible pavement case. The vertical compressive strains beneath the tire center (Figure 5a) from the elastic analysis monotonically increase with depth. These are the resilient strains  $\varepsilon_r$  that are the input for Eq. (6). Consequently, the permanent strains from Eq. (6) will also increase monotonically with depth. The accumulated rutting will therefore be concentrated in the

lower portion of the HMA layer, which as described previously is contrary to field experience. The corresponding vertical compressive strains from the plastic analysis, on the other hand, deviate from the elastic strains in the correct direction, at least qualitatively, with the peak strain occurring near the center of the layer at a depth of about 60 mm. However, rutting in this case is still concentrated at the bottom of the HMA layer. For both analyses, the horizontal strains (Figure 5b) increase monotonically from compression to tension with depth, with the strains from the plastic analysis larger than those from the elastic case, as expected.

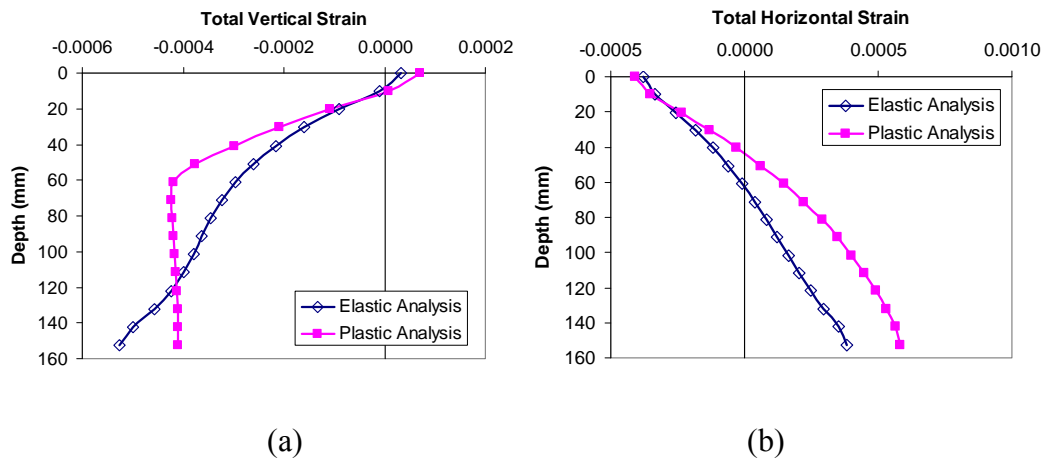


Figure 5. Computed total strains beneath tire center at peak load: (a) vertical; (b) horizontal (Schwartz and Carvalho, 2008).

Elastic stresses and strains at peak load are the inputs to the rutting models in the M-E prediction methodology. However, rutting in physical terms is the permanent deformation remaining after removal of the load. An examination of the residual strains after unloading is therefore instructive. These residual strains for the EPFE analysis are depicted in Figure 6 (the residual stresses and strains for the elastic analysis are zero by definition). The vertical permanent compressive strains after unloading increase with

depth until about 100 mm, after which they decrease sharply and eventually become tensile. The yielding at the bottom of the HMA layer results in residual horizontal compressive stresses after unloading. This residual horizontal compression induces expansive vertical strains—i.e., a decrease in the residual vertical compression--due to the Poisson effect. The residual permanent deformations resulting from this strain distribution will be concentrated in the upper portion of the HMA layer, in better agreement with field experience. No additional depth correction function is required to bring analysis results into qualitative alignment with physical expectations.

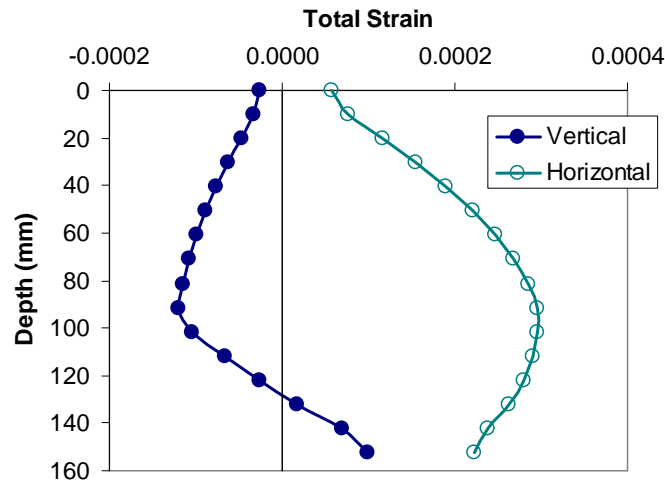


Figure 6. Residual total strains from the EPFE analysis after removal of load.

Another noteworthy feature of the EPFE analysis results is the accumulation of incremental permanent deformations over multiple load cycles. Conventional wisdom often purports that a straightforward strain-hardening plasticity analysis of a constant amplitude cyclic tire loading should produce all permanent deformations in just the first load cycle; since all subsequent load cycles are to the same load magnitude, no additional plastic yielding and/or deformations should develop in the subsequent cycles. As shown

in Figure 7, however, this is not the case. Additional plastic deformations develop in each load cycle, with diminishing magnitude in each successive cycle. The location of maximum residual strain also moves upward in the layer, bringing the distribution in even better agreement with field observations. The locked-in residual horizontal stresses that are the consequence of plastic yielding at the bottom of the HMA layer introduce stress reversals that produce additional plastic yielding and permanent deformation with each successive load cycle.

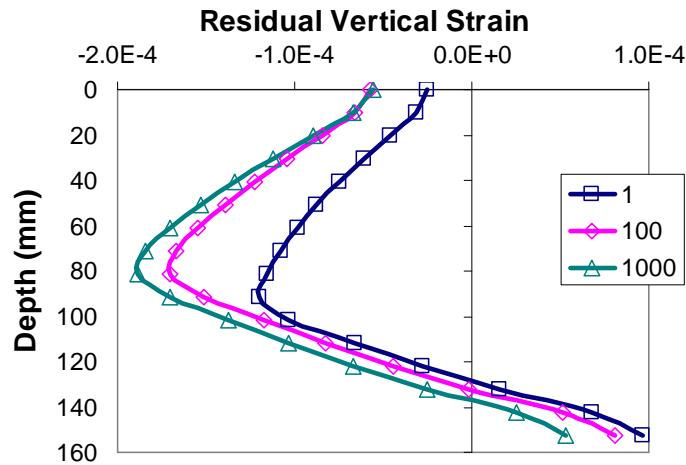


Figure 7. Residual total vertical strains beneath the tire center from EPFE analyses for different number of cycles.

Clearly, the empirical permanent deformation laws described earlier have only a very distant relationship to a realistic nonlinear constitutive response of HMA. Multidimensional confinement and plastic flow interactions, which intuitively should strongly influence the permanent deformation response, are treated only in a very approximate way via the empirical thickness/depth corrections. Simple nonlinear constitutive models based on elasto-plasticity are capable of qualitatively correcting these discrepancies. Therefore, these issues and others can be more rigorously addressed via

nonlinear finite element analysis incorporating more realistic constitutive models for the HMA.

### **2.3. Asphalt Concrete Mechanistic Modeling**

Advanced mechanistic modeling employs theories of mechanics that are more suitable to describe the real material behavior. The shortcoming is the complexity of these theories, and in particular the constitutive models. The constitutive model is the mathematical formulation representing the relationship between stresses, strains, and temperatures (and perhaps other state variables), and governs the material deformation under induced load and variations of temperature. Asphalt concrete is a complex material in which recoverable and irrecoverable strains are dependent on temperature, stress and strain rates. Therefore, viscoelasticity and viscoplasticity theories are most appropriate to model the recoverable and irrecoverable behavior respectively.

The constitutive model used in this research is based on Schapery's nonlinear viscoelastic continuum damage constitutive theory (Schapery, 1984). This theory has been used extensively in previous research to describe the recoverable portion of the deformation. Kim and Little (1990) used a one-dimensional formulation to describe the experimental behavior of asphalt concrete under cyclic strain loading. Park and Schapery (1997) also used a viscoelastic continuum damage uniaxial formulation to model creep in solid fuel propellants, while Ha and Schapery (1998) expanded this formulation into a comprehensive multiaxial model. Recently, several other researchers have used Schapery's nonlinear continuum damage viscoelastic model for predicting the

recoverable response of asphalt materials (Lee and Kim, 1998; Daniel and Kim, 2002; Gibson, 2006; Huang et al., 2007; Masad et al., 2008; Huang et al., 2011a, 2011b).

There are many approaches for modeling the irrecoverable response of asphalt concrete. Often very simple nonlinear modeling can be used with good results, such as the elasto-plastic analyses described in the previous section. Models based on rate-dependent plasticity and creep are found in the literature as well (Perl et al., 1983; Fang et al., 2004). However Perzyna's theory of viscoplasticity is the most common approach used to model asphalt concrete mixtures. The many instances of it in the literature differ primarily in the choice of the yield function, type of flow, and anisotropic effects (Lu and Wright, 1998; Gibson, 2006; Masad et al., 2007; Huang, 2008; Huang et al., 2011a, 2011b). In this research, the Perzyna based viscoplastic with the Hierarchical Single Surface (HiSS) yield function model and associated plastic flow is used (Gibson, 2006).

The key conceptual components that govern the complex behavior of asphalt concrete are: (1) viscoelasticity, (2) microstructural damage and (3) strain-hardening viscoplasticity. The viscoelasticity governs the behavior before plastic yielding occurs. Microstructural damage accounts for changes in the structure due to the formation of microcracks and is expressed in terms of rate-dependent internal state variables. And finally, the strain-hardening viscoplastic model is responsible for determining the plastic deformations (post-yield behavior) and the rate of deformation as the material hardens. Therefore total strains may be separated into viscoelastic, viscoplastic and damage strains as follows:

$$\varepsilon_t = \varepsilon_{ve} + \varepsilon_d + \varepsilon_{vp} \quad (13)$$

in which  $\varepsilon_t$  is the total strain,  $\varepsilon_{ve}$  is the viscoelastic strain,  $\varepsilon_d$  is the damage strain, and  $\varepsilon_{vp}$  is the viscoplastic strain.

The viscoelastic strain is assumed to be linear and independent of stress state and damage. The viscoelastic strain is solely dependent on rate of loading and temperature, which for thermorheologically simple materials can be interchanged using time-temperature superposition. Asphalt concrete is commonly assumed to be thermorheologically simple under small strain ( $<100\mu\varepsilon$ ) linear viscoelastic conditions. Although these factors are expected to have direct effect on the magnitudes of the time-dependent computed internal state variables and on the magnitudes of the damage strain, it is assumed that the effects of loading rate and temperature can be interchanged using conventional time-temperature superposition as well.

It is also assumed that the effects of loading time and temperature on viscoplastic strains can be interchanged using a generalized time-temperature superposition. Previous research has shown that the temperature shift function developed for small strain conditions is also valid, at least for engineering purposes, at larger strain levels of interest in pavement analyses (Chehab et al., 2002; Gibson, 2006). This immensely simplifies the laboratory testing program for calibrating the model.

### *2.3.1. Linear Viscoelastic Behavior*

Linear viscoelastic (LVE) materials exhibit elastic and viscous linear behavior. The elastic component is responsible for the instant response to loading, while the viscous component is responsible for time- and rate-dependent effects. The linear characteristic means that stresses and strains responses can be superimposed. Complex

loading conditions can be broken down into simpler loading configurations and superimposed to achieve the same outcome.

The constitutive relationships for LVE materials are commonly expressed by the following convolution integrals:

$$\sigma = \int_0^t E(t-\tau) \frac{d\varepsilon}{d\tau} d\tau \quad (14)$$

$$\varepsilon = \int_0^t D(t-\tau) \frac{d\sigma}{d\tau} d\tau \quad (15)$$

in which  $E(t)$  and  $D(t)$  are the relaxation modulus and creep compliance respectively,  $\sigma$  is stress, and  $\varepsilon$  is strain. The relaxation modulus is usually obtained through a relaxation test, which consists of applying a prescribed fixed strain and observing the material relax from the initial induced stress. The relaxation modulus is simply defined as:

$$E(t) = \frac{\sigma(t)}{\varepsilon_0} \quad (16)$$

in which  $\sigma(t)$  is the induced stress at a given time and  $\varepsilon_0$  is the prescribed constant strain applied to the specimen.

Conversely, creep compliance is usually obtained from a creep test in which the specimen is subjected to a prescribed constant stress and the strain increase over time is observed. The creep compliance is then defined as:

$$D(t) = \frac{\varepsilon(t)}{\sigma_0} \quad (17)$$

in which  $\varepsilon(t)$  is the induced strain at a given time and  $\sigma_0$  is the prescribed constant stress applied to the specimen.

Since relaxation modulus and creep compliance are just alternate representations of the same underlying viscoelastic behavior, they are related as follows:

$$E(t-\tau) \times D(t-\tau) = 1 \quad (18)$$

Viscoelastic calculations can be simplified by applying two important fundamental principles. Time-temperature superposition, as mentioned before, permits the effects of time and temperature to be interchanged through a shift factor. The other important simplification is the use of the correspondence principle, which states that the time dependence inherent in viscoelastic problems can be removed when physical strains are replaced by pseudo strains defined as follows:

$$\varepsilon_R = \frac{1}{E_R} \int_0^t E(t-\tau) \frac{d\varepsilon}{d\tau} d\tau \quad (19)$$

$$\sigma = E_R \varepsilon_R \quad (20)$$

in which  $\varepsilon_R$  is the pseudo strain,  $E_R$  is a reference modulus, typically taken as one, and  $E(t)$  is the relaxation modulus defined earlier. In addition, recoverable nonlinear behavior can be incorporated through a microstructural damage component, which can be conveniently computed using the correspondence principle, as further detailed in the next section. These simplifications greatly expedite the laboratory testing and calculations required to calibrate the model.

The generalized Maxwell model can be used to represent the relaxation modulus. The generalized Maxwell model consists of a series of dashpots and springs connected in parallel, as shown in Figure 8. The material constants  $E_i$  and  $\rho_i$  correspond respectively to the stiffness of each Maxwell spring and the relaxation times of each dashpot. The generalized Maxwell model provides a good fit to the observed behavior of a wide range

of viscoelastic materials. A Prony series can be conveniently used to represent the relaxation modulus in the generalized Maxwell model (Park and Schapery, 1999):

$$E(t) = E_0 + \sum_{i=1}^m E_i e^{-\frac{t}{\rho_i}} \quad (21)$$

in which  $E_0$  is the long term equilibrium modulus,  $E_i$  and  $\rho_i$  are the elastic springs and relaxation times for the elements in the generalized Maxwell model, and  $m$  represents the number of Maxwell components in the generalized model. A great advantage of the Prony series representation of the relaxation modulus is its fairly simple implementation in algorithms. In combination with recursive algorithms or evaluating the convolution integral in Eq. (19), this mathematical model of the viscoelastic behavior is very attractive from the computation standpoint.

In a similar fashion, creep compliance can also be conveniently modeled using a Prony series as follows:

$$D(t) = D_0 + \sum_{i=1}^m D_i e^{-\frac{t}{\tau_i}} \quad (22)$$

in which the unknown compliance constants ( $D_0, \tau_j, D_j$ ) can be expressed in terms of the known relaxation constants of Eq. (21) –  $E_0, \rho_i, E_i$  – by using a technique developed by Park and Schapery (1999).

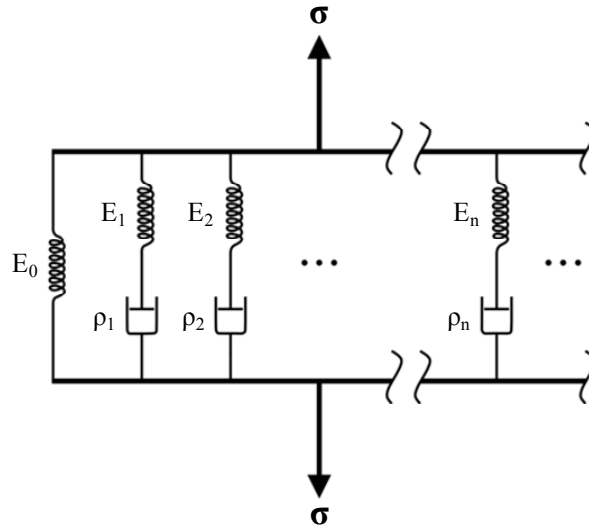


Figure 8. Generalized Maxwell model.

The principal viscoelastic properties required for the Schapery model are the Prony series terms for the relaxation modulus and the temperature shift function for the time-temperature superposition. With these two properties, one can model any type of loading (stress or displacement induced) at any rate and any temperature. The complex modulus test can be used to determine both properties from one single laboratory test.

### Complex Modulus

The complex modulus is defined as the ratio of dynamic stress to dynamic strain under sinusoidal loading. The prescribed stress and induced strain can be represented by the following equations:

$$\begin{aligned}\sigma(t) &= \sigma_0 \cos(\omega t) = \sigma_0 e^{i\omega t} \\ \varepsilon(t) &= \varepsilon_0 \cos(\omega t - \phi) = \varepsilon_0 e^{i(\omega t - \phi)}\end{aligned}\tag{23}$$

in which  $\sigma_0$  is the dynamic stress amplitude,  $\varepsilon_0$  is the dynamic strain amplitude,  $\omega$  is the loading frequency, and  $\phi$  is the phase angle or strain lag, as shown in Figure 9. Based on Eq. (23), the complex modulus is defined as:

$$E^* = \frac{\sigma_0}{\varepsilon_0} e^{i\phi} = \frac{\sigma_0}{\varepsilon_0} (\cos \phi + i \sin \phi) = E' + iE'' \quad (24)$$

in which the storage modulus,  $E'$ , and loss modulus,  $E''$ , represent the real and imaginary components.

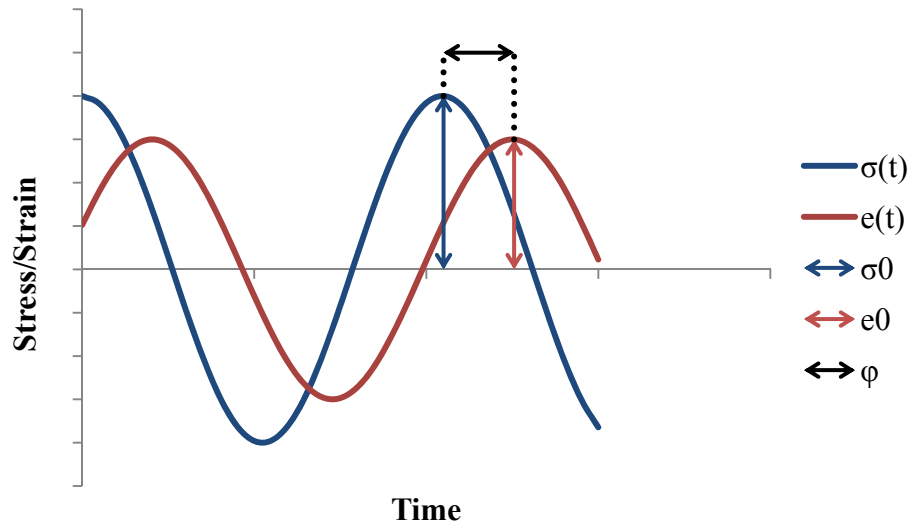


Figure 9. Complex modulus response.

The dynamic modulus,  $|E^*|$ , defined as the ratio of the dynamic stress amplitude to the dynamic strain amplitude, is related to the storage and loss moduli as follows:

$$|E^*| = \frac{\sigma_0}{\varepsilon_0} = \sqrt{(E')^2 + (E'')^2} \quad (25)$$

$$\begin{aligned} E' &= |E^*| \cos \phi \\ E'' &= |E^*| \sin \phi \end{aligned} \quad (26)$$

Dynamic modulus is the most common way to characterize the viscoelastic behavior of asphalt concrete mixtures in practice. It is also the main HMA material property in the Mechanistic-Empirical Pavement Design Guide (MEPDG).

The generalized Maxwell model can be fit to the storage and loss moduli in the frequency domain through a Prony series:

$$\begin{aligned}
 E'(\omega) &= E_0 + \sum_{i=1}^m \frac{\omega^2 \rho_i^2 E_i}{1 + \omega^2 \rho_i^2} \\
 E''(\omega) &= \sum_{i=1}^m \frac{\omega \rho_i E_i}{1 + \omega^2 \rho_i^2}
 \end{aligned}
 \tag{27}$$

in which  $E_i$  are the elastic spring constants and  $\rho_i$  are the relaxation times for the  $m$  elements in the generalized Maxwell model. These terms are the same as defined for the relaxation modulus Prony series in Eq. (21).

#### Time-Temperature Superposition

The effects of temperature and rate of loading on the viscoelastic properties of asphalt concrete can be interchanged using the time-temperature superposition principle. A master stiffness curve is formed by shifting the dynamic modulus data measured at different temperatures to a unified reference temperature. The amount of shifting at each temperature required to align the data along the common master curve describes the temperature dependency of the material. The master curve is described in terms of reduced frequency, which in turn is computed based on the temperature shift factors, as follows:

$$\omega_r = \omega \cdot a(T)
 \tag{28}$$

in which  $\omega_r$  is the reduced frequency,  $\omega$  is the test frequency,  $a(T)$  is the temperature shift factor at temperature  $T$ . An example of a master curve is provided in Figure 10. The temperature shift factors used to create the master curve are provided in Figure 11.

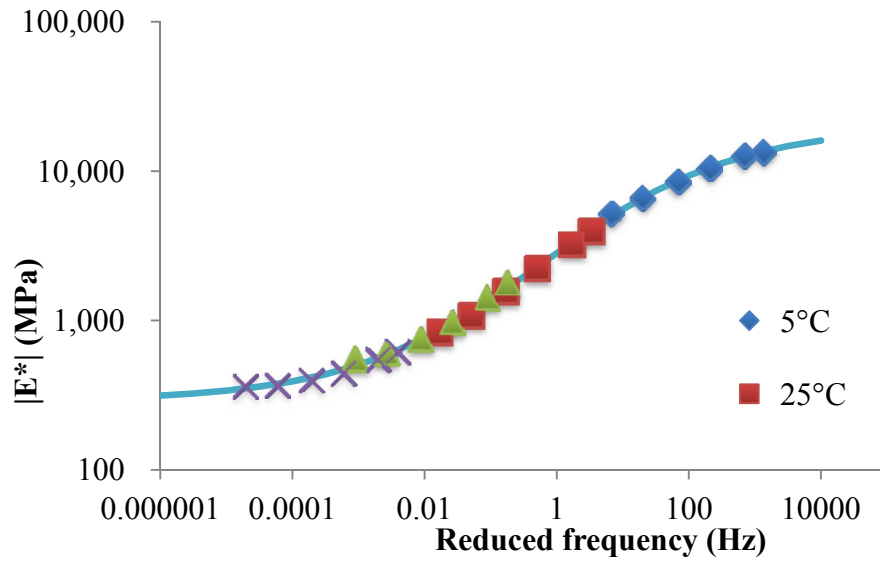


Figure 10. Example of master curve.

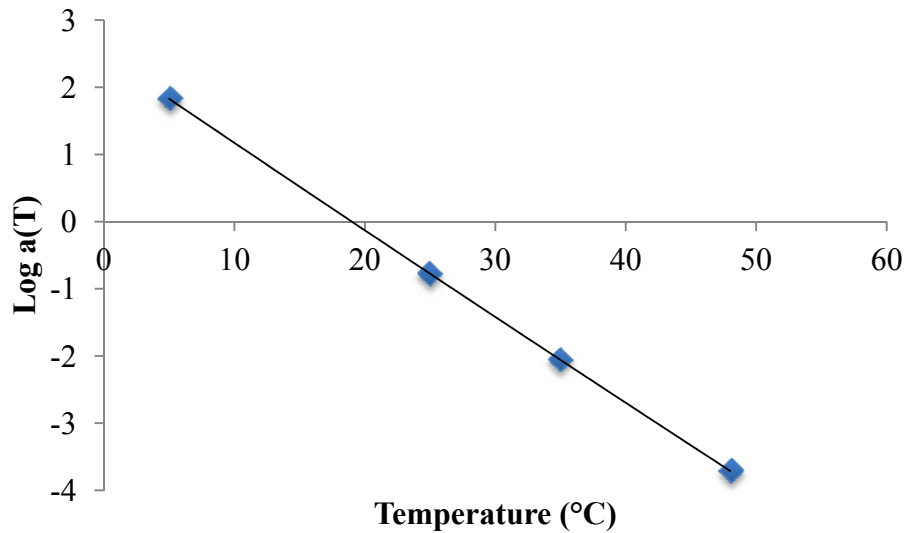


Figure 11. Example of temperature shift function.

The master curve in Figure 10 can be described using a sigmoidal logistic function as follows:

$$\log|E^*| = \delta + \frac{\alpha}{1 + e^{\beta + \gamma(\log \omega_r)}} \quad (29)$$

in which  $|E^*|$  is the dynamic modulus,  $\omega_r$  is the reduced frequency,  $\delta$  is the minimum value of  $|E^*|$  (often called the lower shelf),  $\delta + \alpha$  is maximum value of  $|E^*|$  (often called the upper shelf), and  $\beta$  and  $\gamma$  are fitting parameters describing the horizontal location and slope of the transition region. Research has shown that  $\delta$  and  $\alpha$  parameters depend primarily on binder content, air void content, and aggregate gradation while the  $\beta$  and  $\gamma$  parameters depend on the viscosity characteristics of the asphalt binder (Bonaquist, 2008).

### 2.3.2. Viscoelastic Continuum Damage Behavior

The continuum damage behavior is characterized by macroscale stiffness reduction due to changes in the material, mostly due to the development of microcracks. For asphalt concrete, Schapery's work potential theory based on thermodynamic principles has been used successfully for quantifying damage in HMA (Gibson, 2006; Kim et al, 2009). The material is assumed to be continuum and homogeneous. Although asphalt concrete is not homogeneous and no longer continuous after microcracks develop, this assumption greatly simplifies the mathematical model and it is reasonably acceptable for practical purposes of structural analysis.

## Uniaxial Formulation

Damage is incorporated into the uniaxial viscoelastic model by modifying the linear elastic relationship between uniaxial stress and pseudo strains described earlier in Eq. (20). Recall that the linear viscoelastic problem was converted into a linear elastic one by using the correspondence principle described in Eq. (19). Replacing the reference pseudo modulus term,  $E_R$ , by a damage function, Eq. (20) becomes:

$$\sigma = C(S) \varepsilon_R \quad (30)$$

in which  $\sigma$  and  $\varepsilon_R$  are defined as previously,  $C(S)$  is a stiffness function that varies with material damage, and  $S$  is an internal state variable. Note that if the reference modulus is taken as the unity,  $C(S)$  is equal to one when there is no damage and zero for a totally damaged material. The variable  $S$  quantifies any microstructural changes that result in stiffness reduction.

The damage evolution law governing the changes in the damage internal state variable,  $S$ , is defined as follows:

$$\frac{dS}{dt} = \left( -\frac{\partial W_R}{\partial S} \right)^\alpha \quad (31)$$

in which  $\alpha$  is a material property. For the uniaxial case, a pseudo work function,  $W_R$ , is defined as:

$$W_R = \frac{1}{2} C(S) \varepsilon_R^2 \quad (32)$$

Assuming that the increments of time are sufficiently small,  $\frac{dS}{dt}$  can be replaced by  $\frac{\Delta S}{\Delta t}$  in Eq. (31) and combined with Eq. (32) to yield a discrete solution for  $S$  as follows:

$$S_{i+1} = S_i + \Delta t \left( -\frac{1}{2} \varepsilon_R^2 \frac{\Delta C_i}{\Delta S} \right)^\alpha \quad (33)$$

It is assumed that there is no damage before any loading occurs and thus  $S$  equals zero and  $C$  equals one before loading, assuming unity value for the reference modulus. This numerical process requires the knowledge of the shape of the  $C$  function. An initial function can be assumed and through an iterative process it can be refined until small changes between iterations is found. A typical function for  $C(S)$  takes the form of:

$$C(S) = e^{aS^b} \quad (33)$$

After calculating the value of damage,  $S_i$ , and the incremental damage,  $S_i + \Delta S$ , at a given time step, the corresponding values of  $C$  are found using Eq. (33). The difference between these values ( $\delta C$ ) is then used to calculate damage at the next time step, using Eq. (33). The process is repeated until all data points are processed.

### Multiaxial Formulation

Consider first the elastic strain energy function for a transversely isotropic material (Schapery, 1985):

$$W_0 = \frac{1}{2} \left[ A_{11} e_v^2 + A_{22} e_d^2 + 2A_{12} e_v e_d + A_{44} (\gamma_{13}^2 + \gamma_{23}^2) + A_{66} (\gamma_{12}^2 + e_s^2) \right] \quad (34)$$

in which  $e_v = \varepsilon_{11} + \varepsilon_{22} + \varepsilon_{33}$ ,  $e_s = \varepsilon_{22} - \varepsilon_{11}$ ,  $e_d = \varepsilon_{33} - \frac{e_v}{3}$ ,  $\gamma_{ij}$  are the engineering shear strains, and  $A_{ij}$  are the five elastic components that define the transversely isotropic stiffness matrix.

Schapery suggested the axis of symmetry be oriented in the current maximum principal strain direction because damage is dominated by microcracks on the planes perpendicular to the maximum principal direction. Therefore, in uniaxial compression, the isotropic axis of symmetry is in the axial direction. This special case of multiaxial formulation can be used to determine  $A_{ij}$  components of the stiffness matrix. Eq. (34) can be simplified as follows:

$$W_0 = \frac{1}{2} \left[ A_{11}e_v^2 + A_{22}e_d^2 + 2A_{12}e_ve_d \right] \quad (35)$$

in which  $\varepsilon_{11} = \varepsilon_{22}$ ,  $e_s = 0$ , and  $\gamma_{12} = \gamma_{13} = \gamma_{23} = 0$ . For a symmetry axis  $x_3$ , the following relations are derived from the strain energy function:

$$\begin{aligned} \frac{\partial W_0}{\partial \varepsilon_{11}} = \sigma_{11} &= \left( A_{12} - \frac{A_{22}}{3} \right) \varepsilon_{33} + \left( A_{11} - \frac{2}{3}A_{12} + \frac{A_{22}}{9} \right) e_v \\ \frac{\partial W_0}{\partial e_d} = \sigma_d &= A_{22}\varepsilon_{33} + \left( A_{12} - \frac{A_{22}}{3} \right) e_v \end{aligned} \quad (36)$$

The stiffness matrix can be converted into a pseudo stiffness matrix for the viscoelastic problem using the correspondence principle. Similarly to the uniaxial formulation, the stiffness matrix can be replaced by a pseudo stiffness matrix that depends on damage.

For determining the relationship between the components of the pseudo stiffness matrix and the damage functions, Schapery's work potential theory is used. Schapery

presented the energy density function as a dual energy density function of a monotonic uniaxial loading with confining pressure,  $p$ , as follows:

$$W_d = C_{11}(S) \frac{(\varepsilon)^2}{2} + C_{12}(S) \varepsilon p + \frac{1}{2} C_{22}(S) p^2 \quad (37)$$

in which  $C_{ij}$  are damage functions,  $p$  is the confining pressure, and  $\varepsilon$  is the axial strain.

(Note that all the formulation derived here utilizes the conventional mechanics notation of positive tension, with the exception of the confining pressure  $p$  which is defined as compression positive.) The stress-strain relations can be derived from Eq. (37) as follows:

$$\begin{aligned} \frac{\partial W_d}{\partial \varepsilon} &= \Delta \sigma = C_{11} \varepsilon + C_{12} p \\ \frac{\partial W_d}{\partial p} &= e_v = C_{12} \varepsilon + C_{22} p \end{aligned} \quad (37)$$

in which  $\varepsilon = \varepsilon_{33}$ , and  $\sigma_{11} = \sigma_{22} = -p$  in the multiaxial formulation with symmetry on axis  $x_3$ . Combining Eq. (36) and Eq. (37) yields the following damage dependent stiffness components,  $A_{ij}$ :

$$\begin{aligned} A_{11} &= \frac{1}{9} \left( C_{11} - \frac{(C_{12} - 3)^2}{C_{22}} \right) \\ A_{12} &= \frac{C_{11}}{3} + \frac{C_{12}}{C_{22}} \left( 1 - \frac{C_{12}}{3} \right) \\ A_{22} &= C_{11} - \frac{C_{12}^2}{C_{22}} \\ A_{44} = A_{66} = G_0 &= \frac{E_0}{2(1 + \nu_0)} \end{aligned} \quad (38)$$

The stiffness component  $A_{66}$  was determined based on the assumption that the undamaged material is isotropic and therefore its value should be equal to the initial shear modulus,  $G_0$ . Similar to the uniaxial formulation, the damage functions,  $C_{ij}$ , are

dependent on one internal state variable,  $S$ . It also follows that  $S$  is defined by the same damage evolution law presented previously in Eq. (31).

### 2.3.3. Viscoplastic Behavior

The distinctive components of a viscoplastic constitutive model are: (a) a yield function, which controls the magnitude of viscoplastic flow; (b) a hardening law, which describes changes in the strength of the material accompanying accumulated viscoplastic straining; and (c) a potential function, which controls the direction of the viscoplastic strain increments. These components can be described conceptually in terms of the simply rheological model for elastic-viscoplastic behavior shown in Figure 12.

The deformation of the spring (characterized by the elastic modulus  $E$ ) represents the instantaneous elastic response while the deformation of the dashpot (controlled by the viscosity  $\eta$ ) represents the rate-dependent viscoplastic response once the yield strength  $\sigma_Y$  of the parallel slider element has been exceeded. (The linearly elastic spring could be replaced by a viscoelastic spring and dashpot combination for the more general case of a viscoelastic-viscoplastic constitutive model.) The total strain is then just the sum of the elastic and viscoplastic components:

$$\varepsilon = \varepsilon_e + \varepsilon_{vp} \quad (39)$$

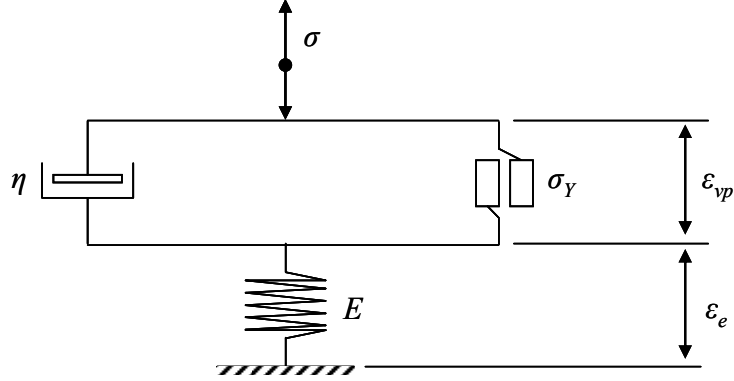


Figure 12. One-dimensional elasto-viscoplastic rheological model.

For viscoplastic strain to occur, the applied stress  $\sigma$  must be larger than the yield stress,  $\sigma_Y$ :

$$f(\sigma) = |\sigma| - \sigma_Y > 0 \quad (40)$$

in which  $f(\sigma)$  is the yield function controlling the magnitude of viscoplastic flow.

Typically, some type of hardening rule (or softening rule) complements the yield function to reflect the tendency of real materials to become stronger (or weaker) as plastic strains accumulate over the load duration. For example, a simple linear hardening rule for one dimensional loading can be expressed as:

$$\sigma_Y = \sigma_{Y_0} + H \varepsilon_{vp} \quad (41)$$

in which  $\sigma_{Y_0}$  is the initial yield and  $H$  is a hardening modulus.

Once flow commences (i.e., Eq. (40) is satisfied), the viscoplastic strain rate  $\dot{\varepsilon}_{vp}$  is governed by the viscous dashpot:

$$\dot{\varepsilon}_{vp} = \frac{\sigma}{\eta} \quad (42)$$

Eqs. (40) and (42) can be written in shorthand notation as:

$$\dot{\epsilon}_{vp} = \frac{\langle f(\sigma) \rangle}{\eta} \frac{\partial g(\sigma)}{\partial \sigma} = \Gamma \langle f(\sigma) \rangle \frac{\partial g(\sigma)}{\partial \sigma} \quad (43)$$

in which  $\Gamma = \frac{1}{\eta}$  is a fluidity material parameter and the notation  $\langle f(\sigma) \rangle$  is interpreted as:

$$\begin{aligned} \langle f(\sigma) \rangle &= f(\sigma) \quad \text{for } f(\sigma) > 0 \\ \langle f(\sigma) \rangle &= 0 \quad \text{for } f(\sigma) \leq 0 \end{aligned} \quad (44)$$

The  $g(\sigma)$  term in Eq. (43) is the viscoplastic potential function controlling the direction of plastic flow. In the simplest formulation, the plastic potential  $g(\sigma)$  is set equal to the yield function  $f(\sigma)$ ; this is termed associated flow viscoplasticity. For associated flow viscoplasticity, Eq. (43) becomes:

$$\dot{\epsilon}_{vp} = \Gamma \langle f(\sigma) \rangle \frac{\partial f(\sigma)}{\partial \sigma} \quad (45)$$

Equation (45) can be integrated in time to predict the viscoplastic strains generated by a given loading history.

### Multidimensional Perzyna Viscoplasticity

Equation (43) is the simple uniaxial form of Perzyna's viscoplastic constitutive theory (Perzyna, 1966). Perzyna's general theory is fully multi-dimensional and broad enough to accommodate a wide variety of yield functions, plastic potentials, and hardening rules. Temperature effects, critical for asphalt concrete, can be incorporated into Perzyna's theory using time-temperature superposition. Time-temperature superposition implies that loading time and temperature are interchangeable and that their combined effects can be incorporated via a single reduced time variable. Schwartz *et al.*

(2002), Chehab *et al.* (2002), Zhao and Kim (2003), and others have demonstrated that time-temperature superposition for asphalt concrete remains valid at strain levels approaching peak strength and beyond.

The multidimensional form of Perzyna's viscoplasticity theory can be expressed as:

$$\frac{d\varepsilon_{ij}^{vp}}{dt_R} = \Gamma \langle f(\mathbf{s}) \rangle \frac{\partial g(\mathbf{s})}{\partial \sigma_{ij}} \quad (46)$$

in which  $\sigma_{ij}$  and  $\dot{\varepsilon}_{ij}^{vp}$  are specific components of stress and viscoplastic strain rate;  $t_R$  is reduced time;  $f(\mathbf{s})$  is the yield function in the multidimensional stress space  $\mathbf{s}$ ; and  $g(\mathbf{s})$  is the viscoplastic potential function. For associated flow viscoplasticity,  $g(\mathbf{s}) = f(\mathbf{s})$ . The yield and potential functions can both be interpreted as surfaces in multidimensional stress space.

Equation (46) states that viscoplastic strains develop when the applied stress state lies outside the flow surface—i.e., when  $f(\mathbf{s}) > 0$ . The magnitude of the viscoplastic strain rate is proportional to the distance between the applied stress state and the flow surface in multidimensional stress space.

As before, the derivative of the viscoplastic potential function  $\frac{\partial g(\mathbf{s})}{\partial \sigma_{ij}}$  governs the direction of the viscoplastic strain increments. For the case of associated viscoplasticity, the direction of the incremental viscoplastic strain vector is always normal to the yield surface.

As for the uniaxial case, the key components of the multidimensional Perzyna viscoplastic constitutive model in Eq. (46) are the yield function, the hardening law, and the viscoplastic potential function. Most of the differences among the various viscoplastic

models in the literature for asphalt concrete center on specific choices for these three components. For example, frictional materials like asphalt concrete, aggregates, and soils are best characterized by yield functions that include the strengthening effects of confining stress. One example of such yield functions is the standard Drucker-Prager generalization of Mohr-Coulomb frictional yield. Extensions to Drucker-Prager theory like the Hierarchical Single Surface (HiSS) model (Desai and Zang, 1987) add other refinements such as a nonlinear yield surface and a cap on viscoplastic flow under hydrostatic compression loading.

A variety of hardening types (e.g., isotropic vs. kinematic) and various specific hardening laws have been employed in models in the literature. And although most implementations employ an associated plasticity assumption for the viscoplastic potential function, this is known to overestimate dilatancy for many geomaterials and as a consequence a variety of nonassociated flow schemes have been proposed.

Recent representative examples of viscoplastic constitutive models for asphalt concrete applications can be found in Schwartz *et al.* (2004), Gibson *et al.* (2003), Chehab *et al.* (2003, 2005), Huang *et al.* (2002, 2004), Masad *et al.* (2005, 2007), Tashman *et al.* (2004, 2005), Uzan (1996, 2005), Saadeh *et al.* (2007), Panneerselvam and Panoskaltsis (2006), Collop *et al.* (2003), Oeser and Moller (2004), and Lu and Wright (1998).

#### Perzyna-HiSS Model Formulation

Frictional materials like asphalt concrete, aggregates, and soils are best characterized by yield functions that include the strengthening effects of confining stress.

One example of such yield functions is the standard Drucker-Prager generalization of Mohr-Coulomb frictional yield. Extensions to Drucker-Prager theory add other refinements such as a nonlinear yield surface and a cap on viscoplastic flow under hydrostatic compression loading. The present study employs the Hierarchical Single Surface (HiSS) model, developed by Desai and Zang (1987), with isotropic hardening and associated flow. The HiSS yield function has the following mathematical formulation:

$$F = 0 = J_{2D} - \left[ \gamma (I_1 + R(\xi))^2 - \alpha(\xi) (I_1 + R(\xi))^n \right] \quad (47)$$

in which,  $J_{2D}$  and  $I_1$  are the shear and volumetric stress invariants,  $\gamma$  and  $n$  are fixed constants that control the size and shape of the growing flow surface,  $\xi$  is the viscoplastic strain trajectory given by the summation of all three principal viscoplastic strains, and  $R(\xi)$  and  $\alpha(\xi)$  are parameter functions governing the size and nature of the capped surface. Figure 13 shows schematically the HiSS flow surface in the principal stress domain. The functions  $R(\xi)$  and  $\alpha(\xi)$  can be formulated as follows:

$$R(\xi) = R_0 + R_A \xi^{k_2} \quad (48)$$

$$\alpha(\xi) = \alpha_0 e^{\xi k_1} \quad (49)$$

Associated flow is assumed,  $\langle f(s) \rangle = \langle g(s) \rangle$ , and:

$$f(s) = A \left( \frac{F}{F_0'} - 1 \right)^N \quad (50)$$

in which  $F$  is the distance in principal stress space from the applied stress to the hydrostatic axis normal to the current flow surface,  $F_0'$  is the portion of this distance from

the current flow surface to the hydrostatic axis, and  $A$  is a calibration parameter that depends on the direction of the plastic flow:

$$A = \left( \frac{\theta}{0.528} \right)^{k_3} \quad (51)$$

in which  $\theta$  is the direction of the stress vector in the  $I_1, J_{2D}$  space and  $k_3$  is a material constant. Figure 14 describes schematically the flow rule and surface hardening.

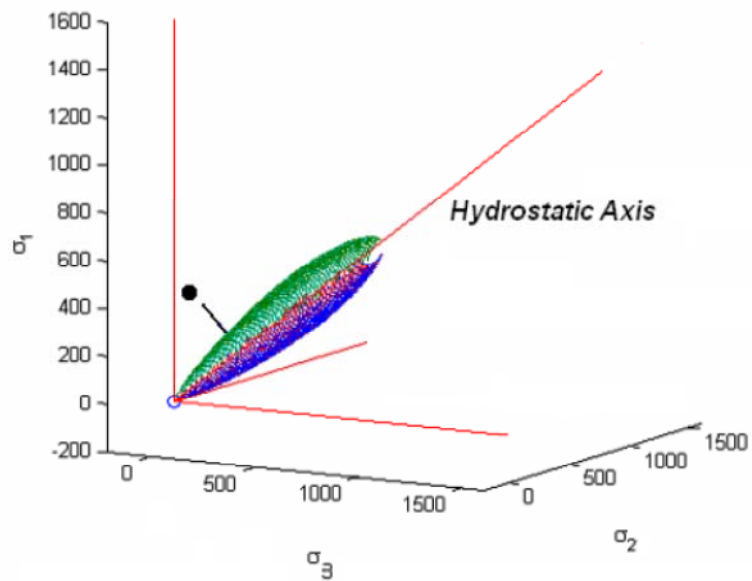


Figure 13. Three-dimensional representation of HiSS surface in principal stress space (Gibson, 2006).

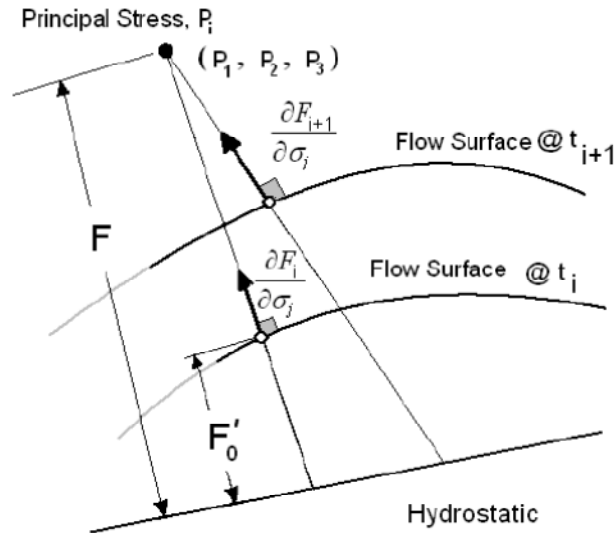


Figure 14. Schematic of flow rule and surface hardening (Gibson, 2006).

## 2.4. Summary

This chapter provided an overview of the rutting problem in pavement structures. Two mechanisms were identified as the main causes of rutting, compaction at early stages of traffic loading and distortion without volume alteration during the later stages. These two mechanisms identify the three stages of rutting until failure. Traffic compaction occurs fairly quick and it is not often modeled. Common maintenance practices prevent pavements from reaching the third stage and failure. Therefore the attention to modeling rutting is given to the secondary stage.

A few models developed over the past 40 years were briefly discussed. They lay the foundation for the current empirical models based on resilient strain. The current model used in the AASHTO's mechanistic-empirical design guide, Darwin-ME, is based on vertical resilient strain and is calibrated using axial repeated load permanent deformation test. An alternative model, termed the Westrack model, is based on maximum shear strain and calibrated using the repeated shear test.

There are significant limitations on the use of empirical models. The most fundamental limitation relies on the applicability of the model. Empirical models are adequate for the conditions at which they were calibrated. Extrapolations are often hazardous. Mechanistic empirical models rely on predictions of mechanistic response. Linear elastic theory is most used due to simplicity. However most of materials used in pavement construction are not linear elastic.

In addition, there are several issues not yet fully resolved in the framework for predicting rutting in the asphalt concrete layers using M-E models. There is still no clear consensus whether rutting is due primarily to axial or shear permanent strains. Current M-E rutting models relate permanent strains (axial or shear) to resilient strains computed using multilayer elastic theory. However, in the absence of correction factors, rutting predicted from these resilient strains is in sharp disagreement with field observations. Thickness or depth correction factors are required to bring predictions in line with observations. These correction factors further weaken the mechanistic linkage between predicted rutting and computed strains in the M-E approach. Current M-E models assume that the mechanisms and distributions of permanent strains are similar for HMA layers in flexible pavements vs. HMA overlays on rigid pavements, which is generally not true. And finally, current M-E models do not explicitly consider the contribution of heaving at the edge of the wheel paths, although this may be implicitly included in the field calibration corrections, given how rutting measurements are taken in the field.

The use of advanced mechanistic modeling can help address some of the issues mentioned and reduce the gap between rutting predictions and field measured performance. Advanced mechanistic modeling employs theories of mechanics that are

more suitable to describe the real material behavior. The shortcoming is the complexity of these theories, and in particular the constitutive models. Asphalt concrete is a complex material in which recoverable and irrecoverable strains are dependent on temperature, stress and strain rates. Therefore, viscoelasticity and viscoplasticity theories are most appropriate to model the recoverable and irrecoverable behavior respectively. A framework for applying a viscoelastic-viscoplastic model based on Schapery's viscoelasticity theory and Perzyna's viscoplasticity formulation was presented. As part of this research, this model will be reviewed, calibrated and implemented in a finite element model for evaluation of pavement structures in three dimensions.

### **Chapter 3 Materials and Test Equipment**

The selection of the asphalt concrete mixture to be used in this research was based in three requirements: (1) availability of full-scale performance data, (2) material availability for preparing laboratory test specimens, and (3) full-scale tests conducted with controlled environment. Since the ultimate objective of this research was to develop a full 3-D model to predict permanent deformation in full-scale pavement sections, obtaining performance data was critical. In addition, it was necessary that enough material be available for preparing laboratory specimens for the mixture characterization. And finally, given the nature of the problem at hand and the computational effort required to mechanistically predict permanent deformation, the ideal full-scale test should be conducted with controlled environmental conditions, more specifically constant temperature.

These conditions were found at the Full-Scale Accelerated Performance Testing for Superpave and Structural Validation Study conducted at the Federal Highway Administration (FHWA) Turner-Fairbank Highway Research Center (TFHRC), part of the Transportation Pooled Fund Study TPF-5(019). Details of this study are provided elsewhere (FHWA, 2011)

This chapter describes the asphalt concrete mixture used in this study, mixture volumetrics and materials, and testing equipment.

### 3.1. Mixture Characteristics

The asphalt concrete mixture chosen was used in lane 11 of the FHWA rutting study. The material is a 12.5 millimeter nominal maximum aggregate size dense graded modified asphalt concrete mixture meeting Virginia Department of Transportation specifications. The fine and coarse aggregates were all crushed diabase from Loudoun Quarry, VA. One percent hydrated lime was used in the mixture to reduce the potential for moisture damage. The aggregate gradation is shown in Figure 15.

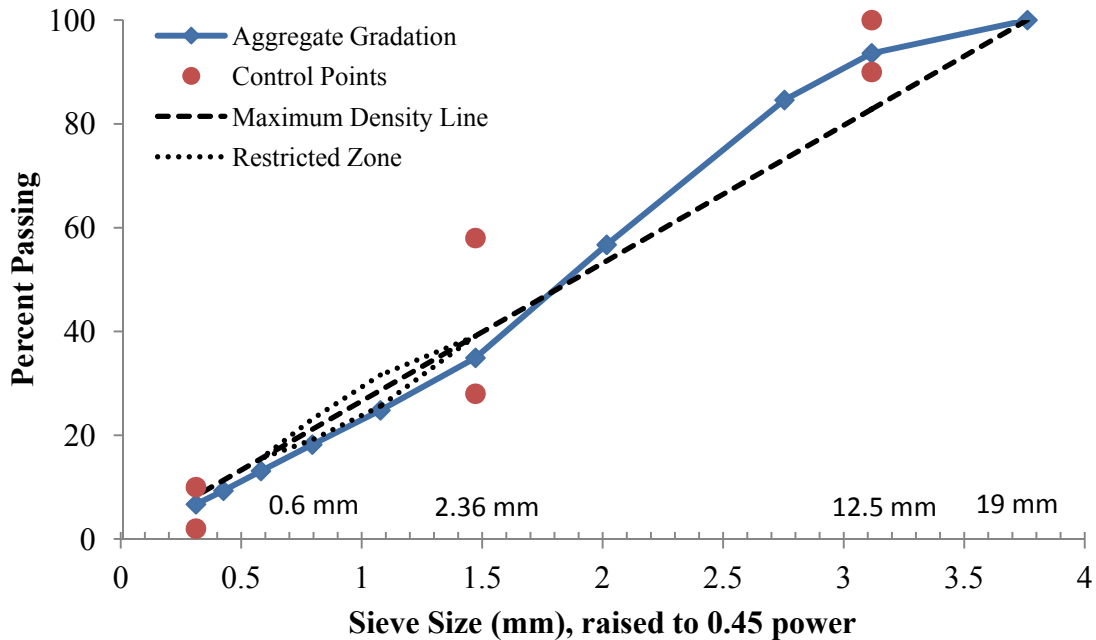


Figure 15. Asphalt concrete mixture aggregate gradation.

The binder used in the mixture was a styrene-butadiene-styrene (SBS) elastomeric polymer modified binder with approximately 3 percent by weight linear grafting, denominated SBS-LG. The Superpave performance grade was PG 70-28. The final mixture design is provided in Table 1. All Superpave mixture design requirements are satisfied.

Table 1. Laboratory mixture design.

<b>Property</b>	<b>Design</b>
Gradation (percent passing)	
19 mm	100
12.5 mm	93.6
9.5 mm	84.6
4.75 mm	56.7
2.36 mm	34.9
1.18 mm	24.8
0.6 mm	18.2
0.3 mm	13.1
0.15 mm	9.3
0.075 mm	6.7
Gmm	2.7
Gsb	2.947
PG-grade	70-28
Binder content (% by mass)	5.3
Effective binder content (% by mass)	4.9
Effective binder content (% by volume)	12.7
Design air voids (%)	4.2
VMA at design air voids (%)	16.9
VFA at design air voids (%)	75.2

### 3.2. Specimen Preparation

Twenty-four test specimens were fabricated at FHWA's Turner-Fairbank Highway Research Center, in McLean, VA. The geometry and instrumentation of the test specimens followed recommendations from the NCHRP Project 9-19 (Witczak, 2005). The recommended dimensions of the cylindrical specimen are 150 mm in height and 100 mm in diameter (height to diameter ratio of 1.5).

The laboratory-blended HMA mixtures were short-term aged in the oven for 4 hours at 275°F before compaction (AASHTO PP2). The mixture was then compacted in a Servopac gyratory compactor to a plug of 150 mm in diameter by 170-180 mm in height. Test specimens were cored from the center of the gyratory plug, and the specimen ends were sawed parallel to produce the final specimen geometry. The desired target air voids was 5.5%, which corresponded to the average in-place air voids for the same mixture at the TFHRC Accelerated Loading Facility (ALF) study 2, lane 11. However, during specimen preparation the actual air voids target was set to a different value corresponding to another lane in the experiment. Consequently, the final average air voids of the specimens was 4.96%. Although this for all practical purpose is within the  $\pm 0.5$  air void tolerance, the laboratory prepared mixture is nonetheless slightly more dense than the field mixture for the lane being evaluated. Possible implications of this small discrepancy will be offered in a later chapter.

Spring-loaded linear variable differential transformers (LVDTs) were used for axial strain measurements. The axial LVDTs were placed vertically on opposite sides of the specimen as shown in Figure 16. Parallel brass studs used to secure the LVDTs in place were located at a distance of 50 mm from the top and bottom of the specimen. The gage length between the studs was 100 mm. The LVDT measurement range was  $\pm 5.0$  mm. However, as a safety measure, the tests were not allowed to exceed 4 mm deformation (4% strain) to avoid damaging the instrumentation. For radial deformations, four externally mounted LVDTs were aligned horizontally and perpendicular to the center of the specimen at 90° intervals. The radial LVDTs set-up is in Figure 17.

Surface friction between the top and bottom of the specimen and the load platens is an important source of shear stresses at the end of the specimen. Two pairs of rubber membranes lubricated with vacuum grease were placed on the top and bottom of each specimen during the testing assembly to minimize the possibility of shear stress developing during the tests.



Figure 16. Axial LVDT instrumentation.

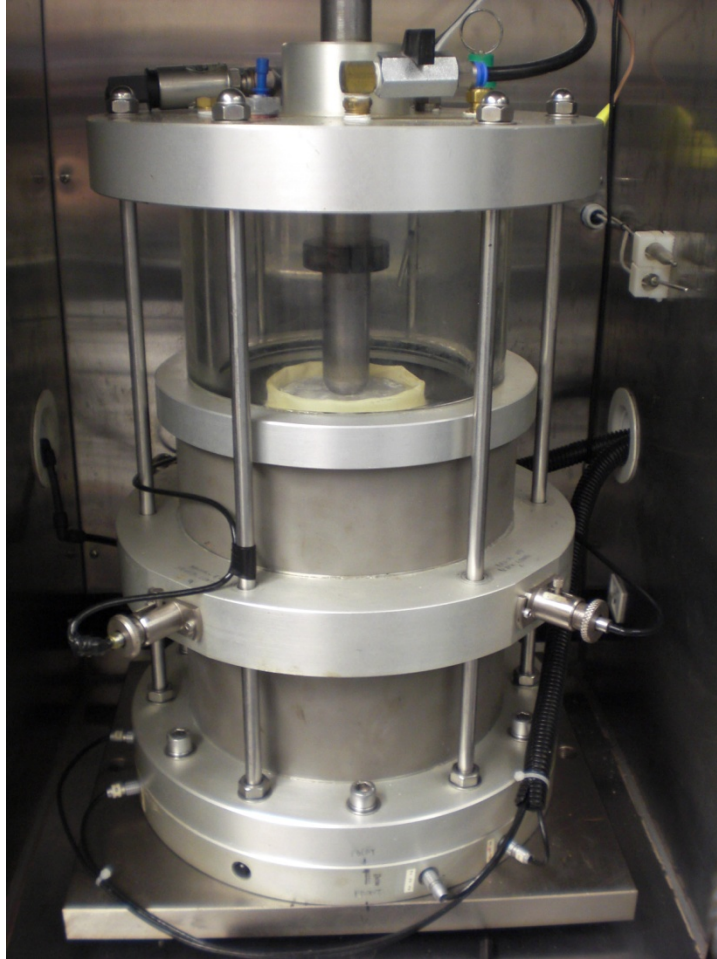


Figure 17. Radial LVDT setup.

All axial strain measurements were the average of two or four axial LVDTs located at  $180^\circ$  or  $90^\circ$  intervals around the specimen circumference, depending on the testing being performed. All radial strain measurements were the average of four radial LVDTs located at  $90^\circ$  intervals around the specimen circumference. Averaging the LVDTs removed specimen bending effects and reduced the overall variability of strain measurements on the specimen.

### 3.3. Testing Equipment

The tests were conducted using a Universal Testing Machine (UTM) 100, manufactured by IPC Global of Victoria, Australia. The UTM-100 is a servohydraulic feedback controlled testing machine capable of performing load and displacement controlled tests. A photo of the UTM-100 system is provided in Figure 12. The axial load capacity of the machine is 100 kN. Gain switches can be used to reduce the load range to 50 kN, 20 kN, or 10 kN for more sensitive tests. The machine is outfitted with an environmental temperature chamber and confining pressure cell for confined tests. Temperature is held constant within the chamber to the desired temperature  $\pm 2^\circ$  F throughout the test. Control and data acquisition is achieved through a Control and Data Acquisition System (CDAS) unit interfaced with a PC via two serial cables. Two forms of test control software available from the manufacturer were used in this study. The first software package (UTM 3) utilizes pre-programmed test templates for dynamic modulus, uniaxial strain rate, and other standard tests. More sophisticated tests can be performed with the second software package (UTM 100), enabling user-defined programs that give the operator much greater flexibility in specifying loading and data acquisition settings.

The UTM-100 is a research grade machine in which almost everything can be adjusted and tuned to achieve the test needs and objectives. Although this a powerful feature that permits the design of a wide range of tests, it also makes the preparation work for any individual test a little cumbersome.

The first step is to define setup for the environmental chamber. From previous research conducted in the same equipment, it was found that variations in room temperature could have an impact on the final temperature achieved inside the chamber.

Moreover, ports for the wiring required for specimen instrumentation was a source for heat leakage. Therefore, a sequence of temperature measurements was performed to determine the correct setup for the various testing temperatures.

One temperature probe was placed inside the chamber near the load actuator to verify the temperature reached at equilibrium for a given temperature setup at the chamber's control panel. One dummy specimen was modified by inserting a temperature probe at its center of gravity. This probe measured the specimen temperature once equilibrium was reached inside the chamber. The two equilibrium temperatures (inside the chamber and inside the specimen) were different for all the desired testing temperatures, especially when the triaxial cell was used.

After a sequence of trials, the nominal temperatures to be set at the chamber's control panel were determined so that the specimen would be in equilibrium at the target testing temperature. The time it took to reach equilibrium was also recorded and was used to schedule the beginning of each test. Given the time required for the specimen temperature reach equilibrium, which could be over 7-8 hours for low temperature, an industrial climate chamber available in the laboratory was used to acclimatize all specimens prior to testing in order to reduce the time spent in the laboratory.

Tuning the machine to respond correctly to the material being tested is also an important step taken to minimize differences in nominal and target stress/strain levels, as well as load pulse shape. Tuning was carried out at each of the target test temperatures.

### **3.4. Summary**

The asphalt concrete mixture used in this research was 12.5 millimeter nominal maximum aggregate size dense graded modified asphalt concrete mixture. The binder used in the mixture was a styrene-butadiene-styrene (SBS) elastomeric polymer modified binder, denominated SBS-LG. The Superpave performance grade was PG 70-28. The target binder content was 5.3% by weight and the air voids, 4.2%.

One Universal Testing Machine (UTM), with 100 kN nominal load capacity was used for all laboratory calibration tests. Chapter 4 will describe in greater detail the tests performed and the calibration procedure used to characterize the mixture behavior.

## **Chapter 4 Model Calibration**

A laboratory testing program was designed to provide the data required to calibrate the linear viscoelastic, damage and viscoplastic components of the constitutive model. Small-strain frequency sweep tests were performed to determine the linear viscoelastic complex modulus and the temperature shift factors. Strain rate tests to failure were performed at low temperatures to calibrate the damage component of the constitutive model. And finally, newly designed creep and recovery tests were used to calibrate the viscoplastic component.

### **4.1. Linear Viscoelastic Component**

The principal viscoelastic properties required for the Schapery model are the relaxation modulus and the time-temperature superposition. With these two properties, one can model any type of loading (stress or displacement induced) at any rate and any temperature. The complex modulus test is used to determine both properties in a single laboratory test.

The viscoelastic strain is assumed to be linear and independent of stress state and damage. The viscoelastic strain is solely dependent on rate of loading and temperature, which can be interchanged using time-temperature superposition. The relaxation modulus master curve and the shift factors for time-temperature superposition are determined from the complex modulus test.

#### *4.1.1. Complex Modulus Testing*

Complex modulus tests were performed in unconfined compression at four temperatures and six frequencies at each temperature. The dynamic modulus obtained in each frequency-temperature sweep was used to develop the dynamic modulus master curve. Dynamic modulus and the measured phase angle can be converted to the relaxation modulus used in the Schapery linear viscoelastic constitutive model.

The dynamic modulus test protocol was developed in NCHRP Projects 9-19 and 1-37A and has been standardized as AASHTO Provisional Standard TP62, “Standard Method of Test for Determining Dynamic Modulus of Hot-Mix Asphalt Concrete Mixtures.” The recommended test sequence in AASHTO TP62 for developing the dynamic modulus master curve consists of testing a minimum of two replicate specimens at temperatures of -10, 4.4, 21.1, 37.8, and 54.4 °C at loading frequencies of 25, 10, 5, 1.0, 0.5, and 0.1 Hz. The 60 dynamic modulus measurements are then used to determine the parameters of the master curve by numerical optimization. The dynamic modulus test was performed using three replicates in this research.

The testing protocol adopted in this research was slightly different than what is proposed in the AASHTO provisional standard. The lowest temperature was very difficult to obtain with the environmental chamber of the UTM. The thermal insulation was insufficient to keep the temperature at the recommended lowest value. This limitation is not problematic. Recent research has suggested that only three temperatures and four frequencies are required for developing the dynamic modulus master curve, with the temperature values depend on the binder grade used in the mixture (Bonaquist, 2008).

The temperatures chosen for the dynamic modulus tests were 5, 25, 35 and 50°C, which are near the recommended values in the AASHTO provisional standard. The temperature range is also similar to that suggested for the Asphalt Mix Performance Tester (AMPT) dynamic modulus test for PG 70-xx binders (i.e., 4, 20 and 40°C). The temperature range is intended to span the operating range for pavements in the field. But more importantly, the range of temperature must be broad enough to provide a full characterization of the master curve including the upper and lower shelves.

The frequencies used were 20 Hz, 10 Hz, 3 Hz, 1 Hz, 0.3 Hz, and 0.1 Hz. These frequencies approximate the full range of loading rates pavements are likely to experience from live traffic ranging from slow congestion to highway speed. The number of cycles applied for each frequency varied from the high to low frequency as follows: 600, 250, 100, 40, 15 and 10.

Prior to running the test, preconditioning was performed at 10 Hz using half the stress level defined for this frequency. This step was suggested as a way to seat any loose aggregates in the specimen and remove any other anomalous strain measurements before the formal frequency testing (Gibson, 2006).

Dynamic modulus is the fundamental property that characterizes the material behavior in the linear viscoelastic domain. Consequently the tests must be performed at conditions in which only viscoelastic strains are generated with no damage or residual strains. This is achieved by limiting the magnitude of the dynamic axial strains to values on the order of 100 microstrain ( $\mu\varepsilon$ ), with a tolerance of  $\pm 25 \mu\varepsilon$ .

In equipment designed for routine production testing (e.g., the Asphalt Mixture Performance Tester), the control software automatically adjusts the applied stress to

produce the strain target range mentioned above. The UTM did not have such capabilities and a trial and error test was therefore conducted using a sacrificial specimen to determine the target stress levels for each frequency and temperature. The final stresses applied are shown in Table 2.

The target strain range was achieved for nearly all temperature and frequencies. The exceptions were observed in tests at the highest temperature (50 °C) and the three highest frequencies. The average dynamic strain obtained throughout the sweep tests was about 85  $\mu\epsilon$ , well within the specified limits. A summary of the testing protocol used is provided in Table 3.

Table 2. Stresses applied in the dynamic modulus test.

Frequency (Hz)	Test Temperature (°C)			
	5	25	35	48
20	1110	328	159	81
10	1043	265	119	63
3	870	172	77	57
1	716	116	57	38
0.3	560	79	36	29
0.1	440	58	26	19

Table 3. Summary of dynamic modulus testing.

Test Temperatures (°C)	5, 25, 35, 50
Frequencies (Hz) (number of cycles)	20, 10, 3, 1, 0.3, 0.1 (600, 250, 100, 40, 15, 10)
Preconditioning	100 cycles at 10 Hz and half the nominal load
Dynamic axial strain	Target range between 75 and 125 $\mu\epsilon$

The tests were conducted starting from the coldest temperature and highest frequency and marching on to the lowest frequency with five minute intervals between

frequencies. The frequency sweep is then repeated at the next warmer temperature until all temperatures have been tested.

#### *4.1.2. Dynamic Modulus Master Curve*

The objective of the complex modulus tests is to determine the magnitude of the dynamic modulus,  $|E^*|$ , and phase angle,  $\phi$ , between the sinusoidal stress and strain responses at different temperatures and frequencies. These values were computed for the last six cycles in each frequency sweep using a built-in algorithm in the IPC software controlling the test and data acquisition. For a given cycle of stress and strain data, the algorithm fits a second order polynomial over 25% of the period on either side of the peak or valley to determine the peak-to-peak dynamic strain, peak-to-peak dynamic stress, and the phase angle defined as the lag in radians between the stress and strain peaks.

After testing was completed, a statistical quality check was performed to assure the results were acceptable for modeling. The coefficient of variation of the measured dynamic modulus at each temperature and frequency averaged 6.8%. The standard deviation of measured phase angle at each frequency and temperature averaged  $1^\circ$  with the maximum of  $2.6^\circ$ . Suggested values for quality acceptance are 7.5% for the dynamic modulus coefficient of variation and a maximum of  $3^\circ$  for the standard deviation of phase angle (Bonaquist, 2008).

Master curves are constructed using the principle of time-temperature superposition. First a standard reference temperature is selected. Next, data at various temperatures are shifted with respect to loading frequency until the curves merge into a

single smooth function. The complete characterization consists of the master curve and the shift factors. The assumed shape for the dynamic modulus master curve is a sigmoidal function of the following form:

$$\log |E^*| = \delta + \frac{\alpha}{1 + e^{\beta + \gamma(\log \omega_r)}} \quad (52)$$

in which  $|E^*|$  is the dynamic modulus;  $\omega_r$  is the reduced frequency (radians/second),  $\delta$  is the minimum value of  $|E^*|$  (i.e., the lower shelf),  $\delta + \alpha$  is the maximum value of  $|E^*|$  (i.e., the upper shelf), and  $\beta$  and  $\gamma$  are parameters describing the location and slope of the transition portion of the sigmoidal function. The reduced frequency,  $\omega_r$ , is given by:

$$\omega_r = \omega(a(T)) \quad (53)$$

in which,  $\omega$  is the frequency (radians/second),  $a(T)$  is the shift factor as a function of the temperature,  $T$  (°C).

The approach selected for developing the master curve was first proposed by Pellinen (2001) and adopted by Gibson (2006). A non-linear optimization algorithm is used to determine the best fit for the master curve equation by adjusting all four parameters in Eq. (52) while simultaneously adjusting the values of  $a(T)$  for each test temperature then fitting a best-fit quadratic curve to the optimized  $a(T)$  values at each temperature. The optimization was achieved using the Solver tool in Microsoft Excel. This procedure is similar to that implemented in the MEPDG.

The temperature-shifted dynamic modulus data and the associated fitted master curve are provided in Figure 18. Each data point in the dynamic modulus master curve is the average of three replicates. The temperature shift factors found during the optimization process and the best-fit quadratic shift function are shown in Figure 19. As

can be seen in Figure 18, the lower shelf of the master curve, which corresponds to low frequencies and/or high temperatures, is well characterized. However, the upper shelf, which corresponds to high frequencies and/or low temperatures, is less well characterized because of the practical difficulties of testing at very low temperatures and/or very high frequencies.

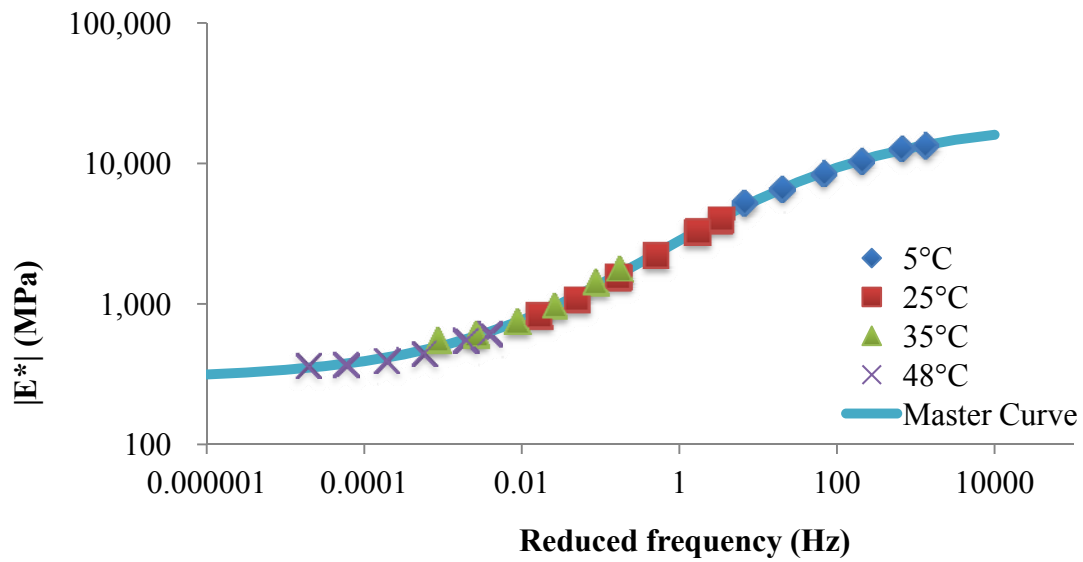


Figure 18. Dynamic modulus master curve.

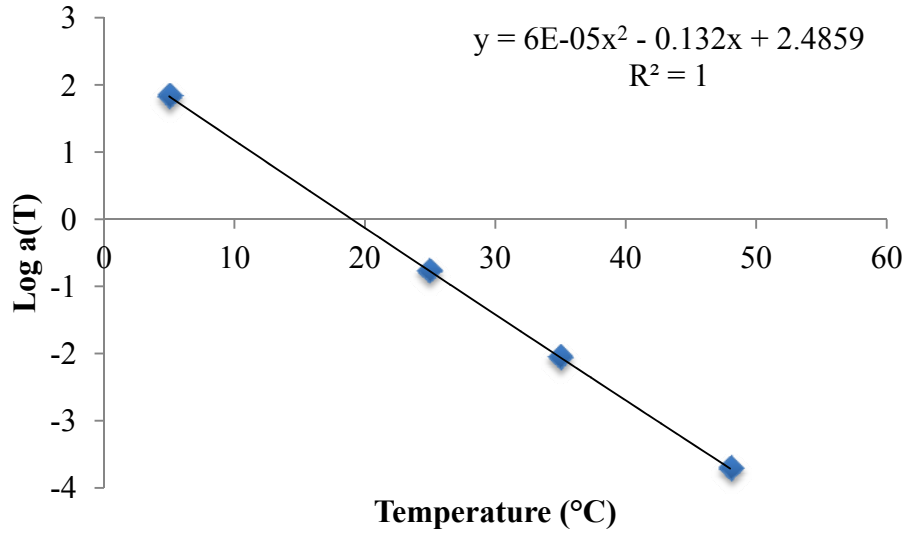


Figure 19. Temperature shift function.

Given the provisional status of the dynamic modulus protocol used, it was decided to try another procedure for developing the master curve. Christensen et al. (2003) developed an approach based on binder stiffness and mixture volumetric data using the Hirsch model as part of NCHRP Projects 9-25 and 9-31. Part of this effort was to develop an abbreviated testing protocol for development of dynamic modulus master curves for routine mixture evaluation and design (Bonaquist, 2008). The need for extreme low temperature testing is avoided by estimating the upper shelf of the master curve using a limiting maximum modulus parameter. The modified master curve equation is given by:

$$\log|E^*| = \delta + \frac{(Max - \delta)}{1 + e^{\beta + \gamma \log \omega_r}} \quad (54)$$

in which,  $|E^*|$  is the dynamic modulus;  $\omega_r$  is the reduced frequency (radians/second),

$Max$  is the limiting maximum modulus and  $\delta$ ,  $\beta$ , and  $\gamma$  are fitting parameters. The

maximum limiting modulus is estimated from mixture volumetric properties using the Hirsch model and a limiting binder modulus of 1 GPa as follows:

$$|E^*|_{\max} = P_c \left[ 4,200,000 \left( 1 - \frac{VMA}{100} \right) + 435,000 \left( \frac{VFA \times VMA}{10,000} \right) \right] + \frac{1 - P_c}{\left[ \frac{\left( 1 - \frac{VMA}{100} \right)}{4,200,000} + \frac{VMA}{435,000(VFA)} \right]} \quad (55)$$

in which VMA is the voids in mineral aggregates (%), VFA is the voids filled with asphalt (%), and  $P_c$  is given by:

$$P_c = \frac{\left( 20 + \frac{435,000(VFA)}{VMA} \right)^{0.58}}{650 + \left( \frac{435,000(VFA)}{VMA} \right)^{0.58}} \quad (56)$$

The reduced frequency is computed using the Arrhenius equation:

$$\log \omega_r = \log \omega + \frac{\Delta E_a}{19.14714} \left( \frac{1}{T} - \frac{1}{T_r} \right) \quad (57)$$

in which,  $\omega$  is the frequency (radians/second),  $a(T)$  is the shift factor as a function of the temperature,  $T$ ,  $T_r$  is the reference temperature, both in °K, and  $\Delta E_a$  is the activation energy, which is treated as a fitting parameter.

The master curve based on the Hirsch model is compared to the MEPDG master curve in Figure 20. There is a very good agreement between the two fitted master curves, which indicates a good characterization including the upper shelf. The master curve determined using the MEPDG procedure was selected for the linear viscoelastic characterization of the asphalt concrete mixture. The final parameters are summarized in Table 4. The reference temperature selected was 19°C.

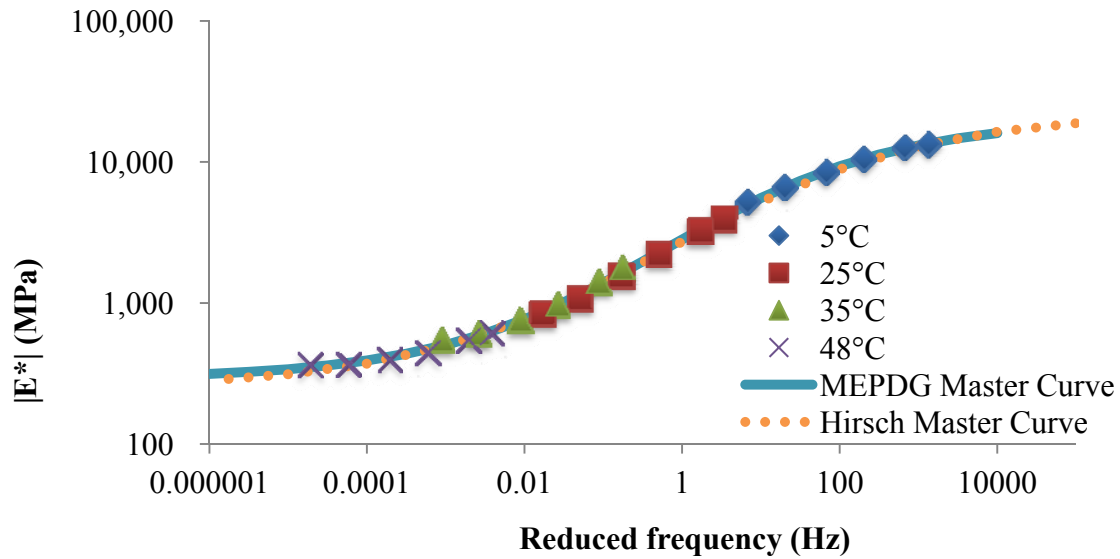


Figure 20. Comparison between MEPDG and Hirsch master curves.

Table 4. Dynamic master curve and temperature shift factors.

Dynamic Modulus Master Curve	$\delta = 2.46239$
	$\alpha = 1.84048$
	$\beta = -0.14792$
	$\gamma = -0.68108$
Temperature Shift Factors	$a(5^{\circ}\text{C}) = 10^{1.8275}$
	$a(25^{\circ}\text{C}) = 10^{-0.7761}$
	$a(35^{\circ}\text{C}) = 10^{-2.0601}$
	$a(48^{\circ}\text{C}) = 10^{-3.7116}$

#### 4.1.3. Relaxation Modulus and Creep Compliance

The relaxation modulus describes the relationship between stress and strain under a constant strain condition. Conversely, creep compliance describes the same relationship under a constant stress condition. The complex modulus test data described in the preceding section were used to determine the relaxation modulus and creep compliance properties of the asphalt concrete mixture.

As described in Chapter 2 , the generalized Maxwell model can be used to represent the complex modulus. Prony series are used to fit the storage modulus,  $E'(\omega)$ , and the loss modulus,  $E''(\omega)$ . The relaxation modulus can then be described using Eq. (21), which for convenience is reproduced here:

$$E(t) = E_0 + \sum_{i=1}^m E_i e^{-\frac{t}{\rho_i}} \quad (58)$$

in which  $E_0$  is the long term equilibrium modulus,  $E_i$  and  $\rho_i$  are the elastic springs and relaxation times for the elements in the generalized Maxwell model, and  $m$  represents the number of single Maxwell instances are in the generalized model. Creep compliance can be also represented by the following Prony series:

$$D(t) = D_0 + \sum_{j=1}^n D_j \left( 1 - e^{-\frac{t}{\tau_j}} \right) \quad (59)$$

in which,  $D_0$ ,  $D_j$  and  $\tau_j$  are Prony series constants. Strain creep and stress relaxation are two aspects of the same viscoelastic behavior and therefore are related. The relationship is given by Eq. (60). Park and Schapery (1999) developed a procedure to determine the creep compliance constants from the relaxation modulus through a system of algebraic linear equations (Gibson, 2006; Kim et al., 2009).

$$\int_0^t E(t-\tau) D(\tau) d\tau = t \quad (60)$$

For the scope of this research, the required property is the relaxation modulus, which is needed for determining the pseudo strains for the continuum damage characterization. Creep compliance, although not necessary, was computed to complete the mixture characterization.

The storage modulus was computed from the dynamic modulus measured in the frequency sweep tests using Eq. (26). A master curve was fit to the storage modulus data following the same process used for the dynamic modulus master curve. Figure 21 illustrates the master curve fit for the storage modulus. Once the master curve has been determined, the Prony series described in Eq. (58) was determined. The final step was the calculation of the creep compliance Prony series constants. The final relaxation modulus and creep compliance determined from this conversion procedure are illustrated in Figure 22. The final Prony series constants for Eqs. (58) and (59) are shown in Table 5.

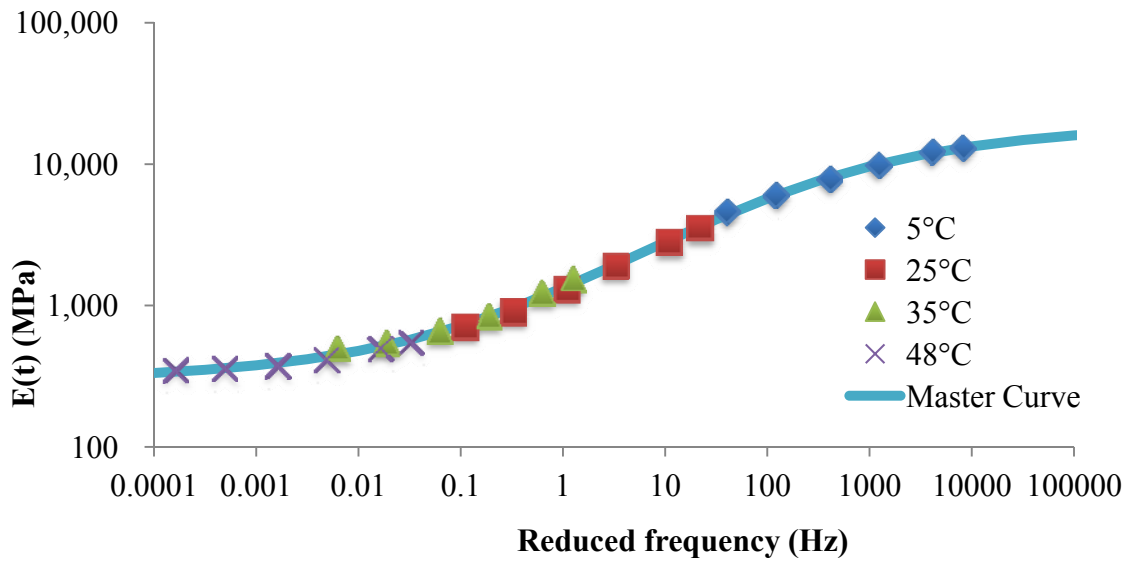


Figure 21. Storage modulus master curve.

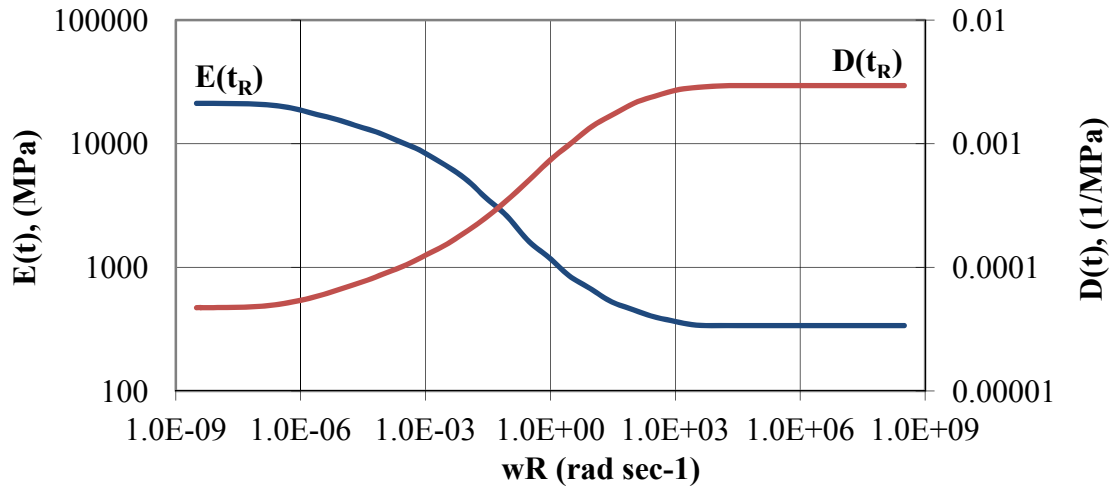


Figure 22. Relaxation modulus and creep compliance.

Table 5. Prony series constants for relaxation modulus and creep compliance.

<i>i</i>	Relaxation Modulus		Creep Compliance	
	$\rho_i$ (sec)	$E_i$ (MPa)	$\tau_j$ (sec)	$D_j$ (MPa <sup>-1</sup> )
0	-	338.2976	-	4.71E-05
1	0.000001	3435.971	5E-07	4.84E-06
2	0.00001	3435.971	0.000005	1.32E-05
3	0.0001	3435.971	0.00005	1.89E-05
4	0.001	3435.971	0.0005	3.15E-05
5	0.01	3435.971	0.005	5.82E-05
6	0.1	2286.747	0.05	0.000126
7	1	850.0592	0.5	0.000352
8	10	351.6168	5	0.000661
9	100	132.8441	50	0.00079
10	1000	73.26597	500	0.000653
11	10000	0.003015	5000	0.000199
12	100000	0.003015	50000	1E-11
<b>Time-temperature superposition</b>				
Temperature	5°C	25°C	35°C	48°C
Log a(T)	1.810225	-0.76011	-2.00601	-3.58657

## 4.2. Continuum Damage Model

The continuum damage behavior is characterized by macroscale stiffness reduction due to the development of microcracks that eventually coalesce into macrofractures and crack propagation. The continuum damage model was calibrated using constant strain rate tests to failure at low temperatures. Unconfined and confined tests at two different strain rates were performed to calibrate the damage functions as defined by Schapery's work potential theory. The energy density function used to relate damage with the stiffness of the material presented previously as Eq. (37) in Chapter 2 is reproduced here for convenience:

$$W_d = C_{11}(S) \frac{(\varepsilon_1^R)^2}{2} + C_{12}(S) \varepsilon_1^R p + \frac{1}{2} C_{22}(S) p^2 \quad (61)$$

in which,  $C_{ij}$  are the damage functions,  $S$  is an internal state variable,  $p$  is the confining pressure and  $\varepsilon_1^R$  is the pseudo axial strain. From Eq. (61), stress-strain relations can be derived as follows:

$$\frac{\partial W_d^R}{\partial \varepsilon_1^R} = \Delta \sigma = C_{11} \varepsilon_1^R + C_{12} p \quad (62)$$

$$\frac{\partial W_d^R}{\partial p} = e_v^R = C_{12} \varepsilon_1^R + C_{22} p \quad (63)$$

in which the additional variable,  $\varepsilon_v^R$ , is the pseudo volumetric strain. In the multiaxial formulation with symmetry on axis  $x_3$ ,  $\sigma_{11} = \sigma_{22} = -p$ . The pseudo strains are computed using the following hereditary convolution integrals:

$$\varepsilon_1^R = \frac{1}{E_R} \int_0^t E(t_R - \tau_R) \frac{d\varepsilon_1}{d\tau_R} d\tau_R \quad (64)$$

$$\varepsilon_v^R = \frac{1}{E_R} \int_0^t E(t_R - \tau_R) \frac{d\varepsilon_v}{d\tau_R} d\tau_R \quad (65)$$

in which  $E(t_R)$  is the relaxation modulus and  $t_R$  is reduced time,  $E_R$  is the reference modulus taken here as equal to 1, and  $\varepsilon_v^R$  is the pseudo volumetric strain. The internal state variable is governed by a damage evolution law as follows:

$$\frac{dS}{dt} = \left( -\frac{\partial W_d}{\partial S} \right)^\alpha \quad (66)$$

in which  $\alpha$  is a material property. Calibration of  $\alpha$  was found to be very difficult. The optimum value is the one that makes all damage curves collapse onto a single master damage curve. Previous attempts to calibrate  $\alpha$  were carried out by trial and error using an incremental approach over values varying from 1.25 to 2.25 (Gibson, 2006). It was found that the optimum value ranged between 1.75 and 2.0. Kim et al (2009), summarizing the efforts by other researchers, suggested that  $\alpha$  was inversely proportional to the absolute maximum slope of the relaxation modulus master curve,  $m$ . This approach suggests a value for  $\alpha$  of 2.1. Different  $\alpha$  values were tried and ultimately a value of 2.0 was adopted.

Following Schapery's work potential theory for a viscoelastic media with damage, it is assumed that the material is isotropic in the undamaged state (Ha, 1996). Therefore, Schapery's energy density function, Eq. (61), must be equivalent to the strain energy function of a typical isotropic material. This assumption yields the following constraints for the damage functions when no damage has occurred:

$$\text{When } S = 0 \rightarrow \begin{cases} C_{11} = E_{ref} \\ C_{12} = 1 - 2\nu \\ C_{22} = -\frac{2(1+\nu)(1-2\nu)}{E_{ref}} \end{cases} \quad (67)$$

in which  $\nu$  is the initial Poisson's ratio and  $E_{ref}$  is the reference modulus – in this case taken as equal to 1.

Unconfined constant strain rate tests to failure were used to determine the damage functions  $C_{11}$  and  $C_{12}$  by applying both stress-strain relations described in Eq. (62). Once  $C_{11}$  and  $C_{12}$  were determined, results from the confined tests were used to determine the remaining damage function,  $C_{22}$ , using Eq. (63). The reference temperature of 19°C was adopted for the damage model calibration. The reduced frequency was calculated using the temperature shift factors provided in Table 4.

#### 4.2.1. Constant Strain Rate Tests to Failure

Unconfined and confined constant strain rate tests to failure were performed at 10°C. The low temperature minimizes the development of viscoplastic strains. Temperatures lower than 10°C would have been better, but there were limitations in the environmental chamber encapsulating the specimen, loading and measurement apparatus. After trying to establish equilibrium at 5°C, it was found that sustained constant temperature was only possible at 10°C.

Sacrificial dummy specimens were used to define the strain rates for the tests. A trial and error procedure was carried out to find out the fastest loading rate that the machine would apply and still fail the specimens before reaching its nominal load limit.

The triaxial chamber pressure was set at 250 kPa for the confined tests. For safety reasons and the measurement limits of the LVDTs, the tests were programmed to end when total deformation reached 4%. Strain rates of 0.0001 and 0.0008  $\epsilon$ /second were selected based on this procedure for both unconfined and confined conditions. Stress *versus* strain plots from the unconfined and confined strain rate tests are shown respectively in Figure 23 and Figure 24.

Some viscoplastic strains were induced along with the viscoelastic plus damage strains. To ensure accurate calibration of the damage model, these viscoplastic strains were removed from the total measured strains using the calibrated viscoplasticity model, which is described in greater detail later in this chapter.

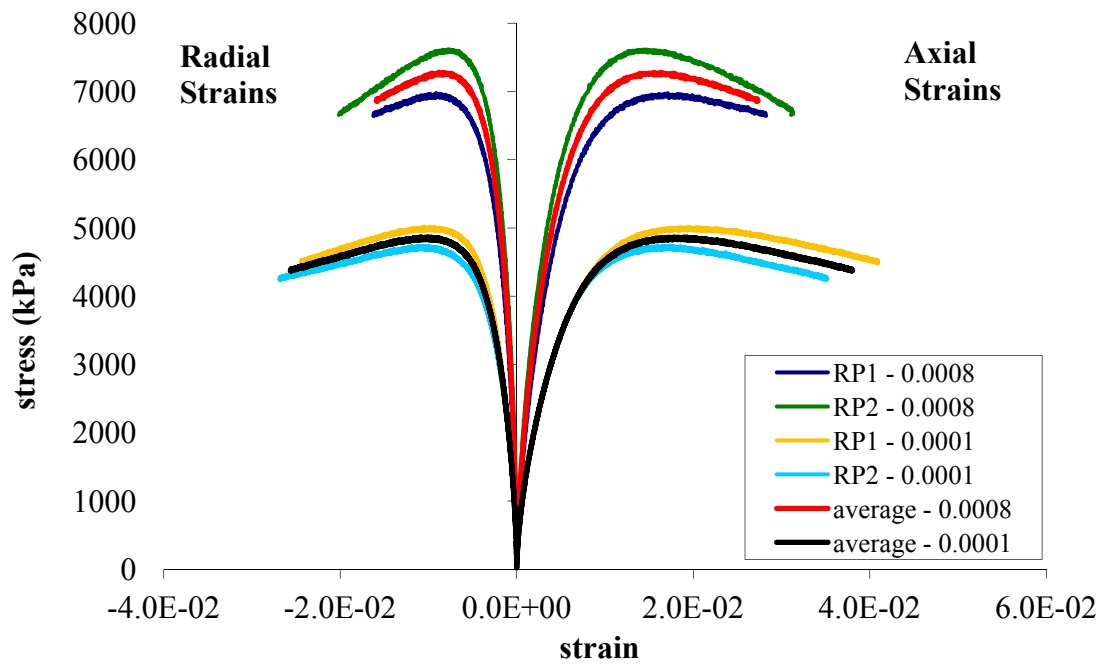


Figure 23. Unconfined strain rate tests at 10°C: stress *versus* strain curves for strain rates of 0.0001 and 0.0008  $\epsilon$ /second.

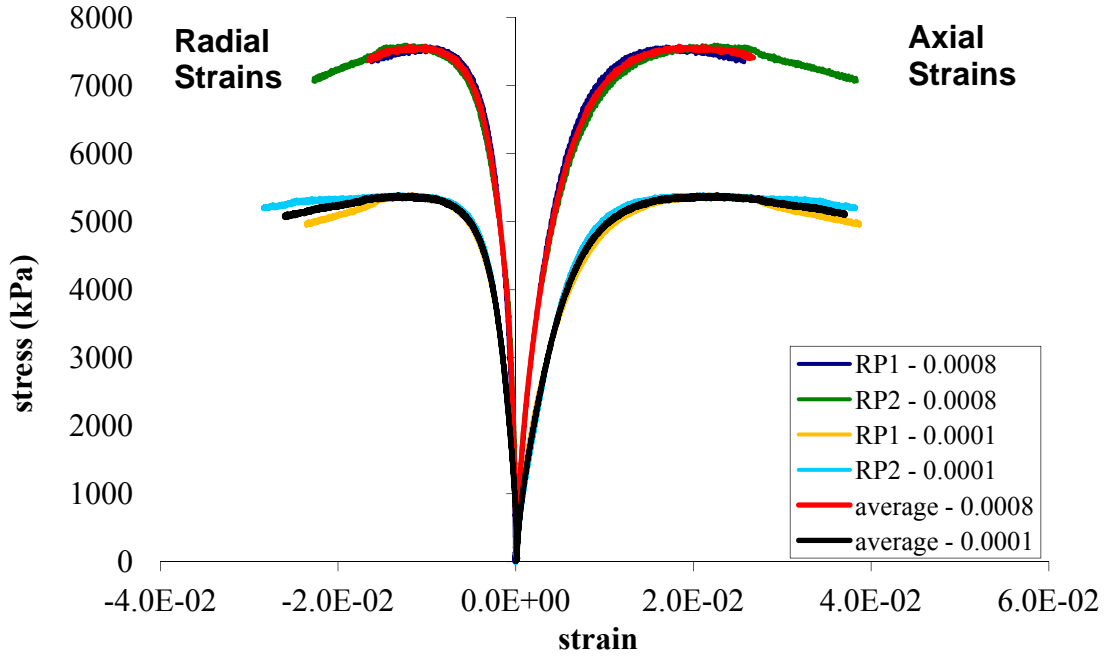


Figure 24. Confined strain rate tests at 10°C: stress *versus* strain curves for strain rates of 0.0001 and 0.0008  $\epsilon$ /second.

#### 4.2.2. Calibration of Damage Function $C_{II}$

Under unconfined conditions (i.e., uniaxial loading), the confinement term in Eq. (62) disappears and the damage function  $C_{II}$  can be defined as:

$$C_{II} = \frac{\Delta\sigma}{\epsilon_1^R} \quad (68)$$

Although  $C_{II}$  can be determined directly from the test, the internal damage variable,  $S$ , cannot. As described in Chapter 2, a discrete solution for  $S$  can be defined as:

$$S_{i+1} = S_i + \Delta t \left( -\frac{1}{2} \epsilon_R^2 \frac{\delta C_i}{\delta S} \right)^\alpha \quad (69)$$

in which  $i$  denotes the time step in the test and  $C_i$  is a simplified notation for  $C_{II}$  at  $t=t_i$ .

The term  $\frac{\delta C_i}{\delta S}$  is computed as the difference in the damage function caused by a small

variation in  $S$  (i.e., 0.1). The internal state variable for the next time step,  $S_{i+1}$ , is then computed using Eq. (69) and the process repeated until all time steps in the test are calculated. The damage function  $C_{II}$  was assumed to have the following form:

$$C(S) = e^{aS^b} \quad (70)$$

in which  $a$  and  $b$  are material constants. Optimization using the Solver tool in Microsoft Excel™ was employed to calibrate the damage function by minimizing the sum squared difference between predicted and calculated damage.

This process was repeated for every specimen replicate and strain rate tested in unconfined conditions. Figure 25 summarizes the results of the calibration process for each replicate and the average calibration considering all replicates simultaneously. For this given mixture, it was found that  $a = -0.00298$  and  $b = 0.5006$ .

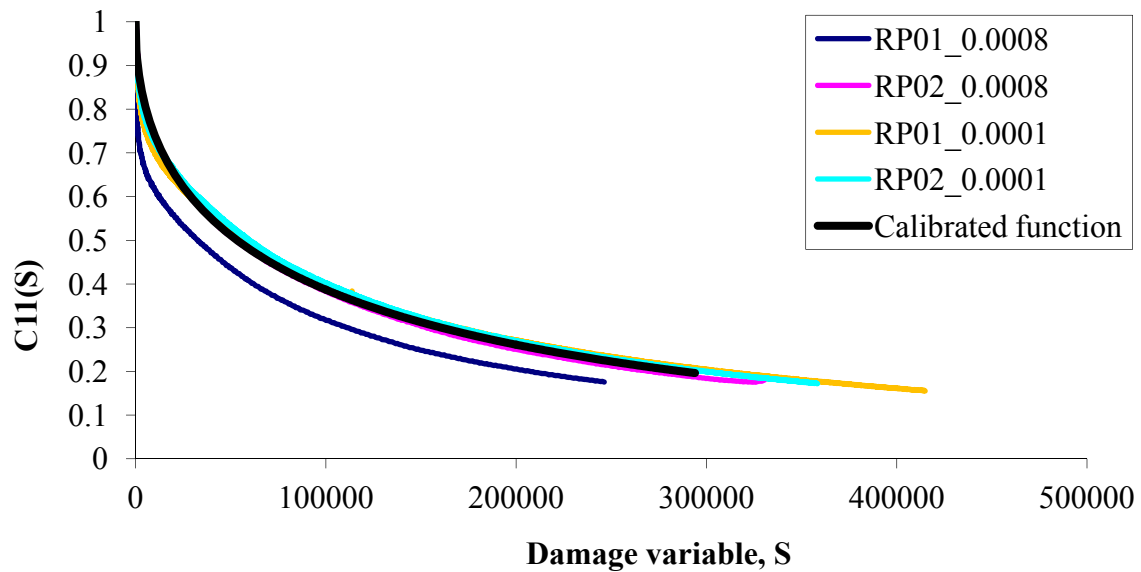


Figure 25. Damage function  $C_{II}$  versus  $S$  for all replicates at 10°C.

#### 4.2.3. Calibration of Damage Function $C_{12}$

Under unconfined conditions ( $p=0$ ),  $C_{12}$  can be calculated from Eq. (63) at any time as follows:

$$C_{12} = \frac{e_v^R}{\varepsilon_1^R} \quad (71)$$

The internal state variable,  $S$ , has already been determined during the calibration of  $C_{11}$ . The damage function  $C_{12}$  was plotted against  $S$  and the following function was fit using a least squares optimization process:

$$C_{12}(S) = (C_{12,ini} - c_1)e^{-c_2S} - c_3S + c_1 \quad (72)$$

in which  $c_i$  are material constants, and  $c_{12,ini} = 1 - 2\nu$  to satisfy Eq. (67).

The strain rate test results showed that the specimens initially exhibited compressive and later expansive volumetric strains. The variation of the Poisson's ratio with time is shown Figure 26. The variation is attributed to internal damage occurring in the material. Ideally,  $C_{12}$  would be a function of a rate-dependent Poisson's ratio, although for simplicity and practical applications, the option chosen was to treat  $C_{12}$  as a function of the initial Poisson's ratio. The exponential functions shown in Figure 26 were used to smooth the data points and the intercepts were averaged to determine the mixture's initial Poisson's ratio value of 0.428. This value is within the range reported by other researchers (Kim et al., 2009). It is worth noting that the Poisson's ratio of 0.5 separates the volume behavior between contraction and dilation. The specimens undergo contraction at the beginning and dilation at the end of the test.

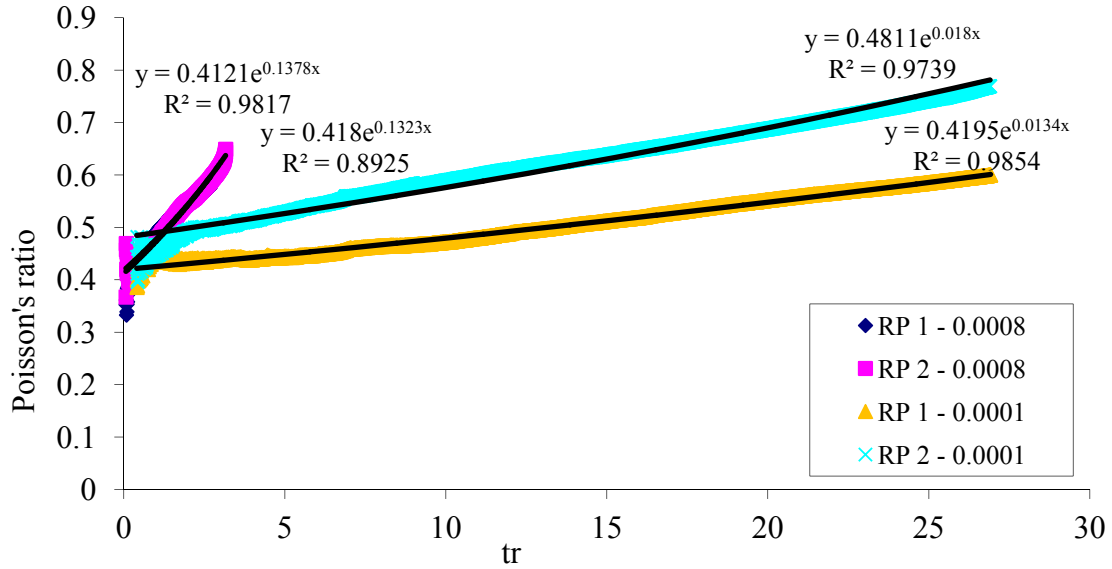


Figure 26. Poisson's ratio variation during the strain rate tests.

The final  $C_{12}$  function is taken as the average of all individually calibrated functions for each replicate. The final model is shown in Table 6. Figure 27 presents the measured damage function  $C_{12}$  versus the internal damage variable,  $S$ , for all replicates and the final calibrated model for all tests. A decreasing  $C_{12}$  is consistent with an increasing Poisson's ratio due to growing damage. The point where  $C_{12}$  changes sign also corresponds to the change in behavior from compression to expansion observed in the specimens during testing.

Table 6. Damage function  $C_{12}$  calibration coefficients.

Constant	Value
$C_{12,ini}$	0.144
$c_1$	0.1423
$c_2$	$1.317 \times 10^{-5}$
$c_3$	$4.103 \times 10^{-7}$

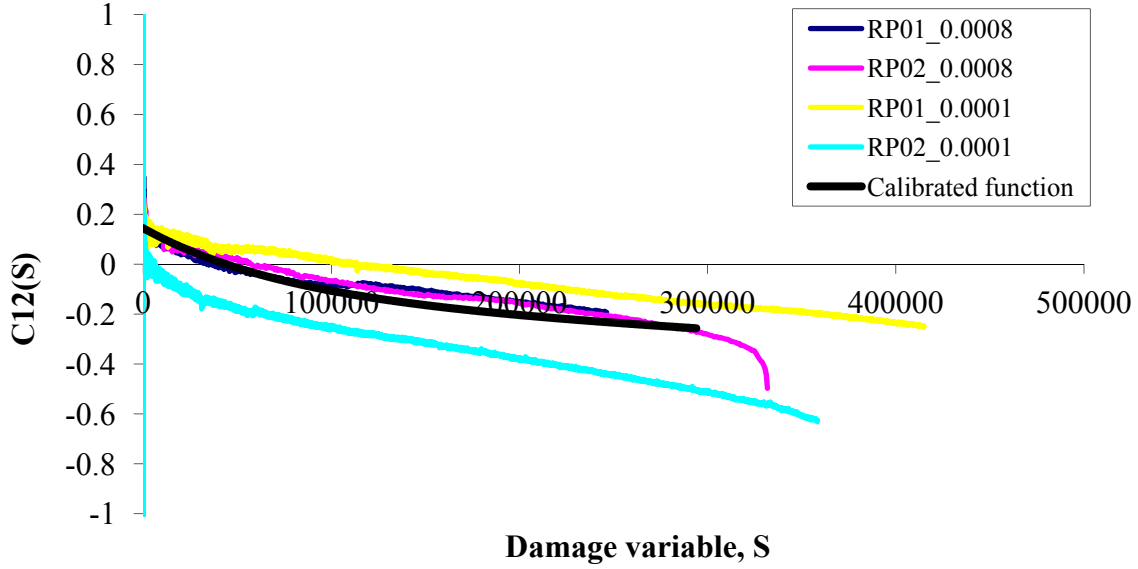


Figure 27. Damage function  $C_{12}$  versus  $S$  for all replicates at  $10^{\circ}\text{C}$ .

#### 4.2.4. Calibration of Damage Function $C_{22}$

The last damage function to be calibrated was  $C_{22}$ . Confined strain rate test results were used to complete the damage characterization of the mixture. After the other damage functions have been established, Eq. (63) was used to solve for  $C_{22}$  as follows:

$$C_{22} = \frac{e_v^R - C_{12}\epsilon_1^R}{p} \quad (73)$$

in which the variables are as described previously. The solution of Eq. (73) requires a different approach because the damage variable,  $S$ , must be calculated at the same time. The approach consisted of using Eq. (62) to compute the deviator stress,  $\Delta\sigma$ , and minimizing the error by fitting the appropriate curve to the damage function  $C_{22}$ .

The nature of the tests and the approach required to calibrate the damage function made it difficult to calibrate the model for confined conditions with the same level of accuracy attained for the unconfined tests. The effects of noise in the data and specimen to specimen variability were magnified because of the small magnitude of measured

strains in the confined tests, especially at earlier stages of testing. Moreover, any errors from computing the damage variable,  $S$ , were propagated to the calibration of  $C_{22}$ .

The function chosen to represent  $C_{22}$  was a second order polynomial function:

$$C_{22} = d_1 + d_2 S^2 \quad (74)$$

in which  $d_1$  and  $d_2$  are material calibration constants. As described previously, the intercept was defined by the requirement for transversely isotropic conditions when the material is undamaged. Figure 28 presents the calculated damage function  $C_{22}$  versus the internal damage variable,  $S$ , for all replicates and the final calibrated model for all tests. The calibrated values of the material constants are  $d_1 = -0.4113$  and  $d_2 = -1.6937 \times 10^{-10}$ .

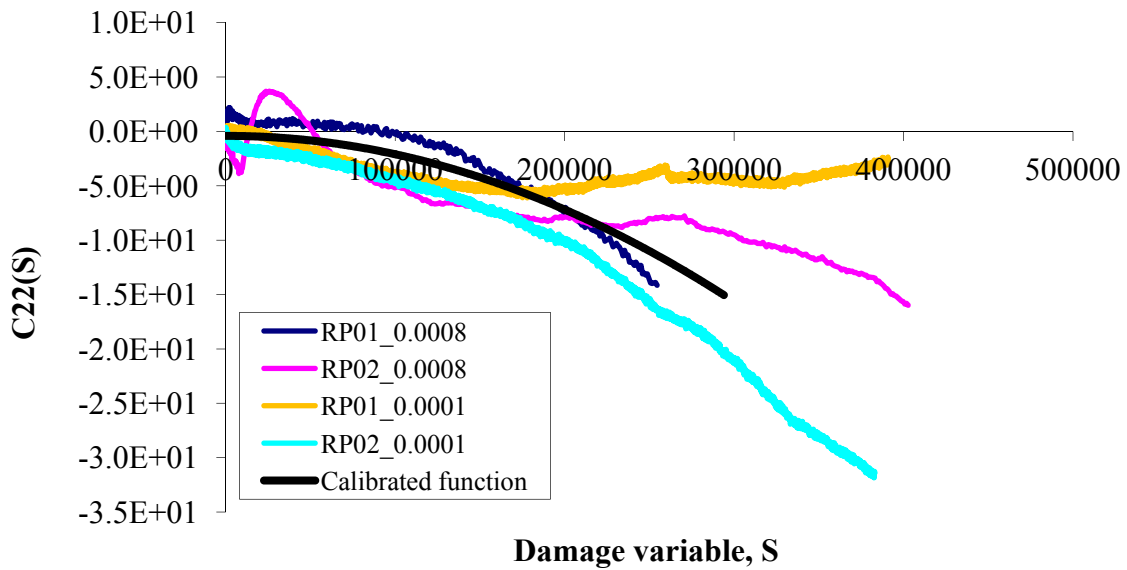


Figure 28. Damage function  $C_{22}$  versus  $S$  for all replicates at  $10^\circ\text{C}$ .

### 4.3. Viscoplastic Model

The constitutive model adopted herein is based on the Perzyna-HiSS model developed by Gibson (2006) with some enhancements to the model calibration process. A new testing procedure was developed to expedite the calibration effort in the laboratory,

while maintaining the range of stresses and frequencies defined by Gibson for the creep and recovery tests.

The Hierarchical Single Surface (HiSS) model (Desai and Zang, 1987) employing isotropic hardening and associated flow was used. The constitutive model, detailed previously in Chapter 2, is summarized here for convenience. The HiSS yield surface is defined as:

$$F = 0 = J_{2D} - \left[ \gamma (I_1 + R(\xi))^2 - \alpha(\xi) (I_1 + R(\xi))^n \right] \quad (75)$$

in which  $J_{2D}$  and  $I_1$  are the shear and volumetric stress invariants,  $\gamma$  and  $n$  are fixed constants that control the size and shape of the growing flow surface,  $\xi$  is the viscoplastic strain trajectory given by the summation of all three principal viscoplastic strains, and  $R(\xi)$  and  $\alpha(\xi)$  are hardening functions governing the size and nature of the capped surface. The functions  $R(\xi)$  and  $\alpha(\xi)$  are formulated as:

$$R(\xi) = R_0 + R_A \xi^{k_2} \quad (76)$$

$$\alpha(\xi) = \alpha_0 e^{\xi k_1} \quad (77)$$

in which,  $R_0$ ,  $R_A$ ,  $k_2$ ,  $\alpha_0$  and  $k_1$  are material constants. Associated flow was assumed,

$\langle f(s) = g(s) \rangle$ , and:

$$f(s) = A \left( \frac{F}{F_0'} - 1 \right)^N \quad (78)$$

in which  $F$  is the distance in principal stress space from the applied stress to the hydrostatic axis normal to the current flow surface,  $F_0'$  is the portion of this distance from the current flow surface to the hydrostatic axis,  $A$  is a calibration parameter that depends on the direction of the plastic flow:

$$A = \left( \frac{\theta}{0.528} \right)^{k_3} \quad (79)$$

in which  $\theta$  is the direction of the stress vector in the  $I_1, J_{2D}$  space, and  $k_3$  is a material constant.

#### 4.3.1. Multi-Stress/Load Duration Tests

The viscoplastic component was calibrated using cyclic creep and recovery tests in unconfined and confined conditions. The confining stress was 250 kPa. A trial was conducted to determine the temperature for the test using sacrificial specimens. Temperatures varying from 60 to 40°C were tried. The specimens tested at high temperatures were failing prematurely with few cycles. The best results were achieved at 40°C. Temperature was measured throughout the test and at the end the final average temperature for all creep and recovery tests was 39 °C.

In the original procedure (Gibson, 2006), the model was calibrated using two separate tests, one in which the deviatoric stress was constant and the duration of the load pulse was increased with each cycle, and a second in which the load duration was constant and the deviatoric stress was increased with each cycle. This procedure has been updated here to reduce the number of specimens and expedite testing.

A combination of load durations and deviatoric stresses were used in a single test to cover a wide range of stress conditions, as shown in Table 7. The same combination of deviatoric stresses and frequencies were used in unconfined and confined tests. An example of the measured total strain history recorded during one test is shown in Figure 29. Each peak corresponds to one cycle. One detailed cycle is provided in the figure inset,

in which all components of the response (elastic, viscoelastic and viscoplastic) can be seen. The permanent response at each cycle was recorded at the end of each rest period.

Three replicates were tested in unconfined and three in confined conditions. The averages of permanent strains measured at the end of each cycle were used in the calibration. Figure 30 shows the average measured axial and radial permanent strains for unconfined and confined conditions.

Table 7. Deviatoric stress and frequency used on multi-stress/load duration test.

<b>Cycle</b>	<b>Deviatoric Stress (kPa)</b>	<b>Duration (s)</b>	<b>Rest period (s)</b>
1	120	2	20
2	120	7	70
3	120	56	560
4	497	2	20
5	497	7	70
6	497	56	560
7	1004	2	20
8	1004	7	70
9	1004	56	560
10	1500	2	20
11	1500	7	70
12	1500	56	560

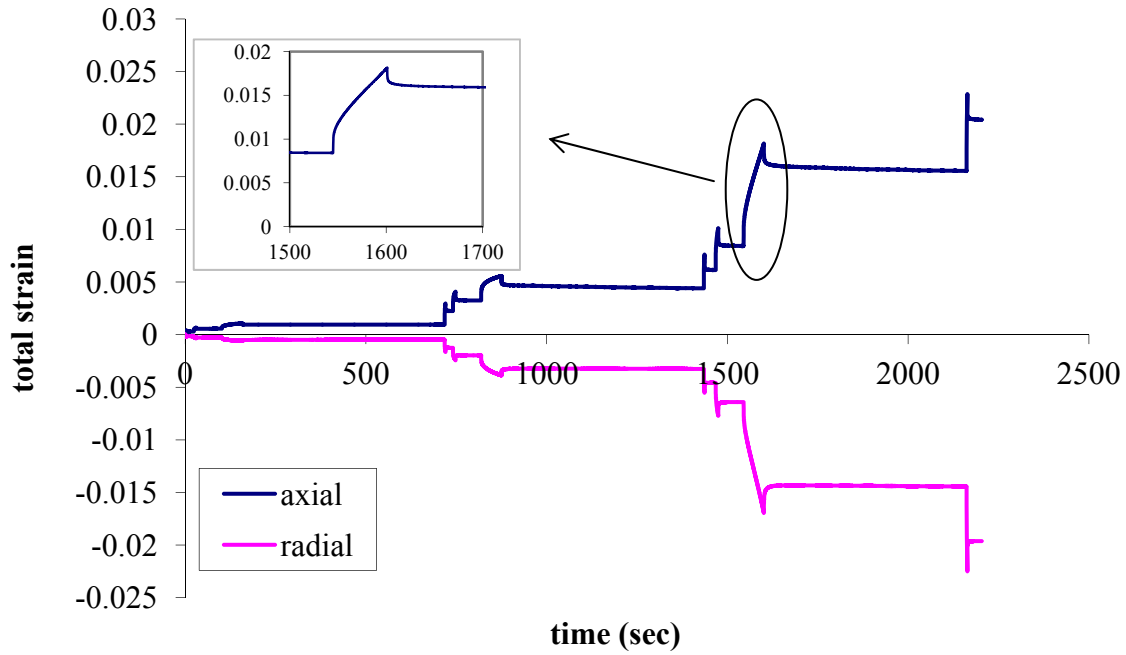


Figure 29. Example of multi-stress/load duration creep and recovery test.

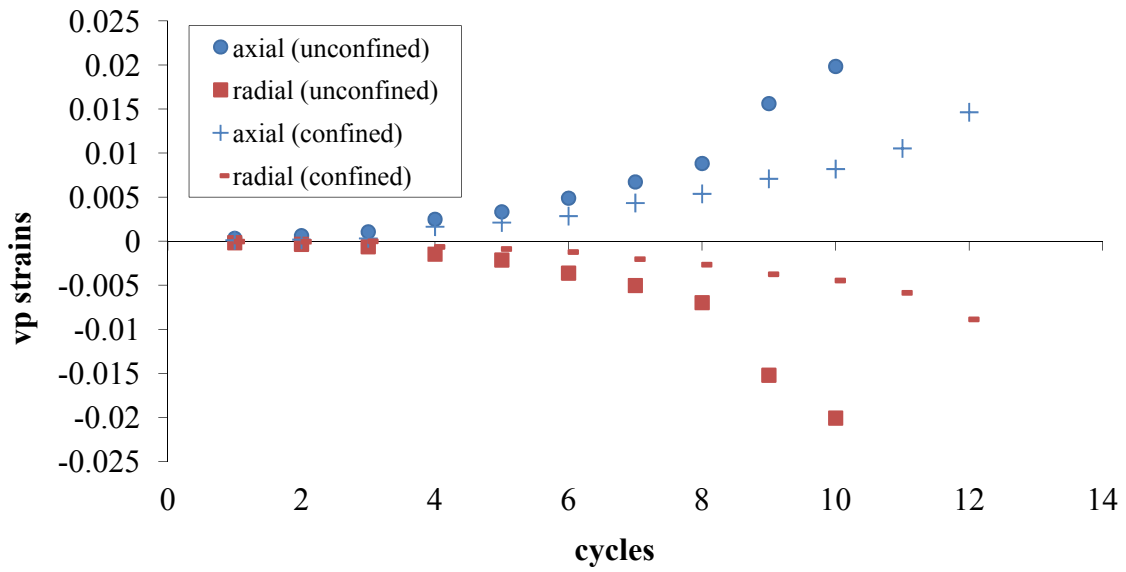


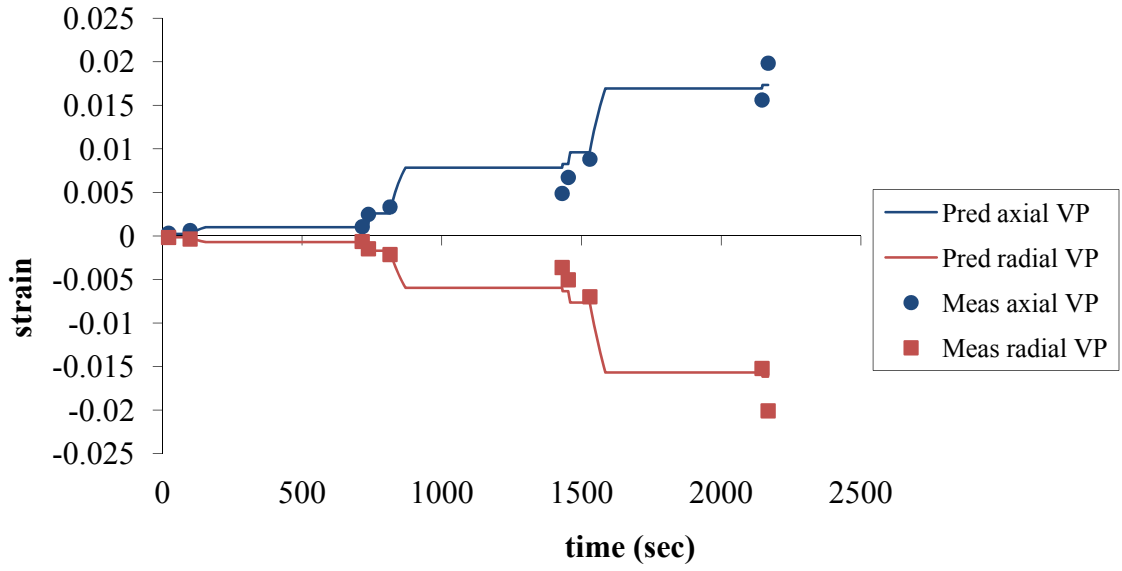
Figure 30. Creep and recovery viscoplastic strains versus load cycles.

#### 4.3.2. Viscoplastic Model Calibration

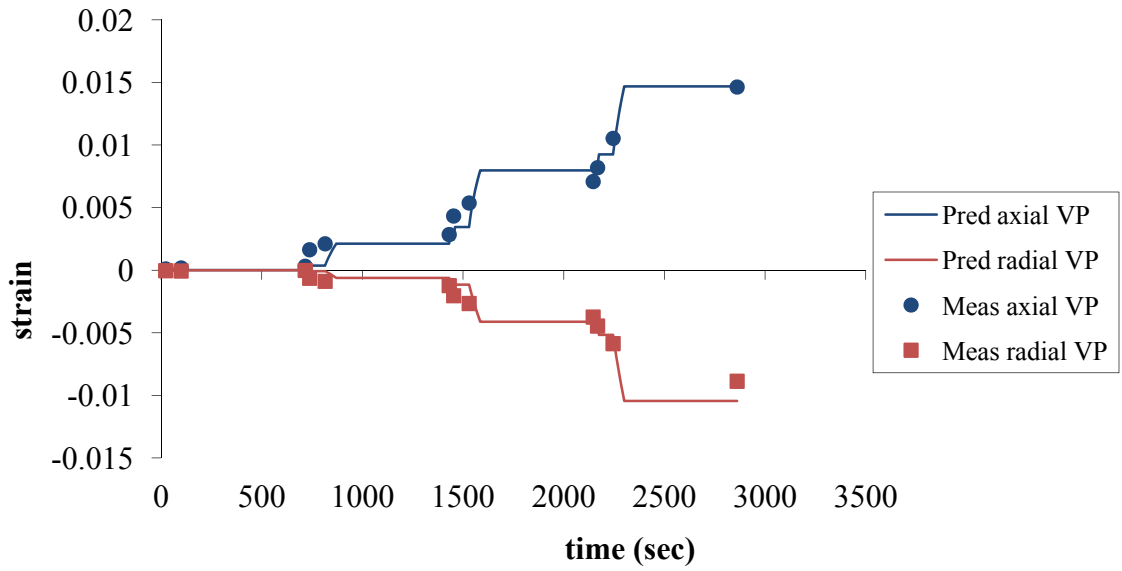
The viscoplastic model was written as a Matlab™ script and the calibration of all model constants was performed simultaneously using the minimization function in Matlab™. The sum of the squared difference between the calculated and measured permanent strains at all cycles in the test was the parameter to be minimized. In order to effectively consider all stress states and magnitudes, unconfined and confined test results were used simultaneously in the minimization function. The reference temperature of 19°C was adopted for the viscoplastic model calibration. The reduced frequency was calculated using the temperature shift factors provided in Table 4. The final model calibration coefficients are presented in Table 8. Predicted vs. measured strain plots are shown in Figure 31.

Table 8. Viscoplastic model calibration coefficients.

<b>Parameter</b>	<b>Calibration Coefficient</b>
$\Gamma$	1.659E-09 (kPa.s) <sup>-1</sup>
$\gamma$	0.04275
$\alpha_0$	0.00683
$k_1$	-68.096
$n$	2.2564
$N$	1.07604
$R_a$	3227.41 (kPa)
$k_2$	0.3306
$R_0$	38.4245 (kPa)
$k_3$	2.5782



(a)



(b)

Figure 31. Viscoplastic model calibration using cyclic creep and recovery tests: (a) unconfined and (b) confined.

#### *4.3.3. Validation with the Flow Number Test*

Researchers at the FHWA Turner-Fairbank Highway Research Center conducted Flow Number (FN) tests on the same mixture tested in the present study. The Flow Number test is a pulsed cyclic load and recovery test with fixed loading/recovery times and a fixed stress level where the permanent strains are measured after each load cycle. The tests can be performed unconfined and confined on cylindrical specimens. The FN test is used as a performance test for rutting susceptibility of asphalt mixtures. In addition, its results are used for calibration of rutting models such as the one used in the mechanistic-empirical pavement design guide (MEPDG). The test can be done using the Asphalt Mixture Performance Tester (AMPT).

These FN tests provided an excellent opportunity for validation since they were performed on the same mixture but conducted at a different laboratory and by different technicians. In addition, the strain measurements were different; high accuracy digital images of the specimen's deformation were used in the FN test, while conventional LVDTs were used during the multi-stress/load duration tests. The end conditions for applying the load at the two tests were also different. Spherical ball was used at the UTM in the University of Maryland, while flat end platen was used in the FN test. And finally the temperature for the FN test was set at 64°C, compared to 40°C for the multi-stress/load duration test.

The FN tests were performed at unconfined and confined conditions using three replicates each. The load was applied as a haversine pulse with a duration 0.1 seconds followed by a rest period of 0.9 seconds for recovery of elastic/viscoelastic strains. Viscoplastic strains were recorded at the end of each rest period. The deviatoric stress

was 207 kPa (30 psi) for the unconfined tests and 827 kPa (120 psi) for confined. The confinement was 68.9 kPa (10 psi).

The calibrated viscoplastic model was used to predict the permanent strains measured in the FN tests. Time-temperature superposition was applied using the temperature shift factors determined from the complex modulus tests.

The comparison between predicted and measured strains is shown in Figure 32. The red vertical bars represent the variability observed in the test. The model predicted the strains of the confined test with reasonable accuracy, but the unconfined strains were underpredicted. This is in part due to the small deviatoric stress applied in the unconfined test. During calibration, responses to small deviatoric stresses were consistently underpredicted as the price for better predictions at higher stress levels. However, for practical applications, the stress conditions used in the confined FN test are more representative of real pavements and thus more relevant to rutting performance.

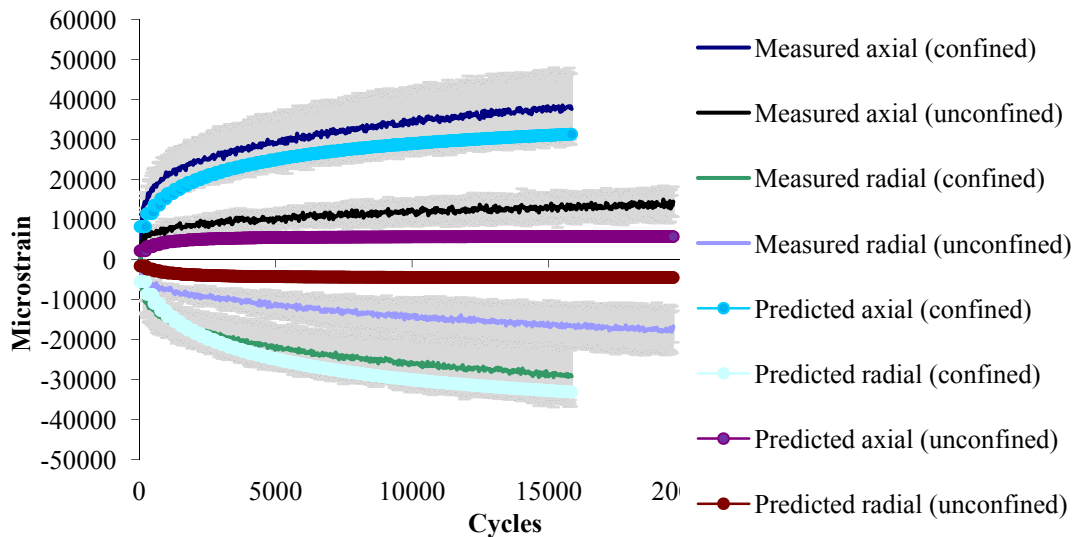


Figure 32. Predicted versus measured strains in the Flow Number validation test.

#### **4.4. Calibration of the Viscoplastic Model Using the Flow Number Test**

The FN tests used to validate the research-grade calibration were also used to recalibrate the model as an internal consistency check. The FN test can be done using the AMPT and is being considered as the test of choice for calibrating the empirical rutting model in the MEPDG. Therefore this exercise, if successful, could simplify the viscoplastic model calibration and minimize the effort for future implementation of a full mechanistic model for rutting prediction.

Following the opposite path taken for the conventional, research-grade calibration, the viscoplastic model was recalibrated using the FN test results. Once the model was recalibrated, it was validated using the multi-stress/load duration tests. The information about load and duration of each cycle was fed into the Matlab™ script and the same optimization algorithm was used to find the material constants of the viscoplastic model. Predicted versus measured strains obtained during calibration are shown in Figure 34. The comparison between the two viscoplastic model calibrations is provided in Table 9. All parameters in the model are calibrated at the same time, therefore large variations in one or more parameters are expected. Overall these variations cancel each other out during the minimization of errors.

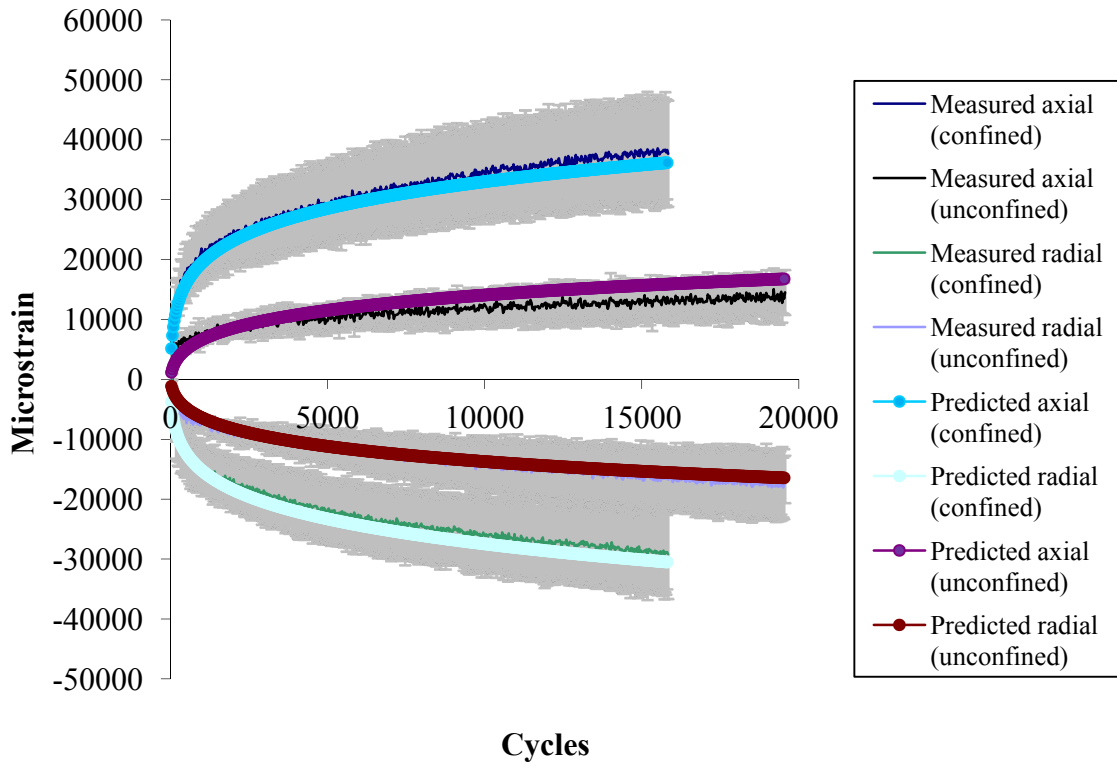


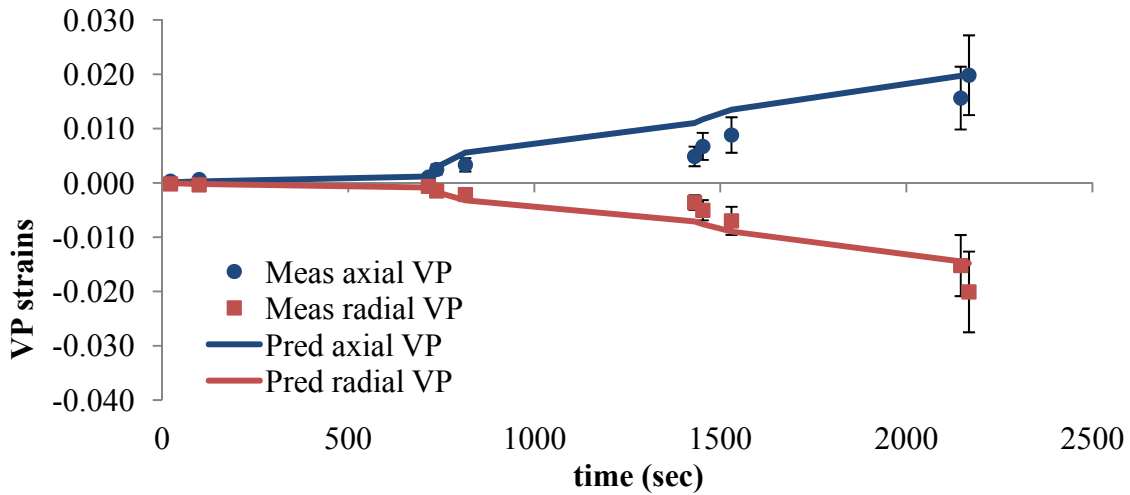
Figure 33. Viscoplastic model calibration using the Flow Number test.

Table 9. Comparison between the two viscoplastic model calibrations.

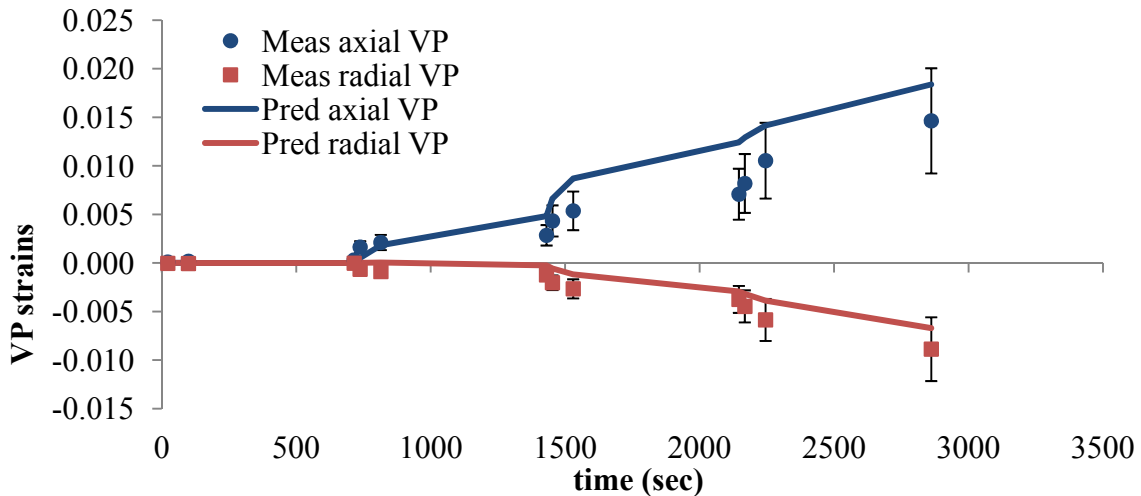
Parameter	Multi-stress/load duration calibrated model	FN calibrated model
$\Gamma, (\text{kPa}\cdot\text{s})^{-1}$	1.659E-09	3.1888E-09
$\gamma$	0.04275	0.04173
$\alpha_0$	0.00683	0.00565
$k_1$	-68.096	-39.642
$n$	2.2564	2.3009
$N$	1.07604	2.55519
$R_a$ (kPa)	3227.41	4192.94
$k_2$	0.3306	0.5241
$R_0$ (kPa)	38.4245	23.9368
$k_3$	2.5782	4.8948

#### 4.4.1. Validation with the Multi-Stress/Load Duration Test

The model calibrated using the FN tests was used to predict the results of the multi-stress/load duration tests. The results, presented in Figure 34, suggest a good agreement between predicted and measured permanent strains. The model calibrated using the FN tests predicted permanent strains that agree well with the measured data.



(a)



(b)

Figure 34. Predicted versus measured viscoplastic strains from multi-stress/load duration creep and recovery tests: (a) unconfined and (b) confined. Predicted strains computed using the FN-calibrated model.

One of the major disadvantages of advanced characterization of asphalt concrete mixtures is the complex calibration process, which often requires one or more research-grade tests. This poses as an obstacle to practitioners and limits the use of advanced modeling as tools for practical applications. The results shown in Figure 34 suggested that the Perzyna-HiSS viscoplastic model can be calibrated using the FN test, a simple test that can be performed easily on a production basis using the AMPT.

#### **4.5. Summary**

This chapter described the calibration process for the viscoelastic-viscoplastic constitutive model. The linear viscoelastic component was calibrated using the complex modulus test. The dynamic modulus master curve, relaxation modulus and creep compliance were determined. The continuum damage component was calibrated using unconfined and confined constant strain rate tests to failure at low temperatures.

The viscoplastic component was calibrated using unconfined and confined cyclic creep and recovery test, termed multi-stress/load duration test, in which different stress levels and load duration were applied in sequence on the same specimen until failure. This test was designed to expedite the calibration process and reduce the number of specimens required. Flow Number (FN) tests were used to verify the calibrated model. These tests were performed independently by FHWA at the Turner-Fairbank Highway Research Center. In addition, the same FN tests were used to recalibrate the viscoplastic model, which was then verified using the multi-stress/load duration test. The results demonstrated that the Perzyna-HiSS viscoplastic model can be successfully calibrated using the simple FN test.

The implementation of the calibrated model in a finite element method is one of the objectives of this research. This implementation is described in detail in Chapter 5. A series of applications follows in Chapter 6.

## **Chapter 5 Finite Element Modeling**

### **5.1. Introduction**

Pavement design requires selecting materials and a structure that will withstand cyclic loading and climate fluctuations over a long period of time. Materials used in pavement construction require advanced constitutive models that are capable of capturing the complexities observed in their behavior. Finite element (FE) methods are ideal for modeling complex material behavior. However, simulating large number of load applications in finite element analyses is a daunting task that requires significant computational effort, which is often prohibitive for practical designs. Nevertheless, FE analysis can improve understanding of material behavior and pavement performance, provide insights on critical locations and behavior phenomena in the pavement structure, and help the design of more effective structures and materials.

The viscoelastic-viscoplastic model developed and calibrated in this research was implemented in ABAQUS™ (2006), a commercial finite element package widely employed in pavement engineering research. The objective was to have a robust but simple to use tool for analyzing permanent deformations in pavements under moving wheel loads. ABAQUS is a good tool for this application for several reasons. It is a mature, well-validated, and well-documented finite element analysis program. It has a user-friendly interface for pre- and post-processing, which facilitates creating models and visualizing results after the analysis is complete. In addition, it has a large variety of constitutive models in its library that can be used to model other layers in the pavement structure (e.g., elastic, elasto-plastic, etc.).

Most importantly, ABAQUS provides the option of incorporating user defined material functions (UMAT) instead of its built-in constitutive models. The UMAT is written in FORTRAN™ and it is called from the analysis module during the simulation process. The constitutive model described in Chapter 4 was implemented in a UMAT. This Chapter provides a briefly overview of the key FEM and ABAQUS components relevant to the moving wheel analyses and a description of how the constitutive model was written in the UMAT.

Version 6.7.8 of ABAQUS was used in this research. It was installed in a workstation with 4 processors Intel Core 2 Extreme, 2.6 GHz, with 4GB of RAM, operated by Windows XP 64-bit. The FORTRAN compiler was Intel™ version 9.0.

## **5.2. Finite Element Method**

The FEM provides numerical approximations to problems that are difficult to solve analytically. It is a piecewise formulation in which the problem is divided in many smaller problems (elements) that are solved simultaneously. The elements are connected to each other at nodes, typically the corners but also sometimes at other points (e.g., mid points at element sides). A continuous polynomial function of the desired response (e.g., displacement) is defined within the element between the nodes, forming an approximate piecewise representation of the response over the entire solution domain. Loads and boundary conditions are applied to the nodes. Equations describing the behavior of each element and the interaction of elements between nodes are assembled for form a set of linear equations that is solved to find the desired primary response, in this case the displacement values at the nodes.

The procedure for computational modeling using the FEM consists of six steps:

- Geometry modeling, including boundary conditions
- Meshing and element definition
- Material property specification
- Loading condition application
- Simulation
- Visualization

#### *5.2.1. Geometric Model and Boundary Conditions*

The pavement geometric model was constructed by using independent parts in the ABAQUS solid modeler. Each part represented one layer in the pavement structure. The geometric model was created in three dimensions (3D) with an axis of symmetry along the longitudinal center of the tire load. Figure 35 shows one pavement cross-section; the different shades of gray represent individual layers.

The axis of symmetry is taken as the center of the tire, hence only half of the problem is modeled. Therefore the direction of traffic was defined along the axis of symmetry. Boundary conditions were applied to all faces of the geometric model to limit displacement in the direction perpendicular to the face. The bottom of the last layer modeling the subgrade was limited to no displacement in all directions (encastre). All predictions of rutting were calculated at the middle cross section of the model. Several models were tested to ensure that the effects of boundary conditions on the mechanistic responses induced by the tire load were insignificant.

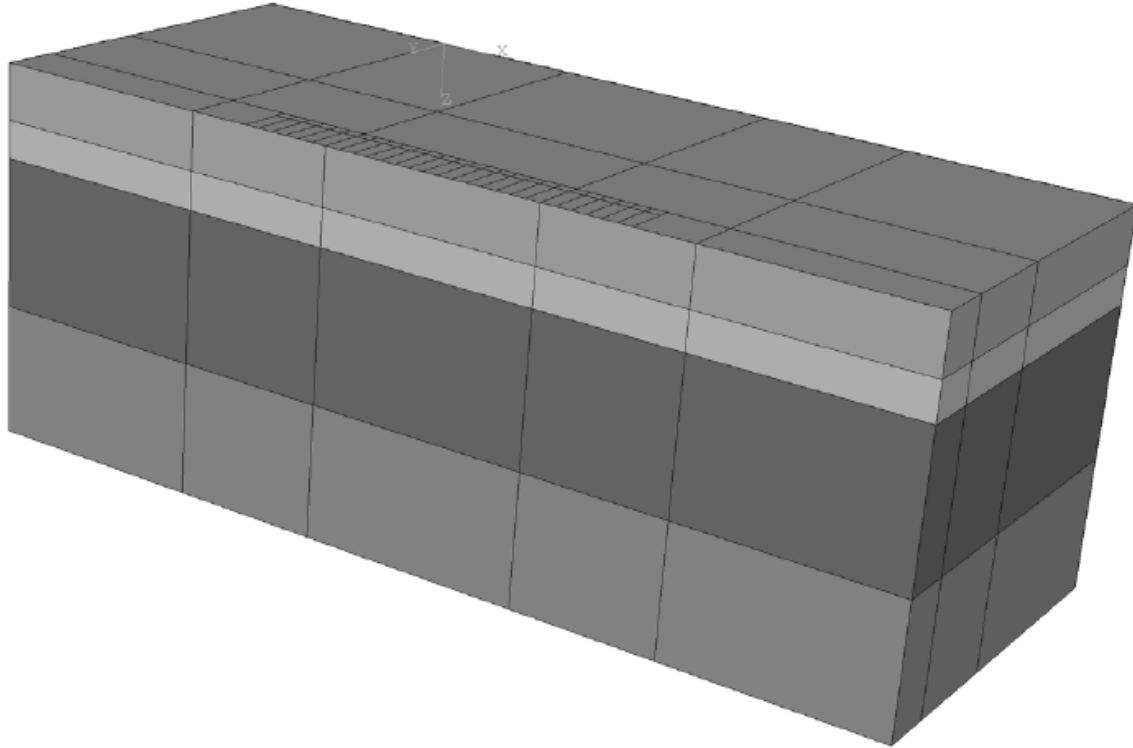


Figure 35. 3D solid model.

### *5.2.2. Meshing and Element Definition*

The meshing process divides the problem domain into the set of elements connected at nodes. The density of elements in a given region of the problem controls the accuracy of the results. In the case of modeling a pavement subjected to a tire load, a high element density is desired near the load. Unfortunately, the more elements, the longer the required computational time. It is therefore necessary to limit the number of elements. The meshing process typically requires several iterations in order to define on an optimum number of elements that will produce a sufficiently accurate solution at a practically realistic computational effort.

The element type and respective number of nodes are defined during the meshing process. The number of nodes defines the type of function that can be used to

approximate the solution within an individual element. Simple 4-node quadrilateral elements in 2-D or 8-node brick elements in 3-D only allow linear approximations of the displacements between the corner nodes. Elements with additional nodes (e.g., at the midpoint of each edge) can accommodate higher order approximating polynomials. However the computational effort increases significantly. The most common approach is to use simple elements and increase the number of elements in regions of high desired accuracy. Eight-node brick elements were used in this model.

The tire load could not be applied instantly in the nonlinear analyses. Incremental loading was required to bring the tire pressure up to the desired peak. Since the ultimate goal was to evaluate responses induced by a moving load, there was no need for additional refinement to the mesh where the tire load was initially applied and later removed at the end of the cycle. In addition, regions distant from the loading zone could also be meshed with fewer elements. Therefore, each layer was divided into several zones and each zone was meshed differently. This effort greatly expedited computational time.

Figure 36 shows the plan view of the pavement surface. The  $\frac{1}{2}$  tire footprint was modeled as a 0.24 x 0.12 m rectangular area. The horizontal and vertical lines define the different meshing zones. The center area was defined as the moving load area, at which the most refined mesh was defined. The two adjacent areas where the tire pressure was loaded and unloaded are also shown in the figure. All layers were modeled using the same zone configuration.

When zone configuration was completed, a mesh study was conducted to determine the optimal mesh density for each area. Figure 37 shows the final mesh for the

surface layer in plan view. A finer mesh is used in areas close to the moving wheel load, and a coarser mesh in more remote areas.

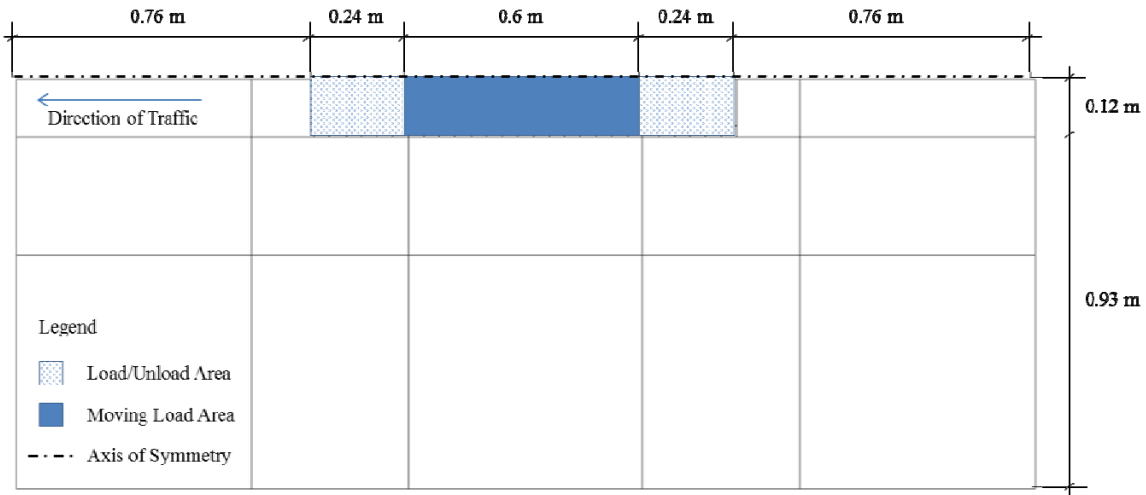


Figure 36. Plan (surface) view of geometric model.



Figure 37. Surface layer mesh in plan view.

Each layer in the pavement structure was modeled as one independent part in the ABAQUS solid modeler. The same principle of meshing by area was applied to all layers in the pavement cross section, following the zone configuration shown in Figure 36.

There is no need for coincidental node positions between parts when the modeling by

parts. This is a great advantage because one can define the mesh of each part separately, which greatly enhance computational time. The final model mesh is shown in Figure 38. It consisted of 20,700 8-node brick elements with 24,855 nodes.

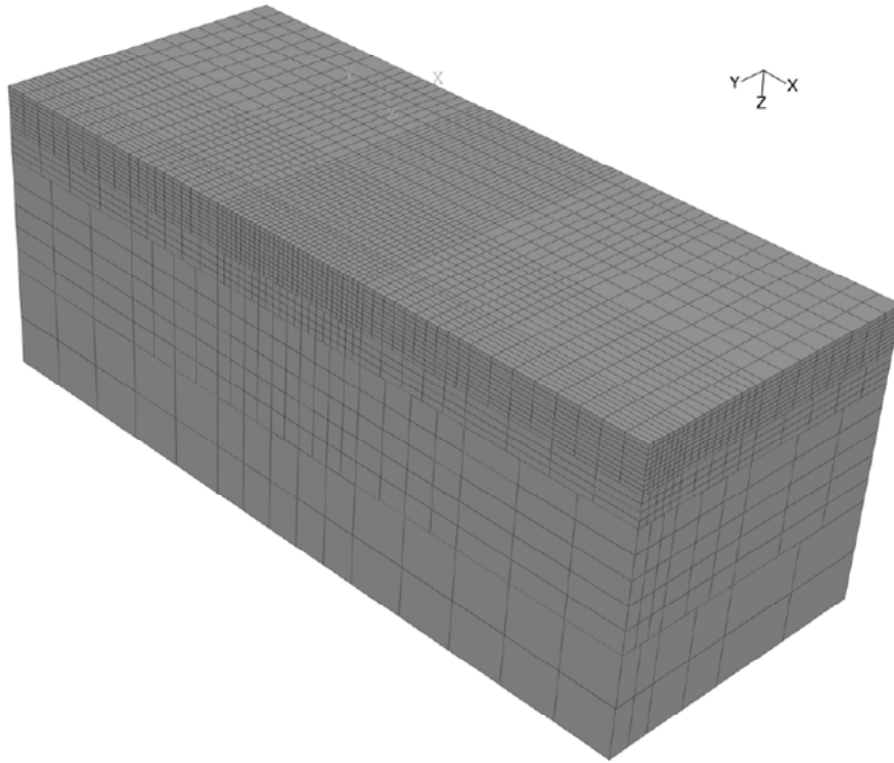


Figure 38. 3D finite element mesh.

### 5.2.3. Material Property Specification

ABAQUS has two options for selecting the constitutive model that governs the material behavior and consequently the material property inputs. For common material behavior, there is a library of constitutive models encompassing typical linear and non-linear models. For less common material behavior, there is an option of creating a user-defined constitutive model or UMAT. For the analyses in this dissertation, all pavement layers other than the asphalt concrete were modeled as homogeneous isotropic linearly elastic materials. The asphalt concrete was modeled using the viscoelastic-viscoplastic

model described in Chapter 2 as implemented in a UMAT. The details about the UMAT are provided in a later section in this Chapter. The remaining material properties used are provided in Chapter 6 with the description of the problems evaluated and results obtained.

#### *5.2.4. Loading Conditions*

The loading condition defines the prescribed loading of the problem. For structural analysis it can be in the form of forces, pressures or displacements. Loads are applied to the nodes. Pressure loads are transformed into nodal forces and applied directly to the nodes within the loaded area. The load cannot be applied instantly in the nonlinear analyses; it must be modeled in increments. To represent instant loading, very small loading time is used. In addition, the type of loading increment can be defined as well. A linear increase over the loading time is typical, although many FE software allow different increment forms, such as exponential, or even sinusoidal for cyclic loading. A linear increase of loading from zero to the defined peak was used in this research. Once the prescribed load is fully reached, a new step is generated which takes the load and places it in an adjacent location, thus simulating the moving of the wheel.

The tire footprint was modeled as a pressure load of 690 kPa (100 psi) applied directly on the set of elements beneath the wheel. As shown in Figure 39, the moving wheel was simulated by incrementally moving the load footprint from one set of elements to the next by adding a new line of loaded elements in the front end of the tire, while removing one line of loaded elements from the back end of the tire. This gives the motion aspect of the load. Although time consuming, this approach is a far better representation

of a moving tire than the step-wise process commonly found in the literature. In addition, the load when modeled as a pressure area applied directly on the surface instead of the actual modeling of the tire as an independent part increases computational performance and reduces the risk of numerical instabilities that could happen at the interface between the two parts (tire and pavement structure).

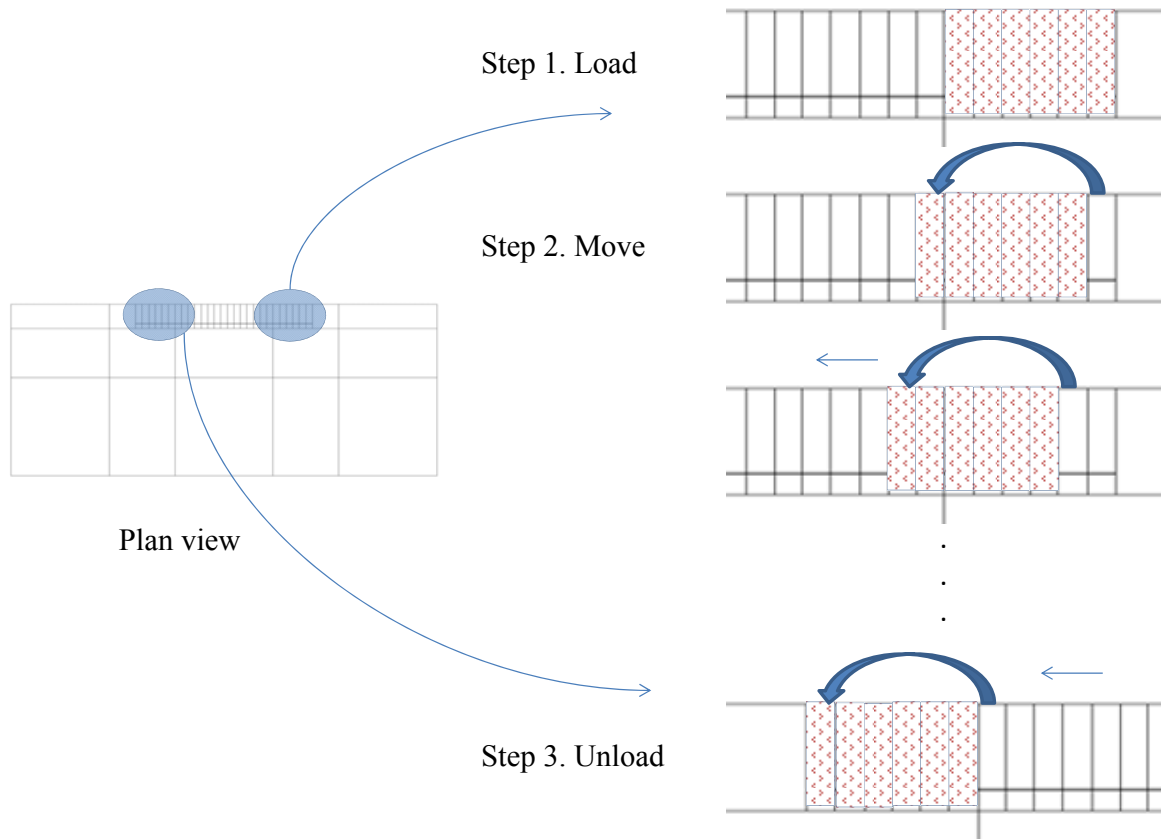


Figure 39. Schematic of moving load.

#### 5.2.5. Simulation

After the numerical model has been assembled, it must be solved. The solution to the system of linear equations gives the values for the response variable at each node of the mesh. The computational effort is directly proportional to the number of equations that are being solved simultaneously, which in turn is a function of the number of

elements/nodes. A direct solution algorithm based on Gauss elimination is most commonly used to solve the set of linear equations. However, when one is dealing with nonlinear problems, which is the case in this research, the load must usually be applied and repositioned in small increments in order to track the nonlinear response. The nonlinear system is approximated as an equivalent linear system for each load increment. An iterative procedure is then applied to solve the equilibrium between the applied loads and the nonlinear stress-strain behavior of the elements.

ABAQUS offers a direct linear equation solver based on Gauss elimination and an iterative nonlinear solver based on a modified Newton-Raphson algorithm. Other options available in ABAQUS were explored, but in the end the stability of the Newton-Raphson method was decisive. The step increment is automatically chosen by ABAQUS, but with some constraints on the maximum step size. Implicit time integration was employed in the analyses for two main reasons. One was unconditionally stability, which proved to be critical even when simple models such as elasto-plasticity were first explored. The second was a software limitation; user-defined constitutive models must be implemented as UMATs using an implicit formulation.

### **5.3. Viscoelastic-Viscoplastic Model Implementation**

The viscoelastic-viscoplastic constitutive model was implemented in ABAQUS as a user defined UMAT. The UMAT subroutine is coded in FORTRAN™ and is compiled and linked into the ABAQUS executable file. The UMAT must provide two outputs to the ABAQUS analysis: (1) updated stress vectors and solution dependent internal

variables at the end of each load step increment (or iteration), and (2) the material stiffness matrix.

The constitutive model is implemented in a three dimensional formulation but has the capabilities for two dimensional axisymmetric or plane strain problems that are also often used in pavement modeling. Documentation on how to create a UMAT is limited. Examples are scarce and often poorly documented. This made the development a difficult task.

The UMAT code is documented and presented in Appendix A. In addition to implementing the viscoelastic-viscoplastic constitutive model described in Chapter 2, it can also be used as step-by-step template for creating other UMATs. The key steps can be outlined as follows:

1. Declaration of variables provided by ABAQUS
2. Declaration of local variables (used within the UMAT during calculations)
3. Definition of material properties and variable initialization
4. Calculation of viscoelastic responses
5. Calculation of viscoplastic responses
6. Update of the stress vector
7. Return of output quantities to ABAQUS

All calculation steps are documented in the UMAT provided in Appendix A. After the displacements are calculated, the stress vector and the stiffness matrix are updated and returned back to ABAQUS at the end of the UMAT.

At the beginning of each step increment calculation, ABAQUS provides certain variables that may be used in the UMAT calculations. It is mandatory that these variables

be declared and imported into the UMAT. Therefore the first step when creating a UMAT is to properly declare the variables that ABAQUS is passing onto the UMAT. The syntax for this declaration is indicated in the documented UMAT in Appendix A. Local variables are declared next. These variables are used in the constitutive model calculations and are not transferred back to ABAQUS. All material property values are also defined at this location for simplicity.

After variable declaration is complete, the constitutive model calculations are coded, starting with the viscoelastic component. The objective is to determine the stress vector at the end of the step increment induced by viscoelastic strains. The first step is the calculation of pseudo strain. This was achieved by using the recursive algorithm proposed by Simo and Hughes (1998) based on the strain history provided at the beginning of the step increment. The principal strain tensor is calculated and inversely ordered ( $\epsilon_{p33} > \epsilon_{p22} > \epsilon_{p11}$ ) to accommodate the axis of symmetry at the principal axis 3. Accordingly the direction cosines matrix is adjusted to reflect this transformation. This is incorporated to comply with the locally transverse isotropy induced by damage in Schapery's theory. Recall that the UMAT is executed at the integration point level. At every step increment, the load is changing, either increasing/decreasing or simply moving from one location to another when a moving load is simulated. Although the principal axes are continuously rotating for a given node as the wheel moves on the surface, it is assumed that there is no rotation within the step increment.

Stresses are computed using the principal pseudo strains and transformed back into global stresses. This process was described in greater detail in Chapter 2 and is documented step-by-step in the UMAT. In addition to the stress vector, the stiffness

matrix must also be calculated. The stiffness matrix is the derivative of stress with respect to strain increment at the end of the step. The recursive algorithm by Simo and Hughes (1998) is used. Recall that all calculations are done at the local coordinate system (i.e., the principal pseudo strains were calculated in the local coordinate system). Therefore the local stiffness matrix and local principal stress vector are transformed back into global stiffness matrix and global stress vector using the direction cosines matrix defined previously.

The final step to complete the viscoelastic calculations is the damage update. A small perturbation in the damage variable is induced and the variation in the pseudo work is computed. The final value for the damage variable is computed using the damage evolution law. The process is also described in Chapter 2 and fully documented in the UMAT provided in Appendix A.

Time-temperature superposition was considered the same way as provided in the model development. Only constant temperature conditions are considered in the implementation. ABAQUS is capable of simulating variations of temperature over time. However, incorporating varying temperatures was beyond the scope of this research.

The viscoplastic component is initiated by computing the principal stress invariants from the current stress vector. The new stress vector is calculated from the strain increment provided by ABAQUS and the stiffness matrix computed in the viscoelastic component. Viscoplastic strains are calculated following a sequence of steps to determine if viscoplastic flow has occurred based on the position of the principal stress vector in relation to the HiSS flow surface. If flow has occurred, the point on the HiSS surface that is normal to the applied stress point must be determined. This was

accomplished by using a Newton-Raphson algorithm (Gibson, 2006). The NR algorithm provides the stress vector at the HiSS surface, the normal vector to the surface in the direction of the applied stress (strain trajectory) and the relative distance from the applied stress to the hydrostatic plane. After the calculation of viscoplastic strains is completed, the global stress and strain vectors are updated and returned back to ABAQUS.

It is important to note that the final objective of the UMAT is to provide the stress vector and the stiffness matrix, both at the global coordinate system, at the end of the step increment for each node in the problem.

Coding and debugging the UMAT was a difficult task. Any error associated with the FORTRAN code had to be debugged outside ABAQUS. The interface and interaction between the UMAT and ABAQUS is not user friendly and no additional information about the source of error in the code is provided. In order to expedite this process, a standalone code of the UMAT was created. The standalone version included steps to create loading scenarios that were otherwise provided directly by ABAQUS. The entire code was then debugged using the Intel™ Fortran compiler. This proved to be vital in the debugging efforts.

### *5.3.1. Numerical Difficulties and Simplifications*

Some difficulties were encountered during the development of the UMAT. The viscoelastic component was adapted from a previous work done by Hinterhoelzl (1999). His UMAT was written to simulate solid propellant for rockets. The adaptation to asphalt concrete required redoing all the damage functions and the procedure for updating the damage variables. A slightly different recursive algorithm was implemented to compute

pseudo strains in the hope that it would expedite the calculations. In the end, the viscoelastic component was the most time consuming part of the analysis. A full 3-D representation of one moving load cycle required about 50 minutes of computation time, of which 40 minutes were exclusively dedicated to the viscoelastic component.

The main objective of this research is the analysis of permanent deformation at high temperatures using the viscoplastic component of the model. A simplified UMAT was therefore created in which the viscoelastic component was replaced by simple isotropic elasticity. The elastic properties were determined from the dynamic modulus master curve of the asphalt concrete for the desired temperature and loading rate in the pavement.

The analysis of one moving load cycle using the new UMAT required less than 10 minutes of computation time. This approach was found to have little effect on the predicted permanent deformations, especially at the intended simulations at high temperatures. Details and examples are provided in Chapter 6.

Another difficulty faced during the development of the UMAT was the ill-conditioned solution of the HiSS function at the intercept with the volumetric stress invariant axis, described in Eq. (75). The normal to the HiSS surface at the volumetric axis is undefined. The surface function intercepts the volumetric axis in a non-normal angle, which makes the normal undefined. Since the Perzyna-HiSS model assumes associated flow, the direction of the incremental viscoplastic strain vector is always normal to the yield surface. Due to the undefined normal vector of the function at the intercept, there are stress state regions where the normal vector cannot be computed.

Figure 40 describes this problem in more detail. It shows the HiSS surface in the stress invariant space. The area marked in the plot and identified by a dotted line is the region where normal vector to the HiSS surface are undefined. For illustration, 4 critical stress paths induced by a moving wheel at different locations in the asphalt concrete layer are plotted: (a) point located at the surface and center of the wheel path, (b) below the center of the wheel path at the bottom of the layer, (c) surface and far outside the rutting profile, and (d) below the center of the wheel path and 50 mm from the surface. None of the critical stress paths were located in the undefined normal vector region. The laboratory tests for model calibration were all done in compression, so none had stress paths in the zone where the problem of an undefined yield surface occurs. However, this problem did occur when the UMAT was applied to pavement structures and was the source for numerical instabilities.

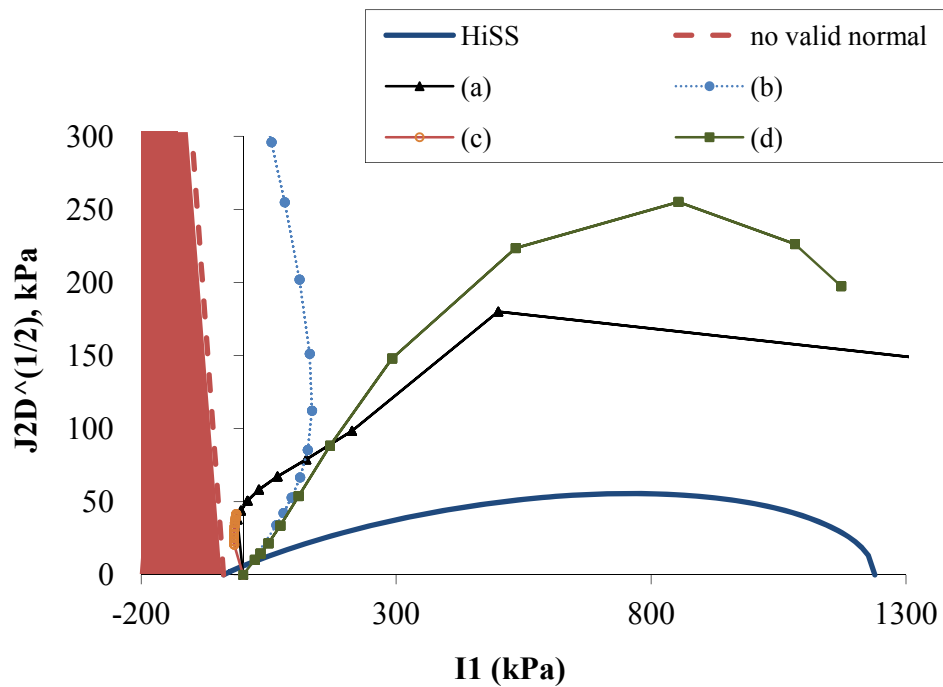


Figure 40. Example of HiSS surface and the limit where normal vectors to the surface can be calculated.

At first, it was thought that only points in pure tension would be susceptible to this problem. A state of pure tension is not usual in pavements, but rather a combination of tension and compression. Investigations revealed that the instability problems developed at undisturbed elements near the boundaries of the problem domain when subjected to small stress levels. It was unclear whether this problem developed during attempts to reach force equilibrium during or at the end of a given load increment. During all the checks and tests to identify the problem, the location remained confined to regions near the boundaries and at low stress levels. Locations critical to the analysis (e.g., around the wheel path) were not affected by this problem, as shown in Figure 40. Therefore the simple solution was to implement a check during the viscoplastic strain calculations to identify if the stress vector was within the undefined normal zone in the model. When the stress point was found within the undefined normal zone, no viscoplastic flow was assumed. Given the remote locations of the problem areas and the infrequency of the instability, this assumption seemed appropriate to address the issue.

#### **5.4. Model Verification**

The implementation of the UMAT was verified using tests performed previously by Gibson, 2006. This provided an independent verification without the extra costs and effort of running new tests.

Gibson (2006) conducted several tests for calibrating the viscoplastic model during its development. One was chosen for this verification. It consisted of a creep and recovery test conducted in uniaxial compression at fixed stress level and varying loading times. The test schematic is provided in Figure 41. Two test results were used, one

unconfined and one confined. Figure 42 and Figure 43 shows the test results and the predictions obtained during calibration (Gibson, 2006), and the predictions obtained when the tests were simulated using ABAQUS. The comparison between predicted during calibration with predicted using ABAQUS show very good agreement, indicating that the viscoplastic model is successfully implemented in ABAQUS.

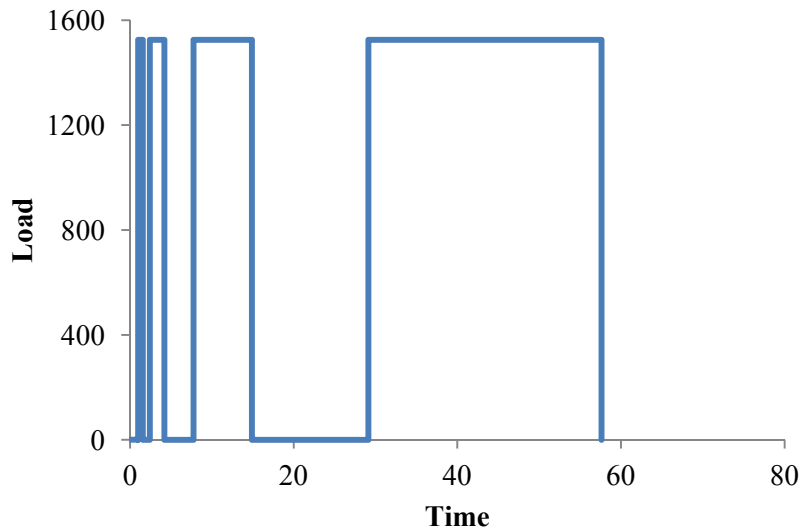


Figure 41. Schematics of creep and recovery test at fixed stress level and varying loading time.

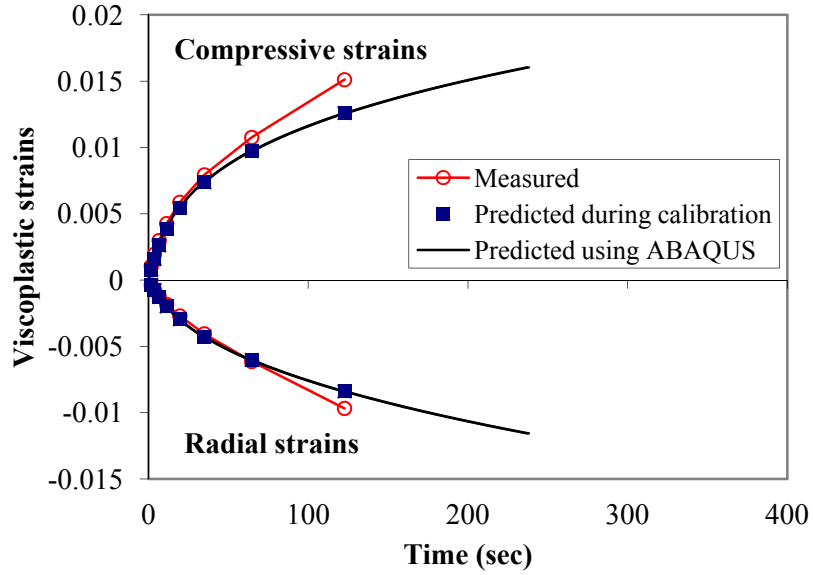


Figure 42. Fixed stress test with 1,500 kPa deviator stress, unconfined, tested at 35°C.

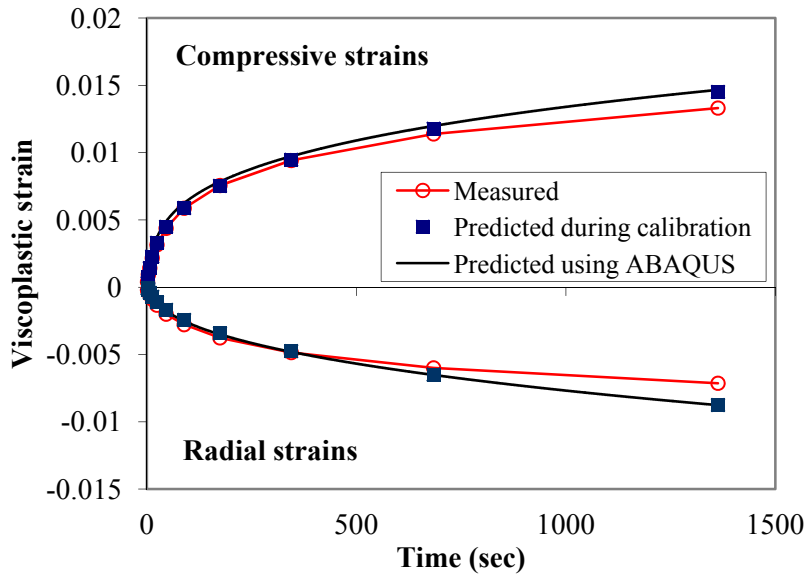


Figure 43. Fixed stress test with 1,500 kPa deviator stress and 250 kPa confining stress, tested at 35°C.

## **5.5. Summary**

This Chapter provided a summary of key aspects and steps required to simulate nonlinear structural response using the finite element method. It also described the implementation of the viscoelastic-viscoplastic model into an ABAQUS user-defined material model subroutine or UMAT. Given the difficulties in finding good documentation on how to write and debug UMATs, the UMAT developed in this research was extensively documented in order provide some clarity on the development process that can serve as a template for future studies. Difficulties during the model implementation were also discussed and the approaches for overcoming these difficulties were presented. Finally a simple, minimum cost, independent validation was presented based on previous results using the same model formulation but calibrated for a different mixture. The results suggest that the code implemented in the UMAT yields results that are in good agreement with the model formulation used during its initial development.

## **Chapter 6 Numerical Applications**

### **6.1. Introduction**

The implementation of the viscoplastic constitutive model into the ABAQUS finite element code was an essential step towards fully mechanistic predictions of permanent deformation in asphalt concrete pavements. The model provides the means for directly simulating the material behavior that leads to rutting. This chapter describes a few applications of the finite element model. The objective is to use these applications to provide insights into the rutting problem.

The effect of simulating a moving wheel versus the more common bouncing wheel approach is investigated and the importance of principal stress rotations and shear stress reversals induced by the moving wheel is evaluated. The effect of pavement type on the rutting profile and its development over time is also examined; this provides the basis for the development of a mechanistic approach to improve the empirical rutting model used in the current Mechanistic-Empirical Pavement Design Guide (MEPDG), a pavement design tool currently recommended by the American Association of State Highway Transportation Officials (AASHTO). And finally one field section from Federal Highway Administration's Accelerated Loading Facility (ALF) is simulated with the finite element model and the results are compared with field measured permanent deformation.

## 6.2. Simplified Finite Element Modeling Approach

The commercial finite element package ABAQUS™ was used to simulate pavement permanent deformations in this research. The UMAT developed for the viscoelastic-viscoplastic constitutive model described in Chapter 5 was used for all of the analyses presented here.

Most of permanent deformation in pavements occurs at high temperature when the binder has low viscosity and is thus more fluid. In this condition, the aggregate skeleton is responsible for carrying most of the traffic load. Plastic deformations are expected as consequence of air voids reduction (volumetric deformations) and particle reorientation (shear deformations). The influence of the binder viscosity is to cause a delay in the material's response to loading. The viscoplastic behavior is the dominant cause of permanent deformations. At high temperatures, viscoelastic effects are not significant and there is far less development of microcracks and damage than at low temperatures.

An example of the dominant effect of viscoplastic behavior in asphalt mixtures at high temperatures can be seen in Figure 44. This figure shows numerical simulations of creep and recovery tests on an asphalt concrete mixture at two different temperatures, 19°C representing a moderate temperature and 45°C a high temperature. (45 °C was chosen because it was the temperature during the accelerated load testing analyzed later in this Chapter.) It can be seen clearly from the figure that the magnitude of viscoplastic strains and its contribution to total strains is significantly magnified when the temperature is high. For the same load duration and magnitude, the viscoplastic strain is nearly eight times higher at 45 °C than it is at 19 °C.

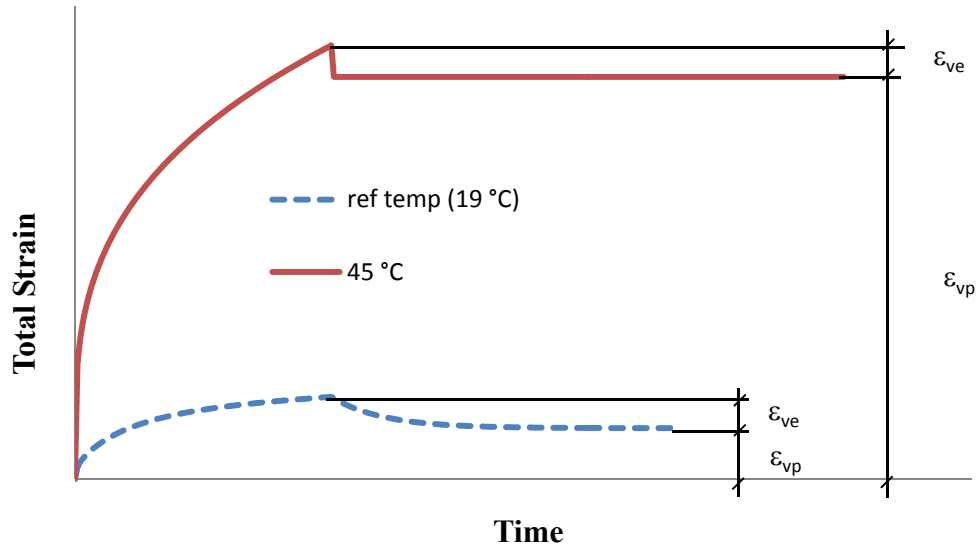


Figure 44. Influence of temperature on viscoplastic behavior of asphalt concrete in a simulated creep and recovery test.

The computational time required to predict the viscoelastic-viscoplastic response of one moving load cycle on a pavement structure was about 50 minutes on a quad core 2.6 GHz Intel™ Core 2 Extreme with 4 GB of RAM running 64-bit Windows XP. This may be reasonable for a few cycles, but the execution time becomes prohibitive if one intends to simulate hundreds or even thousands of cycles.

One way to reduce computational time is to shut off the viscoelastic component of the model and replace it with a much simpler constitutive equation. As illustrated in Figure 44, the viscoelastic continuum damage contribution to the total strains is very small at elevated temperatures. The viscoelastic continuum damage model, which governs the pre-yielding response, was therefore replaced by a simple isotropic elastic model. This constitutive model is termed the elasto-viscoplastic model (EVP). The linear viscoelastic dynamic modulus master curve was still used to determine the material's

instantaneous elastic modulus based on temperature and load frequency as related to the tire speed. The EVP UMAT is presented in the Appendix B.

The creep and recovery test simulations using the complete V EVP model (Figure 44) were repeated using the alternative EVP model. The results are shown in Figure 45. The final total residual strains are the same for both temperatures, which is expected since the viscoplastic component is the same in both constitutive models. At the lower temperature, the models predicted very different responses to the peak strain and the early portion of the recovery, reflecting the influence of the viscoelastic response. However, the difference between the two models is negligible at the higher temperature both before and after the peak strain. Based on these results, it was decided to use the alternative, simpler constitutive model for the numerical simulations of pavement structures at high temperatures.

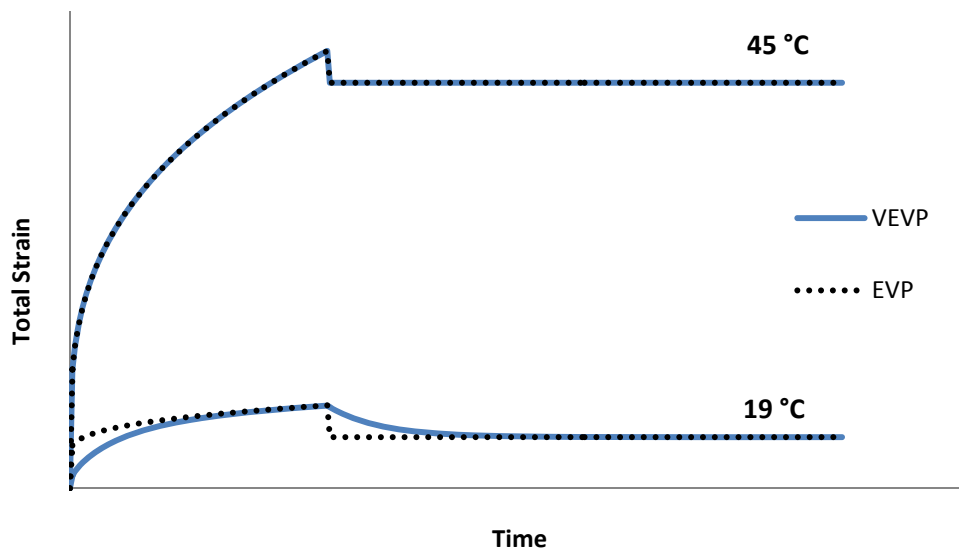


Figure 45. Comparison between viscoelastic-viscoplastic and elasto-viscoplastic simulation of creep and recovery at two different temperatures.

### **6.3. Influence of Shear Stress Reversals**

Permanent deformation accumulates with load cycles over the pavement's life. Simulating thousands or millions of cycles is a daunting task even with current computational capabilities. The most realistic approach is a 3D simulation of a moving wheel. Since such analysis requires great computational effort, simplifications have often been used in the past to cut computational cost and time.

The most typical simplification is the assumption of bouncing wheel instead of a moving wheel. The bouncing wheel applies a cyclic loading with a period equivalent to the load duration at a certain travel speed. Bouncing wheel analyses can usually be performed assuming 2D axial symmetry, which greatly streamlines the calculations. However, a bouncing wheel does not induce shear stress reversal, which is a key mechanism in the development of plastic deformations, especially for the distribution of permanent strains within the asphalt concrete layer.

Limited field studies have found that moving traffic loading on pavement test sections produced higher permanent deformations than did plate loading with similar load magnitude and number of cycles. When the wheel completes a full pass over a fixed reference point in the pavement structure, the direction principal stresses rotate, causing shear stress reversals (e.g., compression to tension or vice-versa). Note that a complete shear reversal requires a 180° or more rotation of the principal stresses. In this dissertation, the term rotation of principal stresses refers to a full rotation that causes shear stress reversals. This is consistent with the terminology found in the literature where these two terms are used interchangeably to describe the same phenomenon.

This phenomenon has been studied more intensely in the unbound layers, where the effects of shear stress reversals can cause large plastic displacements. Investigations carried out at the University of Nottingham's accelerated pavement testing facility suggest that pavements under moving loads develop twice as much rutting as pavements under cyclic plate loading, as illustrated in Figure 46 (Brown et al., 1996, 1999). Moreover, bidirectional loading is more harmful than unidirectional loading due to the two-way shear reversals caused by bidirectional traffic (Brown et al., 1999). Similar tests at the Laboratoire Central des Ponts et Chaussées found that the permanent strains in the granular layers under moving wheel loading were approximately three times as large as those under cyclic plate loads (Hornych et al., 2000). Kim and Tutumluer (2005) examined realistic pavement stresses induced on aggregate base layer by moving aircraft loads and developed models to predict rutting in the unbound layer that considered the shear stress reversal.

Equivalent field studies of paved pavement sections have not been found in the literature. Even though the stress rotations are more pronounced in the surface layer than the underlying unbound granular base in a typical flexible pavement structure, there has been only limited evaluation of the effect of these rotations on the asphalt concrete, none at full scale experiment, nor modeling or numerical simulations. Crockford (1993) performed some experimental evaluation of stress rotation effects in asphalt concrete under laboratory conditions. Based on hollow cylinder testing, Crockford suggested that stress rotations cause about 2.5 times more plastic strain than specimens tested without the stress rotations.

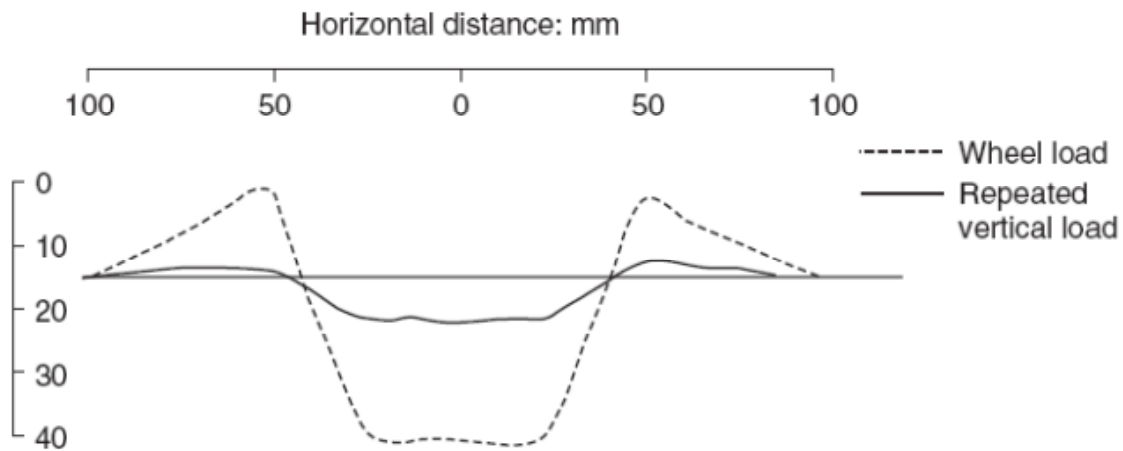


Figure 46. Permanent deformation comparison between a moving wheel load and repeated vertical load (Brown et al., 1996).

A simple exercise was performed to evaluate the ability of the Perzyna-Hiss viscoplastic model to capture the different material response for stress states with and without shear stress reversal. The stress states induced by a moving wheel were obtained numerically using the 3D model described in Chapter 5. All materials were modeled as linear elastic, as the intent was just to approximate the induced stress history caused by a moving load. The stress distributions over the loading cycle were computed at the approximate location of the maximum shear stress (i.e., about 50 mm or 2 in below the pavement surface at the edge of the wheel). Figure 47 describes the computed normal and shear stresses at this location as a function of time.

The case without shear stress reversal was modeled using the stress history for a sinusoidal quasi-static load applied at the center of the loading path. The period of the sinusoidal loading was set equal to the load duration simulated in the moving wheel analysis. Stress histories were computed for the same approximate location of the

maximum shear stress. Figure 48 describes the computed normal and shear stresses at this location as a function of time.

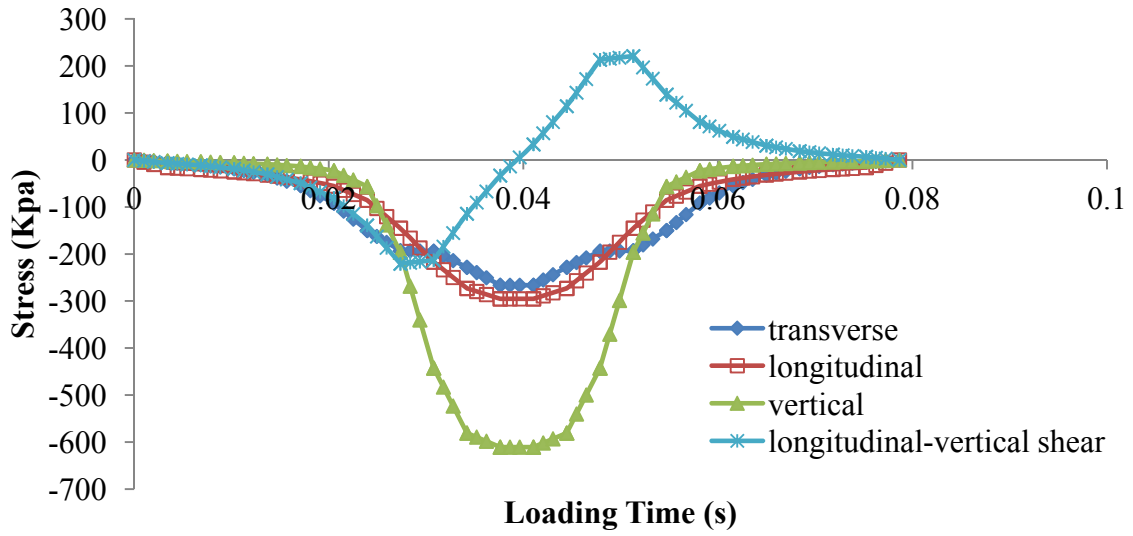


Figure 47. Stress distributions over time at the location of maximum shear for one moving wheel pass.

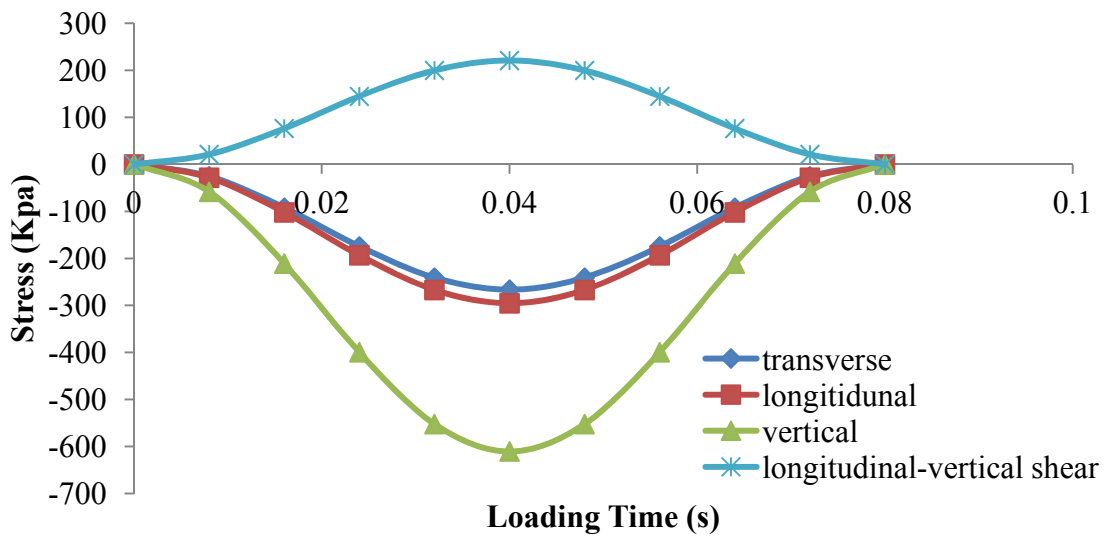


Figure 48. Stress distributions over time at the location of maximum shear for one bouncing wheel load.

The stress distributions shown in Figure 47 and Figure 48 were then applied to a single 3D element using the EVP constitutive model described earlier. The stress histories were applied 1,000 times.

The comparison of permanent strains computed in the two scenarios is shown in Figure 49. The impact of shear stress reversal is clear. The loading with the shear stress reversal induced significantly higher permanent strains than the loading without it. It is important to note that the results represent the induced strains at the point of maximum shear stress in the pavement structure. In the case of the bouncing wheel load, the rate of permanent deformation reduced and then leveled off after about 300 cycles. This is caused by the movement of yield surface towards the stress point (refer to Figure 14 for theoretical details) and is termed viscoplastic saturation. A better representation of the yield surface and the stress state paths at the location of maximum shear is provided in Figure 50, in terms of shear and volumetric stress invariants,  $J_{2D}$  and  $I_1$ . In the case of the moving wheel, the stress state path has a larger excursion above the flow surface during most of the loading cycle, as shown in Figure 50. As a result, more plastic strain occurs as it takes longer for the yield surface to reach the stress state path induced by the moving wheel than it does by the bouncing wheel.

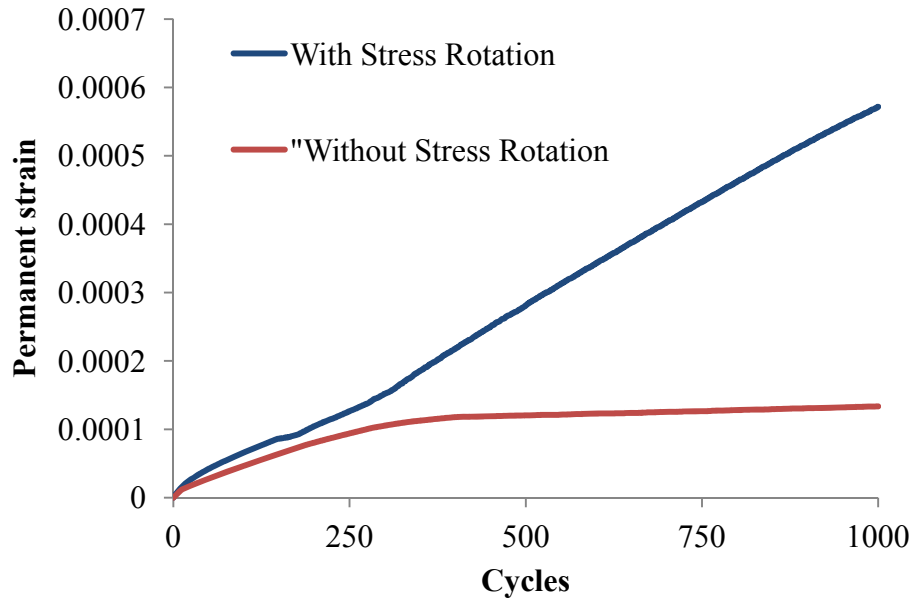


Figure 49. Comparison between permanent vertical strains induced by loading histories with and without principal stress rotations.

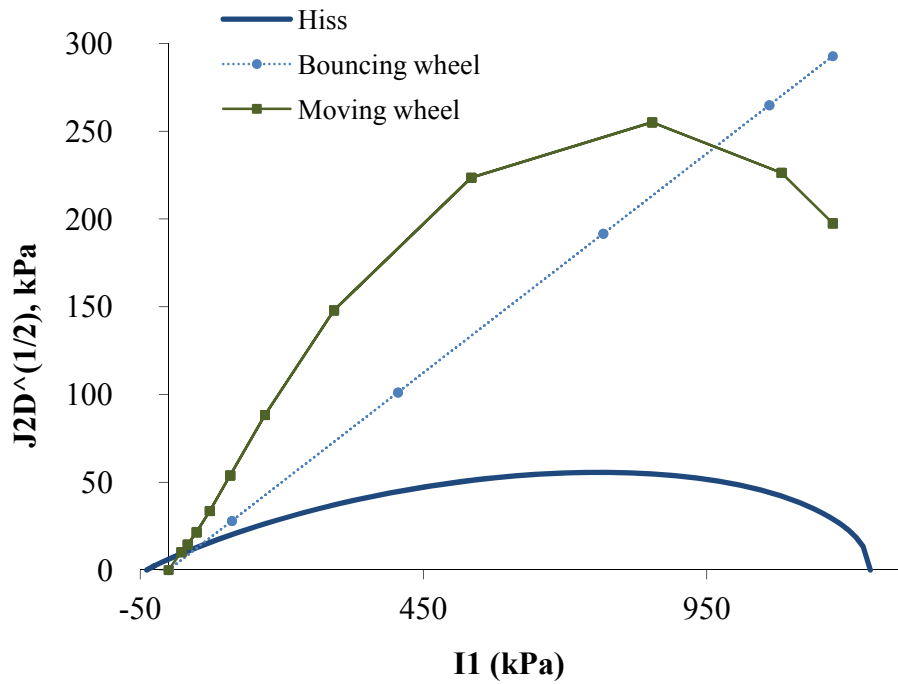


Figure 50. Comparison between stress state paths induced by moving and bouncing wheel at the location of highest shear stress.

This simple example showed that the viscoplastic model is capable of capturing the effects of shear stress reversals on permanent deformations. The large differences between the plastic strains in the moving and bouncing wheel cases in this exercise are possibly magnified as a consequence of the constant loading histories over all loading cycles. In the field, the state of stress is constantly changing as the materials deform, harden/soften, and develop locked-in stresses under the repeated loads. More realistic differences are expected when the full pavement section is simulated.

The 3D finite element analyses for both the moving and the bouncing wheel loadings were repeated with the surface HMA modeled using the EVP model. The elastic component of the HMA elasto-viscoplastic model was computed from the dynamic modulus master curve for the appropriate temperature and loading frequency. The unbound base layer and subgrade are modeled as linear elastic materials as before. The elastic material properties are summarized in Table 10. The viscoplastic material properties for the asphalt concrete were described in Table 8 in Chapter 4.

Table 10. Material properties used for studying the effects of the bouncing versus the moving wheel.

<b>Layer</b>	<b>Thickness (mm)</b>	<b>Elastic Modulus (MPa)</b>	<b>Poisson's Ratio</b>
HMA (45 °C)	150	760.0	0.35
Base	500	289.6	0.40
Subgrade	Infinite	89.6	0.40

The numerical simulations were carried out for 500 cycles and the predicted rutting at the center of the wheel path is shown in Figure 51. The moving wheel produced 1.6 times more rutting than the bouncing wheel. The rate at which rutting increases is also different. Viscoplastic strain saturation is evident in the bouncing wheel analysis,

while rutting increases continually throughout the moving wheel analysis, as expected and illustrated in Figure 50. The rutting values predicted in Figure 51 are small, compared to expected field rutting. The main reason is that the model doesn't predict as much densification as occurs in the field. The problem of densification is further detailed later in this Chapter where field measurements are compared with predictions obtained from the finite element analysis.

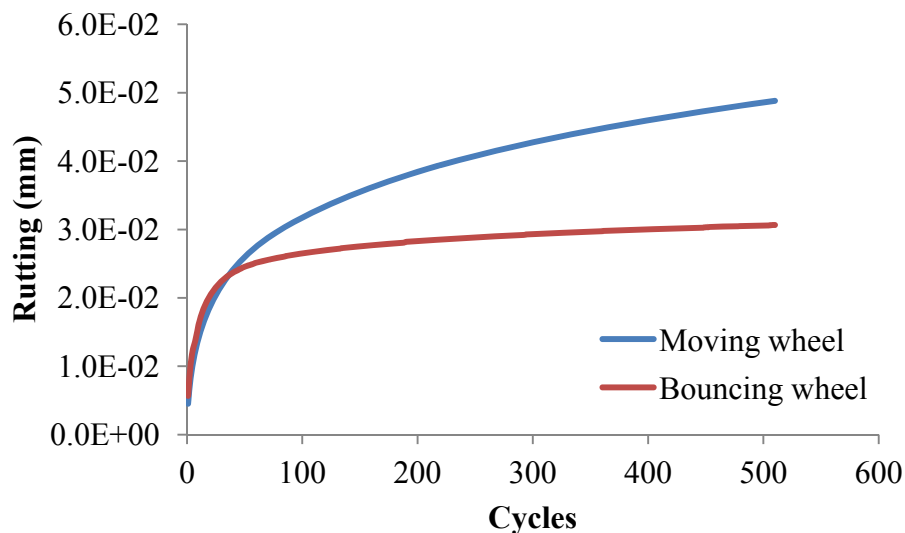


Figure 51. Comparison between moving and bouncing wheel finite element simulations.

The strain distribution within the surface layer is also worth examining. Most of simplified mechanistic-empirical models cannot realistically simulate the vertical strain distribution within the asphalt concrete surface layer. Based on trench studies at MnRoad (MN) and Westrack (NV), it is expected that the majority of permanent deformation will accumulate in the top 100 mm (4 inches) of the asphalt concrete layer, with the peak permanent strains at about 50 mm (2 inches).

The permanent strain distributions versus depth were compared for the moving and bouncing wheel analyzes. Results from the first cycle are plotted in Figure 52. The

strain distribution from the moving wheel simulation is qualitatively similar to the distribution observed in field trenches. Results from the MnRoad test track are plotted in the inset for comparison. The majority of rutting measured in the field comes from the top two lifts, which corresponds to about 100 mm (4 inches). The majority of residual strains predicted occur at the top 100 mm, with a peak at about 30 mm (1.2 inches). Although the strain distribution from the bouncing wheel also reflects the expected field distribution, the results are not in the same good agreement.

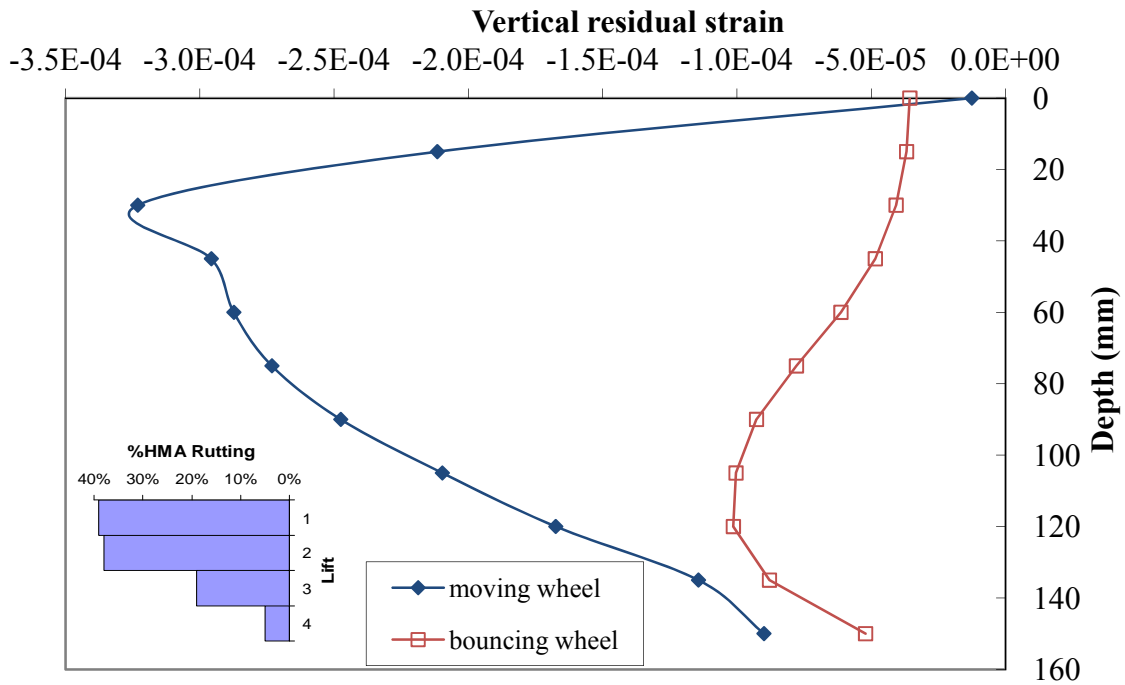


Figure 52. Comparison between strain distributions within the asphalt concrete surface layer when moving and bouncing wheel are considered. MnRoad rutting distribution from trench studies is shown in the inset.

The importance of induced stress reversals in the moving wheel simulation was clearly observed in these comparative analyzes. The total amount of rutting observed at the surface was about 1.6 times greater for the moving vs. bouncing wheel loading. There

was no viscoplastic saturation in the moving wheel simulations as permanent deformation continued to accumulate with each load pass, while a significant reduction in the rate of permanent deformation with increasing cycles was observed for the bouncing wheel load. In addition, the distribution of permanent strains within the asphalt concrete layer was significantly different between the moving and bouncing wheel analyzes. For qualitative comparison, results from MnRoad trench studies were presented to illustrate the good qualitative agreement between distributions measured in the field and the predicted distribution obtained from the moving wheel simulations.

#### **6.4. Practical Applications of Finite Element Simulations**

One of the purposes of numerical simulation is to provide insight into phenomena that would otherwise be difficult or cost-prohibitive to evaluate experimentally. The modeling effort described in this research can be used to evaluate different pavement types, provide understanding of behavior under special loading conditions (e.g., new tires, new loading gears), and ultimately support the development of improved design techniques and pavement performance models by extracting simplified relations based on observations drawn from the complex analyses.

As an example, three distinctly different pavement types were simulated and the predicted rutting results are compared. The magnitude of rutting computed at the center of the wheel path and the transverse permanent deformation profile are evaluated and discussed. The vertical permanent strain distributions are also examined and used to create pavement type-specific depth functions for the MEPDG.

#### *6.4.1. Predicted Rutting Comparison between Different Pavement Structures*

An example comparative study is provided in this section. Three pavement types were simulated using the finite element model described earlier. The objective was to compare quantitatively and qualitatively the predicted asphalt rutting. Of particular interest were the relative magnitudes of the maximum rutting and the shapes of the rutting transverse profiles.

The first structure was a conventional flexible pavement consisting of asphalt concrete as the surface layer, granular crushed aggregate as the base, and the subgrade. The second structure was also a flexible pavement, but a full depth asphalt pavement with only one thick layer of asphalt concrete directly on top of the subgrade. The third structure was a composite pavement consisting of an asphalt concrete surface layer, an underlying stiff Portland Cement Concrete slab, and the subgrade. The properties of the asphalt concrete, granular base and subgrade were as defined previously in Table 8 (viscoplastic properties for the asphalt concrete) and Table 10 (elastic properties for all layers). The elastic properties of the stiff layer in the composite pavement were defined as 30 GPa for the elastic modulus and 0.25 for the Poisson's ratio. Figure 53 shows the three structures. Five hundred moving wheel load cycles were simulated at an asphalt concrete temperature of 45°C for all pavements.

The first difference noticeable between the results was the evolution of rutting over number of cycles. Figure 54 summarizes the asphalt rutting over load cycles for all three pavement structures. Rutting was computed as it is normally measured in the field (i.e., using a straightedge, which gives total rutting as the combination of settlement and heave – see Figure 1). The composite pavement produced the least rutting, about one-

third of that predicted for the conventional flexible pavement at 500 cycles. In addition, the characteristic primary stage produced significantly less rutting and ended sooner than in the flexible pavement cases.

The conventional flexible and full depth pavement structures produced similar rutting predictions. The primary stage is visibly longer than in the composite case and the rate of rutting is higher. It would generally be expected that full depth asphalt pavements exhibit less rutting than a comparable conventional flexible pavement. However, the analyses predicted slightly greater rutting for the full depth structure than for the conventional flexible. This is because only rutting of the asphalt is considered in these analyses. The additional rutting contributions from the granular base and subgrade layers in real flexible pavements would likely give larger total surface rutting for the conventional flexible structure.

Another explanation for the unexpectedly small difference in predicted asphalt rutting between the two flexible pavement structures is the assumption of constant temperature throughout the asphalt layers. This does not reflect real scenarios in which daytime high temperatures decrease with depth in the layer, which results in a stiffer and more permanent deformation resistant material at depth, particularly for the full depth asphalt layer.

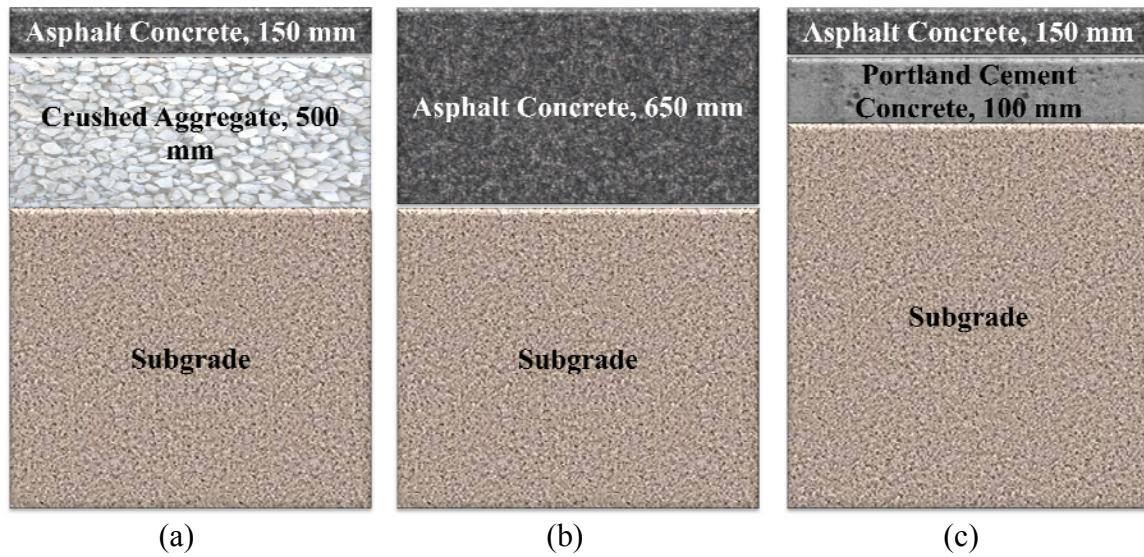


Figure 53. Pavement structures: (a) conventional flexible, (b) full depth asphalt concrete, and (c) composite.

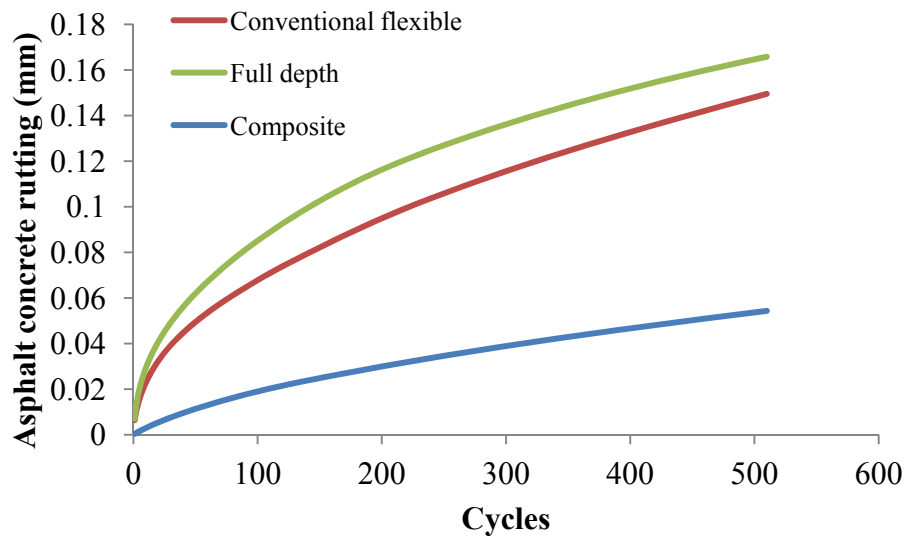


Figure 54. Asphalt rutting for different pavement structures.

An advantage of advanced finite element modeling over traditional mechanistic empirical models is the ability to predict the entire rutting transverse profile. Figure 55 compares rutting transverse profiles of all three pavement structures. The shape of the

rutting transverse profile predicted for each of the structures is different because of the different distributions of stresses within the asphalt layer.

Permanent deformation consists of settlement underneath the tire load and heave immediately outside the loaded area. The rutting profile observed in the flexible pavement case is typical of a structure with good quality base. In these cases, the stresses build up in the surface layer mainly underneath the edge of the tire. This stress build up is the cause of viscoplastic flow in the direction from the center of the load towards the edge of the tire, thus causing substantial heave at the edges of the wheel paths.

The full depth asphalt concrete pavement produces more rutting underneath the tire load than heave at the edge. It can also be noted that there are permanent deformations beyond one meter from the center of the load. This is an indication that the geometric boundaries may have been insufficiently far away for the full depth analysis. This issue was not observed in any of the other simulations performed.

The composite structure produced the least permanent deformation of all pavements simulated, both in terms of settlement and heave. The PCC layer supports the majority of the load. The surface layer remains in compression at the center of the load through its thickness, and there are more confining effects from the horizontal stresses. The consequence is the prediction of less rutting, which matches observations from field structures. One interesting observation for the composite pavement is the uneven distribution of rutting underneath the tire. The plot suggests that there is a gradient of deformation increasing in the direction towards the edge of the tire. This is likely due to the higher confinement at the center and increased shear stresses at the edge of the tire.

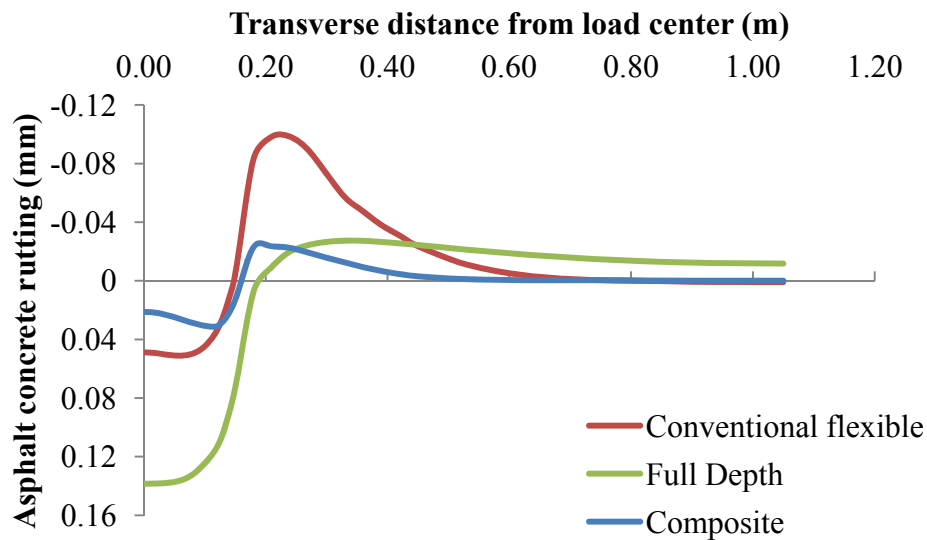


Figure 55. Comparison of rutting transverse profiles for different pavement structures.

Different pavement types produce different permanent strain distributions with depth through the asphalt concrete layer. The comparison of the permanent strain distributions for the three different pavements is provided in Figure 56. Only the top 150 mm of the full depth pavement is shown in these comparisons. The peak permanent strain was calculated at a depth of 30 mm for the conventional flexible pavement, 15 mm for the composite, and 45 mm for the full depth asphalt concrete pavement.

The results agreed qualitatively with expectations from observed field data. For example, data collected at post-mortem trench studies indicated that the majority of asphalt concrete permanent deformation occurred in the upper 100 mm (4 in) of the surface layer (MnRoad, 1998; Epps et al., 2002). The results presented here for all three pavement structures suggest that the location of the maximum deformation and the zone contributing most substantially to the total rutting depend on the type of pavement structure. Intuitively it also depends on thickness of the layer, although this factor was not evaluated in this study. This information can be useful for improving mechanistic-

empirical rutting models, such as those in the MEPDG, that rely on depth adjustment factors for the predicted permanent strains.

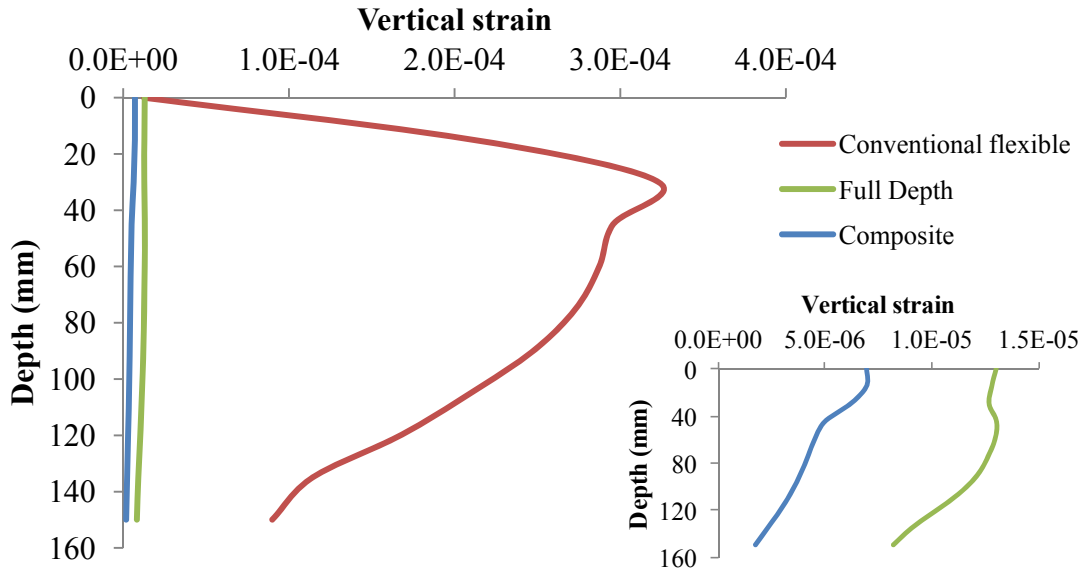


Figure 56. Comparison of permanent strain distributions with depth for different pavement structures.

#### 6.4.2. Analysis of the MEPDG Depth Factor for Rutting Predictions

One of the immediate applications of advanced modeling is to support the improvement of simplified prediction models. A prime example is the rutting model currently used in the MEPDG. A review of the MEPDG rutting model was provided in Chapter 2. The main equation and the depth factor adjustment are reproduced here for convenience.

The MEPDG model predicts vertical unrecoverable strain at the center of the load using the following empirical function:

$$\frac{\epsilon_p}{\epsilon_r} = \left[ 10^{-3.3542} T^{1.5606} N^{0.4792} \right] \quad (80)$$

in which  $\varepsilon_p$  is the plastic strain,  $\varepsilon_r$  is the elastic strain,  $T$  is the temperature,  $N$  is the number of load applications. This function is based on the recoverable vertical strain computed at peak load using linear elasticity models. The magnitude of predicted permanent deformations is a function of number of load applications and the temperature of the asphalt concrete.

Rutting is the permanent deformation after removal of the load. As described in Chapter 2, previous studies have suggested that the material at the bottom of the asphalt concrete layer yields under triaxial confined compression conditions and does not develop horizontal tensions as predicted by elastic analyses. Instead, the plastic flow causes the horizontal stresses remain compressive at all times. When the load is removed, these compressive stresses are locked in the structure creating a multidimensional confinement which induces residual expansive vertical strains at the bottom of the layer. The permanent deformation resulting from the residual compressive strain distribution is concentrated in the upper portion of the layer, as confirmed by field trench studies.

Since the plastic strains predicted in the MEPDG approach using Eq. (80) are proportional to the mechanistically determined elastic vertical strain, the majority of rutting is predicted at the bottom of the layer, contrary to field experience. Therefore a depth correction function was implemented in the MEPDG to adjust the computed plastic strain as described in Eq. (81).

$$\frac{\varepsilon_p}{\varepsilon_r} = \beta_{\sigma_3} \left[ 10^{-3.3542} T^{1.5606} N^{0.4792} \right]$$

$$\beta_{\sigma_3} = (C_1 + C_2 \cdot depth) \cdot 0.328196^{depth}$$

$$C_1 = -0.1039 \cdot h_{AC}^2 + 2.4868 \cdot h_{AC} - 17.342 \quad (81)$$

$$C_2 = 0.0172 \cdot h_{AC}^2 - 1.7331 \cdot h_{AC} + 27.428$$

in which  $\beta_{\sigma_3}$  is the depth correction function,  $depth$  is depth to the strain calculation location,  $h_{AC}$  is the thickness of the asphalt layer, and the other variables are as defined previously. The depth correction function assumes that the mechanisms and distributions of permanent strains are similar for all asphalt concrete layers, with no differentiation by pavement type.

The EVP finite element analyses for the three pavement types (conventional flexible, full depth asphalt, and composite) provide the actual distribution of residual plastic strains vs. depth through the asphalt layer. The comparison between the residual strain distribution predicted by the EVP finite element analysis and the MEPDG computed residual strain distribution is of interest. For better visualization, the vertical strain distributions were normalized. The intent is to compare the shape of the distribution not the magnitude of the strains, therefore a unique multiplier was determined as such that the resulting rutting from the integration of the residual strain distribution was the same. The EVP finite element residual strains were used as reference. The elastic strain distribution was normalized using the same multiplier of the MEPDG computed residual strain distribution.

Figure 57 illustrates the normalized vertical strain distributions in the asphalt concrete layer of the conventional flexible pavement structure. It shows the elastic strain

computed at peak load and the two residual strain distributions under the center of the tire: (1) one named residual computed using the EVP finite element model, and the other named MEDPG computed residual. The MEDPG residual strains were calculated using the current depth function. It is clear from the figure that the MEDPG computed residual strains do not match the actual residual strains computed in the finite element analyses.

A new depth function was developed to better fit the residual response predicted by the finite element model. The functional form was kept consistent with the MEDPG approach, but the coefficients were adjusted to provide a best fit to the EVP plastic strain values. The result is shown in Figure 57 and in Eq. (82).

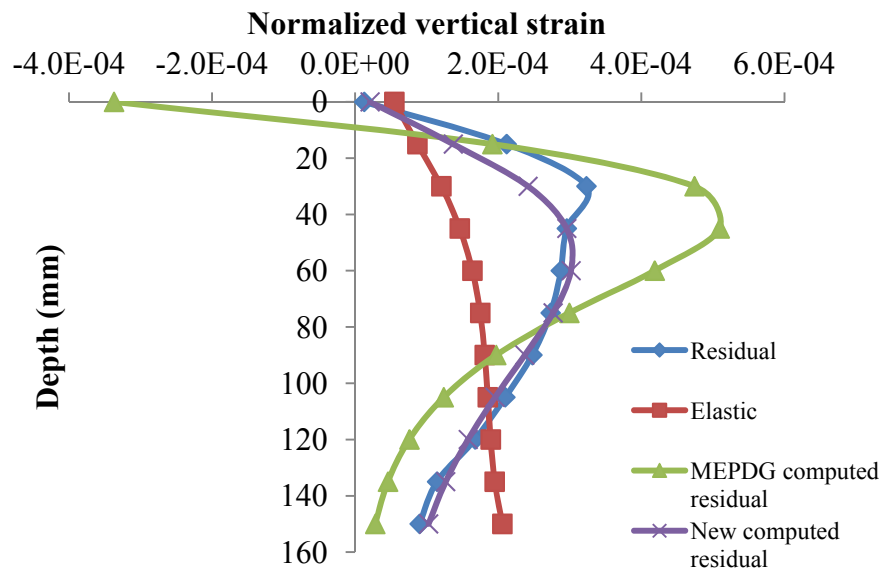


Figure 57. MEDPG depth function analysis for the conventional flexible pavement.

$$\beta_{\sigma_3} = (C_1 + C_2 \cdot \text{depth}) \cdot 0.538337^{\text{depth}}$$

$$C_1 = 0.0656 \cdot h_{AC}^2 + 2.5150 \cdot h_{AC} - 17.3373 \quad (82)$$

$$C_2 = -0.4334 \cdot h_{AC}^2 - 1.8082 \cdot h_{AC} + 27.4155$$

in which the parameters are as described previously.

The above approach can be extended to the full depth asphalt concrete and composite pavements. Figure 58 shows vertical strains distributions in the first 150 mm of the asphalt concrete layer of the full depth structure. The shape of the MEPDG-determined plastic strain distributions is very different from the residual strain computed from the EVP analysis. However, when a new depth correction function is calibrated from the EVP strains, the results are in much better agreement. The new depth function for this case is provided in Eq. (83).

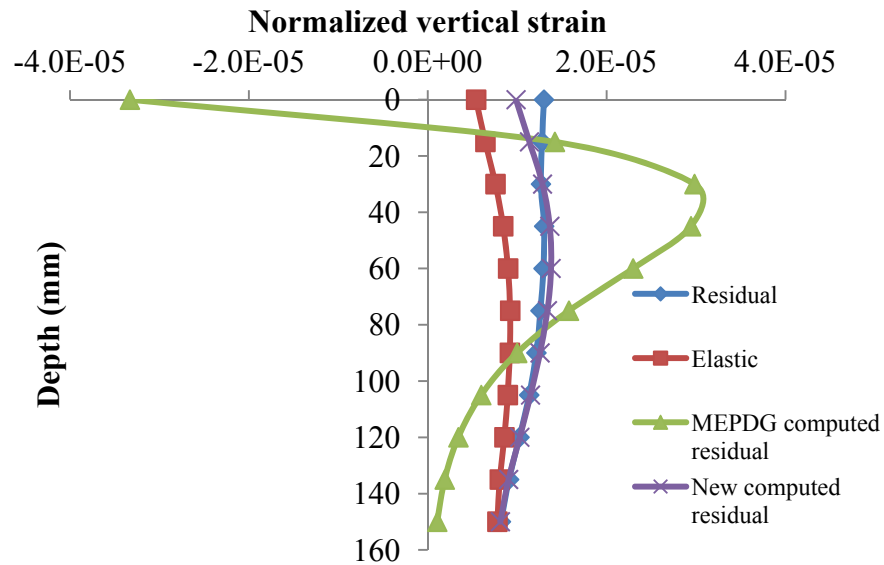


Figure 58. Calibrated depth function results for the full depth asphalt concrete pavement.

$$\beta_{\sigma_3} = (C_1 + C_2 \cdot depth) \cdot 0.8158^{depth}$$

$$C_1 = 0.0629 \cdot h_{AC}^2 + 2.5164 \cdot h_{AC} - 17.3372 \quad (83)$$

$$C_2 = -0.4592 \cdot h_{AC}^2 - 1.8131 \cdot h_{AC} + 27.4147$$

in which the parameters are as described previously.

Figure 59 shows vertical strains distributions in the asphalt concrete layer of the composite pavement structure. As similar to previous results, the MEPDG adjusted

plastic strain does not agree with the residual strain computed from the finite element analysis. Again, the depth correction function was recalibrated to provide better agreement between the two distributions. The new depth function for this case is provided in Eq. (84).

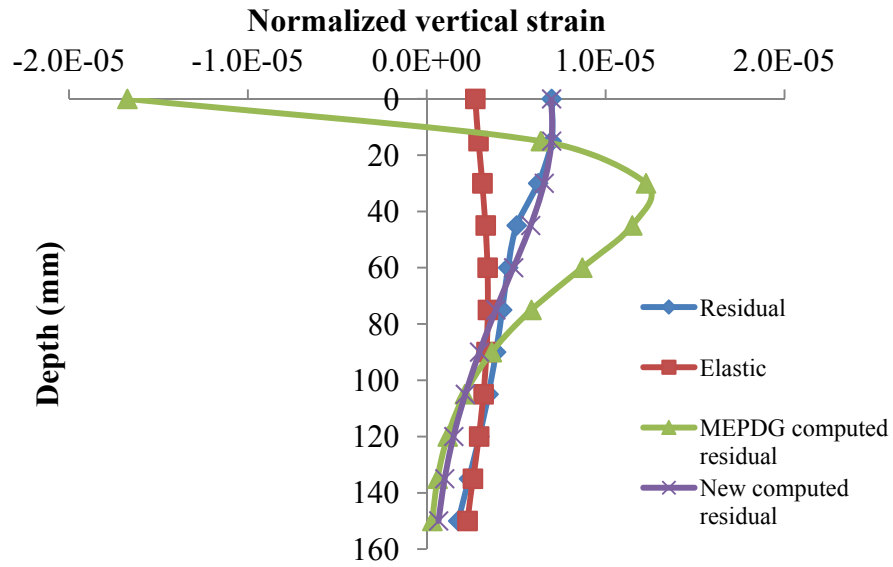


Figure 59. Calibrated depth function results for the composite pavement

$$\beta_{\sigma_3} = (C_1 + C_2 \cdot depth) \cdot 0.5335^{depth}$$

$$C_1 = 0.0629 \cdot h_{AC}^2 + 2.5142 \cdot h_{AC} - 17.3375 \quad (84)$$

$$C_2 = -0.4592 \cdot h_{AC}^2 - 1.8125 \cdot h_{AC} + 27.4146$$

in which the parameters are as described previously.

The depth function equation can be generalized as shown in (85) and the various coefficients for each pavement type can be compared in Table 11.

$$\beta_{\sigma_3} = (C_1 + C_2 \cdot depth) \cdot a^{depth}$$

$$C_1 = a_1 \cdot h_{AC}^2 + a_2 \cdot h_{AC} + a_3 \quad (85)$$

$$C_2 = b_1 \cdot h_{AC}^2 + b_2 \cdot h_{AC} + b_3$$

Table 11. Structure-based depth function coefficients .

<b>Pavement Type</b>	<b>a</b>	<b>a<sub>1</sub></b>	<b>a<sub>2</sub></b>	<b>a<sub>3</sub></b>	<b>b<sub>1</sub></b>	<b>b<sub>2</sub></b>	<b>b<sub>3</sub></b>
Default MEPDG	0.3282	-0.1039	2.4868	-17.342	0.0172	-1.7331	27.428
Conventional Flexible	0.5383	0.0656	2.5150	-17.337	-0.4334	-1.8082	27.4155
Full Depth AC	0.8158	0.0629	2.5164	-17.337	-0.4592	-1.8131	27.4147
Composite	0.5335	0.0629	2.5142	-17.338	-0.4592	-1.8125	27.4146

### 6.4.3. Conclusions

This section described two immediate applications of the mechanistic model for the permanent deformations in asphalt concrete layers. The first showed comparative analyses between three distinct pavement types with asphalt concrete surface layers. The results suggested that the finite element application is capable of identifying fundamental differences on how rutting develops in different pavement structures. There were differences in the evolution of permanent deformation over load cycles, different transverse profile patterns, and different distributions of rutting within the layer. The results agree qualitatively with expected field behavior as determined by trench data from MnRoad and Westrack.

The second application applied the finite element modeling to improve an existing mechanistic-empirical model for predicting asphalt layer rutting. Current mechanistic-empirical models, such as the MEPDG, rely on regression models to transform mechanistic responses into distresses. Discrepancies between elastic predictions of response and field expected permanent strain distribution are resolved by using an

empirical depth correction function. Since the EVP finite element analyses had shown that the shape and magnitude of the permanent strain distribution varies significantly with pavement type, pavement-specific depth functions are thus necessary (although not included in the MEPDG).

The finite element model developed was successfully used to derive pavement-specific MEPDG depth correction functions for three different pavement structure types. The permanent strain distributions after one cycle were used to recalibrate the MEPDG depth function. The new depth functions have the same mathematical formulation as the current MEPDG's depth function to facilitate implementation; only the coefficients in the function are recalibrated. The new depth functions produce plastic strains predictions that are in much better agreement with mechanistically computed residual strains. This approach can be used in future enhancements of the MEPDG.

## **6.5. Field rutting predictions**

### *6.5.1. Description of FHWA ALF*

Federal Highway Administration (FHWA) constructed 12 full-scale lanes of asphalt concrete pavements in 2002 at its Accelerated Loading Facility (ALF) at the Turner-Fairbank Highway Research Center in McLean, VA. The experiment, the second of its nature in this facility, was entitled "Full-Scale Accelerated Performance Testing for Superpave and Structural Validation" (Gibson, 2011). The objective of the study was to validate and refine changes being proposed to the Superpave™ asphalt binder specifications.

The layout of the experiment is presented in Figure 60. Each lane had a width of 4.0 m (13 ft) and a length of 50 m (165 ft). Each lane had four test sites used in various studies. All lanes consisted of an asphalt concrete surface layer on top of an unbound, dense-graded, crushed aggregate base (CAB) over a uniformly prepared, AASHTO A-4 subgrade soil. The total thickness of the HMA and CAB is 660 mm (26 in). Lanes 1 through 7 were constructed with an HMA layer thickness of 100 mm (4.0 in) and were used to evaluate cracking, while lanes 8 through 12 have a thickness of 150 mm (6.0 in) and were tested for permanent deformation. Each lane was constructed with a different binder; these are listed in Figure 60.

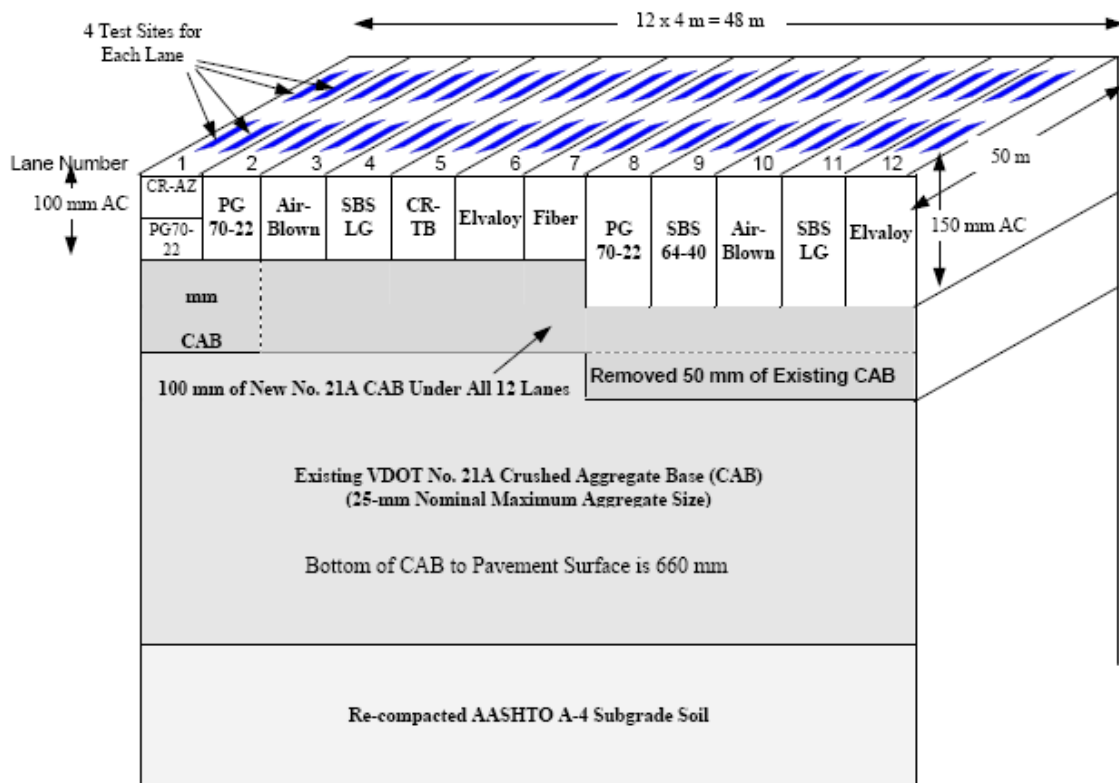


Figure 60. Layout of the 12 as-built pavement lanes (Qi et al., 2004).

The results provided by FHWA for this research came from Lane 11. The binder in this lane was modified with Styrene-Butadiene-Styrene with Linear Grafting (SBS-

LG). The Superpave binder grade was PG 70-28. The mixture gradation was 12.5 mm dense-grade following the Superpave gradation specifications. The design binder content was 5.3% at an air voids of 4.2%. The base layer was crushed aggregate (CAB) with a 25 mm (1 in) nominal maximum aggregate size. Additional details of binder, mixture characteristics and base material can be found at Qi et al. (2004).

The tire used was a super single wide base tire 425/64R22.5. It is known that this type of tire induces greater damage than conventional dual tires, hence its advantage in accelerated load testing (Gibson, 2011). The tire pressure was 689 kPa (100 psi) under a total load of 44kN (10 kip). There was no traffic wander for the rutting portion of the experiment.

Rutting was measured at the center of the wheel path using Layer Deformation Measurement Assemblies (LDMA), which simply measure the change in thickness of the asphalt layer as a consequence of accumulated permanent deformation. The LDMA setup is shown in Figure 61 – the rut depth measurements at the ALF did not include the side heaves. Seven LDMA's were installed per test site. Different temperatures were used for specific groups of lanes and test sites depending on the intended distress development. For the rutting experiment, the temperatures were 45 °C and 64 °C. On lane 11, the target of this research, the temperature was kept constant at 45°C. The temperature was controlled by measurements obtained from thermocouples embedded in the pavement structure. Radiant heaters were mounted along the length of the ALF to provide a source of heat.

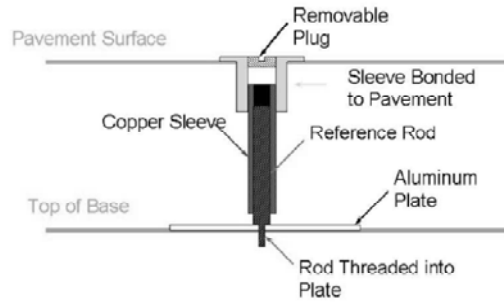


Figure 61. Layer deformation measurement assembly used to measure rut depth (Gibson, 2011)

Lane 11 received 300,000 unidirectional load passes. Figure 62 shows the measured rutting versus number of load passes. It is important to observe that by the time the first measurement was taken at 500 cycles, the accumulated permanent deformation was already at 2.5 mm (0.1 in). This accumulation represents 40% of the total permanent deformation observed at the end of the experiment.

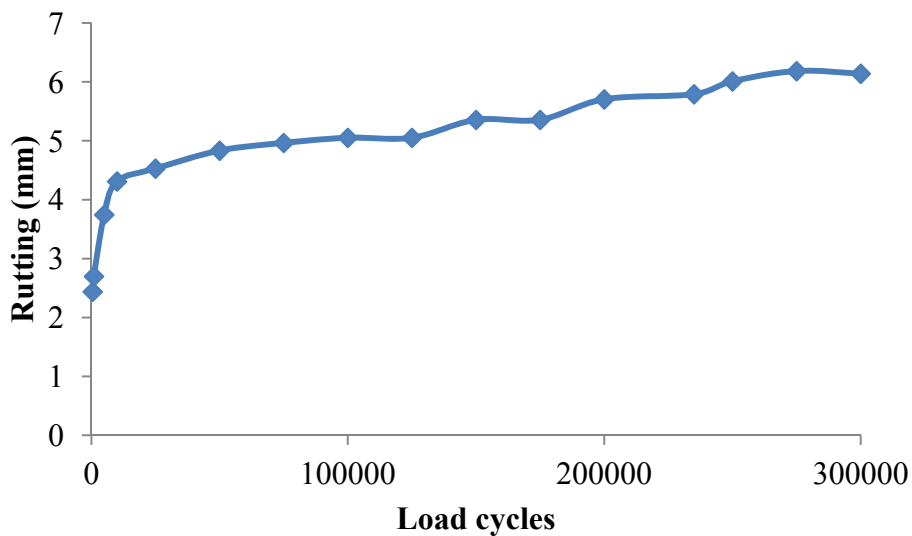


Figure 62. Rutting measurements at Lane 11 of the ALF.

One plausible explanation for this rapid deformation during the first 500 cycles is early densification. Asphalt concrete field compaction is not uniform. The material at the

bottom and top of the lift are often compacted to a lower density than material at the center (Masad et al., 1999). As a consequence, the distribution of air voids is non-uniform through the thickness of the layer (Hua, 2000). Mixture densification under traffic loading is likely to be the cause of such large and early deformation, especially near the surface, where high air voids compress rapidly under even small amounts of traffic.

Air voids were measured from core samples taken from the center of the wheelpath and compared with samples taken from untested area not influenced by the loading. It was found that densification had indeed occurred during the ALF rutting experiment and that the reduction in the air void content averaged 1.5% (Gibson, 2010). The densification primarily occurred at the top and bottom of the layer where high air voids is normally expected due to non-uniform compaction. Therefore it was expected that the SBS-LG mixture that was initially compacted to a 5.4% average air voids during construction densified to about a 3.9% average air voids during the early load cycles. This densification corresponded to 2.25 mm of the total rutting measured, almost all of the early rutting observed in Figure 62.

### *6.5.2. Numerical Simulation*

The material properties described in Table 10 were used to characterize the elastic behavior of the layers. The elasto-viscoplastic UMAT was used to model the asphalt concrete layer. The properties described in Table 8 in Chapter 4 were used.

Ideally all 300,000 cycles applied at the ALF experiment in Lane 11 would be replicated in the finite element simulation. Initially 100 cycles were simulated. The time required to run these simulations was 3.5 days, or 50 minutes per cycle on average. The

computer used in these simulations was the same as described earlier. Based on this initial evaluation, it was concluded that simulating a large number of cycles would be impractical because of the prohibitive computational time and storage requirements for the computed results. The alternative used was to design a load equivalency procedure in which more cycles could be simulated without adding extra computational time and then attempt to extrapolate the results.

There are many forms of applying an equivalent load to save time and effort in numerical analysis (Park, 2004; Yoo et al., 2006; Onyango, 2009). In the most common form the load is applied in one long step representing the entire accumulated load duration over the intended number of load repetitions. The main problem with this approach is that it resembles a load plate testing rather than a moving wheel load and thus cannot capture the principal stress rotations and shear stress reversals. This equivalent load approach also prevents the incremental development of residual stresses after the load is removed between cycles. It has been shown that residual stresses significantly affect the distribution of permanent strains through the asphalt concrete surface layer thickness (Schwartz and Carvalho, 2007, 2008). The better equivalent load approach is one in which the load duration is progressively increased to reflect more cycles while at the same time maintaining most of the development of residual stresses and other moving wheel effects.

In the equivalent load procedure adopted for the ALF simulations, the first 20 cycles are performed using the actual load pass time, which was equivalent to the ALF wheel speed of 18 km/h. After the first 20 cycles, the load duration is increased for each subsequent set of 20 cycles. For example, the load duration is doubled in the second set

of 20 cycles, hence providing the loading time equivalent of 40 cycles instead of 20. This process continues until the equivalent of 500 cycles have been simulated. The equivalent load procedure is illustrated in Figure 63.

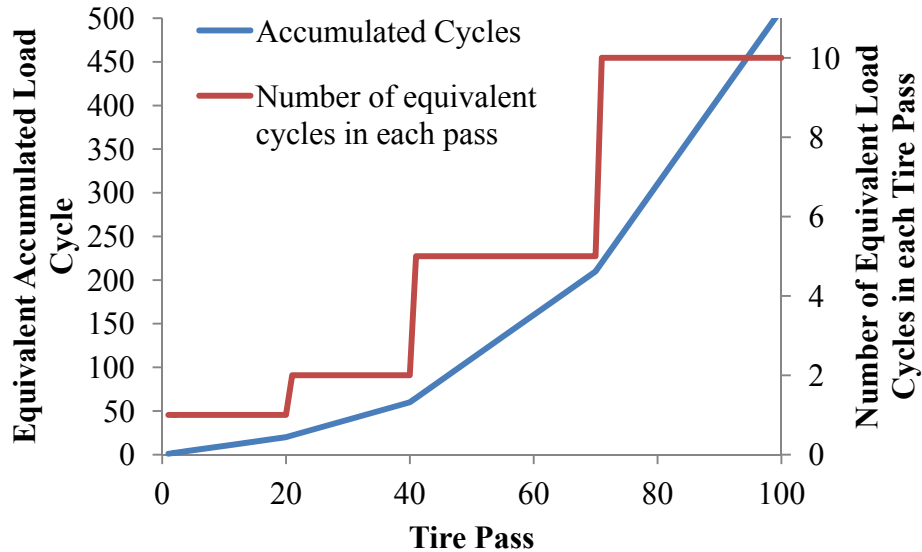


Figure 63. Load equivalency – equivalent accumulated load cycles *versus* tire pass.

Figure 64 shows the rutting predictions for 500 cycles using the equivalent load procedure. The plot also shows the results for the first 100 cycles simulated without the equivalent load procedure. The comparison of this with the simulation using the equivalent loading scheme is very close, with an average difference of less than 0.16%. This suggests that the equivalent loading scheme can be used as an alternative for simulating large number of cycles sequentially, at least for practical purposes. The major advantage of this approach is that it preserves most of the effects of the moving wheel on stress distributions and consequently on permanent deformations.

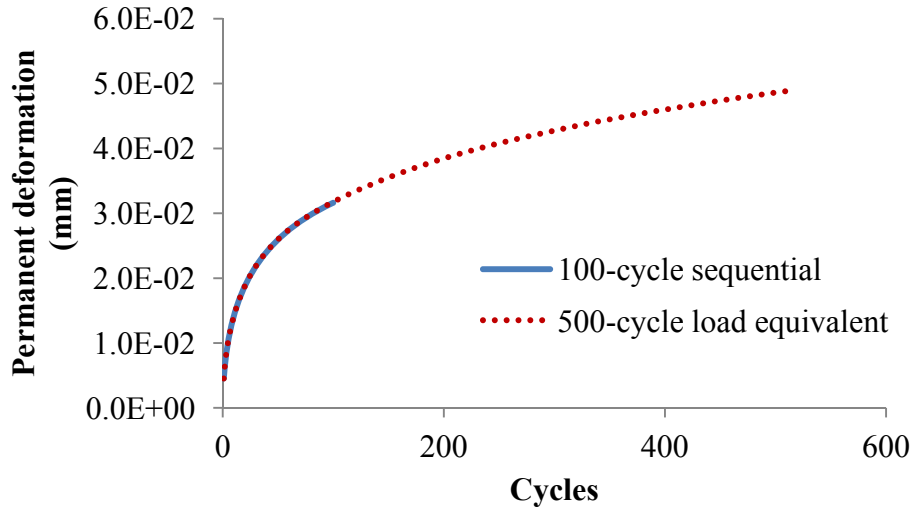


Figure 64. Computed permanent deformation for 100-cycle sequential and 500-cycle load equivalent.

The data shown in Figure 64 were used to extrapolate the predictions to the number of cycles applied to Lane 11. A power function was fit to the data and used to extrapolate the results to higher number of cycles. This did not provide good results, with the extrapolation significantly underpredicting the measured rutting. Examining the results from the finite element simulation, it was hypothesized that the predicted rutting had not yet fully reached the secondary stage and that therefore the power function coefficients had not stabilized.

Power law functions were fit to the finite element model results for the first 500 cycles in increments of 100 cycles. Linear regression analysis was used in the transformed logarithm of both predicted rutting and number of cycles. The transformation and the linear equation fit in log-log space is shown in Figure 65 for the first 100 cycles. The intercept of the linear equation corresponds to the multiplier of N in the power function (a), while the slope corresponds to the exponent of N (b) as follows:

$$RD = aN^b \quad (86)$$

It was noted that the multiplier of the power model was varying as more cycles were added to the dataset, thus indicating that the secondary stage had not been fully reached. An adjustment to correct this value was developed and the model fitted for 100 cycles was used as reference, as follows:

$$AF = \frac{a_N}{a_{100}} = f(N) \quad (87)$$

The ratio between the multiplier of power functions fitted to different number of cycles ( $a_N$ ) and the multiplier fitted to the first 100 cycles ( $a_{100}$ ) is shown in Figure 66. The adjustment factor,  $AF$ , took the form of a convenient power function dependent on the number of cycles,  $N$ , as follows:

$$AF = \frac{a_N}{a_{100}} = 0.47N^{0.164} \quad (88)$$

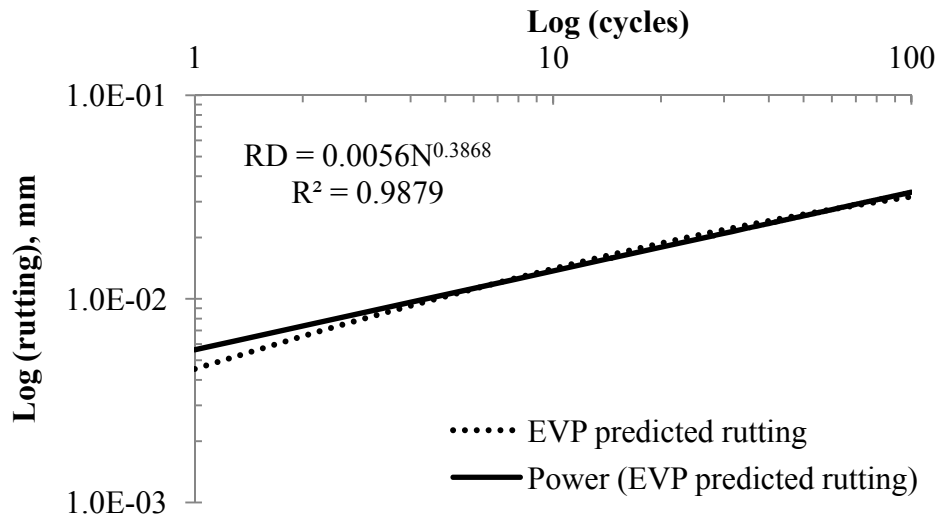


Figure 65. EVP finite element predicted rutting for the first 100 cycles.

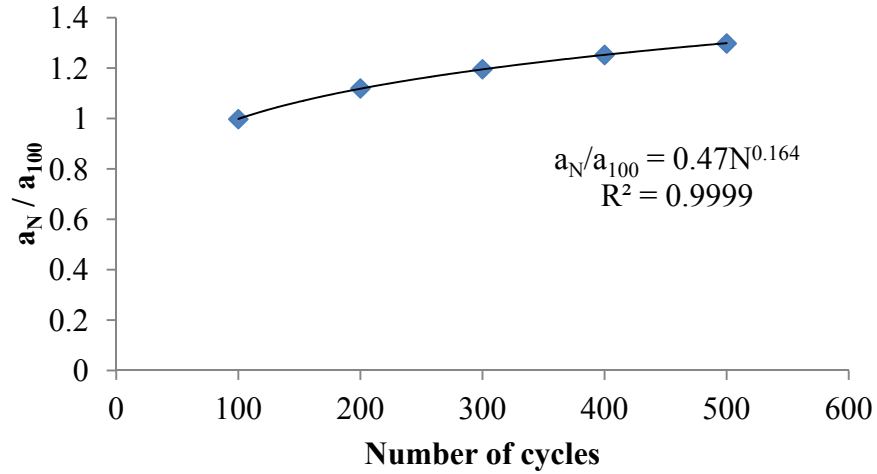


Figure 66. Ratio  $a_N/a_{100}$  as function of number of cycles.

The same approach was attempted for the slope of the power function. Although the slope variations were very small compared to those for the intercept, the power model extrapolations were very sensitive to small slope variation and the results obtained were not realistic. Therefore only the adjustment to the intercept was used. The final adjusted model is described in Eq. (89) and was used to predict the ALF field performance of lane 11.

$$\begin{aligned}
 RD &= (AF \times a_{100}) N^{b_{100}} \\
 RD &= (0.47N^{0.164} \times 0.00564) N^{0.3867} \\
 RD &= 0.00265N^{0.5507}
 \end{aligned} \tag{89}$$

in which,  $RD$  is the rut depth at the center of the wheel path (mm), and  $N$  is the number of cycles.

Measured rutting from lane 11 of the ALF experiment was compared with predicted values obtained from the ABAQUS analysis. Note that measurements at the ALF considered only rutting at the center of the wheel path and not the side heaves, therefore the predictions only took into consideration the settlement computed at the

same location. In this comparison, the deformation due to densification of the mixture by the early load passes was not considered. The calibration of the viscoplastic model used samples that were prepared at the average air voids obtained in the field for the entire lift of the asphalt concrete layer. Field compaction is not uniform, air voids are higher at the top and bottom of the lift than at the center. Therefore the calibrated model cannot capture accurately the behavior of the entire lift. For a better characterization, it would be necessary to calibrate the model using specimens at different air voids in order to capture the high densification that occurs at the top and bottom of the lift.

The predicted rutting values using the fitted model described in Eq. (89) are plotted in Figure 67. The calculated early compaction due to traffic was removed from the measured rutting based on average densification measured in the field. As described previously, this densification was estimated as 1.5% of the asphalt layer thickness, which corresponded to an initial permanent deformation value of 2.25 mm. Overall, the comparisons between predicted and measured rutting are very reasonable considering the intrinsic variability of asphalt concrete and the unavoidable simplifications of the model. The predicted rate of deformation in the secondary stage matches the observed rate quite well. The consistent offset between the predicted and measured rutting yields a difference of 0.86 mm (30% of the total) at the end of the experiment at 300,000 cycles. However if expected errors in rutting measurements are considered, the predicted rutting falls almost within two standard deviations of the error, which is equivalent to a 95% reliability.

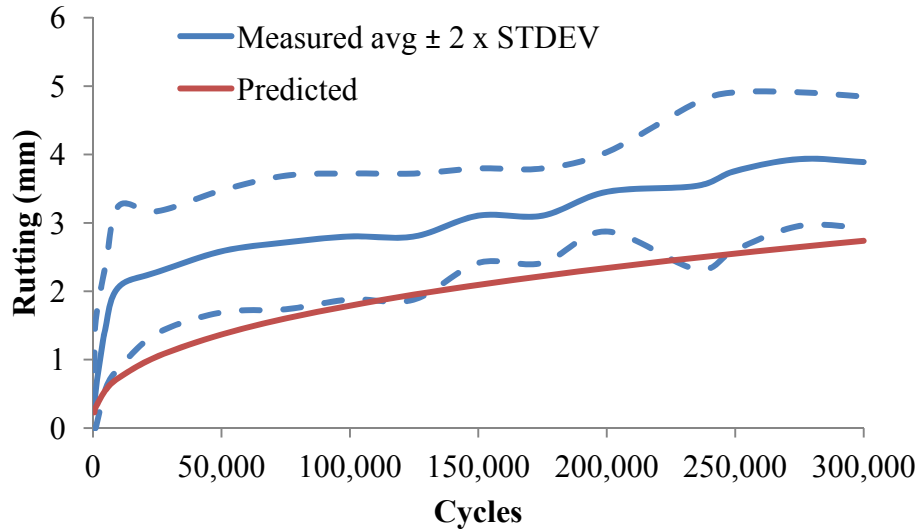


Figure 67. Predicted and measured rutting for the ALF lane 11.

Rutting was also predicted using a bouncing wheel as a replacement for the moving wheel for comparative purposes. Figure 68 shows the comparison between the two predictions. The same adjustment process was applied to both simulations. The results extrapolated to 300,000 cycles clearly show the bouncing wheel analysis predicting less rutting than the moving wheel. The predicted rutting using the moving wheel produced results with the least difference to measured values, as expected. Rutting predicted using the bouncing wheel is about 50% of the value measured at the last cycle. This is twice the 24% error from the moving wheel simulation.

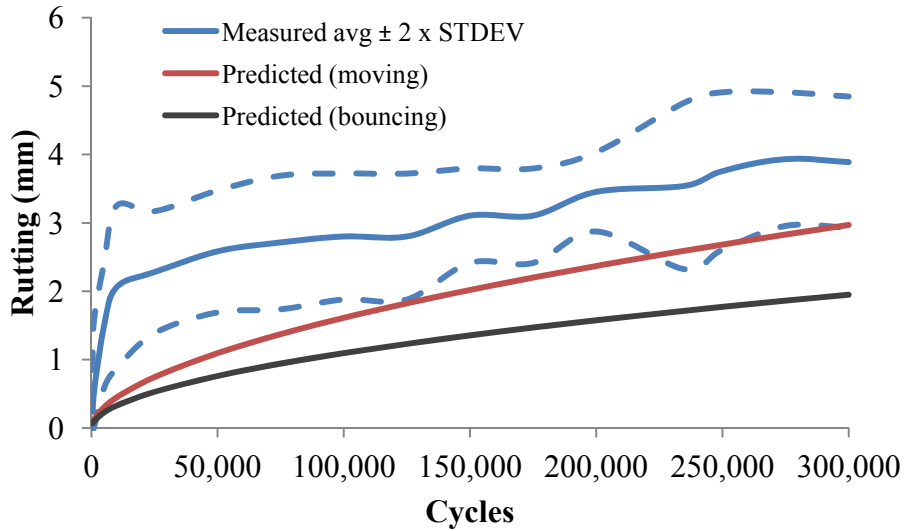


Figure 68. Comparison between predictions using moving and bouncing wheel for the ALF lane 11.

### 6.5.3. Conclusions

The elasto-viscoplastic model implemented in ABAQUS was used to predict rutting at the lane 11 of the FHWA’s ALF experiment. The simulation of the complete experiment was not computationally feasible. Only 500 cycles were simulated using an equivalent loading approach developed to expedite calculations. A power model was fitted to the finite element simulation results and extrapolated for comparison with field data.

Predicted and measured rutting at the center of the wheel path were in good agreement, considering the intrinsic variability of asphalt concrete and the unavoidable simplifications of the model. It was observed that densification had occurred at early stages of loading. The model was calibrated using specimens prepared at average air voids for the entire layer, excluding the regions of high air voids at the top and bottom of the layer. Therefore the predicted permanent deformation was compared with measured

values excluding the densification. The results were within two standard deviations of measured values, which corresponded to almost 95% reliability for predicted values. The consistent offset between the predicted and measured rutting yields a difference of 0.86 mm (or 30%) at the end of the experiment at 300,000 cycles.

Lane 11 was also modeled using a bouncing wheel as a replacement for the moving wheel. The same adjustment process and curve fitting was applied. Rutting predicted at the last cycle using the bouncing wheel was about 50% of the value measured. The use of a 3D model with a moving wheel reduced the error in the prediction by half as compared to the bouncing wheel analysis.

## Chapter 7 Conclusions and Recommendations

Rutting is a common distress observed in flexible pavements caused by the development of permanent deformation in layers of the pavement structure. It is defined as a longitudinal surface depression occurring in the wheel paths of roadways and upheaval along the sides of the rut. It can lead to structural failure and potential danger from hydroplaning. Rutting accumulates incrementally with small permanent deformations from each load application over the life of the pavement.

Two mechanisms are the main causes of permanent deformation in asphalt concrete surface layers. Compaction, or densification, is the primary mechanism at initial stages of loading; it is characterized by volume change of the material underneath the wheel path. The second mechanism is defined as lateral movement of material underneath the wheel path caused by shear (i.e., distortion without volume alteration). These two mechanisms define the first two stages of rutting (see Figure 3). When enough shear deformation has occurred, the asphalt concrete undergoes rapidly increasing rates of shear deformation, leading to failure in the tertiary stage. In practice, most pavements are rehabilitated prior to reaching the tertiary stage to minimize the structural damage and avoid unsafe traffic conditions. The initial stage occurs over the first few hundreds or thousands of load applications, which is a very small portion of the pavement traffic life. Therefore, rutting modeling is usually restricted to the secondary stage.

Several models were developed over the past 40 years that lay the foundation for the current mechanistic-empirical rutting models based on resilient strain. The current model used in the Mechanistic-Empirical Pavement Design Guide (MEPDG) is based on

vertical resilient strain and is calibrated using axial repeated load permanent deformation tests. An alternative model, termed the Westrack model, is based on maximum shear strain and calibrated using repeated shear tests.

There are significant limitations to mechanistic-empirical models. The most fundamental limitation is the range of applicability of the model. The empirical model components are valid only for the conditions for which they were calibrated. Extrapolations beyond these conditions are risky. Moreover, most mechanistic-empirical (M-E) models rely on simple linear elastic predictions of mechanistic response. However most of materials used in pavement construction are not linear elastic.

In addition, there are several issues not yet fully resolved in the framework for predicting rutting in the asphalt concrete layers using M-E models: (1) whether rutting should be modeled using axial or shear permanent strains; (2) dependency on linear elasticity theory to provide the critical pavement responses required in the model formulation; (3) the need for a depth correction factor to bring the predicted plastic strains into better alignment with those observed in the field; (4) related to issue 3, the assumption that the shape and form of plastic strain distributions are similar for asphalt concrete layers in flexible pavements *versus* asphalt concrete overlays on rigid pavements, which is generally not true; and finally (5) the difficulty of characterizing the entire rutting profile, including the contribution of heaving at the edge of the wheel paths.

The key to understanding the rutting problem is to return to its physical definition. Rutting is the accumulated permanent deformation that remains after removal of the load. Rigorous modeling of permanent deformations using nonlinear finite element analysis

based on the more correct physical mechanism of residual deformations after removal of the load can provide important insights into the rutting problem.

Advanced mechanistic modeling employs theories of mechanics that are more suitable to describe the real material behavior. The shortcoming is the complexity of these theories, and in particular the constitutive models. Asphalt concrete is a complex material in which recoverable and irrecoverable strains are dependent on temperature, stress and strain rates. Therefore, viscoelasticity and viscoplasticity theories are most appropriate to model the recoverable and irrecoverable behavior respectively.

This dissertation documents the study of permanent deformation in asphalt concrete in pavement structures using a full mechanistic model. A constitutive model framework based on Schapery's viscoelasticity theory and Perzyna's viscoplasticity was presented. This model, which was developed in previous studies (Gibson, 2006; Kim, 2009), has been enhanced in the present work. An improved calibration process was developed and verified, and the model was implemented in a 3D finite element formulation. Two immediate practical applications were shown and a simulation of a full-scale accelerated pavement test was performed. The results and discussion provide important information about the rutting problem in asphalt concrete and how it develops and evolves over traffic loading; this contributes to the development of better modeling techniques for pavement performance predictions.

### **7.1. Model Calibration**

The majority of the laboratory effort was devoted to the viscoplastic characterization. A new testing procedure was developed to expedite the calibration

process in the laboratory, while maintaining the range of stresses and frequencies recommended from previous research (Gibson, 2006). Instead of using two types of creep and recovery test to evaluate independently the influence of stress magnitude and load frequency, one unique test, termed a multi-stress/load duration creep and recovery test, was developed that combined different stress levels and load durations. The Perzyna-HiSS viscoplastic model was successfully calibrated against the laboratory test results (see Figure 31).

Flow Number (FN) tests were used to verify the calibrated model. These tests were performed independently by FHWA researchers at the Turner-Fairbank Highway Research Center. The calibrated model was capable of predicting the permanent strains of the confined FN test with reasonable accuracy (see Figure 32). Strains of the unconfined FN test were underpredicted because the applied deviatoric stresses were very low and below those used in the multi-stress/load duration calibration tests. For practical applications, the stress conditions in the confined FN test are more characteristic of real pavements and thus more relevant to rutting performance.

One of the shortcomings of advanced characterization of asphalt concrete mixtures is the complex calibration process, which often requires one or more research-grade tests. This issue poses as an obstacle to practitioners and reduces the effort to disseminate advanced modeling as a design tool. This research demonstrated that the Perzyna-HiSS viscoplastic model can be successfully calibrated using the simple FN test (see Figure 33). The calibration was validated using the multi-stress/load duration tests (see Figure 34). The FN test can be easily performed using the Asphalt Mixture

Performance Tester (AMPT) and it is the test of choice for calibrating the empirical rutting model in the MEPDG.

## **7.2. Moving Wheel Analyses**

The importance of induced shear stress reversals due to moving wheel simulation was clearly demonstrated. The total amount of rutting observed after 500 cycles of a moving load was about 1.6 times higher than the rutting beneath an equivalent bouncing wheel. There was no plastic saturation as permanent deformation continued to accumulate with each pass of the moving wheel, as opposed to the significant reduction in the rate of permanent deformation observed in the bouncing wheel load simulation (see Figure 51).

The distribution of permanent strains within the asphalt concrete layer was significantly different between the moving and bouncing wheel analyses (see Figure 52). The results from the moving wheel analysis were in qualitative agreement with field data collected from trench studies at MnRoad. The plastic strain distribution is particularly important for rutting performance prediction and the development of empirical models, in which elastic strains are converted into plastic strains through depth correction functions.

## **7.3. Effect of Different Pavement Structures**

Rutting patterns in three pavement types were simulated the finite element model – conventional flexible pavement, full depth asphalt concrete pavement, and composite pavement. The 3D finite element simulation was capable of identifying fundamental

differences in how rutting develops in different pavement structures and the differences in the transverse profile and distribution of rutting within the layer.

The composite pavement produced the least rutting, about one-third of that in the conventional flexible pavement at 500 cycles. In addition, the characteristic primary stage produced significantly less rutting and ended sooner than in the flexible pavement case. The conventional flexible and full depth pavement structures produced similar rutting predictions (see Figure 54).

Three dimensional pavement simulations using advanced models provide the entire transverse rutting profile. The shape of the profile reflects the response to loading and the distribution of stresses within the layer. The conventional flexible pavement produced the largest heave after 500 cycles. The full depth asphalt concrete pavement produced more rutting underneath the tire load but less heave at the edge of the tire as compared to the conventional flexible pavement. The composite structure produced the least permanent deformation of all pavements, both in terms of settlement and heave (see Figure 55).

Different pavement types produced different permanent strain distributions through the asphalt concrete layer. The results agreed qualitatively with expected field behavior based on previous research studies of trench data (i.e., flexible pavement sections in MnRoad and Westrack). The results presented here for all three pavement structures indicate that the location of the maximum deformation depends on the type of pavement structure (see Figure 56). The permanent strain distribution is particularly important for the development of depth adjustment factors for mechanistic-empirical pavement design procedures like the MEPDG.

#### **7.4. MEPDG Depth Factor for Rutting Predictions**

Mechanistic-empirical models, such as the MEPDG, rely on regression models to transform mechanistic responses into distresses. Discrepancies between elastic predictions of response and expected field results are resolved by using an empirical depth factor. This study demonstrated that the shape and magnitude of the permanent strain distribution varies significantly with pavement type. Therefore, pavement-specific depth factors are necessary.

The difference between the MEPDG computed plastic strain distribution and the residual strain distribution predicted using the finite element model was demonstrated for each pavement type. New depth functions were developed using the same mathematical formulation in the current MEPDG depth function to facilitate the implementation in the MEPDG software. The new depth functions produced plastic strains predictions that are in much better agreement with mechanistically computed residual strains (see Figure 57, Figure 58, and Figure 59). This approach can be used in future enhancements of the MEPDG.

#### **7.5. Field Rutting Predictions**

The elasto-viscoplastic model implemented in ABAQUS was used to predict rutting for lane 11 of the FHWA's ALF experiment. Five hundred cycles were simulated and a procedure to extrapolate the results was formulated to estimate rutting at the end of the experiment. Predicted and measured rutting at the center of the wheel path were in good agreement (see Figure 67). It was observed that densification had occurred at early stages of loading due to low compacted densities at the top and bottom of the asphalt

layer. This type of traffic compaction cannot be predicted by a viscoplastic model that assumes homogeneous initial conditions through the layer. Therefore the predicted permanent deformation was compared with measured values excluding the densification. The results were within two standard deviations of measured values. The consistent offset between the predicted and measured rutting yields a difference of 0.86 mm (or 30%) at the end of the experiment at 300,000 cycles. This difference is within expected variance in rutting measurements.

Lane 11 was also modeled using a bouncing wheel as a replacement for the moving wheel. The same adjustment process and curve fitting was applied. Rutting predicted at the last cycle using the bouncing wheel was about 50% of the value measured (see Figure 68). The use of a 3D model with a moving wheel reduced the error in the prediction by half when compared to the bouncing wheel analysis.

## **7.6. Recommendations**

The viscoelastic-viscoplastic constitutive model implemented in the ABAQUS finite element code is limited for practical design applications. The computational effort is very demanding at present. However, as the state of the art advances, so does computing technology.

A significant amount of time was devoted to implementing the viscoplastic component of the advanced model into the UMAT in ABAQUS. The algorithm should be further refined to improve computational efficiency, especially the procedure to define the growth of the HiSS yield surface and the normal viscoplastic trajectory. The current approach is reliable but often slow. Enhancements to the algorithm would expedite the

calculations and bring advanced pavement modeling analysis closer to becoming part of design procedures.

During the development of the UMAT an ill-conditioned solution of the HiSS function at the intercept with the volumetric stress invariant axis was found (see Figure 40). The normal to the HiSS surface at its intersection with the volumetric axis is undefined. Since the Perzyna-HiSS model assumes associated flow, the direction of the incremental viscoplastic strain vector is always normal to the yield surface and thus is undefined at the intercept where the normal vector cannot be computed. The HiSS surface equation should be refined to avoid this singularity at the intercept with the volumetric axis so that the HiSS surface can be properly evaluated over the entire stress domain.

One of the benefits identified in this research of using the Perzyna-HiSS viscoplasticity model identified in this research is that it can be calibrated using the flow number test, a relatively simple and cost effective procedure. However, only a limited study was done regarding the use of the flow number test. Expanding this finding to other mixtures and determining the ideal testing conditions for model calibration should be performed, especially with regard to calibrating the model for low stress levels.

The moving load simulation was accomplished by applying the tire footprint as a pressure load and directly rolling it over the surface nodes in the finite element model. This approach provided numerical stability and was fast, but it was difficult to model as each strip of pressure load defined separately. New options for simulating the tire load should be investigated with the objective of improving repeatability without jeopardizing computational time.

This research demonstrated the finite element model's potential for determining pavement-specific depth functions used in the MEPDG. The application was limited to three pavement types with one structure of each. A parametric study is recommended to develop a database of depth functions that are pavement structure-specific. This database could be developed as a library of mathematical models and implemented as an artificial neural network that would provide more correct adjustments for the MEDPG rutting model.

## Appendix A. Viscoelastic-Viscoplastic UMAT

### Description of subroutines

Subroutine name	Description
UMAT	Main subroutine called from ABAQUS input file. It is related to the material selection in the input file.
newperpHiSS	This function takes the HiSS surface definition parameters and the stress point to create a normal line from the Hydrostatic line to the stress point. It also finds the line intersection point on the HiSS surface, assuming the two solutions for the points on this line to be a quadratic relation. Adapted from Gibson (2006) for this UMAT.
dHiss	This function computes the normal vector $dF_d$ s on the HiSS surface using the surface parameters and the applied stress point. Adapted from Gibson (2006) for this UMAT.
Gethydrpntext	This function computes the intersection between the line passing by the applied stress, the HiSS stress points and the Hydrostatic line. Adapted from Gibson (2006) for this UMAT.
HNR	This function applies a Newton-Raphson algorithm to find a point on the HiSS surface that is normal to the applied stress point (Gibson, 2006).
Kbacktr	This subroutine is used to transform the 4th order tensor in the local coordinate system (in the principal axes) back into a 4th order tensor in the global coordinate system (global) (Hinterhoelzl, 1999).
Kprind	This subroutine is used to order the principal stress/strain tensor if the form of $e_{33} > e_{22} > e_{11}$ . This will comply with the requirement of symmetry of the transverse isotropy. Accordingly the array of the cosines is also changed to $cs(3,3)$ .
Unitvector	This function computes the unit vector of a given vector.

C U M A T

C

C ABAQUS USER MATERIAL MODEL FOR ViscoElasticity with Continuum Damage  
C and ViscoPlasticity

C VECD component based on Schapery VECD theory and VP based on Perzyna-HiSS

C

C WRITTEN BY REGIS L. CARVALHO, with components adapted from R.

C Hinterhoelzl (1999) and Gibson (2006)

C

C 2008-2011

C

C FILENAME: VEVPI\_1.for

c

c INTRODUCTION

c

c 3-dimensional formulation with adaptation for plane strain problems

c

c Assumptions: small strains

c       small rotations of the principal axes of strain

c

c Material Data:

c It is chosen to define all the material parameters like Prony series, damage

C functions and viscoplastic model.

C Internal State Variables are defined as follows:

c   - Viscoplastic strain components: statev(l), with l = 1 to 6

c   - HiSS surface stress: statev(k), with k = 7 to 9

c   - HiSS normals: statev(j), with j = 10 to 12

c   - Damage: statev(13)

c   - viscoelastic internal variables: statev(h), h = 14 to (13+6\*nE)

C    nE, number of terms of the Prony series = 12

c

c E used in the umat is in [kPa]. So the geometry has to be defined in

c mm and all the loading in [kN] for forces and [mm] for displacement.

c The relaxation times of the Prony series are in [sec]. So all the times in

c the input have to be defined in [sec].

c

c Temperature:

c The influence of the temperature on the time dependent behavior is modeled

c by making use of the time-temperature-superposition-principle (TTSP) for

c thermorheologically simple materials.

c The implementation is done for the definition of the shift factor aT and used

c to compute the reduced time increment dtau.

c

c

c The umat is programmed for a nonlinear viscoelastic boundary value problem.

c No correspondence principle is used. Nevertheless pseudostrains are defined.

c

c Principal axis of the strain 3 is axis of transverse isotropy

c

c The programming will make use of vector and matrix formulations for stress,  
c strain and jacobian instead of tensor formulation.

c

c The user must provide the calculation of (Variables of Abaqus):

c

c ddsdde(ntens,ntens)(Jakobian-Matrix of the constitutive model)

c stress(ntens) (Cauchy stress tensor)

c statev(nstatv) (array containing the solution dep. \*DEPVAR)

c

c and if necessary the calculation of:

c

c sse (specific elastic strain energy)

c spd (plastic dissipation)

c scd (creep-dissipation)

c

c Abaqus provides the following variables:

c

c stran(ntens) (array of the total strain components without the thermal  
c strains)

c dstran(ntens) (array of strain increments without thermal strain incr.)

c time(1) (value of step time at the beginning of the current incr.)

c time(2) (value of the total time at the begin. of the curr. incr.)

c dtime (time increment)

c temp (temperature at the start of the increment)

c dtemp (increment of temperature)

c predef (array of predefined field variables)

c dpred (array of incr. of the predefined field variables)

c cmname (name given on \*MATERIAL)

c ndi (number of direct stress components)

c nshr (number of engineering shear stress components)

c ntens ndi+nshr

c nstatv (number of solution dependent state variables)

c props (array of material constants)

c nprops(nprops)(number of material constants)

c coords(3) (coordinates of this point)

c drot(3,3) (rotation increment matrix)

c celent (characteristic element length)

c dfgrdo(3,3) (deformation gradient at the beginning of the incr.)

c dfgrd1(3,3) (deformation gradient at the end of the incr.)

c noel (elementnumber)

c npt (integration point number)

c layer (composite layer number)

```

c kspt      (sectionpoint number within the current layer)
c kstep     (step number)
c kinc      (increment number)
c
C
C 1. Declaration of variables provided by ABAQUS
C  UMAT subroutine header
C
SUBROUTINE UMAT(STRESS,STATEV,DDSDDE,SSE,SPD,SCD,
1 RPL,DDSDDT,DRPLDE,DRPLDT,
2 STRAN,DSTRAN,TIME,DTEMP,TEMP,DTEMP,PREDEF,DPRED,CMNAME,
3 NDI,NSHR,NTENS,NSTATV,PROPS,NPROPS,COORDS,DROT,PNEWDT,
4 CELENT,DFGRD0,DFGRD1,NOEL,NPT,LAYER,KSPT,KSTEP,KINC)
C
C  INCLUDE 'ABA_PARAM.INC'
C
C  CHARACTER*80 CMNAME
C  DIMENSION STRESS(NTENS),STATEV(NSTATV),
1  DDSDE(NTENS,NTENS),
2  DDSDDT(NTENS),DRPLDE(NTENS),
3  STRAN(NTENS),DSTRAN(NTENS),TIME(2),PREDEF(1),DPRED(1),
4  PROPS(NPROPS),COORDS(3),DROT(3,3),DFGRD0(3,3),DFGRD1(3,3)
C
C
C 2. Declaration of local variables
C
C 2.1. Definition of variables required for the viscoelastic with damage component
c
c Local Variables (just used in umat - user subroutine):
c t=tn      time at the beginning of the increment
c t=tn+1    time at the end of the increment
c E0mat     initial youngs modulus of the stress strain curve or
c           C11(S1=0)
c nue0     poissons ratio
c the relaxation function is defined as prony series:
c nE       number of terms of the prony series
c E0prony  value of the relaxation function for t=0
c Eprony(nE) terms of the prony series
c rho(nE)  relaxation times of the prony series
c Er       reference Modulus, used to transfer the relaxation function
c           to a function of time
c alph0    initial term of the prony series of the relative relax. funct.
c alph(nE) terms of the prony series of the relative relax. funct.
c C11 etc. material functions depending on the damage variable S
c S        damage variable
c A11 etc. material functions depending on C11 etc.

```

c Tr reference temperature  
c C\_1,C\_2 parameters of the WLF equation  
c aT\_n TTSP shift factor for the temp. at the beginning of the incr.  
c aT\_n1 TTSP shift factor for the temp. at the end of the increment  
c h\_n, h\_n1 logarithm with basis e of (1/aT)  
c dtau reduced time increment  
c eps(ntens) strains at t=tn  
c deps(ntens) strain increment  
c epsi(nE,ntens) viscous strains for the i-th term of the prony series  
c epsv(ntens) viscous strains, t=tn+1  
c epsR(ntens) pseudo strains, t=tn+1  
c ps1(3) principal values of strain provided by Abaqus  
c an(3,3) cosines between global axes and principal axes  
c assumed transverse isotropy with the principal axis 3 as axis of symmetry  
c 3 is defined as the axis of the maximum principal strain  
c cs(3,3) cosines between global axes and principal axes for 3 as  
c major axis and axis of symmetry for transverse isotropy  
c e11p,e22p,e33p principal strains for 3 as major principal axis and axis of  
c symmetry for transverse isotropy, e33p>e22p>e11p  
c evR,e2R,e3R pseudo strains for the assumed transverse isotropy  
c WR\_S pseudo strain energy density function  
c dC\_dS2 differentiation of C(S2) with regard to S2  
c dWRdS1,2 differentiation of WR with regard to S1, S2  
c dS increment of damage variable S  
c stresp(3) updated local principal stresses (t=tn+1)  
c deRdde derivation of the global pseudo strains with regard to the  
c global real strains  
c Cij(ntens,ntens) local Jacobian, depending on material functions and time  
c increment dtau  
c c12# calibration parameters of C12 damage function  
c c22# calibration parameters of C22 damage function  
c  
INTEGER nE,i,j,l  
PARAMETER(nE=12)  
REAL\*8 E0mat,nue0,E0prony,Eprony(nE),rho(nE),Er,alph0,alph(nE),  
& S,Sd,C11R,A11,A22,A12,A44,A66,C11,C12,C22,C,Tr,at\_n,  
& aT\_n1,dtau,eps(ntens),deps(ntens), epsi(nE,ntens),  
& epsv(ntens),epsR(ntens),ps1(3),an1(3,3),cs1(3,3),  
& e11p,e22p,e33p,evR,e2R,e3R,WR\_S,WR\_Sd,dWRdS,dC\_dS2,  
& dS,stresp(3),Cij(ntens,ntens),sum,deRdde,  
& C\_1,C\_2,h\_n,h\_n1,c111,c112,c113,c114,c115,c116,  
& c221,c222,c223,c121,c122,c123,c124,c125,alphadamage,  
& ddt,E0calc,Etcalf,yy1,yy2,timer

C

C 2.2. Definition of variables required for the VP subroutine

C

C gamma, alpha, n, R, alpha0, R0, kappa, m, expo, tau, NN - parameters HiSS surface  
 C xi - volumetric viscoplastic strains  
 C ps - vector of applied principal stresses, fixsig11, fixsig22, fixsig33  
 C surfstress - stress vector of HiSS surface point  
 C dFdsigma - vector of derivatives of F with respect to sigma  
 C Dist = (F/F'0) - 1  
 C HiSScentpoints - vector of points on surface at convergence  
 C centnorm - normal vector on the center point of convergence  
 C intestJstress - Second invariant (J2d) of deviatoric stress tensor  
 C intestIstress - First invariant (I1) of stress tensor  
 C intestJsurf - J2d corresponding to I1 on the Hiss Surface  
 C surfintercept - point where the HiSS surface intercepts the Hydrostatic line  
 C perpiii - volumetric stress or pressure = (sigma1 + sigma2 + sigma3)/3  
 C hydrline - point where the line normal to HiSS intercept on the Hydrostatic line  
 C DistA - distance from HiSS surface point and applied stress  
 C DistB - distance form Hydrostatic line and HiSS surface point  
 C devpdt - viscoplastic strain rate  
 C evp - viscoplastic principal strains corresponding to stress increment i  
 C psOLD - previous applied principal stress  
 C surfstressOLD - previous HiSS surface stress  
 C dfdsigmaOLD - previous normals to HiSS surface  
 C an - matrix of direction cosines for stress  
 C evpt - viscoplastic strain tensor corresponding to stress increment i  
 C ane - matrix of direction cosines for viscoplastic strain  
 C stressNEW - new stress tensor (increment i+1)  
 C stressOLD - current stress tensor (increment i)  
 C destran - matrix of six components of elastic strain  
 C vetor - auxiliar vector of principal values (vetor(3))  
 C cs(3,3) - new cosine matrix from the transformation of principal stresses  
 C sit, slopetangent, slopenormal, anglenormal, angleline, anglecheck - auxiliary  
 C variables to define the normal-free zone  
 C  
 REAL\*8 ps(3),surfstress(3),dFdsigma(3),  
 & HiSScentpoints(3),centnorm(3),devpdt(3),evp(3),  
 & psOLD(3),surfstressOLD(3),dfdsigmaOLD(3),an(3,3),evpt(6),  
 & ane(3,3),stressNEW(NTENS),stressOLD(NTENS),destran(NTENS),  
 & vetor(3),cs(3,3)  
 C  
 REAL\*8 alpha0,gamma,R0,n,kappa,m,expo,tau,NN,k3,xi,alpha,R,  
 & Dist,intestJstress,intestIstress,intestJsurf,surfintercept,  
 & perpiii,  
 & hydrline,  
 & DistA,DistB,lambda,A,tempshift,sit,slopetangent,  
 & slopenormal,anglenormal,angleline,anglecheck  
 C  
 C

### C 3. Material properties and variable initialization

C

#### C 3.1. Viscoelastic properties

c

c define the material functions C11(S),C12(S),C22(S)

c they are defined as single statement functions, which are actually part of

c the declaration of the variables; therefor they should come directly after

c the declaration of the variables.

c REVISE ->E0mat and nue0 do not need to be mentioned for C11 etc., they are defined

c later.

c REVISE ->For the material functions C12(S1),C22(S1) it is assumed that in the

c undamaged state the poissons ratio (nue0) is constant.

c

$$C11(S) = \text{EXP}(c111*S**c112)$$

$$C12(S) = (c121 - c122)*\text{EXP}(-c123*S)-c124*S+c122$$

$$C22(S) = c221 + c222*S*S$$

c

c relaxation function E(t) - Prony series (in Kpa and sec)

c if you change the data of the prony series you have to adapt nE in the

c beginning at the variable declaration (see 1.)

$$E0prony = 338297.6$$

$$Eprony(1) = 3435971$$

$$Eprony(2) = 3435971$$

$$Eprony(3) = 3435971$$

$$Eprony(4) = 3435971$$

$$Eprony(5) = 3435971$$

$$Eprony(6) = 2286747$$

$$Eprony(7) = 850059.2$$

$$Eprony(8) = 351616.8$$

$$Eprony(9) = 132844.1$$

$$Eprony(10)= 73265.97$$

$$Eprony(11)= 3.015$$

$$Eprony(12)= 3.015$$

c

$$\rho(1) = 0.000001$$

$$\rho(2) = 0.00001$$

$$\rho(3) = 0.0001$$

$$\rho(4) = 0.001$$

$$\rho(5) = 0.01$$

$$\rho(6) = 0.1$$

$$\rho(7) = 1.0$$

$$\rho(8) = 10.0$$

$$\rho(9) = 100.0$$

$$\rho(10) = 1000.0$$

$$\rho(11) = 10000.0$$

$$\rho(12) = 100000.0$$

c  
nue0 = 0.428  
Er = 1.0

c  
c Define the calibrated functions for the damage functions

c  
c111 = -0.00298  
c112 = 0.5006  
alphadamage = 2.0

c  
c121 = 1.0 - 2.0\*nue0  
c122 = 0.1423  
c123 = 1.317\*10\*\*(-5.)  
c124 = 4.103\*10\*\*(-7.)

c  
c221 = -0.4113  
c222 = -1.6937\*10\*\*(-10.)

c  
c Temperature Shift Factor

c  
tempshift=0.000466

c  
c tempshift=0.002615 for 39°C - lab test at UMD

c  
c tempshift=0.000466 for 45°C

c  
c tempshift=0.00000193 for 64°C

c  
C 3.2. Viscoplastic properties

c  
alpha0=0.0068  
gamma=0.0428  
R0=38.4245  
n=2.2564  
kappa=-68.096  
m=3227.4  
expo=0.3306  
tau=-8.7801  
NN=1.076  
k3=2.5782

c  
C 3.3. Initialization of STATEV in case it is first increment

C  
C The first 12 internal state variables are used in the VP model, as described  
C below. variable 13 stores the damage variable, S, of the VECD model and the  
C remaining 6\*nE variables are auxiliaries in the pseudo strain calculations.

C  
C If the first step and increment, assume xi=0, otherwise

```

C   xi=statev(1)+statev(2)+statev(3)
c   print *, kstep, kinc
    IF (kstep==1 .AND. kinc==1) THEN
C     first six are VP strains, 11,22,33,12,13,23
      STATEV(1)=0.
      STATEV(2)=0.
      STATEV(3)=0.
      STATEV(4)=0.
      STATEV(5)=0.
      STATEV(6)=0.
C     next three are HiSS surface stress in principal domain
      STATEV(7)=0.
      STATEV(8)=0.
      STATEV(9)=0.
C     last three are HiSS normals (dF/dsigma) in principal domain
      STATEV(10)=0.
      STATEV(11)=0.
      STATEV(12)=0.
    END IF
c
c   Read S from the statev(13) provided by Abaqus
c   if you want to start the calculations with from zero different initial value
c   for S, you have to change the value for Safter the two "if" commands
c
      S = statev(13)
      IF (kstep==1) THEN
        IF (kinc==1) THEN
          S=0.d0
        END IF
      END IF
c   If you want to run calculations without damage, means just linear visco-
c   elastic calculations, you have to remove the "c" in front of the next
c   line to set them effective and set S=0.d0 for every iteration.
      S=0.d0
c
C 3.4. Initilization of vectors and matrices
C
      DO I=1,3
        vetor(I)=0.
        psOLD(I)=0.
        ps(I)=0.
        DO J=1,3
          an(I,J)=0.
          cs(I,J)=0.
          ane(I,J)=0.
        END DO
      END DO

```

```

      END DO
c
C
C 4. Viscoelastic with Continuum Damage Calculations
C
c 4.1. Calculate alph(i)
      alph0=E0prony/Er
      do i=1,nE
        alph(i)=Eprony(i)/Er
      end do
c
c 4.2. Define the material functions A11, A22, A12, A44, A66 for the instant t=tn
c
      C11R = C11(S)
      A11 = (1.d0/9.d0)*(C11R-((C12(S)-3.d0)**2.d0)/C22(S))
      A22 = C11R-(C12(S)**2.d0)/C22(S)
      A12 = (1.d0/3.d0)*C11R+(C12(S)/C22(S))*
      & (1.d0-(1.d0/3.d0)*C12(S))
      A44 = C11(0.d0)/(2.0d0*(1.d0+nue0))
      A66 = A44
c
c 4.3 Reduced time
c
      timer=time(1)+dtime
      dtau=dtime !/tempshift
c
c 4.4 Read eps, deps and transform eps(i)+deps(i) in epsR_n1
c
c   Read strain eps(i) and deps(i) from stran(i) and dstran(i) for t=tn
      DO i=1,ntens
        eps(i)=stran(i)
        deps(i)=dstran(i)
      END DO
c
c   This is a new recursive approach based on Simo and Hughes (1998)
c   Here epsi (i,j) is equivalent to h(i) for a strain j (i = 1 to 12 and
c   j = 1 to NTENS)
c
c   l = 13, since the first aux statev is 14.
c
      l=13
      DO j=1,ntens
        epsv(j)=0.d0
        DO i=1,nE
          l=l+1
          epsi(i,j)=0.d0

```

```

    epsi(i,j)= (EXP(-dtau/rho(i)))*statev(1)+
&      deps(j)*((1.d0-EXP(-dtau/rho(i)))/(dtau/rho(i)))
    statev(1)= epsi(i,j)
    epsv(j)= epsv(j)+alph(i)*epsi(i,j)
  END DO
  epsR(j)= alph0*(eps(j)+deps(j)) + epsv(j)
  END DO
c epsv, epsR are at time t=tn+1, eps is at t=tn
c
c 4.5. Find the principal values and axes of epsR(ntens)
c
c   Find the principal values ps(3) and the principal axes an(3,3)
c   the subroutine sprind is provided by Abaqus
  CALL sprind(epsR,ps1,an1,2,ndi,nshr)
c
c   3 is the axis of symmetry of the transverse isotropic material
c   therefor ps(3) are transformed in e33p>e22p>e11p and according to this the
c   cosines of the axes an(3,3) to a new matrix cs(3,3)
  CALL kprind(ps1,an1,cs1,e11p,e22p,e33p)
c
c   define strains for the assumed transversly isotropic material with the
c   principal axis 3 as the axis of symmetry of the transv. isotropic material
  evR= e11p+e22p+e33p
  e2R= e22p-e11p
  e3R= e33p-(evR/3.d0)
c
c 4.6. Calculate updated local principal stresses stresp(3) and
c   transform them to global stresses, stress(ntens)
c
c   Calculate local principal stresses for t=tn+1
c   3 is the axis of the maximum principal strain and axis of symmetry of the
c   transverse isotropy
  stresp(1)= (A11-(1.d0/3.d0)*A12)*evR+(A12-(1.d0/3.d0)*A22)
&      *e3R-A66*e2R
  stresp(2)= (A11-(1.d0/3.d0)*A12)*evR+(A12-(1.d0/3.d0)*A22)
&      *e3R+A66*e2R
  stresp(3)= (A11+(2.d0/3.d0)*A12)*evR+(A12+(2.d0/3.d0)*A22)
&      *e3R
c
c   Transform the local principal stresses stresp(3) to global stresses at t=tn+1
c   normal stresses
  stress(1)=stresp(1)*CS1(1,1)**2.d0+stresp(2)*CS1(2,1)**2.d0
&      +stresp(3)*CS1(3,1)**2.d0
  stress(2)=stresp(1)*CS1(1,2)**2.d0+stresp(2)*CS1(2,2)**2.d0
&      +stresp(3)*CS1(3,2)**2.d0
  stress(3)=stresp(1)*CS1(1,3)**2.d0+stresp(2)*CS1(2,3)**2.d0

```

```

&      +stresp(3)*CS1(3,3)**2.d0
c   Shear stresses
   IF (NTENS==4) THEN
stress(4)=stresp(1)*CS1(1,1)*CS1(1,2)+stresp(2)*CS1(2,1)*CS1(2,2)+
&      stresp(3)*CS1(3,1)*CS1(3,2)
   ELSEIF (NTENS==6) THEN
stress(4)=stresp(1)*CS1(1,1)*CS1(1,2)+stresp(2)*CS1(2,1)*CS1(2,2)+
&      stresp(3)*CS1(3,1)*CS1(3,2)
stress(5)=stresp(1)*CS1(1,1)*CS1(1,3)+stresp(2)*CS1(2,1)*CS1(2,3)+
&      stresp(3)*CS1(3,1)*CS1(3,3)
stress(6)=stresp(1)*CS1(1,2)*CS1(1,3)+stresp(2)*CS1(2,2)*CS1(2,3)+
&      stresp(3)*CS1(3,2)*CS1(3,3)
   END IF
c
c 4.6. Calculate local Jacobian Cij and transform it to global Jacobian
ddsdde(ntens,ntens)
c
c   The Jacobian is the derivation of the stress with regard to the strain
c   or the strain increment deps at t=tn+1.
c   S1 and S2 are assumed to be fixed (indep. of strain) since otherwise the
c   derivation gets too complicated. So not a to the update of the stresses
c   consistent tangent modulus for the global newton iteration is supplied but
c   the secant modulus. This will cause a slower than quadratic convergence.
c
c   dstress/ddeps= dstress/depsR * depsR/ddeps
c
c 1) calculate the derivation of the updated pseudo strains epsR with regard to
c   the increment in the real strains deps:
c           deRdde=depsR/ddeps   ...globally
c
c   This derivation is accomplished by making use of the recursive algorithm
c   (see 4.) derived to solve the hereditary integral increment by increment.
c   It was assumed that the strains vary linearly within the time increment
c   dtau. The result is a function of just the time increment dtau. It is
c   independent of the coordinate system, valid for the local and the global
c   coordinate system.
c
c   sum=0.
c   DO i=1,nE
c     sum= sum + alph(i)*(rho(i)/dtau)*(1.d0-EXP(-dtau/rho(i)))
c   END DO
c
c   deRdde= alph0 + sum
c
c 2) derivate the local principal stresses with regard to the local principal
c   pseudo strains:

```

```

c          dstressp/deiip ...locally
c
c This is multiplied by deRdde=depsR/deps. Since depsR/deps does not depend
c on the coordinate system, this multiplication is already performed in the
c local coordinate system.
c
DO i=1,NTENS
  DO j=1,NTENS
    Cij(i,j)=0.d0
  END DO
END DO
c
IF (NTENS==4) THEN
  Cij(1,1)= (A11+(1.d0/9.d0)*A22-(2.d0/3.d0)*A12+A66)*deRdde
  Cij(2,2)= (A11+(1.d0/9.d0)*A22-(2.d0/3.d0)*A12+A66)*deRdde
  Cij(3,3)= (A11+(4.d0/9.d0)*A22+(4.d0/3.d0)*A12)*deRdde
  Cij(1,2)= (A11+(1.d0/9.d0)*A22-(2.d0/3.d0)*A12-A66)*deRdde
  Cij(1,3)= (A11-(2.d0/9.d0)*A22+(1.d0/3.d0)*A12)*deRdde
  Cij(2,3)= (A11-(2.d0/9.d0)*A22+(1.d0/3.d0)*A12)*deRdde
  Cij(3,1)= Cij(1,3)
  Cij(3,2)= Cij(2,3)
  Cij(2,1)= Cij(1,2)
  Cij(4,4)= A44*deRdde
ELSEIF (NTENS==6) THEN
  Cij(1,1)= (A11+(1.d0/9.d0)*A22-(2.d0/3.d0)*A12+A66)*deRdde
  Cij(2,2)= (A11+(1.d0/9.d0)*A22-(2.d0/3.d0)*A12+A66)*deRdde
  Cij(3,3)= (A11+(4.d0/9.d0)*A22+(4.d0/3.d0)*A12)*deRdde
  Cij(1,2)= (A11+(1.d0/9.d0)*A22-(2.d0/3.d0)*A12-A66)*deRdde
  Cij(1,3)= (A11-(2.d0/9.d0)*A22+(1.d0/3.d0)*A12)*deRdde
  Cij(2,3)= (A11-(2.d0/9.d0)*A22+(1.d0/3.d0)*A12)*deRdde
  Cij(3,1)= Cij(1,3)
  Cij(3,2)= Cij(2,3)
  Cij(2,1)= Cij(1,2)
  Cij(4,4)= A44*deRdde
  Cij(5,5)= A44*deRdde
  Cij(6,6)= A66*deRdde
END IF
c
c 3) transform the local Cij to the global ddsdde
c
call kbacktr(Cij,ddsdde,cs1,NTENS)
c
DO i=1,ntens
  DO j=1,ntens
    ddsdde(i,j)=Cij(i,j)
  END DO

```

```

      END DO
c
c 4.8. Update S
c
c 1) calculate the numerical differentiation of WR with regard to S
c   approximations: take S at instant t=tn and evR,e2R,e3R at t=tn+1
c       update S at the end of the increment (so the
c       calculations in the increment were performed with S
c       at t=tn);
c   These approximations can be made as long as small time incr. are used.
c
      Sd=S+0.1d0
c
      C11Rd=C11(Sd)
c
      A11d=(1.d0/9.d0)*(C11Rd-((C12(Sd)-3.d0)**2.d0)/C22(Sd))
      A22d=C11Rd-(C12(Sd)**2.d0)/C22(Sd)
      A12d=(1.d0/3.d0)*C11Rd+(C12(Sd)/C22(Sd))*
&      (1.d0-(1.d0/3.d0)*C12(Sd))
      A66d=A66
c
      WR_S= 0.5d0*(A11*(evR**2.d0) + A22*(e3R**2.) +
&      2.d0*A12*e3R*evR + A66*(e2R**2.d0))
      WR_Sd=0.5d0*(A11d*(evR**2.d0) + A22d*(e3R**2.d0) +
&      2.d0*A12d*e3R*evR + A66d*(e2R**2.d0))
c
      dWRdS= (WR_Sd - WR_S)/0.1d0
c
c 2) Calcualte the increment dS1 and dS2
      dS = ((-dWRdS)**alphadamage)*dtau
c
c 3) Update S from t=tn to t=tn+1 and update the regarding statev(13)
      S = S + dS
      statev(13) = S
c
C
c 5. ViscoPlastic Calculations
c
C 5.1. Compute principal stresses
C
C   Store current stress (before VP calculations) as stressOLD=STRESS
C
      DO I=1,NTENS
         stressOLD(I)=STRESS(I)
      END DO
C

```

```

C   Transform the old stress tensor into principal stresses vetor(3)
C
C   CALL SPRIND(stressOLD,vetor,an,1,NDI,NSHR)
C
C   Put the principal old stresses in order 33>22>11. This is done so when
C   the sign is changed, (-) compression becomes (+) and 11>22>33.
C
C   CALL princord(vetor,psOLD)
C
C   psOLD comes in normal ABAQUS notation compression (-). The following 3
C   lines changes the sign of the principal values, making compression (+)
C   and shifting the order to 11>>22>>33 as required by VP model.
C
C 5.5. Store old stress, surfstress and dFdsigma
C
C   The stress comes from ABAQUS STRESS variable; surfstress from STATEV(7 to
C   9)
C   and dFdsigma from STATEV(10 to 12).
C
C   psOLD(1)=-psOLD(1)
C   psOLD(2)=-psOLD(2)
C   psOLD(3)=-psOLD(3)
C   surfstressOLD(1)=STATEV(7)
C   surfstressOLD(2)=STATEV(8)
C   surfstressOLD(3)=STATEV(9)
C   dfdsigmaOLD(1)=STATEV(10)
C   dfdsigmaOLD(2)=STATEV(11)
C   dfdsigmaOLD(3)=STATEV(12)
C
C 5.6. Compute new stress for current strain increment
C
C   DO I=1,NTENS
C     stressNEW(I)=STRESS(I)
C     DO J=1,NTENS
C       stressNEW(I)= stressNEW(I)+DDSDDE(I,J)*DSTRAN(J)
C     END DO
C   END DO
C
C   Transform the new stress tensor into principal stresses vetor
C
C   CALL SPRIND(stressNEW,vetor,an,1,NDI,NSHR)
C
C   Put the principal new stresses in order 33>22>11. This is done so when
C   the sign is changed, (-) compression becomes (+) and 11>22>33. The
C   subroutine also change the cossine matrix to accomodate the new order.
C   The new matrix will be called cs(3,3).

```

```

C
  CALL kprind(vetor,an,cs,ps)
C
C 5.7. Compute viscoplastic strains
C
  DO I=1,6
    evpt(I)=STATEV(I)
  END DO
  CALL SPRIND(evpt,evp,ane,2,NDI,NSHR)
  xi=SQRT((evp(1)**2.)+(evp(2)**2.)+(evp(3)**2.))
C
C The VP model was formulated with compression (+), different from ABAQUS
C conventional compression (-). The following three lines change signs of
C principal stresses without changing directions. After the calculations
C are done, the viscoplastic strain signs are changed back to conventional
C notation of compression (-).
  ps(1)=-ps(1)
  ps(2)=-ps(2)
  ps(3)=-ps(3)
c
C Compute initial parameters alpha(xi) and R(xi)
  alpha=alpha0*EXP(xi*kappa)
  R=R0+m*(xi**expo)
C
C Verify if the point perpendicular to the the stress point is either to the
C left or to the right of the intersection of the HiSS surface and the
C Hydrostatic line.
  intestIstress=ps(1)+ps(2)+ps(3)
  surfintercept=(1./3.)*(((alpha/gamma)**(1./(2.-n)))-R)
  perpiii=intestIstress/3.
C
IF (ps(1)==ps(2) .AND. ps(2)==ps(3)) THEN !Point on Hydrostatic
  IF (ps(1)==0.) THEN
    DO i=1,3
      surfstress(i)=0.
      dFdsigma(i)=0.
    END DO
    Dist = 0.
    A = 1.
  ELSEIF (ps(1)<=surfintercept) THEN
    DO i=1,3
      surfstress(i)=0.
      dFdsigma(i)=0.
    END DO
    Dist = 0.
    A = 1.

```

```

ELSE
  DO i=1,3
    surfstress(i)=surfintercept
    dFdsigma(i)=0. !Initialize dFdsigma for subroutine below
  END DO
  intestJstress = (1./3.)*(ps(1)**2+ps(2)**2+ps(3)**2-
&      ps(1)*ps(2)-ps(2)*ps(3)-ps(1)*ps(3))
  CALL dHiSS(gamma, alpha, n, R, surfstress,dFdsigma)
  IF (intestJstress<=0.) THEN
    A = 0.
    Dist = 0.
  ELSE
    A=(ABS(ATAN(SQRT(intestJstress)/intestJstress)/0.528))**k3
    Dist = ((SQRT(3.*(ps(1)-surfintercept)**2)
&      +surfintercept*SQRT(3.))/
&      (surfintercept*SQRT(3.)))-1.
  END IF
C
  END IF
C
ELSE !Point not on Hydrostatic
C  Verify if point is outside the HiSS surface
  intestJstress = (1./3.)*(ps(1)**2+ps(2)**2+ps(3)**2-
&      ps(1)*ps(2)-ps(2)*ps(3)-ps(1)*ps(3))
  IF (intestJstress<-R) THEN !Prevent tension-dominant areas
    intestJsurf = -9999
  ELSE
    intestJsurf = gamma*((intestJstress+R)**2)
&      -alpha*((intestJstress+R)**n)
  END IF
  IF (intestJstress<=3.*surfintercept .AND.
&      intestJstress<=intestJsurf) THEN
    DO i=1,3
      surfstress(i)=0.
      dFdsigma(i)=0.
    END DO
    Dist = 0.
    A = 1.0
C
  ELSE !Outside surface -> VP Flow
C
    !Verify is the point is located in normal free zone
    !Compute tangent to the intercept point in the  $J2D^{(1/2)}xI1$  space
    !at the tension side
c
    !surface intercept at tension side

```

```

sit=-R+1.*10.**(-10.)
!slope of the tangent to the surface intercept in tension
slopetangent=(gamma*(2.*R+2.*sit)-alpha*n*(R+sit)**(n-1.))/
&      (2.*(gamma*(R+sit)**2-alpha*(R+sit)**n)**(1./2.))
!slope of the normal to the surface intercept in tension
slopenormal=TAN(ATAN(slopetangent)+3.1415927/2.)
!angle of the normal
IF (ATAN(slopenormal)>0) THEN
  anglenormal=ATAN(slopenormal)
ELSE
  anglenormal=3.1415927-ABS(ATAN(slopenormal))
END IF
!angle line between surface intercept in tension and stress point
angleline=ATAN((intestIstress**(1./2.))/(intestIstress+R))
c
IF (angleline>0) THEN
  anglecheck=angleline
ELSE
  anglecheck=3.1415927-ABS(angleline)
END IF
c
IF (anglecheck>=anglenormal) THEN
  !inside normal free zone - Supress VP Flow
  A=0.
  Dist=0.
ELSE
  !Outside normal free zone -> VP Flow
C
C      Search for the stress point on HiSS surface normal to the
C      the surface and on the direction of the applied stress point.
C
IF (STATEV(7)+STATEV(8)+STATEV(9)==0.) THEN
C
  lambda=1.
  surfstressOLD(1)=perpii
  surfstressOLD(2)=perpii
  surfstressOLD(3)=perpii
C
IF (surfstressOLD(1)+surfstressOLD(2)+surfstressOLD(3)
&      +R>0.) THEN
  CALL HNR(ps,surfstressOLD,lambda,gamma,alpha,n,R,
&      HiSScentpoints,centnorm)
ELSE
  HiSScentpoints(1)=0.
  HiSScentpoints(2)=0.
  HiSScentpoints(3)=0.

```

```

        centnorm(1)=0.
        centnorm(2)=0.
        centnorm(3)=0.
    END IF
C
    ELSE
        lambda=(((psOLD(1)-surfstressOLD(1))**2+
&          (psOLD(2)-surfstressOLD(2))**2+
&          (psOLD(3)-surfstressOLD(3))**2)**0.5)/
&          ((dfdsigmaOLD(1)**2+dfdsigmaOLD(2)**2+
&          dfdsigmaOLD(3)**2)**0.5)
C
    IF (surfstressOLD(1)+surfstressOLD(2)+surfstressOLD(3)
&      +R>0.) THEN
        CALL HNR(ps,surfstressOLD,lambda,gamma,alpha,n,R,
&          HiSScentpoints,centnorm)
    ELSE
        HiSScentpoints(1)=0.
        HiSScentpoints(2)=0.
        HiSScentpoints(3)=0.
        centnorm(1)=0.
        centnorm(2)=0.
        centnorm(3)=0.
    END IF
    END IF
C
C    Patch to avoid complex number. My original formulation HiSScentpoints(1)=-
R/3.
C    Below is a new try
    IF (HiSScentpoints(1)==HiSScentpoints(2) .AND.
&      HiSScentpoints(2)==HiSScentpoints(3) .AND.
&      HiSScentpoints(1)==0.) THEN
        A=0.
        Dist=0.
    ELSE
        CALL gethydrpntext(ps, HiSScentpoints,hydrline)
        DistA=SQRT((HiSScentpoints(1)-ps(1))**2.+
&          (HiSScentpoints(2)-ps(2))**2.+
&          (HiSScentpoints(3)-ps(3))**2.)
        DistB=SQRT((HiSScentpoints(1)-hydrline)**2.+
&          (HiSScentpoints(2)-hydrline)**2.+
&          (HiSScentpoints(3)-hydrline)**2.)
C
        IF (DistB>surfintercept*SQRT(3.)) THEN
            DistB=surfintercept*SQRT(3.)
        END IF

```

```

Dist=ABS(((DistA+DistB)/DistB)-1.)
IF (intestJstress<=0.) THEN
  A = 0.
ELSE
  A=(ABS(ATAN(SQRT(intestJstress)/intestIstress)
&      /0.528))**k3
  END IF
END IF
C
C   Outputs
C
DO k=1,3
  surfstress(k)=HiSScentpoints(k)
  dFdsigma(k)=centnorm(k)
END DO
END IF
END IF
END IF
C
C   The result from surfHiSS function are: stress vector at the HiSS surface,
C   surfstress(k), the normal vector to the surface on the direction of the
C   applied stress (strain trajectory), dFdsigma(k), and the relative distance
C   from the applied stress to the hydrostatic plane, Dist. With these parameters
C   is possible now to compute the principal viscoplastic strain rates, devpdt(k),
C   and incremental viscoplastic strains, evp(k).
C
DO k=1,3
  devpdt(k)=(10.**tau)*A*(Dist**NN)*dFdsigma(k)
  evp(k)=-devpdt(k)*(dtime)*(1./tempshift)
C   The negative sign is to transform back into compression (-)
END DO
C
C   After the incremental viscoplastic strains are computed in principal plane, it is
C   necessary to bring back the original orientation. In this verification test it is assumed
C   the vertical and horizontal strains corresponds respectively to major and minor and
mid
C   strains.
C
C   normal vp strains
evpt(1)=evp(1)*cs(1,1)**2.+evp(2)*cs(2,1)**2.+
&      evp(3)*cs(3,1)**2.
evpt(2)=evp(1)*cs(1,2)**2.+evp(2)*cs(2,2)**2.+
&      evp(3)*cs(3,2)**2.
evpt(3)=evp(1)*cs(1,3)**2.+evp(2)*cs(2,3)**2.+
&      evp(3)*cs(3,3)**2.
C

```

```

C shear vp strains
evpt(4)=evp(1)*cs(1,1)*cs(1,2)+evp(2)*cs(2,1)*cs(2,2)+
& evp(3)*cs(3,1)*cs(3,2)
evpt(5)=evp(1)*cs(1,1)*cs(1,3)+evp(2)*cs(2,1)*cs(2,3)+
& evp(3)*cs(3,1)*cs(3,3)
evpt(6)=evp(1)*cs(1,2)*cs(1,3)+evp(2)*cs(2,2)*cs(2,3)+
& evp(3)*cs(3,2)*cs(3,3)
C
C 5.8. Update state variables (1-6)vpstrains, (7-9)HiSS surface stress, and
C (10-12) dFdsigma
C
STATEEV(1)=STATEEV(1)+evpt(1)
STATEEV(2)=STATEEV(2)+evpt(2)
STATEEV(3)=STATEEV(3)+evpt(3)
STATEEV(4)=STATEEV(4)+evpt(4)
STATEEV(5)=STATEEV(5)+evpt(5)
STATEEV(6)=STATEEV(6)+evpt(6)
STATEEV(7)=surfstress(1)
STATEEV(8)=surfstress(2)
STATEEV(9)=surfstress(3)
STATEEV(10)=dFdsigma(1)
STATEEV(11)=dFdsigma(2)
STATEEV(12)=dFdsigma(3)
C
C 5.9. Update Stress
C
C For infinitesimal analysis (specimen in the lab), stresses are updated
C without corrections to the elastic strain. The following lines apply
C
C DO k=1,ntens
C STRESS(k)=stressNEW(k)
C END DO
C
C Otherwise the following lines must be active. Remove C's from the lines
C below and put C's on the lines above to activate the viscoplastic
C adjustments of the elastic strains
C
C Compute the recoverable strain increments
C
DO k=1,ntens
destran(k)=DSTRAN(k)-evpt(k)
END DO
C
C Compute adjusted stress
DO I=1,ntens
DO J=1,ntens

```

```

        STRESS(I)= STRESS(I)+DDSDDE(I,J)*destran(J)
    END DO
END DO
C
C
C 6.0 Return back to ABAQUS
C
    RETURN
    END

c
c
c
c 7. Subroutines
c
c=====
=====
    SUBROUTINE kbacktr(C,T,DIR,N)
c=====
=====
c Developed by R. Hinterhoelzl (1999)
c
c Transform the 4th order tensor in the local coordinate system (in the
c principal axes) back into a 4th order tensor in the global coordinate
c system (global).
c
c  C(N,N): Jacobian in the local coordinate system of the principal axes
c  T(N,N): Jacobian in the global (original) coordinate system
c  DIR(I,J): DIRECTION COSINE BETWEEN Xi'(PRIN.) TO Xj (GLOBAL).
c  N: Number of stresses (4 - axisymmetric and plane strain problems
c      6 - full 3D problems)
c      OBSERVATION: Not coded for plane stress problems
c
c  stress(1)=stress(1,1)  strain(1)=strain(1,1)
c  stress(2)=stress(2,2)  strain(2)=strain(2,2)
c  stress(3)=stress(3,3)  strain(3)=strain(3,3)
c  stress(4)=stress(1,2)  strain(4)=strain(1,2)
c  stress(5)=stress(1,3)  strain(5)=strain(1,3)
c  stress(6)=stress(2,3)  strain(6)=strain(2,3)
c
c
c
c  INCLUDE 'aba_param.inc'
c  REAL*8 DIR(3,3)
c  REAL*8 T(N,N),C(N,N),C0(3,3,3,3)
c
c 1) find the 4th order tensor C0(3,3,3,3) in the local coordinate system
c from the 6x6 matrix C(NTENS,NTENS)

```

```

c
DO I=1,3
  DO J=1,3
    DO K=1,3
      DO L=1,3
        C0(I,J,K,L)=0.d0
      END DO
    END DO
  END DO
END DO

```

```

c
IF (N==4) THEN

  C0(1,1,1,1)=C(1,1)
  C0(1,1,2,2)=C(1,2)
  C0(1,1,3,3)=C(1,3)
  C0(2,2,1,1)=C(2,1)
  C0(2,2,2,2)=C(2,2)
  C0(2,2,3,3)=C(2,3)
  C0(3,3,1,1)=C(3,1)
  C0(3,3,2,2)=C(3,2)
  C0(3,3,3,3)=C(3,3)

```

```

C
  C0(1,2,1,2)=C(4,4)
  C0(1,2,2,1)=C(4,4)
  C0(2,1,1,2)=C(4,4)
  C0(2,1,2,1)=C(4,4)
ELSEIF (N==6) THEN
  C0(1,1,1,1)=C(1,1)
  C0(1,1,2,2)=C(1,2)
  C0(1,1,3,3)=C(1,3)
  C0(2,2,1,1)=C(2,1)
  C0(2,2,2,2)=C(2,2)
  C0(2,2,3,3)=C(2,3)
  C0(3,3,1,1)=C(3,1)
  C0(3,3,2,2)=C(3,2)
  C0(3,3,3,3)=C(3,3)
  C0(1,2,1,2)=C(4,4)
  C0(1,3,1,3)=C(5,5)
  C0(2,3,2,3)=C(6,6)

```

```

c
  C0(1,2,2,1)=C(4,4)
  C0(1,3,3,1)=C(5,5)
  C0(2,3,3,2)=C(6,6)
  C0(2,1,1,2)=C(4,4)
  C0(3,1,1,3)=C(5,5)

```

```

C0(3,2,2,3)=C(6,6)
C0(2,1,2,1)=C(4,4)
C0(3,1,3,1)=C(5,5)
C0(3,2,3,2)=C(6,6)
END IF

```

c

c 2) find the NTENSxNTENS matrix T(N,N) in the global coordinate system from the  
c 4th order tensor in the local coordinate system C0(3,3,3,3)

```

DO I=1,N
  DO J=1,N
    T(I,J)=0.d0
  END DO
END DO

```

c

```

DO M=1,3
  T(M,M)=0.d0
  DO I=1,3
    DO J=1,3
      DO K=1,3
        DO L=1,3
          T(M,M)=T(M,M)+DIR(I,M)*DIR(J,M)*DIR(K,M)*DIR(L,M)*
&          C0(I,J,K,L)
        END DO
      END DO
    END DO
  END DO
END DO

```

c

```

DO I=1,3
  DO J=1,3
    DO K=1,3
      DO L=1,3
        IF (N==4) THEN
          T(4,4)=T(4,4)+DIR(I,1)*DIR(J,2)*DIR(K,1)*DIR(L,2)*
&          C0(I,J,K,L)
          T(1,2)=T(1,2)+DIR(I,1)*DIR(J,1)*DIR(K,2)*DIR(L,2)*
&          C0(I,J,K,L)
          T(1,3)=T(1,3)+DIR(I,1)*DIR(J,1)*DIR(K,3)*DIR(L,3)*
&          C0(I,J,K,L)
          T(2,3)=T(2,3)+DIR(I,2)*DIR(J,2)*DIR(K,3)*DIR(L,3)*
&          C0(I,J,K,L)
        ELSE IF (N==6) THEN
          T(4,4)=T(4,4)+DIR(I,1)*DIR(J,2)*DIR(K,1)*DIR(L,2)*
&          C0(I,J,K,L)
          T(5,5)=T(5,5)+DIR(I,1)*DIR(J,3)*DIR(K,1)*DIR(L,3)*
&          C0(I,J,K,L)

```

```

      T(6,6)=T(6,6)+DIR(I,2)*DIR(J,3)*DIR(K,2)*DIR(L,3)*
&      C0(I,J,K,L)
      T(1,2)=T(1,2)+DIR(I,1)*DIR(J,1)*DIR(K,2)*DIR(L,2)*
&      C0(I,J,K,L)
      T(1,3)=T(1,3)+DIR(I,1)*DIR(J,1)*DIR(K,3)*DIR(L,3)*
&      C0(I,J,K,L)
      T(2,3)=T(2,3)+DIR(I,2)*DIR(J,2)*DIR(K,3)*DIR(L,3)*
&      C0(I,J,K,L)
      END IF
    END DO
  END DO
END DO
c
  T(2,1)=T(1,2)
  T(3,1)=T(1,3)
  T(3,2)=T(2,3)
c
  RETURN
  END
c
c
c
  SUBROUTINE kprind(ps,an,cs,e1 1p,e22p,e33p)
c
c Developed by R. Hinterhoelzl (1999)
c
  INCLUDE 'aba_param.inc'
  REAL*8 an(3,3),cs(3,3),ps(3)
c
c the principal values ps(3) are not ordered;
c now they are ordered to e33p>e22p>e1 1p since 3 will become the axis of
c symmetry of the transverse isotropy; accordingly the array of the cosines is
c changed to cs(3,3);
c
c 1) Change the direction of the normal vector if det(an)=-1 to get a
c coordinate system that satisfies the right hand rule
c
  det=(an(1,1)*an(2,2)*an(3,3)+an(1,2)*an(2,3)*an(3,1)+
&  an(1,3)*an(2,1)*an(3,2)-an(1,3)*an(2,2)*an(3,1)-
&  an(1,2)*an(2,1)*an(3,3)-an(1,1)*an(2,3)*an(3,2))
c
  IF(det<(-0.999d0)) THEN
    an(1,1)=-an(1,1)
    an(1,2)=-an(1,2)
    an(1,3)=-an(1,3)

```

```

an(2,1)=-an(2,1)
an(2,2)=-an(2,2)
an(2,3)=-an(2,3)
an(3,1)=-an(3,1)
an(3,2)=-an(3,2)
an(3,3)=-an(3,3)
END IF

```

c

c 2) find 3 as the major axis

```

imax=1
smax=ps(1)
DO i=2,3
  IF(ps(i)>=smax) THEN
    imax=i
    smax=ps(i)
  END IF
END DO

```

c

```

e33p=ps(imax)

```

c

```

cs(3,1)=an(imax,1)
cs(3,2)=an(imax,2)
cs(3,3)=an(imax,3)

```

c

c 3) find the next two axes

```

IF(imax==1) THEN
  i2=2
  i3=3
ELSE IF(imax==2) THEN
  i2=1
  i3=3
ELSE
  i2=1
  i3=2
END IF

```

c

```

med=i2
min=i3
IF(ps(i3)>ps(i2)) THEN
  i3= med
  i2= min
END IF

```

c

```

e22p=ps(i2)
e11p=ps(i3)
DO k=1,3

```

```

        cs(2,k)=an(i2,k)
        cs(1,k)=an(i3,k)
    END DO
c
    RETURN
    END
C
C
C
    SUBROUTINE newperpHiSS(gamma1,alpha1,n1,R1,sigmaij,stressHiSS)
C
C Developed based on algorithm written by Gibson (2006)
C
C This function takes the HiSS surface definition parameters and the stress point to
C create a normal line from the Hydrostatic line to the stress point. It also finds the
C line intersection point on the HiSS surface, assuming the two solutions for the
C points on this line to be a quadratic relation. Three points are generated from an old
C Newton-Rapshon scheme that then calls a function to find the coefficients and roots.
C
    INCLUDE 'aba_param.inc' !Required for ABAQUS UMAT
C
C Definition of Variables
C
C gamma - parameter gamma for the HiSS surface
C alpha - parameter alpha for the HiSS surface
C n - parameter n for the HiSS surface
C R - parameter R for the HiSS surface
C sigmaii - vector of principal stresses given
C stressHiSS - stress vector of HiSS surface point
C surfintercept
C sigaa
C a,b,c,d - define two point parametric equation of a line in 3D
C s1, surferr, count
C sigmaiia,sigmaiib
C s1newa,s1newb
C F,dF
C rootsel - variable to select the appropriate root from the N-R scheme
C xpoint - vector of three x points defining the polynomial
C ypoint - vector of three y points defining the polynomial
C qa,qb,qc - polynomial coefficients
C qc1,qc2,qc3,qc4 - parameters to determine qa,qb,qc from the (x,y) points
C
    REAL*8 sigmaij(3),stressHiSS(3),stressHiSSa(3),stressHiSSb(3),
    &    gamma1,alpha1,n1,R1,surfintercept1,sigaa,a,b,c,d,s1,
    &    F,dF,s1newa,rootsel
C Variables required for the root calculation

```

```

REAL*8 xpoint(3),ypoint(3),roots(2),
&    qa,qb,qc,qc1,qc2,qc3,qc4
C
surfintercept1=(1./3.)*(((alpha1/gamma1)**(1./(2.-n1))))-R1)
C
C Determine the hydrostatic stress point (sigaa) that creates a perpendicular line
C from the given stress point to the hydrostatic axis using the dot product rule for
C 90 degrees
sigaa=(sigmaj(1)+sigmaj(2)+sigmaj(3))/3.
C
IF (ABS(sigaa-surfintercept1)<0.00001) THEN
    stressHiSS(1)=surfintercept1
    stressHiSS(2)=surfintercept1
    stressHiSS(3)=surfintercept1
ELSE
C Point 1 is (sigmaii(1),sigmaii(2),sigmaii(3)) and point 2 is (sigaa,sigaa,sigaa)
C Slope and intercept for equation of sigmaii(2)=f(sigmaii(1)) using two point
C parametric equation for line in 3D space.
a=(sigmaj(2)-sigaa)/(sigmaj(1)-sigaa)
b=(-sigaa)*a+sigaa
C Slope and intercept for equation of sigmaii(3)=f(sigmaii(1))
c=(sigmaj(3)-sigaa)/(sigmaj(1)-sigaa)
d=(-sigaa)*c+sigaa
C This linear equations are substituted for sigmaii(2) and sigmaii(3) in the
C HiSS surface equation.
C
s1=sigaa !This term sets the initial value for sigma11
C
C The following is the Newton-Raphson iteration given the function and its
C derivative. An additional component is required to compute both solutions to the
C flow surface (quadratic equation) and allow the algorithm to select the desired
C solution which is the one between the hydrostatic sigaa and the actual stressij
C (sigmaj).
C
C Initialize Newton-Raphson to compute three points for the quadratic function.
DO k=0,3
    F=(1./3.)*((s1**2)+((a*s1+b)**2)+((c*s1+d)**2)-(s1*(a*s1+b))-
&    ((a*s1+b)*(c*s1+d))-(s1*(c*s1+d))-gamma1*((s1+(a*s1+b)+
&    (c*s1+d)+R1)**2)+alpha1*((s1+(a*s1+b)+(c*s1+d)+R1)**n1)
C The following equation had a bug fixed at 2*c*c*s1 term on the first line.
C Originally 2*c*s1
dF=(1./3.)*(2.*s1+2.*a*a*s1+2.*a*b+2.*c*s1+2.*c*d+2.*a*s1+b+
&    2.*a*c*s1+b*c+a*d+2.*c*s1+d)-
&    2.*gamma1*(s1+a*s1+b+c*s1+d+R1)*(1.+a+c)+
&    n1*alpha1*((s1+a*s1+b+c*s1+d+R1)**(n1-1.))*(1.+a+c)
    s1newa=s1-(F/dF)

```

```

    IF (k==1) THEN
      xpoint(1)=s1
      ypoint(1)=F
    ELSEIF (k==2) THEN
      xpoint(2)=s1
      ypoint(2)=F
    ELSEIF (k==3) THEN
      xpoint(3)=s1
      ypoint(3)=F
    END IF
    s1=s1newa
  END DO
C   Compute the roots of the quadratic function originated from the N-R
  qc1=xpoint(1)*(ypoint(2)-ypoint(3))-
&   xpoint(2)*(ypoint(1)-ypoint(3))+
&   xpoint(3)*(ypoint(1)-ypoint(2))
  qc2=xpoint(1)*xpoint(1)*(ypoint(2)-ypoint(3))-
&   xpoint(2)*xpoint(2)*(ypoint(1)-ypoint(3))+
&   xpoint(3)*xpoint(3)*(ypoint(1)-ypoint(2))
  qc3=xpoint(1)*xpoint(1)*(xpoint(2)-xpoint(3))-
&   xpoint(2)*xpoint(2)*(xpoint(1)-xpoint(3))+
&   xpoint(3)*xpoint(3)*(xpoint(1)-xpoint(2))
  qc4=xpoint(1)*xpoint(1)*(xpoint(2)*ypoint(3)-xpoint(3)*ypoint(2))-
&   xpoint(2)*xpoint(2)*(xpoint(1)*ypoint(3)-xpoint(3)*ypoint(1))+
&   xpoint(3)*xpoint(3)*(xpoint(1)*ypoint(2)-xpoint(2)*ypoint(1))
  qc2=-qc2
  qc4=-qc4
C
  qa=-qc1/qc3
  qb=-qc2/qc3
  qc=-qc4/qc3
C
  roots(1)=(-qb+SQRT(qb*qb-4.*qa*qc))/(2.*qa)
  roots(2)=(-qb-SQRT(qb*qb-4.*qa*qc))/(2.*qa)
C
  stressHiSSa(1)=roots(1)
  stressHiSSa(2)=a*roots(1)+b
  stressHissa(3)=c*roots(1)+d
C
  stressHiSSb(1)=roots(2)
  stressHiSSb(2)=a*roots(2)+b
  stressHissb(3)=c*roots(2)+d
C
  rootsel=(stressHiSSa(1)-sigaa)*(sigmaj(1)-sigaa)+
&   (stressHiSSa(2)-sigaa)*(sigmaj(2)-sigaa)+
&   (stressHiSSa(3)-sigaa)*(sigmaj(3)-sigaa)

```

```

IF (rootse1>0.) THEN
  stressHiSS(1)=stressHiSSa(1)
  stressHiSS(2)=stressHiSSa(2)
  stressHiSS(3)=stressHiSSa(3)
ELSE
  stressHiSS(1)=stressHiSSb(1)
  stressHiSS(2)=stressHiSSb(2)
  stressHiSS(3)=stressHiSSb(3)
END IF
END IF
RETURN
END

C
C
C
  SUBROUTINE dHiss(gamma2,alpha2,n2,R2,sii,dFds)
C
C Developed based on algorithm written by Gibson (2006)
C
C This function computes the normal vector dFds on the HiSS surface using the surface
C parameters and the applied stress point as inputs
C
  INCLUDE 'aba_param.inc' !Required for ABAQUS UMAT
C
C Definition of variables
C
C gamma - parameter gamma for the HiSS surface
C alpha - parameter alpha for the HiSS surface
C n - parameter n for the HiSS surface
C R - parameter R for the HiSS surface
C sii - vector of principal stresses
C dFds - normal vector to the HiSS surface
C
  REAL*8 sii(3),dFds(3),gamma2,alpha2,n2,R2
C
  dFds(1)=(1./3.)*(2.*sii(1)-sii(2)-sii(3))-
& 2.*gamma2*(sii(1)+sii(2)+sii(3)+R2)+
& n2*alpha2*((sii(1)+sii(2)+sii(3)+R2)**(n2-1.))
  dFds(2)=(1./3.)*(2.*sii(2)-sii(1)-sii(3))-
& 2.*gamma2*(sii(1)+sii(2)+sii(3)+R2)+
& n2*alpha2*((sii(1)+sii(2)+sii(3)+R2)**(n2-1.))
  dFds(3)=(1./3.)*(2.*sii(3)-sii(1)-sii(2))-
& 2.*gamma2*(sii(1)+sii(2)+sii(3)+R2)+
& n2*alpha2*((sii(1)+sii(2)+sii(3)+R2)**(n2-1.))
  RETURN
  END

```

```

C
C
C
  SUBROUTINE unitvector(vec,uvec)
C
C This function computes the unit vector of a given vector
C
  INCLUDE 'aba_param.inc' !Required for ABAQUS UMAT
C
C Definition of variables
C
C vec - vector
C uvec - unit vector
C
  REAL*8 vec(3),uvec(3)
C
  DO k=1,3
    uvec(k)=vec(k)*(1./(SQRT(vec(1)*vec(1)+
&          vec(2)*vec(2)+vec(3)*vec(3))))
  END DO
  RETURN
  END
C
C
C
  SUBROUTINE gethydrpntext(sigii,pointHiSS,hydrostress)
C
C Developed based on algorithm written by Gibson (2006)
C
C This function computes the intersection between the line passing by the applied stress
C and the HiSS stress points and the Hydrostatic line
C
  INCLUDE 'aba_param.inc' !Required for ABAQUS UMAT
C
C Definition of Variables
C
C sigii - vector of applied stress
C pointHiSS - vector of point on HiSS surface
C hydrostress - output of this function - the intercept
C s13slope - slope of the 3D line
C
  REAL*8 sigii(3),pointHiSS(3),s13slope,hydrostress
C
  s13slope=(pointHiSS(1)-sigii(1))/(pointHiSS(3)-sigii(3))
C
  IF (1.-s13slope==0.) THEN
C
  hydrostress = 0.

```

```

C   ELSE
      hydrostress = (pointHiSS(1)-(s13slope*pointHiSS(3)))/(1.-s13slope)
C   END IF
      RETURN
      END
C
C
C
      SUBROUTINE HNR(g,u,lambda1,gamma1,alpha1,n1,R1,
&                stressHiSS,dFds)
C
C Developed based on algorithm written by Gibson (2006)
C
C This function applies a Newton-Raphson algorithm to find a point on the Hiss
C surface that is normal to the applied stress point.
C
      REAL*8 g(3),u(3),stressHiSS(3),dFds(3),unew(3)
      REAL*8 lambda1,gamma1,alpha1,n1,R1

      REAL*8 F1,F2,F3,F4,vct1,vct2,vct3,vct4,vct1store,vct2store,
&    vct3store,vct4store,dF1d1,dF1d2,dF1d3,dF1dlm,dF2d1,dF2d2,
&    dF2d3,dF2dlm,dF3d1,dF3d2,dF3d3,dF3dlm,dF4d1,dF4d2,dF4d3,
&    dF4dlm,dF1d1store,dF1d2store,dF1d3store,dF1dlmstore,
&    dF2d1store,dF2d2store,dF2d3store,dF2dlmstore,dF3d1store,
&    dF3d2store,dF3d3store,dF3dlmstore,dF4d1store,dF4d2store,
&    dF4d3store,dF4dlmstore,magold,magnew,errold,ernew,
&    surfintercept1
      INTEGER FLAG,imax
C
      surfintercept1=(1./3.)*(((alpha1/gamma1)**(1./(2.-n1)))-R1)
      FLAG = 0 !Flag if solution is complex
c   Compute magnitude for error analysis
      magold=SQRT(u(1)**2.+u(2)**2.+u(3)**2.)
      errold=1.
      imax=20
      DO i=1,imax
c
c   IF (FLAG==0) THEN
      F1=(g(1)-u(1))-lambda1*(((1./3.)*(2.*u(1)-u(2)-u(3))-2.*gamma1*
&    (u(1)+u(2)+u(3)+R1)+alpha1*n1*((u(1)+u(2)+u(3)+R1)**(n1-1.))))
      F2=(g(2)-u(2))-lambda1*(((1./3.)*(2.*u(2)-u(1)-u(3))-2.*gamma1*
&    (u(1)+u(2)+u(3)+R1)+alpha1*n1*((u(1)+u(2)+u(3)+R1)**(n1-1.))))
      F3=(g(3)-u(3))-lambda1*(((1./3.)*(2.*u(3)-u(2)-u(1))-2.*gamma1*
&    (u(1)+u(2)+u(3)+R1)+alpha1*n1*((u(1)+u(2)+u(3)+R1)**(n1-1.))))
      F4=(1./3.)*(u(1)*u(1)+u(2)*u(2)+u(3)*u(3)-u(1)*u(2)-u(2)*u(3)-
&    u(1)*u(3))-gamma1*((u(1)+u(2)+u(3)+R1)**2.)+alpha1*((u(1)+

```

```

& u(2)+u(3)+R1)**n1)
C
dF1d1=-1.-lambda1*((1./3.)*(2.)-2.*gamma1*(1.)+alpha1*n1*
7 (n1-1.)*((u(1)+u(2)+u(3)+R1)**(n1-2.))*1.)
dF1d2=-lambda1*((1./3.)*(-1.)-2.*gamma1*(1.)+alpha1*n1*(n1-1.)*
& ((u(1)+u(2)+u(3)+R1)**(n1-2.))*1.)
dF1d3=-lambda1*((1./3.)*(-1.)-2.*gamma1*(1.)+alpha1*n1*(n1-1.)*
& ((u(1)+u(2)+u(3)+R1)**(n1-2.))*1.)
dF1dlm=-((1./3.)*(2*u(1)-u(2)-u(3))-2.*gamma1*(u(1)+u(2)+u(3)+
& R1)+alpha1*n1*((u(1)+u(2)+u(3)+R1)**(n1-1.)))
C
dF2d2=-1.-lambda1*((1./3.)*(2.)-2.*gamma1*(1.)+alpha1*n1*
& (n1-1.)*((u(1)+u(2)+u(3)+R1)**(n1-2.))*1.)
dF2d1=-lambda1*((1./3.)*(-1.)-2.*gamma1*(1.)+alpha1*n1*(n1-1.)*
& ((u(1)+u(2)+u(3)+R1)**(n1-2.))*1.)
dF2d3=-lambda1*((1./3.)*(-1.)-2.*gamma1*(1.)+alpha1*n1*(n1-1.)*
& ((u(1)+u(2)+u(3)+R1)**(n1-2.))*1.)
dF2dlm=-((1./3.)*(2.*u(2)-u(1)-u(3))-2.*gamma1*(u(1)+u(2)+u(3)+
& R1)+alpha1*n1*((u(1)+u(2)+u(3)+R1)**(n1-1.)))
C
dF3d3=-1.-lambda1*((1./3.)*(2.)-2.*gamma1*(1.)+alpha1*n1*
& (n1-1.)*((u(1)+u(2)+u(3)+R1)**(n1-2.))*1.)
dF3d2=-lambda1*((1./3.)*(-1.)-2.*gamma1*(1.)+alpha1*n1*(n1-1.)*
& ((u(1)+u(2)+u(3)+R1)**(n1-2.))*1.)
dF3d1=-lambda1*((1./3.)*(-1.)-2.*gamma1*(1.)+alpha1*n1*(n1-1.)*
& ((u(1)+u(2)+u(3)+R1)**(n1-2.))*1.)
dF3dlm=-((1./3.)*(2.*u(3)-u(2)-u(1))-2.*gamma1*(u(1)+u(2)+u(3)+
$ R1)+alpha1*n1*((u(1)+u(2)+u(3)+R1)**(n1-1.)))
C
dF4d1=((1./3.)*(2.*u(1)-u(2)-u(3))-2.*gamma1*(u(1)+u(2)+u(3)+R1)+
& alpha1*n1*((u(1)+u(2)+u(3)+R1)**(n1-1.)))
dF4d2=((1./3.)*(2.*u(2)-u(1)-u(3))-2.*gamma1*(u(1)+u(2)+u(3)+R1)+
& alpha1*n1*((u(1)+u(2)+u(3)+R1)**(n1-1.)))
dF4d3=((1./3.)*(2.*u(3)-u(2)-u(1))-2.*gamma1*(u(1)+u(2)+u(3)+R1)+
& alpha1*n1*((u(1)+u(2)+u(3)+R1)**(n1-1.)))
dF4dlm=0.
C
vct1store=-F1+dF1d1*u(1)+dF1d2*u(2)+dF1d3*u(3)+dF1dlm*lambda1
vct2store=-F2+dF2d1*u(1)+dF2d2*u(2)+dF2d3*u(3)+dF2dlm*lambda1
vct3store=-F3+dF3d1*u(1)+dF3d2*u(2)+dF3d3*u(3)+dF3dlm*lambda1
vct4store=-F4+dF4d1*u(1)+dF4d2*u(2)+dF4d3*u(3)+dF4dlm*lambda1
C
vct1=vct4store
vct2=vct1store
vct3=vct2store
vct4=vct3store

```

```

C
dF1d1store=dF1d1
dF1d2store=dF1d2
dF1d3store=dF1d3
dF1dlmstore=dF1dlm
C
dF2d1store=dF2d1
dF2d2store=dF2d2
dF2d3store=dF2d3
dF2dlmstore=dF2dlm
C
dF3d1store=dF3d1
dF3d2store=dF3d2
dF3d3store=dF3d3
dF3dlmstore=dF3dlm
C
dF4d1store=dF4d1
dF4d2store=dF4d2
dF4d3store=dF4d3
dF4dlmstore=dF4dlm
C
dF1d1=dF4d1store
dF1d2=dF4dlmstore
dF1d3=dF4d2store
dF1dlm=dF4d3store
C
dF2d1=dF1d1store
dF2d2=dF1dlmstore
dF2d3=dF1d2store
dF2dlm=dF1d3store
C
dF3d1=dF2d1store
dF3d2=dF2dlmstore
dF3d3=dF2d2store
dF3dlm=dF2d3store
C
dF4d1=dF3d1store
dF4d2=dF3dlmstore
dF4d3=dF3d2store
dF4dlm=dF3d3store
C
C   begin Gauss-Jordan Elminiation
C
C   normalize first row
dF1d1store=dF1d1
dF1d1=1.

```

$dF1d2 = dF1d2 / dF1d1 \text{store}$   
 $dF1d3 = dF1d3 / dF1d1 \text{store}$   
 $dF1dlm = dF1dlm / dF1d1 \text{store}$   
 $vct1 = vct1 / dF1d1 \text{store}$

C

C

column1  
 $dF4d1 \text{store} = dF4d1$   
 $dF4d1 = 0.$   
 $dF4d2 = dF4d2 - dF1d2 * dF4d1 \text{store}$   
 $dF4d3 = dF4d3 - dF1d3 * dF4d1 \text{store}$   
 $dF4dlm = dF4dlm - dF1dlm * dF4d1 \text{store}$   
 $vct4 = vct4 - vct1 * dF4d1 \text{store}$

C

$dF3d1 \text{store} = dF3d1$   
 $dF3d1 = 0.$   
 $dF3d2 = dF3d2 - dF1d2 * dF3d1 \text{store}$   
 $dF3d3 = dF3d3 - dF1d3 * dF3d1 \text{store}$   
 $dF3dlm = dF3dlm - dF1dlm * dF3d1 \text{store}$   
 $vct3 = vct3 - vct1 * dF3d1 \text{store}$

C

$dF2d1 \text{store} = dF2d1$   
 $dF2d1 = 0.$   
 $dF2d2 = dF2d2 - dF1d2 * dF2d1 \text{store}$   
 $dF2d3 = dF2d3 - dF1d3 * dF2d1 \text{store}$   
 $dF2dlm = dF2dlm - dF1dlm * dF2d1 \text{store}$   
 $vct2 = vct2 - vct1 * dF2d1 \text{store}$

C

C

normalize second row  
 $dF2d2 \text{store} = dF2d2$   
 $dF2d1 = dF2d1 / dF2d2 \text{store}$   
 $dF2d2 = 1.$   
 $dF2d3 = dF2d3 / dF2d2 \text{store}$   
 $dF2dlm = dF2dlm / dF2d2 \text{store}$   
 $vct2 = vct2 / dF2d2 \text{store}$

C

C

column2  
 $dF4d2 \text{store} = dF4d2$   
 $dF4d2 = 0.$   
 $dF4d3 = dF4d3 - dF2d3 * dF4d2 \text{store}$   
 $dF4dlm = dF4dlm - dF2dlm * dF4d2 \text{store}$   
 $vct4 = vct4 - vct2 * dF4d2 \text{store}$

C

$dF3d2 \text{store} = dF3d2$   
 $dF3d2 = 0.$   
 $dF3d3 = dF3d3 - dF2d3 * dF3d2 \text{store}$   
 $dF3dlm = dF3dlm - dF2dlm * dF3d2 \text{store}$

```

vct3=vct3-vct2*dF3d2store
C
C   normalize third row
dF3d3store=dF3d3
dF3d1=dF3d1/dF3d3store
dF3d2=dF3d2/dF3d3store
dF3d3=1.
dF3dlm=dF3dlm/dF3d3store
vct3=vct3/dF3d3store
C
C   column3
dF4d3store=dF4d3
dF4d3=0.
dF4dlm=dF4dlm-dF3dlm*dF4d3store
vct4=vct4-vct3*dF4d3store
C
C   solveforallnewstuff
unew(3)=vct4/dF4dlm
unew(2)=(vct3-dF3dlm*unew(3))/dF3d3
lambda1=(vct2-dF2dlm*unew(3)-dF2d3*unew(2))/dF2d2
unew(1)=(vct1-dF1dlm*unew(3)-dF1d3*unew(2)-dF1d2*lambda1)/dF1d1
c
IF (unew(1)<-R1/3. .OR. unew(1)>surfintercept1) THEN
  u(1)=0
  u(2)=0.
  u(3)=0.
  FLAG=1
  EXIT
END IF
IF (unew(2)<-R1/3. .OR. unew(2)>surfintercept1) THEN
  u(1)=0
  u(2)=0.
  u(3)=0.
  FLAG=1
  EXIT
END IF
IF (unew(3)<-R1/3. .OR. unew(3)>surfintercept1) THEN
  u(1)=0
  u(2)=0.
  u(3)=0.
  FLAG=1
  EXIT
END IF

IF (unew(1)+unew(2)+unew(3)+R1<0.) THEN
  u(1)=0.

```

```

    u(2)=0.
    u(3)=0.
    FLAG=1
    EXIT
ELSE
    u(1)=unew(1) !0.
    u(2)=unew(2) !0.
    u(3)=unew(3) !0.
END IF
C   Verify error with tolerance
magnew=SQRT(u(1)**2.+u(2)**2.+u(3)**2.)
errnew=ABS(magold-magnew)/magnew
IF (errnew <=0.01) THEN
C   test=1
    EXIT
ELSE
    !IF (errnew>errold) THEN
    ! countconver=countconver+1
    !ENDIF
    !IF (countconver >=10) THEN
    ! !FLAG=1
    ! !EXIT
    !END IF
END IF
magold=magnew
errold=errnew
c
END IF
END DO
IF (i>imax) THEN
    stressHiSS(1)=0.
    stressHiSS(2)=0.
    stressHiSS(3)=0.
    dFds(1)=0.
    dFds(2)=0.
    dFds(3)=0.
ELSE
    stressHiSS(1)=u(1)
    stressHiSS(2)=u(2)
    stressHiSS(3)=u(3)
    IF (FLAG==0) THEN
        dFds(1)=(((1./3.)*(2.*u(1)-u(2)-u(3))-2.*gamma1*(u(1)+u(2)+u(3)+
&      R1)+alpha1*n1*((u(1)+u(2)+u(3)+R1)**(n1-1.))))
        dFds(2)=(((1./3.)*(2.*u(2)-u(1)-u(3))-2.*gamma1*(u(1)+u(2)+u(3)+
&      R1)+alpha1*n1*((u(1)+u(2)+u(3)+R1)**(n1-1.))))
        dFds(3)=(((1./3.)*(2.*u(3)-u(2)-u(1))-2.*gamma1*(u(1)+u(2)+u(3)+

```

```

&      R1)+alpha1*n1*((u(1)+u(2)+u(3)+R1)**(n1-1.)))
      ELSE
        dFds(1)=0.
        dFds(2)=0.
        dFds(3)=0.
      END IF
C
      END IF
      RETURN
      END
C
C
C
      SUBROUTINE princord(pps,psor)
c
c  pps - principal stress obtain from ABAQUS subroutine sprind
c  psor - ordered principal p33>>p22>>p11
c
      INCLUDE 'aba_param.inc'
      REAL*8 pps(3),psor(3)
c
c the principal values ps(3) are not ordered;
c now they are ordered to psor(3)>psor(2)>psor(1), being compression (-).
c
      imax=1
      smax=pps(1)
      DO i=2,3
        IF (pps(i)>=smax) THEN
          imax=i
          smax=pps(i)
        END IF
      END DO
c
      psor(3)=pps(imax)
c
      IF (imax==1) THEN
        i2=2
        i3=3
      ELSEIF (imax==2) THEN
        i2=1
        i3=3
      ELSE
        i2=1
        i3=2
      END IF
c

```

```
med=i2
min=i3
IF (pps(i3)>pps(i2)) THEN
  i3= med
  i2= min
END IF
c
psor(2)=pps(i2)
psor(1)=pps(i3)
c
RETURN
END
C
C
C
```

## Appendix B. Elasto-Viscoplastic UMAT

### Description of subroutines

Subroutine name	Description
UMAT	Main subroutine called from ABAQUS input file. It is related to the material selection in the input file.
newperpHiSS	This function takes the HiSS surface definition parameters and the stress point to create a normal line from the Hydrostatic line to the stress point. It also finds the line intersection point on the HiSS surface, assuming the two solutions for the points on this line to be a quadratic relation. Adapted from Gibson (2006) for this UMAT.
dHiss	This function computes the normal vector $dFds$ on the HiSS surface using the surface parameters and the applied stress point. Adapted from Gibson (2006) for this UMAT.
Gethydrpntext	This function computes the intersection between the line passing by the applied stress, the HiSS stress points and the Hydrostatic line. Adapted from Gibson (2006) for this UMAT.
HNR	This function applies a Newton-Raphson algorithm to find a point on the Hiss surface that is normal to the applied stress point (Gibson, 2006).
Kbacktr	This subroutine is used to transform the 4th order tensor in the local coordinate system (in the principal axes) back into a 4th order tensor in the global coordinate system (global) (Hinterhoelzl, 1999).
Kprind	This subroutine is used to order the principal stress/strain tensor if the form of $e_{33p} > e_{22p} > e_{11p}$ . This will comply with the requirement of symmetry of the transverse isotropy. Accordingly the array of the cosines is also changed to $cs(3,3)$ .
Unitvector	This function computes the unit vector of a given vector.

C U M A T

C

C ABAQUS USER MATERIAL MODEL FOR Elasto-ViscoPlasticity

C Linear Elastic Theory and VP based on Perzyna-HiSS

C

C WRITTEN BY REGIS L. CARVALHO, with components adapted from

C Gibson (2006)

C

C 2008-2011

C

C FILENAME: evphiss8a\_SBS.for

c

c INTRODUCTION

c

c 3-dimensional formulation with adaptation for plane strain problems

c

c Assumptions: small strains

c       small rotations of the principal axes of strain

c

c Material Data:

c It is chosen to define all the material parameters like prony series, damage

C functions and viscoplastic model.

C Internal State Variables are defined as follows:

c   - Viscoplastic strain components: statev(l), with l = 1 to 6

c   - HiSS surface stress: statev(k), with k = 7 to 9

c   - HiSS normals: statev(j), with j = 10 to 12

c

c E used in the umat is in [kPa]. So the geometry has to be defined in

c mm and all the loading in [kN] for forces and [mm] for displacement.

c

c Temperature:

c The influence of the temperature on the time dependent behavior is modelled

c by making use of the time-temperature-superposition-principle (TTSP) for

c thermorheological simple materials.

c The implementation is done for the definition of the shift factor aT and used

c to compute the reduced time increment dtau.

c

c

c The umat is programmed for a nonlinear viscoelastic boundary value problem.

c No correspondence principle is used. Nevertheless pseudostrains are defined.

c

c Principal axis of the strain 3 is axis of transverse isotropy

c

c The programming will make use of vector and matrix formulations for stress,

c strain and jacobian instead of tensor formulation.

```

c
c The user must provide the calculation of (Variables of Abaqus):
c
c   ddsdde(ntens,ntens)(Jakobian-Matrix of the constitutive model)
c   stress(ntens)   (Cauchy stress tensor)
c   statev(nstatv)  (array containing the solution dep. *DEPVAR)
c
c   and if necessary the calculation of:
c
c   sse   (specific elastic strain energy)
c   spd   (plastic dissipation)
c   scd   (creep-dissipation)
c
c Abaqus provides the following variables:
c
c   stran(ntens) (array of the total strain components without the thermal
c               strains)
c   dstran(ntens) (array of strain increments without thermal strain incr.)
c   time(1)      (value of step time at the beginning of the current incr.)
c   time(2)      (value of the total time at the begin. of the curr. incr.)
c   dtime        (time increment)
c   temp         (temperature at the start of the increment)
c   dtemp        (increment of temperature)
c   predef       (array of predefined field variables)
c   dpred        (array of incr. of the predefined field variables)
c   cmname       (name given on *MATERIAL)
c   ndi          (number of direct stress components)
c   nshr         (number of engineering shear stress components)
c   ntens        ndi+nshr
c   nstatv       (number of solution dependent state variables)
c   props        (array of material constants)
c   nprops(nprops)(number of material constants)
c   coords(3)    (coordinates of this point)
c   drot(3,3)    (rotation increment matrix)
c   celent       (characteristic element length)
c   dfgrdo(3,3) (deformation gradient at the beginning of the incr.)
c   dfgrd1(3,3) (deformation gradient at the end of the incr.)
c   noel         (elementnumber)
c   npt          (integration point number)
c   layer        (composite layer number)
c   kspt         (sectionpoint number within the current layer)
c   kstep        (step number)
c   kinc         (increment number)
c
C

```

## C 1. Declaration of variables provided by ABAQUS

```

C  UMAT subroutine header
C
SUBROUTINE UMAT(STRESS,STATEV,DDSDDE,SSE,SPD,SCD,
1 RPL,DDSDDT,DRPLDE,DRPLDT,
2 STRAN,DSTRAN,TIME,DTIME,TEMP,DTEMP,PREDEF,DPRED,CMNAME,
3 NDI,NSHR,NTENS,NSTATV,PROPS,NPROPS,COORDS,DROT,PNEWDT,
4 CELENT,DFGRD0,DFGRD1,NOEL,NPT,LAYER,KSPT,KSTEP,KINC)
C
INCLUDE 'ABA_PARAM.INC'
C
CHARACTER*80 CMNAME
DIMENSION STRESS(NTENS),STATEV(NSTATV),
1 DDSDDE(NTENS,NTENS),
2 DDSDDT(NTENS),DRPLDE(NTENS),
3 STRAN(NTENS),DSTRAN(NTENS),TIME(2),PREDEF(1),DPRED(1),
4 PROPS(NPROPS),COORDS(3),DROT(3,3),DFGRD0(3,3),DFGRD1(3,3)
C
C 2. Declaration of local variables
C
C 2.1. Definition of variables required for the elastic component
C
C mu, lambda - elastic properties, lamé constants
C
REAL*8 mu,lambda2
C
C 2.2. Definition of variables required for the VP subroutine
C
C gamma, alpha, n, R, alpha0, R0, kappa, m, expo, tau, NN - parameters HiSS surface
C xi - volumetric viscoplastic strains
C ps - vector of applied principal stresses, fixsig11, fixsig22, fixsig33
C surfstress - stress vector of HiSS surface point
C dFdsigma - vector of derivatives of F with respect to sigma
C Dist = (F/F'0) - 1
C HiSScentpoints - vector of points on surface at convergence
C centnorm - normal vector on the center point of convergence
C intestJstress - Second invariant (J2d) of deviatoric stress tensor
C intestIstress - First invariant (I1) of stress tensor
C intestJsurf - J2d corresponding to I1 on the Hiss Surface
C surfintercept - point where the HiSS surface intercepts the Hydrostatic line
C perpiii - volumetric stress or pressure = (sigma1 + sigma2 + sigma3)/3
C hydrline - point where the line normal to HiSS intercept on the Hydrostatic line
C DistA - distance from HiSS surface point and applied stress
C DistB - distance form Hydrostatic line and HiSS surface point
C devpdt - viscoplastic strain rate
C evp - viscoplastic principal strains corresponding to stress increment i
C psOLD - previous applied principal stress

```

C surfstressOLD - previous HiSS surface stress  
C dfdsigmeOLD - previous normals to HiSS surface  
C an - matrix of direction cosines for stress  
C evpt - viscoplastic strain tensor corresponding to stress increment i  
C ane - matrix of direction cosines for viscoplastic strain  
C stressNEW - new stress tensor (increment i+1)  
C stressOLD - current stress tensor (increment i)  
C destran - matrix of six components of elastic strain  
C vetor - auxiliar vector of principal values (vetor(3))  
C cs(3,3) - new cosine matrix from the transformation of principal stresses  
C sit, slopetangent,slopenormal,anglenormal,angleline,anglecheck - auxiliary  
C variables to define the normal-free zone  
C  
REAL\*8 ps(3),surfstress(3),dFdsigma(3),  
& HiSScentpoints(3),centnorm(3),devpdt(3),evp(3),  
& psOLD(3),surfstressOLD(3),dfdsigmaOLD(3),an(3,3),evpt(6),  
& ane(3,3),stressNEW(NTENS),stressOLD(NTENS),destran(NTENS),  
& vetor(3),cs(3,3)  
C  
REAL\*8 alpha0,gamma,R0,n,kappa,m,expo,tau,NN,k3,xi,alpha,R,  
& Dist,intestJstress,intestIstress,intestJsurf,surfintercept,  
& perpiii,  
& hydrline,  
& DistA,DistB,lambda,A,tempshift,sit,slopetangent,  
& slopenormal,anglenormal,angleline,anglecheck  
C  
C  
C 3. Material properties and variable initialization  
C  
C 3.1. Elastic properties  
C  
mu=759973./(2.\*(1+.35)) !Equivalent to 0.018 Hz ~28.6 kph  
lambda2=(.35\*759973.)/((1+.35)\*(1-.2\*.35))  
C  
C E=365836 (for 64°C), 759973 (for 45°C) and 1087552 (for 39°C)  
C lambda=65172.41  
c  
C 3.2. Viscoplastic properties  
c  
alpha0=0.0068  
gamma=0.0428  
R0=38.4245  
n=2.2564  
kappa=-68.096  
m=3227.4  
expo=0.3306

```

tau=-8.7801
NN=1.076
k3=2.5782
c
c Temperature Shift Factor
c
tempshift=0.000466
c
c tempshift=0.002615 for 39°C - lab test at UMD
c tempshift=0.000466 for 45°C
c tempshift=0.00000193 for 64°C
c
C 3.3. Initialization of STATEV in case it is first increment
C
C The first 12 internal state variables are used in the VP model, as described
C below. variable 13 stores the damage variable, S, of the VECD model and the
C remaining 6*nE variables are auxiliaries in the pseudo strain calculations.
C
C If the first step and increment, assume xi=0,otherwise
C xi=statev(1)+statev(2)+statev(3)
c print *, kstep, kinc
IF (kstep==1 .AND. kinc==1) THEN
C first six are VP strains, 11,22,33,12,13,23
STATEV(1)=0.
STATEV(2)=0.
STATEV(3)=0.
STATEV(4)=0.
STATEV(5)=0.
STATEV(6)=0.
C next three are HiSS surface stress in principal domain
STATEV(7)=0.
STATEV(8)=0.
STATEV(9)=0.
C last three are HiSS normals (dF/dsigma) in principal domain
STATEV(10)=0.
STATEV(11)=0.
STATEV(12)=0.
END IF
c
c Read S from the statev(13) provided by Abaqus
c if you want to start the calculations with from zero different initial value
c for S, you have to change the value for Safter the two "if" commands
c
S = statev(13)
IF (kstep==1) THEN
IF (kinc==1) THEN

```

```

S=0.d0
END IF
END IF

```

- c If you want to run calculations without damage, means just linear visco-
- c elastic calculations, you have to remove the "c" in front of the next
- c line to set them effective and set S=0.d0 for every iteration.

```
S=0.d0
```

c

### C 3.4. Initialization of vectors and matrices

C

```

DO I=1,3
  vetor(I)=0.
  psOLD(I)=0.
  ps(I)=0.
  DO J=1,3
    an(I,J)=0.
    cs(I,J)=0.
    ane(I,J)=0.
  END DO
END DO

```

c

C

### C 4. Elastic Calculations

C

#### C 4.1. Initialize Jacobian matrix and stressOLD=STRESS

C

```

DO I=1,NTENS
  stressOLD(I)=STRESS(I)
  DO J=1,NTENS
    ddsdde(I,J)=0.
  END DO
END DO

```

C

#### C 4.2. Compute jacobian

C

```

DO I=1,NDI
  DO J=1,NDI
    DDSDDDE(I,J)=lambda2
  END DO
  DDSDDDE(I,I)=lambda2+2*mu
END DO
DO I=NDI+1,NTENS
  DDSDDDE(I,I)=mu
END DO

```

C

### c 5. ViscoPlastic Calculations

```

c
C 5.1. Compute principal stresses
C
C   Store current stress (before VP calculations) as stressOLD=STRESS
C
C   DO I=1,NTENS
C     stressOLD(I)=STRESS(I)
C   END DO
C
C   Transform the old stress tensor into principal stresses vetor(3)
C
C   CALL SPRIND(stressOLD,vetor,an,1,NDI,NSHR)
C
C   Put the principal old stresses in order 33>22>11. This is done so when
C   the sign is changed, (-) compression becomes (+) and 11>22>33.
C
C   CALL princord(vetor,psOLD)
C
C   psOLD comes in normal ABAQUS notation compression (-). The following 3
C   lines changes the sign of the principal values, making compression (+)
C   and shifting the order to 11>>22>>33 as required by VP model.
C
C 5.5. Store old stress, surfstress and dFdsigma
C
C   The stress comes from ABAQUS STRESS variable; surfstress from STATEV(7 to
C   9)
C   and dFdsigma from STATEV(10 to 12).
C
C   psOLD(1)=-psOLD(1)
C   psOLD(2)=-psOLD(2)
C   psOLD(3)=-psOLD(3)
C   surfstressOLD(1)=STATEV(7)
C   surfstressOLD(2)=STATEV(8)
C   surfstressOLD(3)=STATEV(9)
C   dfdsigmaOLD(1)=STATEV(10)
C   dfdsigmaOLD(2)=STATEV(11)
C   dfdsigmaOLD(3)=STATEV(12)
C
C 5.6. Compute new stress for current strain increment
C
C   DO I=1,NTENS
C     stressNEW(I)=STRESS(I)
C     DO J=1,NTENS
C       stressNEW(I)= stressNEW(I)+DDSDDE(I,J)*DSTRAN(J)
C     END DO
C   END DO

```

```

C
C Transform the new stress tensor into principal stresses vector
C
CALL SPRIND(stressNEW,vetor,an,1,NDI,NSHR)
C
C Put the principal new stresses in order 33>22>11. This is done so when
C the sign is changed, (-) compression becomes (+) and 11>22>33. The
C subroutine also change the cosine matrix to accomodate the new order.
C The new matrix will be called cs(3,3).
C
CALL kprind(vetor,an,cs,ps)
C
C 5.7. Compute viscoplastic strains
C
DO I=1,6
  evpt(I)=STATEV(I)
END DO
CALL SPRIND(evpt,evp,ane,2,NDI,NSHR)
xi=SQRT((evp(1)**2.)+(evp(2)**2.)+(evp(3)**2.))
C
C The VP model was formulated with compression (+), different from ABAQUS
C conventional compression (-). The following three lines change signs of
C principal stresses without changing directions. After the calculations
C are done, the viscoplastic strain signs are changed back to conventional
C notation of compression (-).
ps(1)=-ps(1)
ps(2)=-ps(2)
ps(3)=-ps(3)
c
C Compute initial parameters alpha(xi) and R(xi)
alpha=alpha0*EXP(xi*kappa)
R=R0+m*(xi**expo)
C
C Verify if the point perpendicular to the the stress point is either to the
C left or to the right of the intersection of the HiSS surface and the
C Hydrostatic line.
intestIstress=ps(1)+ps(2)+ps(3)
surfintercept=(1./3.)*(((alpha/gamma)**(1./(2.-n)))-R)
perpIII=intestIstress/3.
C
IF (ps(1)==ps(2) .AND. ps(2)==ps(3)) THEN !Point on Hydrostatic
  IF (ps(1)==0.) THEN
    DO i=1,3
      surfstress(i)=0.
      dFdsigma(i)=0.
    END DO
  
```

```

    Dist = 0.
    A = 1.
ELSEIF (ps(1)<=surfintercept) THEN
    DO i=1,3
        surfstress(i)=0.
        dFdsigma(i)=0.
    END DO
    Dist = 0.
    A = 1.
ELSE
    DO i=1,3
        surfstress(i)=surfintercept
        dFdsigma(i)=0. !Initialize dFdsigma for subroutine below
    END DO
    intestJstress = (1./3.)*(ps(1)**2+ps(2)**2+ps(3)**2-
&                ps(1)*ps(2)-ps(2)*ps(3)-ps(1)*ps(3))
    CALL dHiSS(gamma, alpha, n, R, surfstress,dFdsigma)
    IF (intestJstress<=0.) THEN
        A = 0.
        Dist = 0.
    ELSE
        A=(ABS(ATAN(SQRT(intestJstress)/intestJstress)/0.528))**k3
        Dist = ((SQRT(3.*(ps(1)-surfintercept)**2)
&                +surfintercept*SQRT(3.)))/
&                (surfintercept*SQRT(3.))-1.
    END IF
C
    END IF
C
ELSE !Point not on Hydrostatic
C    Verify if point is outside the HiSS surface
    intestJstress = (1./3.)*(ps(1)**2+ps(2)**2+ps(3)**2-
&                ps(1)*ps(2)-ps(2)*ps(3)-ps(1)*ps(3))
    IF (intestJstress<-R) THEN !Prevent tension-dominant areas
        intestJsurf = -9999
    ELSE
        intestJsurf = gamma*((intestJstress+R)**2)
&                -alpha*((intestJstress+R)**n)
    END IF
    IF (intestJstress<=3.*surfintercept .AND.
&    intestJstress<=intestJsurf) THEN
        DO i=1,3
            surfstress(i)=0.
            dFdsigma(i)=0.
        END DO
        Dist = 0.

```

```

A = 1.0
C
ELSE !Outside surface -> VP Flow
C
!Verify is the point is located in normal free zone
!Compute tangent to the intercept point in the  $J2D^{(1/2)} \times I1$  space
!at the tension side
c
!surface intercept at tension side
sit=-R+1.*10.**(-10.)
!slope of the tangent to the surface intercept in tension
slopetangent=(gamma*(2.*R+2.*sit)-alpha*n*(R+sit)**(n-1.))/
&      (2.*(gamma*(R+sit)**2-alpha*(R+sit)**n)**(1./2.))
!slope of the normal to the surface intercept in tension
slopenormal=TAN(ATAN(slopetangent)+3.1415927/2.)
!angle of the normal
IF (ATAN(slopenormal)>0) THEN
    anglenormal=ATAN(slopenormal)
ELSE
    anglenormal=3.1415927-ABS(ATAN(slopenormal))
END IF
!angle line between surface intercept in tension and stress point
angleline=ATAN(((intestIstress)**(1./2.))/(intestIstress+R))
c
IF (angleline>0) THEN
    anglecheck=angleline
ELSE
    anglecheck=3.1415927-ABS(angleline)
END IF
c
IF (anglecheck>=anglenormal) THEN
    !inside normal free zone - Supress VP Flow
    A=0.
    Dist=0.
ELSE
    !Outside normal free zone -> VP Flow
C
    Search for the stress point on HiSS surface normal to the
C
    the surface and on the direction of the applied stress point.
C
C
IF (STATEV(7)+STATEV(8)+STATEV(9)==0.) THEN
C
    lambda=1.
    surfstressOLD(1)=perpii
    surfstressOLD(2)=perpii
    surfstressOLD(3)=perpii

```

```

C
& IF (surfstressOLD(1)+surfstressOLD(2)+surfstressOLD(3)
& +R>0.) THEN
& CALL HNR(ps,surfstressOLD,lambda,gamma,alpha,n,R,
& HiSScentpoints,centnorm)
ELSE
HiSScentpoints(1)=0.
HiSScentpoints(2)=0.
HiSScentpoints(3)=0.
centnorm(1)=0.
centnorm(2)=0.
centnorm(3)=0.
END IF

C
ELSE
lambda=(((psOLD(1)-surfstressOLD(1))**2+
& (psOLD(2)-surfstressOLD(2))**2+
& (psOLD(3)-surfstressOLD(3))**2)**0.5)/
& ((dfdsigmaOLD(1)**2+dfdsigmaOLD(2)**2+
& dfdsigmaOLD(3)**2)**0.5)

C
IF (surfstressOLD(1)+surfstressOLD(2)+surfstressOLD(3)
& +R>0.) THEN
& CALL HNR(ps,surfstressOLD,lambda,gamma,alpha,n,R,
& HiSScentpoints,centnorm)
ELSE
HiSScentpoints(1)=0.
HiSScentpoints(2)=0.
HiSScentpoints(3)=0.
centnorm(1)=0.
centnorm(2)=0.
centnorm(3)=0.
END IF
END IF

C
C Patch to avoid complex number. My original formulation HiSScentpoints(1)=-
R/3.
C Below is a new try
IF (HiSScentpoints(1)==HiSScentpoints(2) .AND.
& HiSScentpoints(2)==HiSScentpoints(3) .AND.
& HiSScentpoints(1)==0.) THEN
A=0.
Dist=0.
ELSE
CALL gethydrpntext(ps, HiSScentpoints,hydrline)
DistA=SQRT((HiSScentpoints(1)-ps(1))**2.+

```

```

&          (HiSScentpoints(2)-ps(2))**2.+
&          (HiSScentpoints(3)-ps(3))**2.)
DistB=SQRT((HiSScentpoints(1)-hydrline)**2.+
&          (HiSScentpoints(2)-hydrline)**2.+
&          (HiSScentpoints(3)-hydrline)**2.)
C
IF (DistB>surfintercept*SQRT(3.)) THEN
  DistB=surfintercept*SQRT(3.)
END IF
Dist=ABS(((DistA+DistB)/DistB)-1.)
IF (intestJstress<=0.) THEN
  A = 0.
ELSE
  A=(ABS(ATAN(SQRT(intestJstress)/intestIstress)
&    /0.528))**k3
END IF
END IF
C
C   Outputs
C
DO k=1,3
  surfstress(k)=HiSScentpoints(k)
  dFdsigma(k)=centnorm(k)
END DO
END IF
END IF
END IF
C
C   The result from surfHiSS function are: stress vector at the HiSS surface,
C   surfstress(k), the normal vector to the surface on the direction of the
C   applied stress (strain trajectory), dFdsigma(k), and the relative distance
C   from the applied stress to the hydrostatic plane, Dist. With these parameters
C   is possible now to compute the principal viscoplastic strain rates, devpdt(k),
C   and incremental viscoplastic strains, evp(k).
C
DO k=1,3
  devpdt(k)=(10.**tau)*A*(Dist**NN)*dFdsigma(k)
  evp(k)=-devpdt(k)*(dtime)*(1./tempshift)
C   The negative sign is to transform back into compression (-)
END DO
C
C   After the incremental viscoplastic strains are computed in principal plane, it is
C   necessary to bring back the original orientation. In this verification test it is assumed
C   the vertical and horizontal strains corresponds respectively to major and minor and
mid
C   strains.

```

```

C
C   normal vp strains
evpt(1)=evp(1)*cs(1,1)**2.+evp(2)*cs(2,1)**2.+
&   evp(3)*cs(3,1)**2.
evpt(2)=evp(1)*cs(1,2)**2.+evp(2)*cs(2,2)**2.+
&   evp(3)*cs(3,2)**2.
evpt(3)=evp(1)*cs(1,3)**2.+evp(2)*cs(2,3)**2.+
&   evp(3)*cs(3,3)**2.
C
C   shear vp strains
evpt(4)=evp(1)*cs(1,1)*cs(1,2)+evp(2)*cs(2,1)*cs(2,2)+
&   evp(3)*cs(3,1)*cs(3,2)
evpt(5)=evp(1)*cs(1,1)*cs(1,3)+evp(2)*cs(2,1)*cs(2,3)+
&   evp(3)*cs(3,1)*cs(3,3)
evpt(6)=evp(1)*cs(1,2)*cs(1,3)+evp(2)*cs(2,2)*cs(2,3)+
&   evp(3)*cs(3,2)*cs(3,3)
C
C 5.8. Update state variables (1-6)vpstrains, (7-9)HiSS surface stress, and
C (10-12) dFdsigma
C
STATEEV(1)=STATEEV(1)+evpt(1)
STATEEV(2)=STATEEV(2)+evpt(2)
STATEEV(3)=STATEEV(3)+evpt(3)
STATEEV(4)=STATEEV(4)+evpt(4)
STATEEV(5)=STATEEV(5)+evpt(5)
STATEEV(6)=STATEEV(6)+evpt(6)
STATEEV(7)=surfstress(1)
STATEEV(8)=surfstress(2)
STATEEV(9)=surfstress(3)
STATEEV(10)=dFdsigma(1)
STATEEV(11)=dFdsigma(2)
STATEEV(12)=dFdsigma(3)
C
C 5.9. Update Stress
C
C   For infinitesimal analysis (specimen in the lab), stresses are updated
C   without corrections to the elastic strain. The following lines apply
C
C   DO k=1,ntens
C     STRESS(k)=stressNEW(k)
C   END DO
C
C   Otherwise the following lines must be active. Remove C's from the lines
C   below and put C's on the lines above to activate the viscoplastic
C   adjustments of the elastic strains
C

```

```

C   Compute the recoverable strain increments
C
  DO k=1,ntens
    destran(k)=DSTRAN(k)-evpt(k)
  END DO
C
C   Compute adjusted stress
  DO I=1,ntens
    DO J=1,ntens
      STRESS(I)= STRESS(I)+DDSDDE(I,J)*destran(J)
    END DO
  END DO
C
C
C 6.0 Return back to ABAQUS
C
  RETURN
  END
c
c
c
c 7. Subroutines
c
c=====
=====
  SUBROUTINE kbacktr(C,T,DIR,N)
c=====
=====
c Developed by R. Hinterhoelzl (1999)
c
c Transform the 4th order tensor in the local coordinate system (in the
c principal axes) back into a 4th order tensor in the global coordinate
c system (global).
c
c   C(N,N): Jacobian in the local coordinate system of the principal axes
c   T(N,N): Jacobian in the global (original) coordinate system
c   DIR(I,J): DIRECTION COSINE BETWEEN Xi'(PRIN.) TO Xj (GLOBAL).
c   N: Number of stresses (4 - axisymmetric and plane strain problems
c       6 - full 3D problems)
c       OBSERVATION: Not coded for plane stress problems
c
c   stress(1)=stress(1,1)   strain(1)=strain(1,1)
c   stress(2)=stress(2,2)   strain(2)=strain(2,2)
c   stress(3)=stress(3,3)   strain(3)=strain(3,3)
c   stress(4)=stress(1,2)   strain(4)=strain(1,2)
c   stress(5)=stress(1,3)   strain(5)=strain(1,3)

```

```

c stress(6)=stress(2,3) strain(6)=strain(2,3)
c
c
c INCLUDE 'aba_param.inc'
c REAL*8 DIR(3,3)
c REAL*8 T(N,N),C(N,N),C0(3,3,3,3)
c
c 1) find the 4th order tensor C0(3,3,3,3) in the local coordinate system
c from the 6x6 matrix C(NTENS,NTENS)
c
c DO I=1,3
c DO J=1,3
c DO K=1,3
c DO L=1,3
c C0(I,J,K,L)=0.d0
c END DO
c END DO
c END DO
c
c IF (N==4) THEN
c
c C0(1,1,1,1)=C(1,1)
c C0(1,1,2,2)=C(1,2)
c C0(1,1,3,3)=C(1,3)
c C0(2,2,1,1)=C(2,1)
c C0(2,2,2,2)=C(2,2)
c C0(2,2,3,3)=C(2,3)
c C0(3,3,1,1)=C(3,1)
c C0(3,3,2,2)=C(3,2)
c C0(3,3,3,3)=C(3,3)
c
c C
c C0(1,2,1,2)=C(4,4)
c C0(1,2,2,1)=C(4,4)
c C0(2,1,1,2)=C(4,4)
c C0(2,1,2,1)=C(4,4)
c ELSEIF (N==6) THEN
c C0(1,1,1,1)=C(1,1)
c C0(1,1,2,2)=C(1,2)
c C0(1,1,3,3)=C(1,3)
c C0(2,2,1,1)=C(2,1)
c C0(2,2,2,2)=C(2,2)
c C0(2,2,3,3)=C(2,3)
c C0(3,3,1,1)=C(3,1)
c C0(3,3,2,2)=C(3,2)
c C0(3,3,3,3)=C(3,3)

```

```

C0(1,2,1,2)=C(4,4)
C0(1,3,1,3)=C(5,5)
C0(2,3,2,3)=C(6,6)

```

c

```

C0(1,2,2,1)=C(4,4)
C0(1,3,3,1)=C(5,5)
C0(2,3,3,2)=C(6,6)
C0(2,1,1,2)=C(4,4)
C0(3,1,1,3)=C(5,5)
C0(3,2,2,3)=C(6,6)
C0(2,1,2,1)=C(4,4)
C0(3,1,3,1)=C(5,5)
C0(3,2,3,2)=C(6,6)

```

END IF

c

c 2) find the NTENSxNTENS matrix T(N,N) in the global coordinate system from the  
c 4th order tensor in the local coordinate system C0(3,3,3,3)

```

DO I=1,N
  DO J=1,N
    T(I,J)=0.d0
  END DO
END DO

```

c

```

DO M=1,3
  T(M,M)=0.d0
  DO I=1,3
    DO J=1,3
      DO K=1,3
        DO L=1,3
          T(M,M)=T(M,M)+DIR(I,M)*DIR(J,M)*DIR(K,M)*DIR(L,M)*
&          C0(I,J,K,L)
        END DO
      END DO
    END DO
  END DO
END DO

```

c

```

DO I=1,3
  DO J=1,3
    DO K=1,3
      DO L=1,3
        IF (N==4) THEN
          T(4,4)=T(4,4)+DIR(I,1)*DIR(J,2)*DIR(K,1)*DIR(L,2)*
&          C0(I,J,K,L)
          T(1,2)=T(1,2)+DIR(I,1)*DIR(J,1)*DIR(K,2)*DIR(L,2)*
&          C0(I,J,K,L)

```

```

      T(1,3)=T(1,3)+DIR(I,1)*DIR(J,1)*DIR(K,3)*DIR(L,3)*
&      C0(I,J,K,L)
      T(2,3)=T(2,3)+DIR(I,2)*DIR(J,2)*DIR(K,3)*DIR(L,3)*
&      C0(I,J,K,L)
      ELSE IF (N==6) THEN
      T(4,4)=T(4,4)+DIR(I,1)*DIR(J,2)*DIR(K,1)*DIR(L,2)*
&      C0(I,J,K,L)
      T(5,5)=T(5,5)+DIR(I,1)*DIR(J,3)*DIR(K,1)*DIR(L,3)*
&      C0(I,J,K,L)
      T(6,6)=T(6,6)+DIR(I,2)*DIR(J,3)*DIR(K,2)*DIR(L,3)*
&      C0(I,J,K,L)
      T(1,2)=T(1,2)+DIR(I,1)*DIR(J,1)*DIR(K,2)*DIR(L,2)*
&      C0(I,J,K,L)
      T(1,3)=T(1,3)+DIR(I,1)*DIR(J,1)*DIR(K,3)*DIR(L,3)*
&      C0(I,J,K,L)
      T(2,3)=T(2,3)+DIR(I,2)*DIR(J,2)*DIR(K,3)*DIR(L,3)*
&      C0(I,J,K,L)
      END IF
      END DO
      END DO
      END DO
      END DO
c
      T(2,1)=T(1,2)
      T(3,1)=T(1,3)
      T(3,2)=T(2,3)
c
      RETURN
      END
c
c
c
c
      SUBROUTINE kprind(ps,an,cs,e1 1p,e22p,e33p)
c
c Developed by R. Hinterhoelzl (1999)
c
      INCLUDE 'aba_param.inc'
      REAL*8 an(3,3),cs(3,3),ps(3)
c
c the principal values ps(3) are not ordered;
c now they are ordered to e33p>e22p>e1 1p since 3 will become the axis of
c symmetry of the transverse isotropy; accordingly the array of the cosines is
c changed to cs(3,3);
c
c 1) Change the direction of the normal vector if det(an)=-1 to get a
c coordinate system that satisfies the right hand rule

```

```

c
det=(an(1,1)*an(2,2)*an(3,3)+an(1,2)*an(2,3)*an(3,1)+
& an(1,3)*an(2,1)*an(3,2)-an(1,3)*an(2,2)*an(3,1)-
& an(1,2)*an(2,1)*an(3,3)-an(1,1)*an(2,3)*an(3,2))

```

```

c
IF(det<(-0.999d0)) THEN
  an(1,1)=-an(1,1)
  an(1,2)=-an(1,2)
  an(1,3)=-an(1,3)
  an(2,1)=-an(2,1)
  an(2,2)=-an(2,2)
  an(2,3)=-an(2,3)
  an(3,1)=-an(3,1)
  an(3,2)=-an(3,2)
  an(3,3)=-an(3,3)
END IF

```

```

c
c 2) find 3 as the major axis
  imax=1
  smax=ps(1)
  DO i=2,3
    IF(ps(i)>=smax) THEN
      imax=i
      smax=ps(i)
    END IF
  END DO

```

```

c
  e33p=ps(imax)

```

```

c
  cs(3,1)=an(imax,1)
  cs(3,2)=an(imax,2)
  cs(3,3)=an(imax,3)

```

```

c
c 3) find the next two axes
  IF(imax==1) THEN
    i2=2
    i3=3
  ELSE IF(imax==2) THEN
    i2=1
    i3=3
  ELSE
    i2=1
    i3=2
  END IF

```

```

c
  med=i2

```

```

    min=i3
    IF(ps(i3)>ps(i2)) THEN
        i3= med
        i2= min
    END IF
c
    e22p=ps(i2)
    e11p=ps(i3)
    DO k=1,3
        cs(2,k)=an(i2,k)
        cs(1,k)=an(i3,k)
    END DO
c
    RETURN
    END
C
C
C
C
    SUBROUTINE newperpHiSS(gamma1,alpha1,n1,R1,sigmaij,stressHiSS)
C
C Developed based on algorithm written by Gibson (2006)
C
C This function takes the HiSS surface definition parameters and the stress point to
C create a normal line from the Hydrostatic line to the stress point. It also finds the
C line intersection point on the HiSS surface, assuming the two solutions for the
C points on this line to be a quadratic relation. Three points are generated from an old
C Newton-Raphson scheme that then calls a function to find the coefficients and roots.
C
    INCLUDE 'aba_param.inc' !Required for ABAQUS UMAT
C
C Definition of Variables
C
C gamma - parameter gamma for the HiSS surface
C alpha - parameter alpha for the HiSS surface
C n - parameter n for the HiSS surface
C R - parameter R for the HiSS surface
C sigmaii - vector of principal stresses given
C stressHiSS - stress vector of HiSS surface point
C surfintercept
C sigaa
C a,b,c,d - define two point parametric equation of a line in 3D
C s1, surferr, count
C sigmaiia,sigmaiib
C s1newa,s1newb
C F,dF
C rootsel - variable to select the appropriate root from the N-R scheme

```

```

C xpoint - vector of three x points definining the polynomial
C ypoint - vector of three y points definining the polynomial
C qa,qb,qc - polynomial coefficients
C qc1,qc2,qc3,qc4 - parameters to determine qa,qb,qc from the (x,y) points
C
  REAL*8 sigmaij(3),stressHiSS(3),stressHiSSa(3),stressHiSSb(3),
  &   gamma1,alpha1,n1,R1,surfintercept1,sigaa,a,b,c,d,s1,
  &   F,dF,s1newa,rootsel
C   Variables required for the root calculation
  REAL*8 xpoint(3),ypoint(3),roots(2),
  &   qa,qb,qc,qc1,qc2,qc3,qc4
C
  surfintercept1=(1./3.)*(((alpha1/gamma1)**(1./(2.-n1)))-R1)
C
C   Determine the hydrostatic stress point (sigaa) that creates a perpendicular line
C   from the given stress point to the hydrostatic axis using the dot product rule for
C   90 degrees
  sigaa=(sigmaij(1)+sigmaij(2)+sigmaij(3))/3.
C
  IF (ABS(sigaa-surfintercept1)<0.00001) THEN
    stressHiSS(1)=surfintercept1
    stressHiSS(2)=surfintercept1
    stressHiSS(3)=surfintercept1
  ELSE
C   Point 1 is (sigmaii(1),sigmaii(2),sigmaii(3)) and point 2 is (sigaa,sigaa,sigaa)
C   Slope and intercept for equation of sigmaii(2)=f(sigmaii(1)) using two point
C   parametric equation for line in 3D space.
    a=(sigmaij(2)-sigaa)/(sigmaij(1)-sigaa)
    b=(-sigaa)*a+sigaa
C   Slope and intercept for equation of sigmaii(3)=f(sigmaii(1))
    c=(sigmaij(3)-sigaa)/(sigmaij(1)-sigaa)
    d=(-sigaa)*c+sigaa
C   This linear equations are substituted for sigmaii(2) and sigmaii(3) in the
C   HiSS surface equation.
C
    s1=sigaa !This term sets the initial value for sigma11
C
C   The following is the Newton-Raphson iteration given the function and its
C   derivative. An additional component is required to compute both solutions to the
C   flow surface (quadratic equation) and allow the algorithm to select the desired
C   solution which is the one between the hydrostatic sigaa and the actual stressij
C   (sigmaij).
C
C   Initialize Newton-Raphson to compute three points for the quadratic function.
  DO k=0,3
    F=(1./3.)*((s1**2)+((a*s1+b)**2)+((c*s1+d)**2)-(s1*(a*s1+b))-

```

```

&    ((a*s1+b)*(c*s1+d)-(s1*(c*s1+d))-gamma1*((s1+(a*s1+b)+
&    (c*s1+d)+R1)**2)+alpha1*((s1+(a*s1+b)+(c*s1+d)+R1)**n1)
C    The following equation had a bug fixed at 2*c*c*s1 term on the first line.
C    Originally 2*c*s1
dF=(1./3.)*(2.*s1+2.*a*a*s1+2.*a*b+2.*c*s1+2.*c*d+2.*a*s1+b+
&    2.*a*c*s1+b*c+a*d+2.*c*s1+d)-
&    2.*gamma1*(s1+a*s1+b+c*s1+d+R1)*(1.+a+c)+
&    n1*alpha1*((s1+a*s1+b+c*s1+d+R1)**(n1-1.))*(1.+a+c)
s1newa=s1-(F/dF)
IF (k==1) THEN
    xpoint(1)=s1
    ypoint(1)=F
ELSEIF (k==2) THEN
    xpoint(2)=s1
    ypoint(2)=F
ELSEIF (k==3) THEN
    xpoint(3)=s1
    ypoint(3)=F
END IF
s1=s1newa
END DO
C    Compute the roots of the quadratic function originated from the N-R
qc1=xpoint(1)*(ypoint(2)-ypoint(3))-
&    xpoint(2)*(ypoint(1)-ypoint(3))+
&    xpoint(3)*(ypoint(1)-ypoint(2))
qc2=xpoint(1)*xpoint(1)*(ypoint(2)-ypoint(3))-
&    xpoint(2)*xpoint(2)*(ypoint(1)-ypoint(3))+
&    xpoint(3)*xpoint(3)*(ypoint(1)-ypoint(2))
qc3=xpoint(1)*xpoint(1)*(xpoint(2)-xpoint(3))-
&    xpoint(2)*xpoint(2)*(xpoint(1)-xpoint(3))+
&    xpoint(3)*xpoint(3)*(xpoint(1)-xpoint(2))
qc4=xpoint(1)*xpoint(1)*(xpoint(2)*ypoint(3)-xpoint(3)*ypoint(2))-
&    xpoint(2)*xpoint(2)*(xpoint(1)*ypoint(3)-xpoint(3)*ypoint(1))+
&    xpoint(3)*xpoint(3)*(xpoint(1)*ypoint(2)-xpoint(2)*ypoint(1))
qc2=-qc2
qc4=-qc4
C
qa=-qc1/qc3
qb=-qc2/qc3
qc=-qc4/qc3
C
roots(1)=(-qb+SQRT(qb*qb-4.*qa*qc))/(2.*qa)
roots(2)=(-qb-SQRT(qb*qb-4.*qa*qc))/(2.*qa)
C
stressHiSSa(1)=roots(1)
stressHiSSa(2)=a*roots(1)+b

```

```

stressHissa(3)=c*roots(1)+d
C
stressHiSSb(1)=roots(2)
stressHiSSb(2)=a*roots(2)+b
stressHissb(3)=c*roots(2)+d
C
rootsel=(stressHiSSa(1)-sigaa)*(sigmaj(1)-sigaa)+
& (stressHiSSa(2)-sigaa)*(sigmaj(2)-sigaa)+
& (stressHiSSa(3)-sigaa)*(sigmaj(3)-sigaa)
IF (rootsel>0.) THEN
stressHiSS(1)=stressHiSSa(1)
stressHiSS(2)=stressHiSSa(2)
stressHiSS(3)=stressHiSSa(3)
ELSE
stressHiSS(1)=stressHiSSb(1)
stressHiSS(2)=stressHiSSb(2)
stressHiSS(3)=stressHiSSb(3)
END IF
END IF
RETURN
END
C
C
C
SUBROUTINE dHiss(gamma2,alpha2,n2,R2,sii,dFds)
C
C Developed based on algorithm written by Gibson (2006)
C
C This function computes the normal vector dFds on the HiSS surface using the surface
C parameters and the applied stress point as inputs
C
INCLUDE 'aba_param.inc' !Required for ABAQUS UMAT
C
C Definition of variables
C
C gamma - parameter gamma for the HiSS surface
C alpha - parameter alpha for the HiSS surface
C n - parameter n for the HiSS surface
C R - parameter R for the HiSS surface
C sii - vector of principal stresses
C dFds - normal vector to the HiSS surface
C
REAL*8 sii(3),dFds(3),gamma2,alpha2,n2,R2
C
dFds(1)=(1./3.)*(2.*sii(1)-sii(2)-sii(3))-
& 2.*gamma2*(sii(1)+sii(2)+sii(3)+R2)+

```

```

&    n2*alpha2*((sii(1)+sii(2)+sii(3)+R2)**(n2-1.))
dFds(2)=(1./3.)*(2.*sii(2)-sii(1)-sii(3))-
&    2.*gamma2*(sii(1)+sii(2)+sii(3)+R2)+
&    n2*alpha2*((sii(1)+sii(2)+sii(3)+R2)**(n2-1.))
dFds(3)=(1./3.)*(2.*sii(3)-sii(1)-sii(2))-
&    2.*gamma2*(sii(1)+sii(2)+sii(3)+R2)+
&    n2*alpha2*((sii(1)+sii(2)+sii(3)+R2)**(n2-1.))
RETURN
END
C
C
C
SUBROUTINE unitvector(vec,uvec)
C
C This function computes the unit vector of a given vector
C
INCLUDE 'aba_param.inc' !Required for ABAQUS UMAT
C
C Definition of variables
C
C vec - vector
C uvec - unit vector
C
REAL*8 vec(3),uvec(3)
C
DO k=1,3
uvec(k)=vec(k)*(1./(SQRT(vec(1)*vec(1)+
&    vec(2)*vec(2)+vec(3)*vec(3))))
END DO
RETURN
END
C
C
C
SUBROUTINE gethydrpntext(sigii,pointHiSS,hydrostress)
C
C Developed based on algorithm written by Gibson (2006)
C
C This function computes the intersection between the line passing by the applied stress
C and the HiSS stress points and the Hydrostatic line
C
INCLUDE 'aba_param.inc' !Required for ABAQUS UMAT
C
C Definition of Variables
C
C sigii - vector of applied stress

```

```

C pointHiSS - vector of point on HiSS surface
C hydrostress - output of this function - the intercept
C s13slope - slope of the 3D line
C
  REAL*8 sigii(3),pointHiSS(3),s13slope,hydrostress
C
  s13slope=(pointHiSS(1)-sigii(1))/(pointHiSS(3)-sigii(3))
C   IF (1.-s13slope==0.) THEN
C     hydrostress = 0.
C   ELSE
C     hydrostress = (pointHiSS(1)-(s13slope*pointHiSS(3)))/(1.-s13slope)
C   END IF
  RETURN
  END
C
C
C
  SUBROUTINE HNR(g,u,lambda1,gamma1,alpha1,n1,R1,
&               stressHiSS,dFds)
C
C Developed based on algorithm written by Gibson (2006)
C
C This function applies a Newton-Raphson algorithm to find a point on the Hiss
C surface that is normal to the applied stress point.
C
  REAL*8 g(3),u(3),stressHiSS(3),dFds(3),unew(3)
  REAL*8 lambda1,gamma1,alpha1,n1,R1

  REAL*8 F1,F2,F3,F4,vct1,vct2,vct3,vct4,vct1store,vct2store,
& vct3store,vct4store,dF1d1,dF1d2,dF1d3,dF1dlm,dF2d1,dF2d2,
& dF2d3,dF2dlm,dF3d1,dF3d2,dF3d3,dF3dlm,dF4d1,dF4d2,dF4d3,
& dF4dlm,dF1d1store,dF1d2store,dF1d3store,dF1dlmstore,
& dF2d1store,dF2d2store,dF2d3store,dF2dlmstore,dF3d1store,
& dF3d2store,dF3d3store,dF3dlmstore,dF4d1store,dF4d2store,
& dF4d3store,dF4dlmstore,magold,magnew,errolld,ernnew,
& surfintercept1
  INTEGER FLAG,imax
C
  surfintercept1=(1./3.)*(((alpha1/gamma1)**(1./(2.-n1))))-R1)
  FLAG = 0 !Flag if solution is complex
c   Compute magnitude for error analysis
  magold=SQRT(u(1)**2.+u(2)**2.+u(3)**2.)
  errolld=1.
  imax=20
  DO i=1,imax
c

```

IF (FLAG==0) THEN

F1=(g(1)-u(1))-lambda1\*(((1./3.)\*(2.\*u(1)-u(2)-u(3))-2.\*gamma1\*  
& (u(1)+u(2)+u(3)+R1)+alpha1\*n1\*((u(1)+u(2)+u(3)+R1)\*\*(n1-1.))))  
F2=(g(2)-u(2))-lambda1\*(((1./3.)\*(2.\*u(2)-u(1)-u(3))-2.\*gamma1\*  
& (u(1)+u(2)+u(3)+R1)+alpha1\*n1\*((u(1)+u(2)+u(3)+R1)\*\*(n1-1.))))  
F3=(g(3)-u(3))-lambda1\*(((1./3.)\*(2.\*u(3)-u(2)-u(1))-2.\*gamma1\*  
& (u(1)+u(2)+u(3)+R1)+alpha1\*n1\*((u(1)+u(2)+u(3)+R1)\*\*(n1-1.))))  
F4=(1./3.)\*(u(1)\*u(1)+u(2)\*u(2)+u(3)\*u(3)-u(1)\*u(2)-u(2)\*u(3)-  
& u(1)\*u(3))-gamma1\*((u(1)+u(2)+u(3)+R1)\*\*2.))+alpha1\*((u(1)+  
& u(2)+u(3)+R1)\*\*n1)

C

dF1d1=-1.-lambda1\*(((1./3.)\*(2.-2.\*gamma1\*(1.))+alpha1\*n1\*  
7 (n1-1.))\*((u(1)+u(2)+u(3)+R1)\*\*(n1-2.))\*1.)  
dF1d2=-lambda1\*(((1./3.)\*(-1.-2.\*gamma1\*(1.))+alpha1\*n1\*(n1-1.)\*  
& ((u(1)+u(2)+u(3)+R1)\*\*(n1-2.))\*1.)  
dF1d3=-lambda1\*(((1./3.)\*(-1.-2.\*gamma1\*(1.))+alpha1\*n1\*(n1-1.)\*  
& ((u(1)+u(2)+u(3)+R1)\*\*(n1-2.))\*1.)  
dF1dlm=-((1./3.)\*(2.\*u(1)-u(2)-u(3))-2.\*gamma1\*(u(1)+u(2)+u(3)+  
& R1)+alpha1\*n1\*((u(1)+u(2)+u(3)+R1)\*\*(n1-1.)))

C

dF2d2=-1.-lambda1\*(((1./3.)\*(2.-2.\*gamma1\*(1.))+alpha1\*n1\*  
& (n1-1.))\*((u(1)+u(2)+u(3)+R1)\*\*(n1-2.))\*1.)  
dF2d1=-lambda1\*(((1./3.)\*(-1.-2.\*gamma1\*(1.))+alpha1\*n1\*(n1-1.)\*  
& ((u(1)+u(2)+u(3)+R1)\*\*(n1-2.))\*1.)  
dF2d3=-lambda1\*(((1./3.)\*(-1.-2.\*gamma1\*(1.))+alpha1\*n1\*(n1-1.)\*  
& ((u(1)+u(2)+u(3)+R1)\*\*(n1-2.))\*1.)  
dF2dlm=-((1./3.)\*(2.\*u(2)-u(1)-u(3))-2.\*gamma1\*(u(1)+u(2)+u(3)+  
& R1)+alpha1\*n1\*((u(1)+u(2)+u(3)+R1)\*\*(n1-1.)))

C

dF3d3=-1.-lambda1\*(((1./3.)\*(2.-2.\*gamma1\*(1.))+alpha1\*n1\*  
& (n1-1.))\*((u(1)+u(2)+u(3)+R1)\*\*(n1-2.))\*1.)  
dF3d2=-lambda1\*(((1./3.)\*(-1.-2.\*gamma1\*(1.))+alpha1\*n1\*(n1-1.)\*  
& ((u(1)+u(2)+u(3)+R1)\*\*(n1-2.))\*1.)  
dF3d1=-lambda1\*(((1./3.)\*(-1.-2.\*gamma1\*(1.))+alpha1\*n1\*(n1-1.)\*  
& ((u(1)+u(2)+u(3)+R1)\*\*(n1-2.))\*1.)  
dF3dlm=-((1./3.)\*(2.\*u(3)-u(2)-u(1))-2.\*gamma1\*(u(1)+u(2)+u(3)+  
\$ R1)+alpha1\*n1\*((u(1)+u(2)+u(3)+R1)\*\*(n1-1.)))

C

dF4d1=((1./3.)\*(2.\*u(1)-u(2)-u(3))-2.\*gamma1\*(u(1)+u(2)+u(3)+R1)+  
& alpha1\*n1\*((u(1)+u(2)+u(3)+R1)\*\*(n1-1.)))  
dF4d2=((1./3.)\*(2.\*u(2)-u(1)-u(3))-2.\*gamma1\*(u(1)+u(2)+u(3)+R1)+  
& alpha1\*n1\*((u(1)+u(2)+u(3)+R1)\*\*(n1-1.)))  
dF4d3=((1./3.)\*(2.\*u(3)-u(2)-u(1))-2.\*gamma1\*(u(1)+u(2)+u(3)+R1)+  
& alpha1\*n1\*((u(1)+u(2)+u(3)+R1)\*\*(n1-1.)))  
dF4dlm=0.

C

$vct1store = -F1 + dF1d1 * u(1) + dF1d2 * u(2) + dF1d3 * u(3) + dF1dlm * lambda1$   
 $vct2store = -F2 + dF2d1 * u(1) + dF2d2 * u(2) + dF2d3 * u(3) + dF2dlm * lambda1$   
 $vct3store = -F3 + dF3d1 * u(1) + dF3d2 * u(2) + dF3d3 * u(3) + dF3dlm * lambda1$   
 $vct4store = -F4 + dF4d1 * u(1) + dF4d2 * u(2) + dF4d3 * u(3) + dF4dlm * lambda1$

C

$vct1 = vct4store$   
 $vct2 = vct1store$   
 $vct3 = vct2store$   
 $vct4 = vct3store$

C

$dF1d1store = dF1d1$   
 $dF1d2store = dF1d2$   
 $dF1d3store = dF1d3$   
 $dF1dlmstore = dF1dlm$

C

$dF2d1store = dF2d1$   
 $dF2d2store = dF2d2$   
 $dF2d3store = dF2d3$   
 $dF2dlmstore = dF2dlm$

C

$dF3d1store = dF3d1$   
 $dF3d2store = dF3d2$   
 $dF3d3store = dF3d3$   
 $dF3dlmstore = dF3dlm$

C

$dF4d1store = dF4d1$   
 $dF4d2store = dF4d2$   
 $dF4d3store = dF4d3$   
 $dF4dlmstore = dF4dlm$

C

$dF1d1 = dF4d1store$   
 $dF1d2 = dF4dlmstore$   
 $dF1d3 = dF4d2store$   
 $dF1dlm = dF4d3store$

C

$dF2d1 = dF1d1store$   
 $dF2d2 = dF1dlmstore$   
 $dF2d3 = dF1d2store$   
 $dF2dlm = dF1d3store$

C

$dF3d1 = dF2d1store$   
 $dF3d2 = dF2dlmstore$   
 $dF3d3 = dF2d2store$   
 $dF3dlm = dF2d3store$

C

$dF4d1 = dF3d1store$

```

dF4d2=dF3dlmstore
dF4d3=dF3d2store
dF4dlm=dF3d3store
C
C   begin Gauss-Jordan Elminiation
C
C   normalize first row
dF1d1store=dF1d1
dF1d1=1.
dF1d2=dF1d2/dF1d1store
dF1d3=dF1d3/dF1d1store
dF1dlm=dF1dlm/dF1d1store
vct1=vct1/dF1d1store
C
C   column1
dF4d1store=dF4d1
dF4d1=0.
dF4d2=dF4d2-dF1d2*dF4d1store
dF4d3=dF4d3-dF1d3*dF4d1store
dF4dlm=dF4dlm-dF1dlm*dF4d1store
vct4=vct4-vct1*dF4d1store
C
dF3d1store=dF3d1
dF3d1=0.
dF3d2=dF3d2-dF1d2*dF3d1store
dF3d3=dF3d3-dF1d3*dF3d1store
dF3dlm=dF3dlm-dF1dlm*dF3d1store
vct3=vct3-vct1*dF3d1store
C
dF2d1store=dF2d1
dF2d1=0.
dF2d2=dF2d2-dF1d2*dF2d1store
dF2d3=dF2d3-dF1d3*dF2d1store
dF2dlm=dF2dlm-dF1dlm*dF2d1store
vct2=vct2-vct1*dF2d1store
C
C   normalize second row
dF2d2store=dF2d2
dF2d1=dF2d1/dF2d2store
dF2d2=1.
dF2d3=dF2d3/dF2d2store
dF2dlm=dF2dlm/dF2d2store
vct2=vct2/dF2d2store
C
C   column2
dF4d2store=dF4d2

```

```

dF4d2=0.
dF4d3=dF4d3-dF2d3*dF4d2store
dF4d1m=dF4d1m-dF2d1m*dF4d2store
vct4=vct4-vct2*dF4d2store

```

C

```

dF3d2store=dF3d2
dF3d2=0.
dF3d3=dF3d3-dF2d3*dF3d2store
dF3d1m=dF3d1m-dF2d1m*dF3d2store
vct3=vct3-vct2*dF3d2store

```

C

C

```

normalize third row
dF3d3store=dF3d3
dF3d1=dF3d1/dF3d3store
dF3d2=dF3d2/dF3d3store
dF3d3=1.
dF3d1m=dF3d1m/dF3d3store
vct3=vct3/dF3d3store

```

C

C

```

column3
dF4d3store=dF4d3
dF4d3=0.
dF4d1m=dF4d1m-dF3d1m*dF4d3store
vct4=vct4-vct3*dF4d3store

```

C

C

```

solveforallnewstuff
unew(3)=vct4/dF4d1m
unew(2)=(vct3-dF3d1m*unew(3))/dF3d3
lambda1=(vct2-dF2d1m*unew(3)-dF2d3*unew(2))/dF2d2
unew(1)=(vct1-dF1d1m*unew(3)-dF1d3*unew(2)-dF1d2*lambda1)/dF1d1

```

c

```

IF (unew(1)<-R1/3. .OR. unew(1)>surfintercept1) THEN
  u(1)=0
  u(2)=0.
  u(3)=0.
  FLAG=1
  EXIT
END IF
IF (unew(2)<-R1/3. .OR. unew(2)>surfintercept1) THEN
  u(1)=0
  u(2)=0.
  u(3)=0.
  FLAG=1
  EXIT
END IF
IF (unew(3)<-R1/3. .OR. unew(3)>surfintercept1) THEN

```

```

    u(1)=0
    u(2)=0.
    u(3)=0.
    FLAG=1
    EXIT
END IF

IF (unew(1)+unew(2)+unew(3)+R1<0.) THEN
    u(1)=0.
    u(2)=0.
    u(3)=0.
    FLAG=1
    EXIT
ELSE
    u(1)=unew(1) !0.
    u(2)=unew(2) !0.
    u(3)=unew(3) !0.
END IF
C   Verify error with tolerance
    magnew=SQRT(u(1)**2.+u(2)**2.+u(3)**2.)
    errnew=ABS(magold-magnew)/magnew
IF (errnew <=0.01) THEN
C   test=1
    EXIT
ELSE
    !IF (errnew>errold) THEN
    ! countconver=countconver+1
    !ENDIF
    !IF (countconver >=10) THEN
    ! !FLAG=1
    ! !EXIT
    ! !ENDIF
END IF
magold=magnew
errold=errnew
c
END IF
END DO
IF (i>imax) THEN
    stressHiSS(1)=0.
    stressHiSS(2)=0.
    stressHiSS(3)=0.
    dFds(1)=0.
    dFds(2)=0.
    dFds(3)=0.
ELSE

```

```

stressHiSS(1)=u(1)
stressHiSS(2)=u(2)
stressHiSS(3)=u(3)
IF (FLAG==0) THEN
  dFds(1)=(((1./3.)*(2.*u(1)-u(2)-u(3))-2.*gamma1*(u(1)+u(2)+u(3)+
&      R1)+alpha1*n1*((u(1)+u(2)+u(3)+R1)**(n1-1.))))
  dFds(2)=(((1./3.)*(2.*u(2)-u(1)-u(3))-2.*gamma1*(u(1)+u(2)+u(3)+
&      R1)+alpha1*n1*((u(1)+u(2)+u(3)+R1)**(n1-1.))))
  dFds(3)=(((1./3.)*(2.*u(3)-u(2)-u(1))-2.*gamma1*(u(1)+u(2)+u(3)+
&      R1)+alpha1*n1*((u(1)+u(2)+u(3)+R1)**(n1-1.))))
  ELSE
    dFds(1)=0.
    dFds(2)=0.
    dFds(3)=0.
  END IF
C
  END IF
  RETURN
  END
C
C
C
SUBROUTINE princord(pps,psor)
c
c  pps - principal stress obtain from ABAQUS subroutine sprind
c  psor - ordered principal p33>>p22>>p11
c
  INCLUDE 'aba_param.inc'
  REAL*8 pps(3),psor(3)
c
c the principal values ps(3) are not ordered;
c now they are ordered to psor(3)>psor(2)>psor(1), being compression (-).
c
  imax=1
  smax=pps(1)
  DO i=2,3
    IF (pps(i)>=smax) THEN
      imax=i
      smax=pps(i)
    END IF
  END DO
c
  psor(3)=pps(imax)
c
  IF (imax==1) THEN
    i2=2

```

```

    i3=3
ELSEIF (imax==2) THEN
    i2=1
    i3=3
ELSE
    i2=1
    i3=2
END IF
c
med=i2
min=i3
IF (pps(i3)>pps(i2)) THEN
    i3= med
    i2= min
END IF
c
psor(2)=pps(i2)
psor(1)=pps(i3)
c
RETURN
END
C
C
C

```

## References

- ABAQUS (2006). ABAQUS Analysis Users Manual (v6.6), HKS, Inc., Providence, RI.
- Bonaquist, R. (2008), "Refining the Simple Performance Tester for Use in Routine Practice," National Cooperative Highway Research Program Project 9-29, Report 614, Transportation Research Board of the National Academies, Washington, DC.
- Brown, S. F., and B. V. Brodrick (1999), 25 Years' Experience with the Pilot-Scale Nottingham Pavement Test Facility. Presented at the International Conference on Accelerated Pavement Testing, Reno, NV.
- Brown, S.F. and F.W.K Chan (1996), Reduced Rutting in Unbound Granular Pavement Layers Through Improved Grading Design, *Proceedings of the Institution of Civil Engineers: Transport*, Vol. 117, No. 1, pp. 40-49.
- Chehab, G.R., Y.R Kim, R.A. Schapery, M.W. Witzcak, and R. Bonaquist, "Time Temperature Superposition Principle for Asphalt Concrete Mixtures with Growing Damage in Tension State," *Journal of the Association of Asphalt Paving Technologists*, Vol. 71, 2002, pp. 559-593.
- Chehab, G.R., Y.R. Kim, R.A. Schapery, R.A., M.W. Witzcak, and R. Bonaquist (2003). "Characterization of Asphalt Concrete in Uniaxial Tension using a Viscoelastoplastic Model," *Journal of the Association of Asphalt Paving Technologists*, pp. 315-355.

Christensen, D.W., T.K. Pellinen, and R.F. Bonaquist (2003), “Hirsch Model for Estimating the Modulus of Asphalt Concrete,” *Journal of the Association of Asphalt Paving Technologists*, Vol. 72, pp. 97–121.

Claussen, A.I.M., J.M. Edwards, P. Sommer, P. Udge (1977), “Asphalt Pavement Design - The Shell Method,” *Proceedings of the Fourth International Conference on the Structural Design of Asphalt Pavements*, pp. 39-74, Ann Arbor, MI.

Crockford, W.W. (1993), “Role of Principal-Plane Rotation in Flexible Pavement Deformation,” *Journal of Transportation Engineering*, Vol. 119, No. 1, pp. 124-141.

Deacon, J. A., J.T. Harvey, I. Guada, L. Popescu, and C.L. Monismith (2002), “Analytically Based Approach to Rutting Prediction,” *Transportation Research Record*, No. 1806, pp 9-18.

Epps, J.A., Hand, A., Seeds, S., Schulz, T., Alavi, S., Ashmore, C., Monismith, C.L., Deacon, J.A., Harvey, J.T., Leahy, R. 2002. Recommended Performance-Related Specification for Hot-Mix Asphalt Construction: Results of the Westrack Project. NCHRP Report 455, Transportation Research Board, National Research Council, Washington, DC.

Fang, H., J.E. Haddock, T.D. White, A.J. Hand (2004), “On the Characterization of Flexible Pavement Rutting Using Creep Model-based Finite Element Analysis,” *Finite Elements in Analysis and Design*, Vol. 41, pp. 49-73.

FHWA (2003), “Distress Identification Manual for the Long-Term Pavement Performance Program,” Fourth Revised Edition FHWA-RD-03-031, Washington, DC.

Finn, F., C. Saraf, R. Kulkarni, K. Nair, W. Smith, A. Abdullah (1977), “The Use of Distress Prediction Subsystems for the Design of Pavement Structures,” *Proceedings of Fourth International Conference Structural Design of Asphalt Pavements*, pp. 3-37, Ann Arbor, MI.

Gibson, N.H. (2006). “A Viscoelastoplastic Continuum Damage Model for the Compressive Behavior of Asphalt Concrete,” Ph.D. dissertation, University of Maryland, College Park, MD.

Gibson, N.H. (2011). “Full-Scale Accelerated Performance Testing for Superpave and Structural Validation: Transportation Pooled Fund Study TPF-5(019) and SPR-2(174) Accelerated Pavement Testing of Crumb Rubber Modified Asphalt Pavements,” Federal Highway Administration, Report No. FHWA-HRT-11-045, McLean, VA.

Ha, K. (1996), “Evaluation of Three-Dimensional of Viscoelastic Constitutive Model of Solid Propellant with Distributed Damage,” Ph.D. Dissertation, University of Texas, Austin, TX.

Ha, K. and R.A. Schapery (1998), “A Three-Dimensional Viscoelastic Constitutive Model for Particulate Composites with Growing Damage and Its Experimental Verification,” *International Journal of Solids and Structures*, Vol. 35, No. 26-27, pp. 3497-3517.

Hornych, P., A. Kazai, and A. Quibel (2000), "Modeling a Full-Scale Experiment of Two Flexible Pavement Structures with Unbound Granular Bases," *Unbound Aggregates in Road Construction*, Rotterdam, Netherlands, pp. 359–367.

Hua, J. (2000), "Finite Element Modeling and Analysis of Accelerated Pavement Testing Devices and Rutting Phenomenon," Ph.D. Dissertation, Purdue University, West Lafayette, IN.

Huang, B., L. Mohammad, W. Wathugala (2002), "Development of a Thermo-Viscoplastic Constitutive Model for HMA Mixtures," *Journal of the Association of Asphalt Paving Technologists*, Vol. 71, pp. 594-618.

Huang, Chien-Wei, R.K. Abu Al-Rub, E.A. Masad, D.N. Little (2011a), "Three-Dimensional Simulations of Asphalt Pavement Permanent Deformation Using a Nonlinear Viscoelastic and Viscoplastic Model," *Journal of Materials in Civil Engineering*, Vol. 23, No. 1, pp. 56-68.

Huang, Chien-Wei, R.K. Abu Al-Rub, E.A. Masad, D.N. Little, G.D. Airey (2011b), "Numerical implementation and validation of a nonlinear viscoelastic and viscoplastic model for asphalt mixes," *International Journal of Pavement Engineering*, Vol. 12, No. 4, pp. 433-447.

Kassem, E., E. Masad, A. Chowdhury, and G. Claros (2008), "Influence of field compaction pattern on asphalt pavement uniformity," *Journal of the Association of Asphalt Paving Technologists*, Vol. 77, pp. 257-298

Kenis, W.J (1977), "Predictive Design Procedures - A Design Method for Flexible Pavements Using the VESYS Structural Subsystem," *Proceedings of the*

*Fourth International Conference on the Structural Design of Asphalt Pavements*, pp. 101-130, Ann Arbor, MI.

Kim, I.T., E. Tutumluer (2005), “Unbound Aggregate Rutting Models for Stress Rotations and Effects of Moving Wheel Loads,” *Transportation Research Record*, Vol. 1913, pp. 41-49.

Kim, Y. R., M.N. Guddati, B.S. Underwood, T.Y. Yun, V. Subramanian, and S. Savadatti (2009), “Development of a Multiaxial Viscoelastoplastic Continuum Damage Model for Asphalt Mixtures,” Federal Highway Administration Report FHWA-HRT-08-073, Washington, DC.

Leahy, R.B (1989), “Permanent Deformation Characteristics of Asphalt Concrete,” Ph.D. Dissertation, University of Maryland, College Park, MD.

Lee, H.J., and Y.R. Kim (1998), “Viscoelastic Constitutive Model for Asphalt Concrete Under Cyclic Loading,” *Journal of Engineering Mechanics*, ASCE, Vol. 124, No. 1, pp. 32-40.

Lu, Y., P.J., Wright (1998), “Numerical Approach of Visco-Elastoplastic Analysis for Asphalt Mixtures,” *Computers and Structures*, Vol. 69, pp 139-157.

Masad, E., B. Muhunthan, N. Shashidhar, and T. Harman (1999), “Internal Structure Characterization of Asphalt Concrete Using Image Analysis,” *Journal of Computing in Civil Engineering*, Vol. 13, No. 2, pp. 88-95.

Masad, E., C.W. Huang, G. Airey, A. Muliana (2008), “Nonlinear Viscoelastic Analysis of Unaged and Aged Asphalt Binders,” *Construction and Building Materials*, Vol. 22, pp 2170-2179.

Massad, E., L., Tashman, D. Little, H. Zbib (2005), “Viscoplastic Modeling of Asphalt Mixes with the Effects of Anisotropy, Damage, and Aggregate Characteristics,” *Journal of Mechanics of Materials*, Vol. 37, pp. 1242-1256.

MnRoad. 1998. Minnesota Road Research Project (MnRoad), Minnesota Department of Transportation, Minneapolis, MN.

Monismith, C.L., L. Popescu, and J.T. Harvey (2006), “Rut Depth Estimation for Mechanistic-Empirical Pavement Design Using Simple Shear Test Results,” *Association of Asphalt Paving Technologists*, Vol. 75, 1294-1338.

NCHRP (2004), “Development of the 2002 Guide for the Design of New and Rehabilitated Pavement Structures: Phase II,” National Cooperative Highway Research Program, Project 1-37A Final Report, Washington, DC.

Onyango, M. (2009), “Verification of Mechanistic Prediction Models for Permanent Deformation in Asphalt Mixes Using Accelerated Pavement Testing,” Ph.D. Dissertation, Kansas State University, Manhattan, KS

Park, D. (2004), “Characterization of Permanent Deformation in Asphalt Concrete Using a Laboratory Prediction Method and an Elastic-Viscoplastic Model,” Ph.D. Dissertation, Texas A&M University, College Station, TX.

Park, S.W. and R.A. Schapery (1997), “Viscoelastic constitutive model for particulate composites with growing damage,” *International Journal of Solids and Structures*, Vol. 34, No. 8, p 931-947.

Park, S.W., Y.R. Kim, and R.A. Schapery (1996), “A Viscoelastic Continuum Damage Model and Its Application to Uniaxial Behavior of Asphalt Concrete,” *Mechanics of Materials*, Vol. 24, pp. 241-255.

Perl, M., J. Uzan, A.Sides (1983), “Visco-elasto-plastic Constitutive Law for Bituminous Mixture Under Repeated Loading,” *Transportation Research Record*, No. 911, pp. 20-26.

Perl, M., J. Uzan, A.Sides (1983), “Visco-elasto-plastic Constitutive Law for Bituminous Mixture Under Repeated Loading,” *Transportation Research Record*, No. 911, pp. 20-26.

Qi, X., M.W. Witczak (1998), “Time-dependent permanent deformation models for asphaltic mixtures,” *Transportation Research Record*, Vol. 1639, pp. 83-93.

Qi, Xicheng, Al-Khateeb, G., Mitchell, T., Stuart, K., Youtcheff, J., (2004), “Determining Modified Asphalt Binder Properties for the Superpave Specification,” Report on the Construction of Pavements with Modified Asphalt Binders, Federal Highway Administration.

Rauhut, J.B (1980), “Permanent Deformation Characterization of Bituminous Mixtures for Predicting Pavement Rutting,” *Transportation Research Record*, Vol. 777, pp. 9-14.

Sadd, M.H., D.Q. Parameswaran, A. Shukla (2004), “Simulation of Asphalt Materials Using Finite Element Micromechanical Model with Damage Mechanics,” *Transportation Research Record*, Vol. 1832, pp. 86-95.

Schapery, R.A. (1985), “A Micromechanical Model for Non-Linear Viscoelastic Behavior of Particle-Reinforced Rubber with Distributed Damage,” *Engineering Fracture Mechanics*, Vol. 25, No. 5-6, p 845-867.

Schwartz, C.W., N.H. Gibson, R.A. Schapery, and M.W. Witczak (2002). "Time-Temperature Superposition for Asphalt Concrete at Large Compressive Strains," *Transportation Research Record*, No. 1789, pp. 101-112.

Schwartz, C.W., R.L. Carvalho (2007). "The complex guiding the simple: Enhancement of mechanistic-empirical pavement rutting models using nonlinear finite element analysis," *Proceedings of the Advanced Characterization of Pavement and Soil Engineering Materials Conference*, Athens, Greece, Vol. 1, pp. 441-449.

Schwartz, C.W., R.L. Carvalho (2008). "Distribution of permanent deformations within HMA layers," *Proceedings of ASCE 2008 Airfield & Highway Pavements Conference*, Bellevue, WA, p 86-98.

Seibi, A.C., M.G. Sharma, G.A. Ali, W.J. Kenis (2001), "Constitutive Relations for Asphalt Concrete Under High Rates of Loading," *Transportation Research Record*, Vol. 1767, pp. 111-119.

Shook, J.F., F.N. Finn, M.W. Witczak, C.L. Monismith (1982), "Thickness Design of Asphalt Pavements - The Asphalt Institute Method," *Proceedings of the Fifth International Conference on the Structural Design of Asphalt Pavements*, pp. 17-44, Delft, Netherlands.

Simpson, A. L., J. F. Daleiden, and W. O. Hadley, "Rutting Analysis From a Different Perspective," *Transportation Research Record*, Vol. 1473, pp. 9-17.

Sousa, J. B., J. A. Deacon, S. Weissman, J. T. Harvey, C. L. Monismith, R. B. Leahy, G. Paulsen, and J. S. Coplantz (1994), "Permanent Deformation Response of Asphalt-Aggregate Mixes," Report No SHRP-A-415, Strategic Highway Research Program, National Research Council, Washington, D.C.

Tashman, L., E. Massad, D. Little, H. Zbib (2004), "A Microstructure-Based Viscoplastic Model for Asphalt Concrete," *International Journal of Plasticity*, Vol. 2, pp. 1659-1685.

White, T.D., J.E. Haddock, A.J.T. Hand, H. Fang (2002), "Contributions of Pavement Structural Layers to Rutting of Hot Mix Asphalt Pavements," National Cooperative Highway Research Program, Report 468, Washington, DC

Yoo, P.J., I.L. Al-Qadi, M.A. Elseifi, I. Janajreh (2006), "Flexible Pavement Responses to Different Loading Amplitudes Considering Layer Interface Condition and Lateral Shear Forces," *The International Journal of Pavement Engineering*, Vol. 7, No. 1, pp. 73-86.

Zhao, Y. and Y.R. Kim (2003), "Time-Temperature Superposition for Asphalt Mixtures with Growing Damage and Permanent Deformation in Compression," *Transportation Research Record*, No. 1832, pp. 161-172.